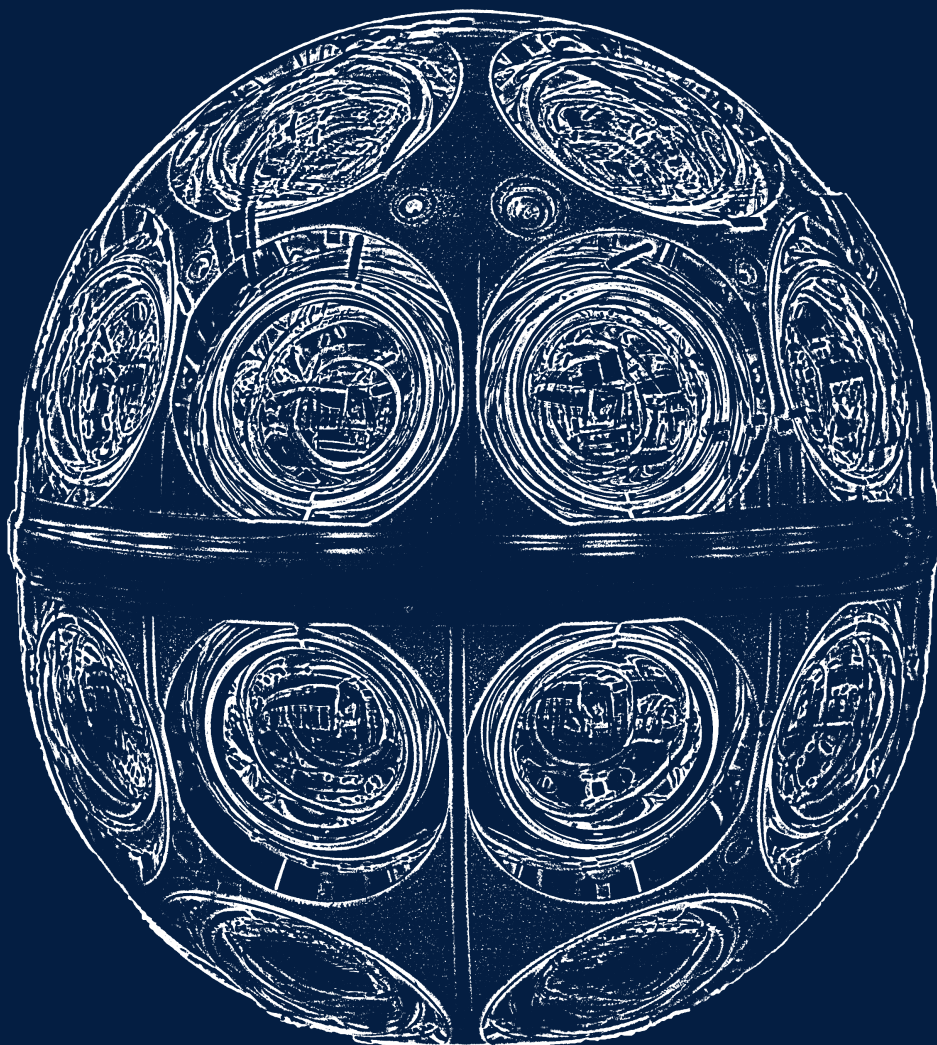




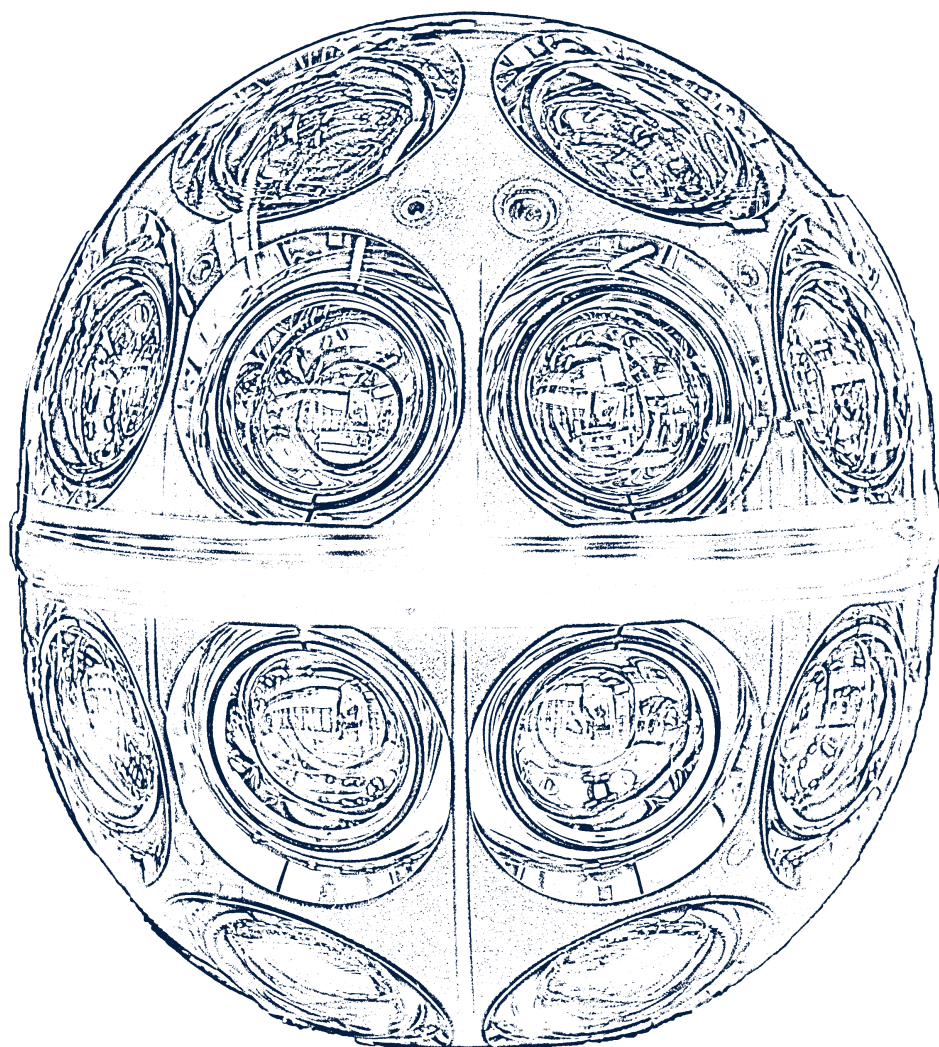
Friedrich-Alexander-Universität  
Erlangen-Nürnberg



# Characterization of the mDOM light detection and signal processing system for the IceCube Upgrade



submitted by Judith Schneider



Cover page illustration by Martin Schneider; photograph by S. Niedworok/DESY



Friedrich-Alexander-Universität  
Erlangen-Nürnberg



# Characterization of the mDOM light detection and signal processing system for the IceCube Upgrade

Charakterisierung des mDOM-Lichtdetektions- und Signal-  
verarbeitungssystems für das IceCube Upgrade

Der Naturwissenschaftlichen Fakultät  
der Friedrich-Alexander-Universität Erlangen-Nürnberg  
zur Erlangung des Doktorgrades Dr. rer. nat.



vorgelegt von  
**Judith Schneider**  
aus Bamberg



Als Dissertation genehmigt von der Naturwissenschaftlichen Fakultät  
der Friedrich-Alexander-Universität Erlangen-Nürnberg

Tag der mündlichen Prüfung: 25. Juli 2024

Gutachter/in: Prof. Dr. Gisela Anton  
Prof. Dr. Ulrich Katz

# Abstract

The IceCube Neutrino Observatory (IceCube) is a cubic-kilometer neutrino detector built in the glacier ice at the South Pole. In the near future, IceCube will be extended by the IceCube Upgrade, which is the low energy extension of IceCube. This thesis focuses on characterization measurements of different system components of the multi-PMT Digital Optical Module (mDOM) for the IceCube Upgrade. The mDOM is a novel optical module using 24 small photomultiplier tubes (PMTs) instead of one large PMT. Most measurements were performed during the development stage of the mDOM before the first module was built. The following components were characterized in more detail: PMTs, analog front end (AFE), and an integrated mDOM. Different PMT types of two manufacturers were investigated during mass tests of about 150 PMTs. Based on the results of this thesis, the PMT type to be used for the mDOM was chosen, thus guaranteeing excellent directional and energy resolution of the IceCube Upgrade. Furthermore, a dedicated setup as well as measurement and analysis techniques were developed to investigate different AFE designs. In close cooperation with the electronics engineer, an AFE design was finally developed which not only enables to trigger on single photons, but also covers the relevant energy range for neutrino detection in the IceCube Upgrade. This design was used for the revision 1 mainboard of the first mDOMs. Lastly, the first two integrated mDOMs were characterized. For the first time, an mDOM was tested at temperatures expected during detector operation. It was shown that the cooling of the mDOM works sufficiently and the mDOM works as expected. In conclusion, this thesis contributed to developing and building working mDOMs which meet the requirements for the application in the IceCube Upgrade.



# Zusammenfassung

Diese Dissertation mit dem Titel „Charakterisierung des mDOM-Lichtdetektions- und Signalverarbeitungssystems für das IceCube Upgrade“ beschäftigt sich hauptsächlich mit Charakterisierungsmessungen verschiedener Hardwarekomponenten des mDOMs, welches eines der neuartigen Module ist, die für die zukünftige niederenergetische Erweiterung des IceCube, IceCube Upgrade genannt, entwickelt wurden. Zusammenfassend wurden drei verschiedene Hardware-Systeme in dieser Arbeit charakterisiert: Photomultiplier-Röhren (photomultiplier tubes (PMTs)), Analog-Front-End (analog front end) und ein integriertes digitales optisches Modul bestehend aus mehreren PMTs (multi-PMT Digital Optical Module (mDOM)).

Insgesamt wurden vier verschiedene PMT-Typen der zwei Hersteller Hamamatsu Photonics K.K. und HZC Photonics untersucht. Durch regelmäßigen Kontakt mit den Herstellern konnte das PMT-Design dahingehend verbessert werden, dass es die Anforderungen an die Verwendung im mDOM erfüllt. Dadurch werden nicht nur eine exzellente Richtungs- und Energieauflösung des IceCube Upgrades sichergestellt, sondern auch eine gute Rekonstruktion der Neutrinoereignisse. Für etwa 150 PMTs wurden die folgenden PMT-Charakteristika vermessen: Variation der Signallaufzeit (transit time spread), Quanteneffizienz (quantum efficiency), Dunkelrate (darkrate) und korreliertes Rauschen (correlated noise), welches die drei Rauscharten Prepulsing, Delayed Pulsing und Afterpulsing zusammenfasst. Verglichen mit den PMTs von HZC Photonics erbrachten die PMTs von Hamamatsu Photonics K.K. insgesamt eine bessere Leistung. Basierend auf den Messungen, die in dieser Arbeit beschrieben werden, entschied die IceCube-Kollaboration, PMTs des Herstellers Hamamatsu Photonics K.K. für die mDOMs zu verwenden, um eine exzellente Zeitauflösung zu gewährleisten, die detektierte Lichtmenge zu maximieren und insgesamt Rauschsignale zu minimieren. Nachdem geringfügige Änderungen an den vorangegangenen PMT-Typen vorgenommen worden waren, wurden 19 PMTs des finalen PMT-Typs R15458-20 überprüft. Es zeigte sich, dass die PMTs die Anforderungen an das mDOM erfüllen. Nur ein PMT wurde an den Hersteller zurückgeschickt, da dessen gemessene Dunkelrate die Anforderung an die maximale Dunkelrate stark überschritt. Zusätzlich zur Überprüfung der Anforderung an das mDOM wurden die Parameter der PMT-Linearitätsfits des finalen PMT-Typs in der Simulation des IceCube Upgrade-Detektors verwendet.

Ähnliche Messungen wurden mit dem Analog-Front-End durchgeführt. Damit wurde sichergestellt, dass mit dem IceCube Upgrade einzelne Photonen nachgewiesen werden können und der für das IceCube Upgrade relevante Energiebereich der nachzuweisenden Neutrinos abgedeckt wird. Um die unterschiedlichen Analog-Front-End-Designs untersuchen zu können, wurde ein spezieller Messaufbau konstruiert. Außerdem wurden spezielle Mess- und Analysemethoden entwickelt, um die folgenden Charakteristika zu untersuchen: Signal-zu-Rausch-Verhältnis (signal-to-noise ratio), dynamischer Bereich (dynamic range) und Linearität (linearity). Alle Parameter wurden sowohl bei Raumtemperatur als auch bei Temperaturen zwischen  $-20^{\circ}\text{C}$  und  $-42^{\circ}\text{C}$  gemessen.

nen. Diese niedrigen Temperaturen unter  $0^{\circ}\text{C}$  sind typisch für den Detektorbetrieb des IceCube Upgrade. Zuerst wurden drei verschiedene Analog-Front-End-Designs mit unterschiedlichen Signal-Verstärkungsfaktoren verglichen um das Design zu finden, welches den für den Nachweis der Neutrinos relevanten Energiebereich am besten abdeckt. Während dieser Messungen sind zwei Probleme aufgetreten. Zum einen birgt die Messmethode zur Bestimmung des dynamischen Bereichs und der Linearität große systematische Fehler aufgrund von Temperaturänderungen während der Messungen, welche die Helligkeit der verwendeten LED beeinflussten. Somit konnten mit dieser Messmethode keine verlässlichen Ergebnisse erzielt werden. Zum anderen waren die gemessenen PMT-Ladungsverteilungen, deren Mittelwert etwa 19 p.e. überschritt, stark verformt, was vermutlich durch ein Problem mit der Bandbreite des Analog-Front-Ends hervorgerufen wurde. Beide Probleme konnten gelöst werden. Die Messmethode wurde insoweit angepasst, dass ein Referenz-PMT verwendet wurde, mit dem die Helligkeit der LED überprüft werden konnte. Außerdem tauschte der Elektroingenieur den Vorverstärker des Analog-Front-Ends, was zu dem Design „channel 0b“ führte. Für dieses Design wurden das Signal-zu-Rausch-Verhältnis, der dynamische Bereich und die Linearität bei  $+25^{\circ}\text{C}$ ,  $-22^{\circ}\text{C}$  und  $-38^{\circ}\text{C}$  getestet sowie die Stabilität der Diskriminatorschwelle (discriminator threshold stability) bei  $-38^{\circ}\text{C}$ . Das Analog-Front-End-Design channel 0b erfüllt alle Anforderungen, die für das IceCube Upgrade vorgegeben sind, abgesehen von der Anforderung an die Linearität bei  $+25^{\circ}\text{C}$  und bei  $-38^{\circ}\text{C}$ . Dennoch wurde die Leistung des channel 0b als ausreichend für die Anwendung im mDOM für das IceCube Upgrade befunden. Somit wurde channel 0b für die erste Version des mDOM-Mainboards verwendet.

Als letztes wurden zwei integrierte mDOMs in einer zeitabhängigen Studie bei den Temperaturen  $-27^{\circ}\text{C}$  und  $-49^{\circ}\text{C}$  untersucht. Im IceCube Upgrade werden die mDOMs im Eis bei ähnlichen Temperaturen betrieben und erst angeschaltet, sobald das Eis nach dem Installationsprozess wieder gefroren ist. Zum ersten Mal wurde ein Kaltstart eines mDOMs durchgeführt. Für beide mDOMs wurden die Temperatur an verschiedenen Stellen innerhalb des mDOM, der Leistungsverbrauch (power consumption), der Druck und die PMT-Hochspannung abhängig von der absoluten Zeit gemessen. Befindet sich das mDOM im thermischen Gleichgewicht und im Normalbetrieb, steigt die Temperatur der sich am stärksten erwärmenden Komponente des mDOMs (der FPGA auf dem Mainboard) auf circa 70 K bis 77 K über die Umgebungstemperatur. Zudem beträgt der durchschnittliche Leistungsverbrauch 9 W. Des Weiteren wurde keinerlei Gas-Austritt beobachtet und die PMT-Hochspannung blieb stabil. Darüber hinaus wurde die Zeit bestimmt, die ein mDOM bei  $-27^{\circ}\text{C}$  benötigt, um nach An- oder Abschalten des Mainboards ins thermische Gleichgewicht zu gelangen. Während das mDOM nach etwa 30 h nach Anschalten des Mainboards im thermischen Gleichgewicht war, benötigte es circa 40 h, um nach Abschalten des Mainboards abzukühlen. Beide mDOMs funktionierten wie erwartet. Keine der elektronischen Komponenten wurde außerhalb ihrer Spezifikationen betrieben und die Kühlung der mDOMs funktionierte zufriedenstellend.

Zusammenfassend trug diese Arbeit entscheidend dazu bei, ein erfolgreiches mDOM-Design zu entwickeln, sodass funktionsfähige mDOMs für das IceCube Upgrade gebaut werden konnten. Die Funktionsfähigkeit der mDOMs wurde in umfangreichen Tests, welche von unterschiedlichen Personen durchgeführt wurden, überprüft. Darüber hinaus wird jedes gefertigte mDOM eingehenden Akzeptanztests unterzogen, welche zum Zeitpunkt der Veröffentlichung dieser Arbeit bereits durchgeführt werden. Im August 2024 werden die ersten 117 mDOMs an den Südpol verschickt, gefolgt von den restlichen 288 mDOMs ein Jahr später. Im antarktischen Sommer 2025/26 werden alle 405 mDOMs zusammen mit 279 D-Eggs, 14 PDOMs sowie mehreren Kalibrationsgeräten in

---

einem dichteren instrumentierten Volumen als dem bestehenden IceCube-Detektor im Gletschereis installiert. Mit dem IceCube Upgrade kann die Sensitivität auf die Messung des Erscheinens von Tau-Neutrinos verbessert werden, was die Sensitivität auf die Neutrinooszillationsparameter verbessert und verwendet werden kann, um die Unitarität der PMNS-Matrix zu überprüfen. Weiterhin werden die optischen Eigenschaften des Gletschereises detailliert vermessen, womit die Richtungsrekonstruktion von IceCube wesentlich verbessert werden kann.



# Contents

<b>Abstract</b>	<b>I</b>
<b>Zusammenfassung</b>	<b>III</b>
<b>Contents</b>	<b>VII</b>
<b>Introduction</b>	<b>XI</b>
<b>1 Scientific background</b>	<b>1</b>
1.1 Neutrino astronomy . . . . .	2
1.1.1 Neutrino sources . . . . .	2
1.1.2 Neutrino interactions . . . . .	4
1.1.3 Neutrino detection . . . . .	5
1.2 Neutrino experiments . . . . .	6
1.2.1 IceCube Neutrino Observatory . . . . .	6
1.2.2 IceCube Upgrade . . . . .	8
1.3 Photomultiplier tubes . . . . .	12
1.3.1 Structure and working principle . . . . .	12
1.3.2 Gain . . . . .	13
1.3.3 Characteristics . . . . .	14
1.3.4 Technical aspects . . . . .	18
<b>2 The multi-PMT Digital Optical Module for the IceCube Upgrade</b>	<b>23</b>
2.1 Challenges and advantages of the mDOM . . . . .	23
2.2 Design . . . . .	25
2.3 Working principle . . . . .	27
2.4 Components relevant for this work . . . . .	29
2.4.1 Photomultiplier tubes . . . . .	29
2.4.2 PMT base . . . . .	29
2.4.3 Analog front end . . . . .	31
2.4.4 Mainboard . . . . .	32
2.5 Data acquisition and operation in ice . . . . .	35

<b>3 PMT characterization measurements</b>	<b>37</b>
3.1 Overview of investigated PMT types . . . . .	38
3.2 PMT calibration . . . . .	39
3.2.1 Setup . . . . .	39
3.2.2 Gain calculation . . . . .	39
3.2.3 HV calibration . . . . .	42
3.3 Determination of the PMT characteristics . . . . .	43
3.3.1 Transit time spread (TTS) . . . . .	43
3.3.2 Quantum efficiency . . . . .	44
3.3.3 Darkrate . . . . .	46
3.3.4 Correlated noise . . . . .	47
3.4 Comparison of Hamamatsu and HZC PMT types . . . . .	51
3.5 Characterization of the final PMT type . . . . .	54
3.6 Summary . . . . .	56
<b>4 Measurements with the analog front end (AFE)</b>	<b>59</b>
4.1 AFE configuration . . . . .	60
4.2 Investigated AFE requirements for the mDOM . . . . .	60
4.3 Characterization of different AFE channel designs . . . . .	61
4.3.1 Measurement setup and calibration . . . . .	61
4.3.2 Investigated parameters . . . . .	63
4.3.3 Comparison of channel characteristics . . . . .	79
4.3.4 Problems . . . . .	80
4.4 Characterization of the AFE channel design of the revision 1 mainboard . . . . .	84
4.4.1 Measurement setup . . . . .	84
4.4.2 Functionality test . . . . .	85
4.4.3 Investigated parameters . . . . .	87
4.4.4 Conclusion . . . . .	94
4.5 Summary . . . . .	95
<b>5 Measurements with an integrated mDOM</b>	<b>97</b>
5.1 Setup . . . . .	97
5.2 Measurement procedure . . . . .	99
5.3 Temperature behavior of an mDOM . . . . .	100
5.3.1 Simulation . . . . .	101
5.3.2 Power consumption . . . . .	104
5.3.3 Equilibrium temperatures . . . . .	105
5.3.4 Warm-up and cooling times . . . . .	111
5.4 Further parameters . . . . .	114
5.4.1 Pressure . . . . .	114
5.4.2 PMT high voltage . . . . .	115
5.5 Summary and discussion . . . . .	116
<b>6 Summary &amp; Outlook</b>	<b>119</b>
<b>Additional material</b>	<b>121</b>

---

<b>List of Abbreviations</b>	<b>125</b>
<b>Bibliography</b>	<b>127</b>
<b>Danksagung</b>	<b>137</b>



# Introduction

Neutrinos are one of the most abundant particles in the Universe, and they have been studied for more than 90 years since they were postulated by Wolfgang Pauli in 1930 [1] and directly detected by Clyde Cowan and Frederick Reines in 1956 [2]. Some of their properties such as their masses or the values of some of their oscillation parameters remain to be determined, but nevertheless, neutrinos play an important role in the field of multi-messenger astronomy. Unlike cosmic rays, neutrinos lack an electric charge, and are not deflected by magnetic fields during their propagation to the Earth, thus traveling in straight trajectories. Furthermore, their small interaction cross-section allows neutrinos to propagate through dense regions as for example star clouds almost unhindered. However, their small interaction cross-section makes neutrinos hard to detect. Since large detector volumes are needed, naturally occurring resources are often used as detector media. One operating detector is the IceCube Neutrino Observatory (IceCube) which uses the glacier ice at the South Pole as detection medium. After seven years of construction, IceCube was completed in 2010 [3]. Three years later, in 2013, IceCube discovered the high-energy cosmic neutrino flux [4]. Another four years later, IceCube was part of the multimessenger<sup>1</sup> observation of the blazar TXS 0506+056 [5]. More precisely, IceCube detected a high energetic neutrino with a reconstructed energy of approximately 290 TeV of likely extragalactic origin. This observation triggered an alert which was distributed worldwide to other telescopes and follow-up observations indicated that the direction of the neutrino measured by IceCube is consistent with the position of the blazar TXS 0506+056. In 2022, IceCube found evidence that the galaxy NGC 1068 emits high-energetic neutrinos [6]. Using ten years of data, IceCube searched for neutrinos from sources of astrophysical origin. As a result, an excess of about 80 neutrinos was found to originate from the galaxy NGC 1068 with a significance of  $4.2\sigma$ .

Despite the achievements mentioned above, the current design of IceCube has some limitations. First, the sensitivity of IceCube to tau neutrinos—which are relevant for neutrino oscillation studies—is low. Second, the understanding of the optical properties of the glacier ice and thus, the neutrino-direction-reconstruction quality, is limited. For these two reasons, the existing IceCube detector will be extended by 2025/26. This extension is called IceCube Upgrade, and it will increase the detector’s sensitivity to neutrinos with energies between 1 GeV and 10 GeV [7]. The increased sensitivity to tau neutrino appearance measurements can be used to probe the unitarity of the Pontecorvo-Maki-Nakagawa-Sakata (PMNS) matrix and increase the sensitivity to neutrino oscillation parameters. In addition, new calibration devices will be installed which aim for detailed measurements of the optical ice properties. To enhance the sensitivity, novel optical module types will be installed as part of the IceCube Upgrade. One of these modules is the multi-PMT Digital

---

<sup>1</sup>Multimessenger astronomy is a combination of observations with cosmic rays, neutrinos, gravitational waves, and electromagnetic radiation across a broad range of wavelengths.

Optical Module (mDOM). In contrast to IceCube using one large photomultiplier tube (PMT) in each module, the mDOM uses 24 small PMTs to measure the Cherenkov light induced by the secondary particles generated by the neutrinos.

This thesis was developed in the context of hardware design and characterization for the IceCube Upgrade, and describes studies performed on different components of the mDOM. Several PMT candidates were characterized and compared, including the PMT type that was finally chosen for the mDOM. This choice was made on the basis of the measurements reported in this thesis. Moreover, this thesis reports how multiple candidates for the analog front end (AFE) design for the mDOM mainboard were characterized and compared. Therefore, a dedicated setup as well as dedicated measurement techniques were developed. As a result, defects were fixed, and the AFE design was improved. Finally, measurements of the temperature distribution inside the mDOM were performed. These measurements proved that the heat dissipation of the mDOM is sufficient. In addition, the time needed to reach thermal equilibrium was determined which can be used as an estimate for future laboratory measurements with the mDOM.

Chapter 1 focuses on the scientific background of this thesis. This background includes the sources, the interactions, and the detection of neutrinos as well as the description of the IceCube detector and the IceCube Upgrade. Furthermore, the relevant aspects of PMTs are described. In Chapter 2, the mDOM is introduced. The design and working principle of the mDOM is explained along with the components relevant for this work. Chapter 3 presents the characterization measurements of different PMT candidates for the mDOM together with the characterization of the final PMT type choice. In Chapter 4, three different AFE designs are characterized and compared. Moreover, the AFE design used for the revision 1 mainboard is characterized. Chapter 5 presents measurements with an integrated mDOM. These measurements include mainly the temperature distribution inside an mDOM along with the times to reach thermal equilibrium, but in addition, measurements of the power consumption, the pressure, and the PMT high voltage. Finally, Chapter 6 summarizes the work of this thesis.

# Chapter 1

## Scientific background

---

<b>1.1</b>	<b>Neutrino astronomy</b>	<b>2</b>
1.1.1	Neutrino sources	2
1.1.2	Neutrino interactions	4
1.1.3	Neutrino detection	5
<b>1.2</b>	<b>Neutrino experiments</b>	<b>6</b>
1.2.1	IceCube Neutrino Observatory	6
1.2.2	IceCube Upgrade	8
<b>1.3</b>	<b>Photomultiplier tubes</b>	<b>12</b>
1.3.1	Structure and working principle	12
1.3.2	Gain	13
1.3.3	Characteristics	14
1.3.3.1	Time characteristics	14
1.3.3.2	Quantum efficiency	15
1.3.3.3	Darkrate	16
1.3.3.4	Correlated noise	17
1.3.4	Technical aspects	18
1.3.4.1	Base types	18
1.3.4.2	High voltage polarity	20
1.3.4.3	PMT operation modes	21

---

This chapter focuses on the scientific background of this thesis. In Section 1.1, the sources of neutrinos, neutrino interactions as well as the principle of neutrino detection is explained. Section 1.2 describes an existing neutrino telescope and its planned extension. Last, Section 1.3 introduces the structure and properties of PMTs, which are the photosensors typically used for neutrino telescopes.

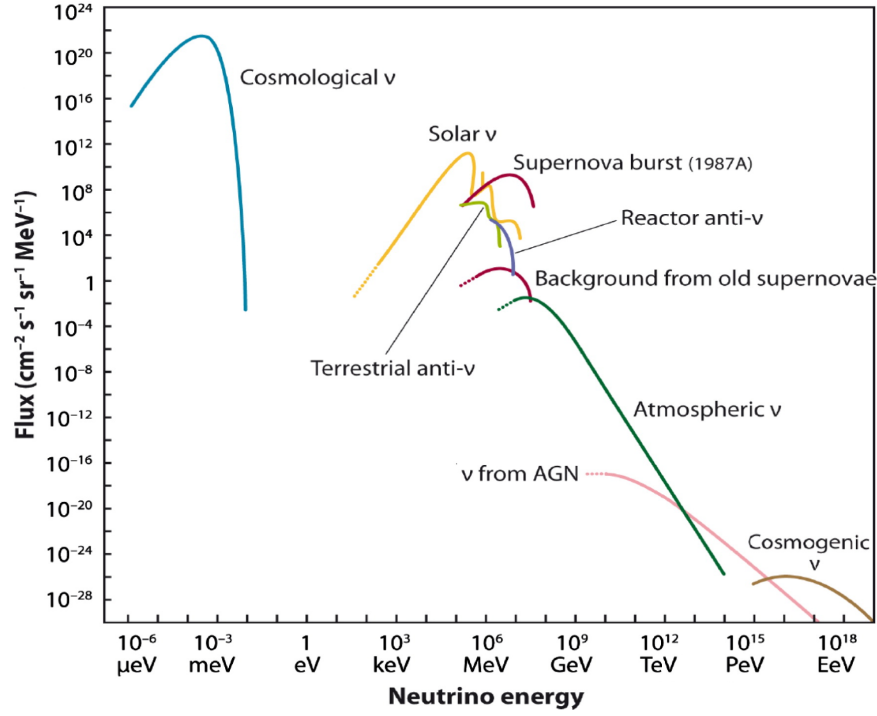


**Figure 1.1:** Neutrino sources and their flux versus the energy. Figure taken from [9].

## 1.1 Neutrino astronomy

Neutrinos are almost massless elementary particles with spin  $1/2$ . Furthermore, the neutrino is electrically neutral and has no color charge. Therefore, the neutrino can interact only via the weak force and gravity. In the Standard Model of particle physics, three neutrino flavors exist: Electron neutrino  $\nu_e$ , muon neutrino  $\nu_\mu$ , and tau neutrino  $\nu_\tau$ . In Subsection 1.1.1, the different sources of neutrinos are described. Subsection 1.1.2 focuses on the interaction of neutrinos. Finally, Subsection 1.1.3 explains the principles of the detection of neutrinos using the Cherenkov radiation.

### 1.1.1 Neutrino sources

Neutrinos originate from different sources. A detailed description can be found in [8]. Figure 1.1 shows an overview of terrestrial and cosmic neutrinos sources along with the neutrino flux at Earth and the corresponding energy. Depending on the source of origin, the neutrinos have different energies and fluxes. It is expected that the so-called cosmological neutrinos have the lowest energies in the range of  $\mu\text{eV}$  to  $\text{meV}$ . These neutrinos were generated approximately one second after the Big Bang when they decoupled from other forms of matter. Cosmological neutrinos are also called cosmic neutrino background. The expected flux is about  $10^8 \text{ cm}^{-2} \text{ s}^{-1} \text{ sr}^{-1} \text{ MeV}^{-1}$  to  $10^{20} \text{ cm}^{-2} \text{ s}^{-1} \text{ sr}^{-1} \text{ MeV}^{-1}$ .

Neutrino energies between  $\text{keV}$  and  $\text{MeV}$  are dominated by solar, terrestrial, and reactor neutrinos. Solar neutrinos are produced as a byproduct from nuclear fusion processes in the core of the Sun. The flux of solar neutrinos is about  $10^{12} \text{ cm}^{-2} \text{ s}^{-1} \text{ sr}^{-1} \text{ MeV}^{-1}$ . Natural radioactive decays as for example  $n \rightarrow p + e^- + \bar{\nu}_e$  produce terrestrial neutrinos at energies with around  $1 \text{ MeV}$  and a

flux of about  $10^7 \text{ cm}^{-2} \text{ s}^{-1} \text{ sr}^{-1} \text{ MeV}^{-1}$ . Underlying the same decay process, reactor neutrinos have similar energies, but a lower flux around  $10^4 \text{ cm}^{-2} \text{ s}^{-1} \text{ sr}^{-1} \text{ MeV}^{-1}$ .

Furthermore, neutrinos are emitted by supernovae. When a star collapses, neutrinos with energies from few to several MeV are generated via different reaction mechanisms. The supernova 1987A is the only supernova so far which could be observed via the detection of neutrinos. The measured neutrino flux was approximately  $10^{12} \text{ cm}^{-2} \text{ s}^{-1} \text{ sr}^{-1} \text{ MeV}^{-1}$ . All neutrinos from supernovae which occurred since the Big Bang sum up to a background having an expected neutrino flux of about  $50 \text{ cm}^{-2} \text{ s}^{-1} \text{ sr}^{-1} \text{ MeV}^{-1}$ .

In general, atmospheric neutrinos are generated when cosmic rays interact with the Earth's atmosphere. This process can be described in different steps. First, a proton  $p$ —which is the main component of cosmic rays—interacts with a nucleus  $X$ . As a result, another nucleus  $Y$  and a charged pion  $\pi^\pm$  are created:

$$p + X \rightarrow Y + \pi^\pm. \quad (1.1)$$

This pion then decays. In case of a  $\pi^+$ , the pion decays into an antimuon and a muon neutrino. A  $\pi^-$ , however, decays into a muon and an antimuon neutrino:

$$\pi^+ \rightarrow \mu^+ + \nu_\mu \quad \pi^- \rightarrow \mu^- + \bar{\nu}_\mu \quad (1.2)$$

$$\mu^+ \rightarrow e^+ + \nu_e + \bar{\nu}_\mu \quad \mu^- \rightarrow e^- + \bar{\nu}_e + \nu_\mu. \quad (1.3)$$

The muons and antimuons produced as described in the reactions shown in Equation 1.2 decay as shown in Equation 1.3. An antimuon decays into a positron, an electron neutrino, and an antimuon neutrino. In contrast, a muon decays into an electron, an antielectron neutrino, and a muon neutrino. The thus produced atmospheric neutrinos have energies between several MeV and TeV with a flux between approximately  $10^{-2} \text{ cm}^{-2} \text{ s}^{-1} \text{ sr}^{-1} \text{ MeV}^{-1}$  and  $10^{-24} \text{ cm}^{-2} \text{ s}^{-1} \text{ sr}^{-1} \text{ MeV}^{-1}$ .

The main contribution to the neutrino flux in the TeV to PeV range is believed to come from cosmic ray accelerators. These objects accelerate protons, which can subsequently interact with matter or ambient radiation through processes like the ones described by Equations 1.1, 1.2, 1.3, leading to the production of neutrinos. It is expected that neutrinos from these extragalactic accelerators have a flux between approximately  $10^{-18} \text{ cm}^{-2} \text{ s}^{-1} \text{ sr}^{-1} \text{ MeV}^{-1}$  and  $10^{-26} \text{ cm}^{-2} \text{ s}^{-1} \text{ sr}^{-1} \text{ MeV}^{-1}$ . The best candidates for such extragalactic accelerators are active galactic nuclei (AGNs) and gamma-ray bursts (GRBs). Basically, an AGN is the center of a galaxy which emits photons of nonstellar origin. It is assumed that this emission is generated by a supermassive black hole which accretes material from its surroundings. In contrast to this continuous emission, GRBs are transient bursts releasing photons with energies between approximately 100 keV and 1 MeV within few seconds [10]. How these GRBs are formed is not resolved so far. Possible explanations for GRBs are the death of a massive star [8] or the merging of two compact objects such as black holes or neutron stars [11].

In contrast to the neutrinos expected from AGNs and GRBs, which are expected to be observed as point sources, a diffuse neutrino flux is assumed at energies in the range of PeV to EeV. These neutrinos are called cosmogenic neutrinos. Their origin is believed to be the following production mechanism. Protons from cosmic rays with energies close to  $10^{20} \text{ eV}$  [12] interact with photons  $\gamma$  from the cosmic microwave background (CMB) or from extragalactic background light (EBL). Thereby, baryons  $\Delta^+(1232)$  are produced:

$$p + \gamma \rightarrow \Delta^+(1232). \quad (1.4)$$

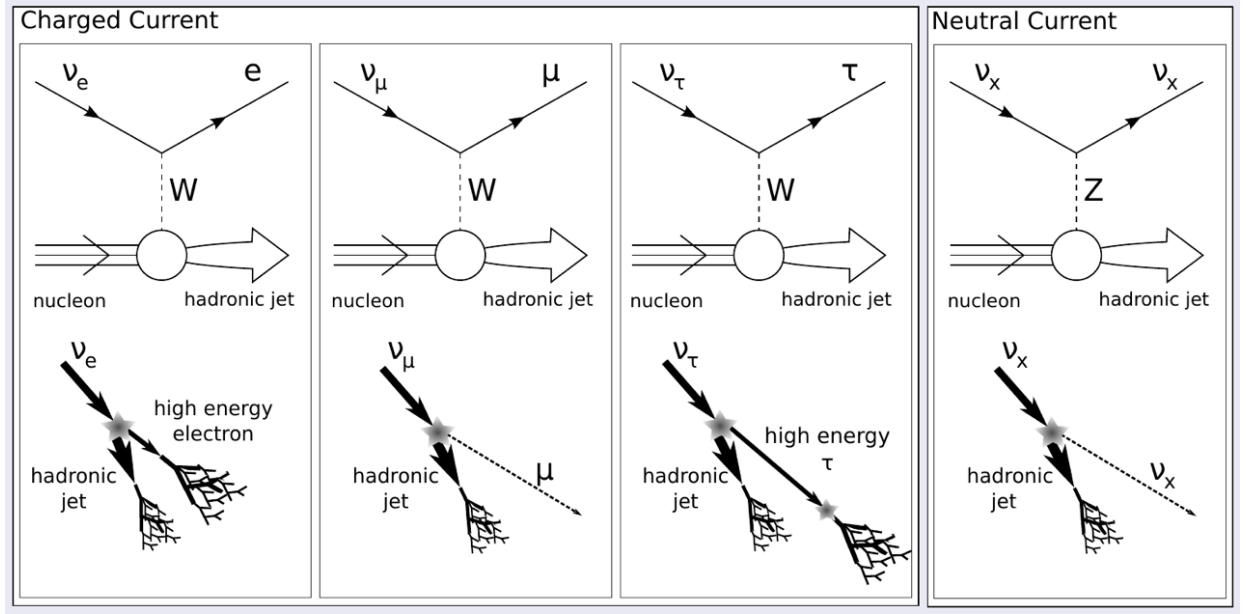


**Figure 1.2:** Overview of the charged current and neutral current interactions of neutrinos via the weak force in case of deep inelastic scattering. Figure modified from [14].

Afterwards, this  $\Delta^+(1232)$  baryon decays mostly via one of the following reactions:

$$\Delta^+(1232) \rightarrow p + \pi^0 \qquad \Delta^+(1232) \rightarrow n + \pi^+ . \qquad (1.5)$$

In case a  $\pi^+$  is generated, this charged pion then decays into an antimuon and a muon neutrino as shown in the left reaction of Equation 1.2. The antimuon, on the other hand, decays as described in the left reaction of Equation 1.3 producing further neutrinos. Because cosmic rays with energies close to  $10^{20}$  eV are suppressed due to the reaction with photons of the CMB (GZK cutoff [12, 13]), a neutrino excess is expected with a flux of approximately  $10^{-26} \text{ cm}^{-2} \text{ s}^{-1} \text{ sr}^{-1} \text{ MeV}^{-1}$ .

### 1.1.2 Neutrino interactions

As mentioned in the beginning of Section 1.1, neutrinos can interact with matter only via the weak force or gravity. When neglecting gravity due to the very small neutrino mass, the neutrino interactions can be distinguished into charged current and neutral current interactions. Furthermore, different interaction types exist. At high energies (above approximately 10 GeV), deep inelastic scattering is dominant. Figure 1.2 shows an overview of the four interaction types considering only deep inelastic scattering. The upper row shows the corresponding simplified Feynman diagram with the time evolving from left to right whereas the lower row sketches the particle propagation not to scale.

In case of the charged current interactions, the neutrino exchanges a  $W$  boson with a nucleon. As a result, a hadronic jet is produced as well as a charged lepton of the same flavor as the incoming neutrino. An electron neutrino generates an electron which produces an electromagnetic shower. A muon neutrino, instead, produces a muon which has a lifetime of approximately  $2 \mu\text{s}$  [15]. Depending on the kinetic energy, the muon can propagate several kilometers until it decays via one of the reactions shown in Equation 1.3. In contrast, a tau neutrino generates a tau lepton

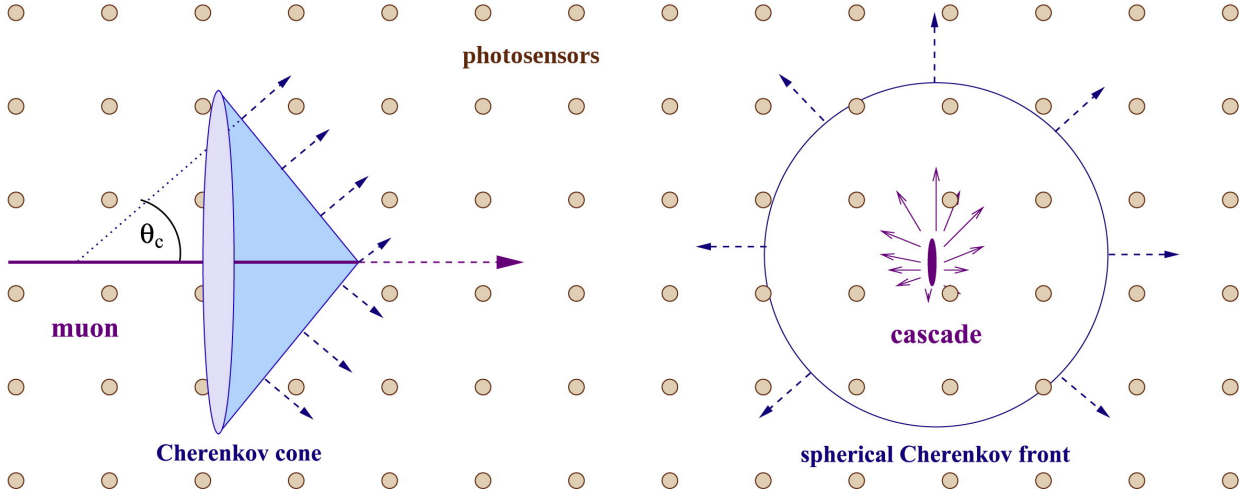


**Figure 1.3:** Detection principle of the Cherenkov light produced by the secondary particles of neutrinos. Figure modified from [9].

which decays after a very short time (the mean lifetime of a tau lepton is approximately 290 fs [15]) producing another hadronic jet.

For the neutral current interaction, the signature of the reaction is the same for all three flavors. The neutrino exchanges a  $Z$  boson with the nucleon, produces a hadronic jet and propagates further.

### 1.1.3 Neutrino detection

In general, neutrinos are detected indirectly via the detection of secondary particles. Different techniques exist to detect neutrinos. This subsection concentrates on water Cherenkov detectors. Such detectors use the Cherenkov radiation [16]. When a charged particle as for example an electron travels through a medium faster than the speed of light in the medium ( $v > c/n$  with  $v$  the velocity of the charged particle,  $c$  the speed of light in vacuum, and  $n$  the refractive index of the medium), Cherenkov light is emitted under the angle  $\theta_C$ :

$$\cos(\theta_C) = \frac{1}{\beta \cdot n}, \quad (1.6)$$

where  $\beta = v/c$ . This Cherenkov light is detected via photosensors. Therefore, a medium transparent to optical light is needed such as water or glacier ice. This medium is equipped with an array of photosensors as sketched in Figure 1.3 (yellow circles). The left sketch of Figure 1.3 shows the detection principle for the charged current interaction of a muon neutrino producing a muon which almost maintains the direction of motion of the previous muon neutrino. While this muon propagates through the medium faster than the speed of light in the medium, it induces the emission of Cherenkov light along the Cherenkov cone. Muons can travel several kilometers emitting Cherenkov light which generates a track-like signature in the detector array. Therefore, such events are called track-like events. In contrast, the right sketch of Figure 1.3 shows the detection principle of the charged current interactions of electron and tau neutrinos as well as the neutral current interaction. For these scenarios, the sum of hadronic jet(s) and electromagnetic showers form a cascade which induces a spherical Cherenkov front. Such events are called cascade-like events.

From the distributions of the Cherenkov light measured by the photosensors, the direction, energy, and the flavor of the incoming neutrino can be determined. For instance, while the muon propagates through the medium and Cherenkov light is emitted, this light is detected by the photosensors. The different arrival times of the light at the photosensors allow to reconstruct the muon track and thus, its direction. From the muon direction, the direction of the muon neutrino can be reconstructed. The neutrino energy, in turn, is determined from the measured light intensity of the Cherenkov light. For track-like events, the directional reconstruction is more accurate than for cascade-like events. However, the energy reconstruction is more accurate for cascade-like events than for track-like events. Finally, the neutrino flavor can be determined from the event signature.

The basic detection principle shown in Figure 1.3 and the previously mentioned methods to determine the direction and energy of the incoming neutrino imply several properties which the photosensors used for the detection of the Cherenkov light should have. First, the intensity  $I$  of the emitted Cherenkov light depends on the wavelength  $\lambda$  of the emitted photons as follows:  $I \propto 1/\lambda^2$ . However, the absorption of electromagnetic radiation in ice strongly increases for photons with wavelengths below 170 nm [17]. Therefore, most Cherenkov photons propagating through the ice have wavelengths within the blue or ultraviolet (UV) range. Consequently, the photosensors should be sensitive to blue or UV light. Second, the number of emitted Cherenkov photons is relatively small (about 200/cm [18]). As a result, the photosensors should be able to detect low light intensities down to single photons. Third, the direction is reconstructed from the different arrival times of the Cherenkov light at the photosensors. Thus, the response of the photosensors must be fast enough (within nanoseconds) to resolve the different arrival times. Fourth, the energy is reconstructed from the number of detected photons. To detect as many photons as possible, the detection efficiency of the photosensors, which is the probability that an incident photon is detected, should be as large as possible. All these requirements are fulfilled by the photosensor described in Section 1.3.

However, the detection of neutrinos is challenging due to their small interaction cross-section. While this property makes them ideal as messengers for astrophysical point sources, at the same time, their low interaction probability complicates the detection of neutrinos. To compensate for the low interaction cross-section, large detector volumes of cubic kilometers are needed. Therefore, natural resources are usually used such as for the detectors described in Section 1.2.

## 1.2 Neutrino experiments

Several neutrino detectors in operation use the detection principle described in Subsection 1.1.3. This section focuses on one of the largest neutrino telescopes currently in operation, IceCube described in Subsection 1.2.1, and its planned low energy extension, the IceCube Upgrade which will be discussed in Subsection 1.2.2.

### 1.2.1 IceCube Neutrino Observatory

The IceCube Neutrino Observatory (IceCube) [3] is a cubic-kilometer neutrino detector built in the ice of the South Pole and using the glacier ice as interaction medium. A detailed description can be found in [19]. To reduce the background from cosmic ray muons and sunlight, the three-dimensional (3D) array of 5160 Digital Optical Modules (DOMs) is installed at depths between 1450 m and 2450 m below the surface of the ice as shown in Figure 1.4. The downward facing

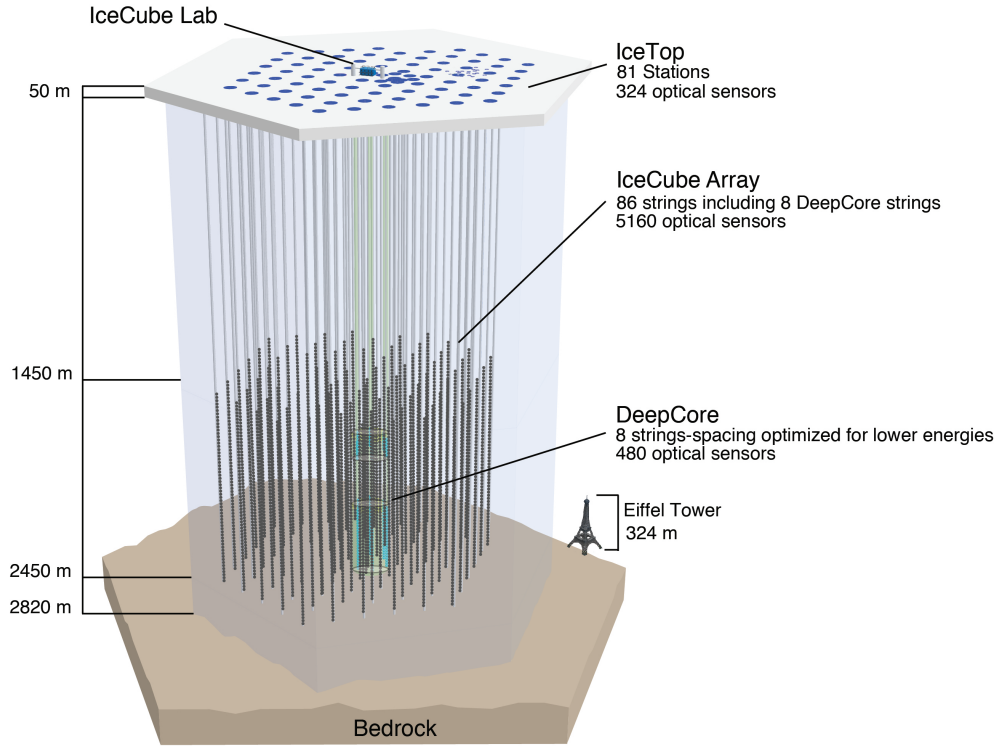


**Figure 1.4:** Schematic illustration of the IceCube detector. Figure modified from [19].

DOMs are arranged in 86 vertical strings with 60 DOMs per string. Instrumenting a volume of one cubic kilometer of ice, the primary in-ice array consists of 78 strings having a vertical spacing of about 17 m. In horizontal direction, the strings are arranged within a hexagonal grid with a horizontal spacing of 125 m. Within the center of the primary in-ice array, eight additional strings using high-quantum-efficiency PMTs are installed (a footprint is shown in Figure 1.6). These additional strings form a denser instrumented volume which is called DeepCore [20]. While these eight additional strings are installed with a horizontal spacing of about 70 m, the vertical spacing of the DOMs is 7 m. A total of 81 stations on the surface of the ice, each station located above an in-ice string, forms an air shower array called IceTop [21]. Each station consists of two tanks filled with ice. In each tank, two downward facing DOMs are placed. One DOM contains a PMT operated at a lower gain while the second DOM contains a PMT operated at a higher gain, thus increasing the dynamic range. In addition to the detection of air showers, IceTop can also be used as a muon veto for the in-ice array. Located in the center of IceTop, the IceCube Laboratory (IceCube Lab) is the central operation building acquiring all data measured by the DOMs.

Figure 1.5 shows a schematic illustration of a DOM [23] which is used to detect the Cherenkov photons resulting from the propagation of relativistic charged particles through the ice. Each DOM houses a 10-inch PMT [24] detecting the light. To reduce the influence of the magnetic field on the PMTs, the PMT head is caged in a mu-metal mesh. A high voltage control board generates the necessary PMT high voltage (HV) which is distributed to the PMT via the PMT base board. Communication, control, data acquisition, power supply, and calibration are performed by the

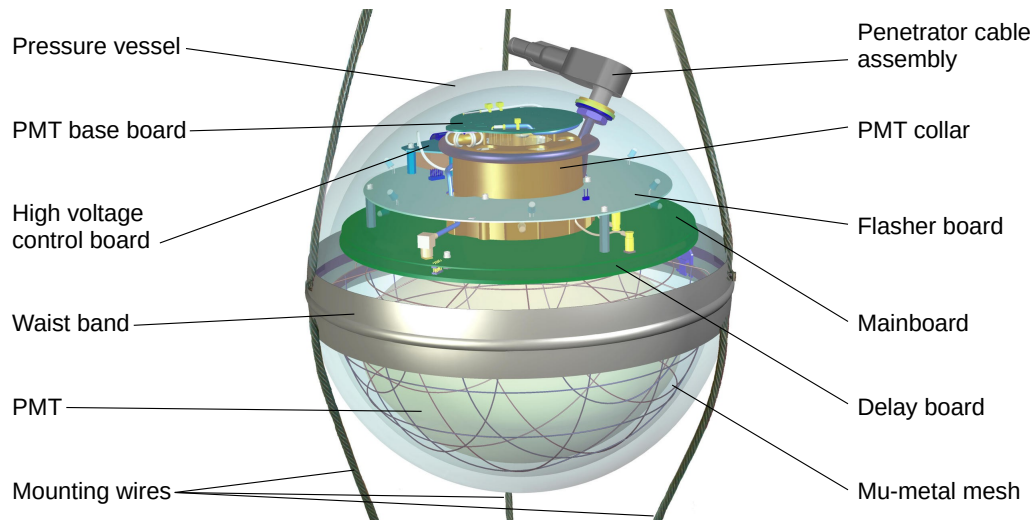


**Figure 1.5:** Schematic illustration of the used DOM for the IceCube detector. Figure modified from [22].

mainboard. For the signal processing, an additional delay board is used. The flasher board controls several light-emitting diodes (LEDs) which are used to generate calibration light flashes. The PMT as well as all electronic components are placed in an approximately 13 mm thick pressure vessel made of borosilicate glass. The pressure vessel consists of two half spheres with an outer diameter of about 330 mm surrounded by a waist band. All electronic cables to or from the DOM are routed through a special cable which is the penetrator cable assembly. Three mounting wires attached to the waist band hold the DOM in place.

Along with its primary scientific goal, the detection of astrophysical neutrinos, IceCube furthermore observes cosmic rays interacting with the Earth's atmosphere, studies neutrino properties such as atmospheric neutrino oscillations, searches for neutrinos from dark matter self-annihilation in the Earth and the Sun, and investigates the properties of the Antarctic glacial ice. From the broad energy range shown in Figure 1.1, the primary in-ice array observes neutrinos with energies from 100 GeV to few PeV (atmospheric neutrinos and neutrinos from cosmic accelerators such as AGNs). DeepCore, instead, was optimized to detect neutrinos with energies between 10 GeV and 100 GeV (atmospheric neutrinos). Air showers from primary cosmic rays are detected between 300 TeV to 1 EeV by IceTop. However, IceCube is limited. On the one hand, the statistics of detected tau neutrinos is low. On the other hand, the directional resolution of IceCube is limited due to an insufficient ice model built out of insufficient measurements of the optical ice properties, which are scattering and absorption of the Cherenkov photons. Both limitations are addressed by the IceCube Upgrade which will be described in Subsection 1.2.2.

### 1.2.2 IceCube Upgrade

The IceCube Upgrade [7] is the future low energy extension of IceCube and it will be sensitive to neutrinos with energies between approximately 1 GeV and 10 GeV [7]. It is planned to complete the IceCube Upgrade in the Antarctic summer season of 2025/26. Inside the current in-ice array of DeepCore, seven new strings will be installed as shown in Figure 1.6. At depths between 2150 m and 2425 m (physics region), about 700 new modules will be installed. On average, the

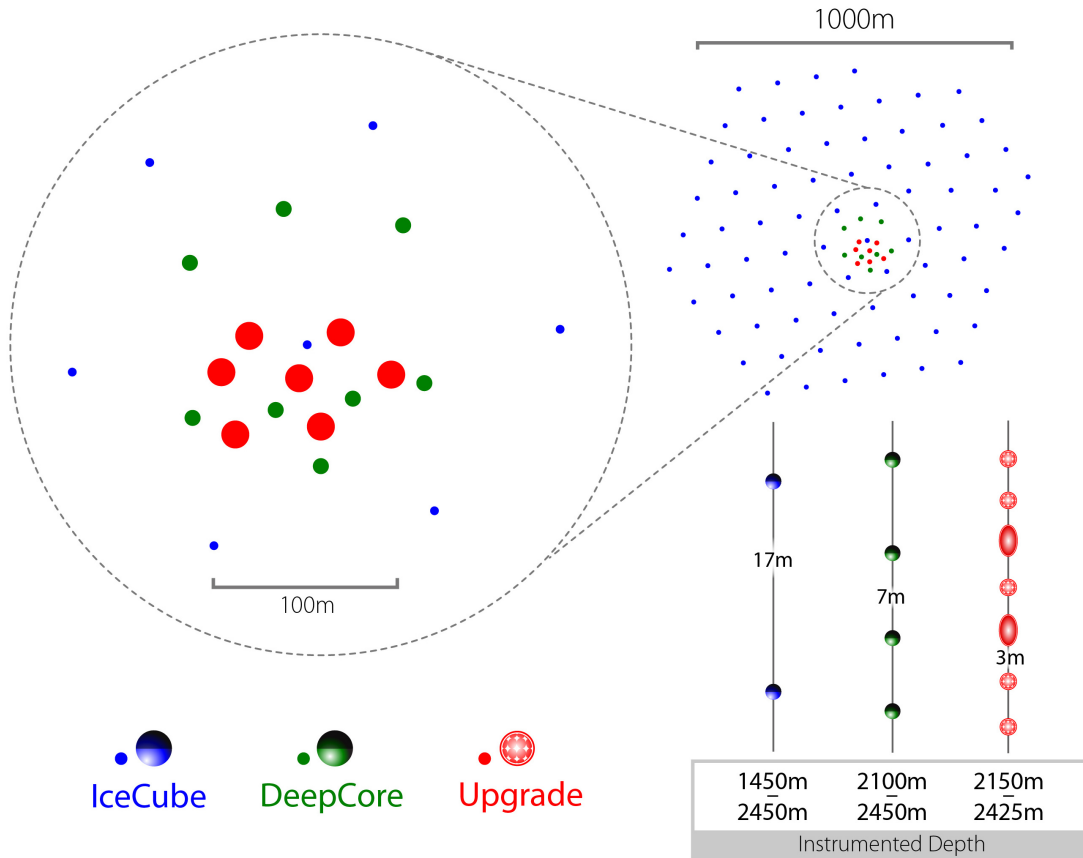


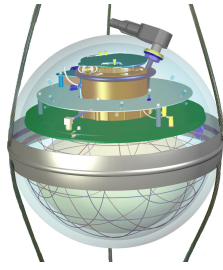
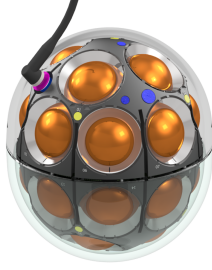

**Figure 1.6:** Footprint to scale of the primary in-ice array (IceCube in blue), DeepCore (green), and IceCube Upgrade (red). Picture taken from [7].

seven strings will be approximately 20 m apart while the vertical module-to-module distance will be about 3 m. Each string will consist of about 100 modules. As part of the IceCube Upgrade, novel optical module types will be used. Table 1.1 gives an overview of the three module types planned to be installed in the physics region: The PINGU Digital Optical Module (PDOM), the multi-PMT Digital Optical Module (mDOM), and the Dual optical sensors in an Ellipsoid Glass for Gen2 (D-Egg).

Basically, the PDOM is a refurbished version of the IceCube DOM described in Figure 1.5 using the same glass sphere and PMT, but new data acquisition electronics. The term “PDOM” originates from a planned IceCube extension called Precision IceCube Next Generation Upgrade (PINGU) [27] which was never realized. In contrast to the two other modules used for the IceCube Upgrade, the PDOM consists of a sphere with a diameter of about 330 mm containing one single 10-inch PMT. Being produced at the Wisconsin IceCube Particle Astrophysics Center (WIPAC), it is planned to install 14 PDOMs in total as part of the IceCube Upgrade. These PDOMs are mainly used for a cross-calibration between the existing IceCube detector and the IceCube Upgrade.

Based on the design of the optical modules used for the KM3NeT experiment [28, 29] featuring several small instead of one large PMT, the mDOM [30] contains 24 3-inch PMTs. Compared to the PDOM, the mDOM is larger with a diameter of 356 mm and a height of 408 mm. Chapter 2 describes the mDOM in more detail. All in all, 405 mDOMs will be installed, being produced at

**Table 1.1:** Overview of the planned optical modules for the IceCube Upgrade. Diameter and height refer to the outer dimensions of the glass pressure vessel. PDOM picture taken from [22], mDOM picture taken from [25], D-Egg picture modified from [26].

	PDOM	mDOM	D-Egg
			
<b>Diameter</b>	330 mm	356 mm	300 mm
<b>Height</b>	330 mm	408 mm	534 mm
<b>Number of PMTs</b>	1	24	2
<b>PMT diameter</b>	10-inch	3-inch	8-inch
<b>Number of planned modules</b>	14	405	279
<b>Production site</b>	WIPAC	DESY, MSU	ICEHAP

Deutsches Elektronen-Synchrotron DESY (DESY), Zeuthen site, as well as at the Michigan State University (MSU).

Proceeding from the idea of stacking two PDOMs facing in different directions, the D-Egg [26] features two 8-inch PMTs pointing in opposite directions. The PMTs are placed inside an elongated glass sphere with a diameter of only 300 mm and a height of 534 mm. For the IceCube Upgrade, 279 D-Eggs will be installed, all produced at the International Center for Hadron Astrophysics, Chiba University (ICEHAP).

Using modules with a larger photocathode area and a denser instrumentation than the existing IceCube detector enhance the amount of detected light, therefore improving the trigger efficiency as well as the reconstruction quality. Both improvements have a direct impact on the sensitivity to tau neutrino appearance measurements which can serve as a probe of the unitarity of the PMNS matrix, as well as on the sensitivity to neutrino oscillation parameters. Figure 1.7 shows the expected performance of the IceCube Upgrade for the atmospheric neutrino oscillation parameters  $\Delta m_{31}^2$  and  $\sin^2(\theta_{23})$ . The black line refers to the 90 % confidence contour of the combined sensitivities using twelve years of DeepCore and three years of IceCube Upgrade data compared to other sensitive experiments including the current results of IceCube in light purple. The combination of IceCube

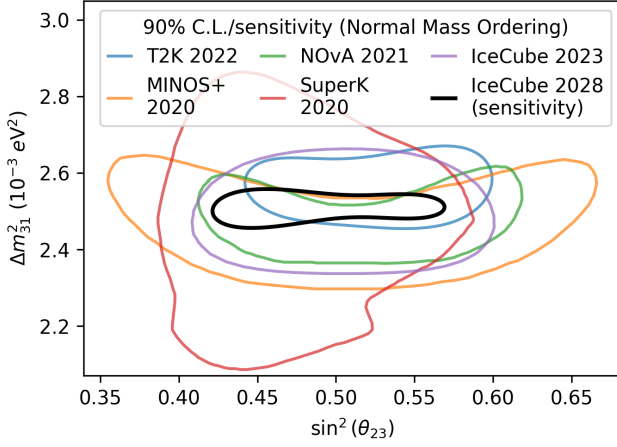


**Figure 1.7:** Comparison of the expected 90 % confidence contours in the  $\sin^2(\theta_{23})$  and  $\Delta m_{31}^2$  plane for IceCube Upgrade + DeepCore (black) compared to the contours of current measurements assuming normal mass ordering. Picture taken from [31] with data from [32, 33, 34, 35, 36].

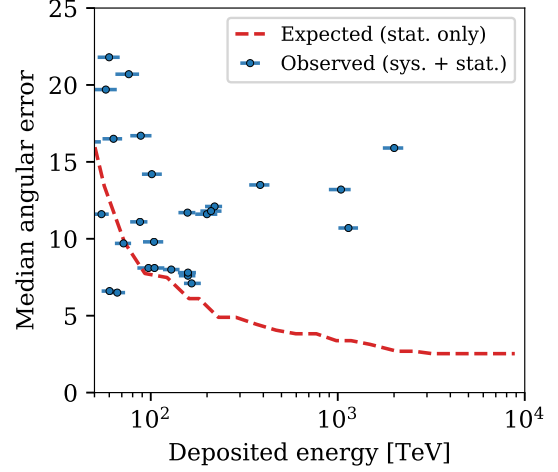


**Figure 1.8:** Median angular error in degrees of the directional reconstruction of cascades versus the reconstructed deposited energy in TeV. Data in blue and reconstruction performance without systematic errors as red dashed line. Picture taken from [7].

Upgrade and DeepCore is expected to perform with a comparable precision as NO $\nu$ A [37], T2K [38], and MINOS [39].

Besides proving the unitarity of the PMNS matrix, the second main scientific goal of the IceCube Upgrade is the detailed measurement and calibration of the ice properties of the glacial Antarctic ice. All reconstruction algorithms used for IceCube are based on measurements of the bulk ice properties. So far, the ice properties are not sufficiently understood, thus imposing a large systematic error on the directional reconstruction of cascade-like neutrino events. Figure 1.8 compares the median angular error of measured data using the current ice model (blue data points) with the error in case the optical ice properties and detector response were understood perfectly (red dashed line, assuming no systematic errors). Especially for events above 200 TeV, the median angular error can be reduced from more than  $10^\circ$  to less than  $5^\circ$  when eliminating the systematic error. As a result, understanding the ice properties is essential to reconstruct the neutrino events measured by IceCube. To measure the bulk ice properties in more detail, about 50 novel calibration devices such as the Precision Optical Calibration Module (POCAM) [40] and the Pencil Beam device (see Section 6 in [41]) will be installed as part of the IceCube Upgrade. The POCAM emits polychromatic light isotropically which is detected by neighboring optical modules. In contrast, the Pencil Beam emits a narrow, collimated, and monochromatic light beam. The Pencil Beam can be pointed to any direction of the 3D space, thus covering a solid angle of  $4\pi$  sr. This light source allows to measure the scattering probability as a function of the angle. Furthermore, each of the approximately 700 new optical modules (PDOM, mDOM, D-Egg) will be equipped with several calibration devices such as cameras and illumination LEDs, which will be used to investigate the optical properties of the ice as described in [42]. With more precise measurements of the ice properties, the ice model used for the reconstruction algorithms can be improved and thus, the directional resolution can be improved. These corrected reconstruction algorithms will not only

be used for the data measured by the IceCube Upgrade, but also for the reanalysis of the data measured by IceCube since the completion of the detector.

Last, the IceCube Upgrade is also a proof of concept for the (optical part of the) future IceCube-Gen2 [43, 44], which is a planned high energy extension of IceCube. In the IceCube Upgrade, the concept of using several PMTs per module is introduced. This concept will be further used and improved for IceCube-Gen2. In addition to PDOM, mDOM, D-Egg, and devices to calibrate the ice properties, several prototype sensors will be installed for the IceCube Upgrade. For instance, prototypes of the optical modules designed for IceCube-Gen2 will be installed. These IceCube-Gen2 DOMs use 16 or 18 PMTs in an elongated glass sphere with a diameter of 312 mm or 318 mm, respectively [45]. Besides, the Acoustic Module will be installed [46]. It uses acoustic signals to determine the position of the module via trilateration. This concept is tested in the IceCube Upgrade to be used for IceCube-Gen2.

### 1.3 Photomultiplier tubes

Photomultiplier tubes (PMTs) are light sensors which are capable of detecting single photons. For the IceCube experiment as well as for the IceCube Upgrade, PMTs are used to detect the Cherenkov light which is generated by the secondary particles produced by neutrinos. In the following, the structure and working principle of the PMTs, the gain, the relevant PMT characteristics, and some technical aspects are explained. Most descriptions of this section are based on [47, 48, 49, 50].

#### 1.3.1 Structure and working principle

Figure 1.9 shows the structure of a PMT. Basically, a PMT consists of an evacuated glass tube which contains a photocathode, focusing electrodes, an electron multiplier system, and an anode. For the PMTs used for the mDOM, the photocathode is placed at the front of the PMT (head-on

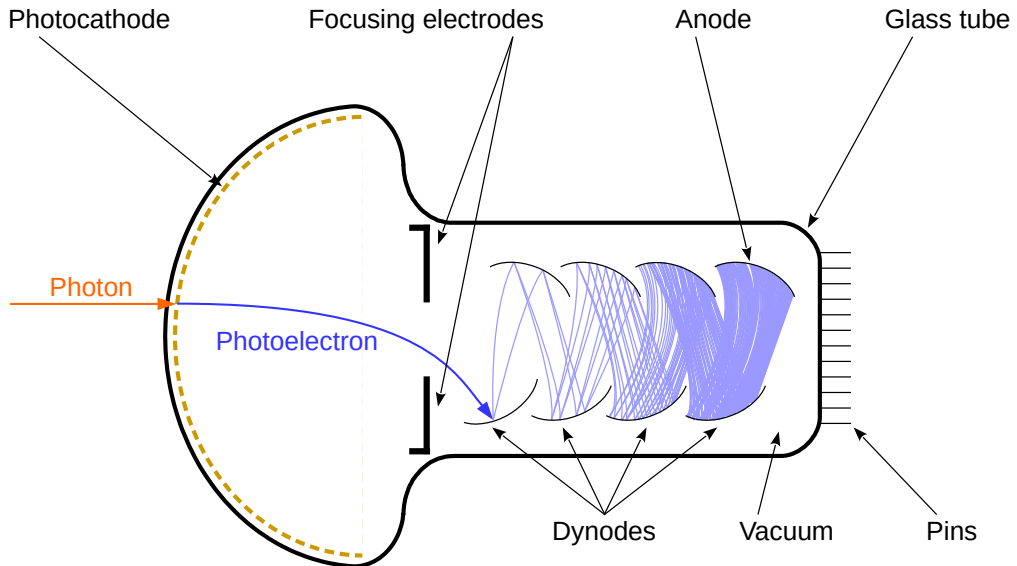


**Figure 1.9:** Schematic structure of a PMT with its main components.

PMT type). In this case, the semitransparent photocathode is deposited on the inner surface of the glass tube as shown in Figure 1.9. When light impinges on the photocathode, a photoelectron can be produced via the photoelectric effect. Subsequently, the photoelectron is directed and accelerated to the first dynode of the electron multiplier system by the focusing electrodes. When the photoelectron impinges on the first dynode, secondary electrons are produced. These secondary electrons are directed to the second dynode producing further secondary electrons. This mechanism continues up to the last dynode which is the anode. The amplification is so high that photoelectrons generated by single photons produce a measurable signal at the anode. The corresponding signal at the anode is characterized by the term photon equivalent (p.e.). One detected photon produces a signal of 1 p.e., two detected photons a signal of 2 p.e., and so on. In the following, the expression “p.e.” is used to describe the charge of the corresponding signal (one detected photon produces a charge of 1 p.e. and so on). To accelerate the electrons on and on, each dynode has to be on a higher potential compared to the previous one or the photocathode, respectively. This potential difference is achieved by applying a high voltage (HV) to each dynode as well as to the photocathode. How this HV supply works, is explained in Subsection 1.3.4 in more detail. Depending on the intended use of the PMT, the number of dynodes can vary between 8 to 19 stages [49]. Moreover, the dynodes can be arranged in different ways. For instance, the dynodes can be ordered in a circle or, as shown in Figure 1.9, in a linear manner. The arrangement of the dynodes influences the timing behavior as well as the PMT size. A more detailed description can be found in [48]. For the mDOM PMT, a circular and linear-focused dynode structure is used. Consequently, the PMTs are relatively compact while having a fast time response (few nanoseconds [48]) as well as a very good pulse linearity. The electrical connections of the photocathode and the dynode is provided by the pins at the back of the PMT. Furthermore, the signal is read out via the corresponding pin at the back of the PMT.

### 1.3.2 Gain

The gain is the amplification factor of a PMT. Two parameters influence the gain. First, not all electrons emitted by the  $i$ -th dynode also impinge on dynode  $i + 1$ . This fraction is described by the collection efficiency  $ce_i$  of the  $i$ -th dynode:

$$ce_i = \frac{N_{e,i+1}^{IN}}{N_{e,i}^{OUT}}, \quad (1.7)$$

where  $N_{e,i+1}^{IN}$  is the number of electrons reaching dynode  $i + 1$  and  $N_{e,i}^{OUT}$  is the number of electrons emitted by dynode  $i$ . For the PMT shown in Figure 1.9, the collection efficiency of all seven dynodes is 1. In reality, however, the collection efficiency depends on the applied interdynode HV and the dynode type.

Second, the number of secondary electrons produced by each dynode influences the PMT gain. This number is described by the secondary emission coefficient  $\delta_i$  of the  $i$ -th dynode:

$$\delta_i = \frac{N_{e,i}^{OUT}}{N_{e,i}^{IN}}, \quad (1.8)$$

where  $N_{e,i}^{OUT}$  is the number of produced secondary electrons and  $N_{e,i}^{IN}$  is the number of incident electrons. Similar to the collection efficiency, the secondary emission coefficient depends on the

interdynode HV as well as on the dynode material. Typical values for  $\delta$  are 2–10 [48, 47]. In Figure 1.9, the secondary emission coefficient of all seven dynodes is 2.

With the collection efficiencies and the secondary emission coefficients of the dynodes, the gain of a PMT can be calculated. For the measurements of this thesis, however, the gain denotes the amplification factor of only the PMT multiplier system neglecting the collection efficiency between photocathode and first dynode. Thus, the gain  $G$  is defined as [47]:

$$G = \frac{N_{e,\text{coll}}}{N_{e,\text{imp}}} = \prod_i ce_i \cdot \delta_i, \quad (1.9)$$

where  $N_{e,\text{coll}}$  is the number of electrons collected at the anode and  $N_{e,\text{imp}}$  is the number of photoelectrons impinging on the first dynode. For the PMT shown in Figure 1.9, the gain can be calculated as follows:

$$G = 2^7 = 128,$$

assuming  $ce_i = 1$  and  $\delta_i = 2$ . Together with the number of dynodes, both the collection efficiency as well as the secondary emission coefficient influence the gain which is typically about  $10^6$ . Due to its dependency on collection efficiency and secondary emission coefficient, the gain increases exponentially with increasing HV.

### 1.3.3 Characteristics

In this subsection, the PMT characteristics relevant for this work are explained. These characteristics include time characteristics such as transit time and transit time spread (TTS), the quantum efficiency (QE), the darkrate, and correlated noise such as prepulsing, delayed pulsing, and afterpulsing. The characteristics explained in this subsection are investigated for different PMT types in Chapter 3.

#### 1.3.3.1 Time characteristics

When a PMT is illuminated with a short light pulse (ideally, a delta peak), the PMT output can be described by certain time characteristics shown in Figure 1.10. The electrons arriving at the PMT anode produce a current which is typically measured via a resistor as voltage pulse over time (PMT signal). The time between the occurrence of the light signal and the PMT signal crossing a certain threshold is called transit time. For identical light pulses impinging on the same part of the photocathode, however, the transit time can vary. This fluctuation is called transit time spread (TTS) (to measure the TTS, the light pulse should be much shorter than the TTS of the PMT). Different photoelectron flight paths as well as different initial photoelectron velocities are reasons for the TTS. Because the TTS falsifies the real arrival time, the TTS directly limits the time resolution of the PMT. To reduce the TTS and increase the time resolution of the mDOM PMTs, the photocathode is shaped like a mushroom head as shown in Figure 1.9, so that the different paths from photocathode to the focusing electrodes have almost the same distance.

Three more parameters characterize a PMT signal. The rise time is the time the PMT signal needs to increase from 10 % to 90 % of the pulse height. Similarly, the fall time is the time the PMT signal needs to decrease from 90 % to 10 % of the pulse height. Finally, the signal length can be described by the full width at half maximum (FWHM).

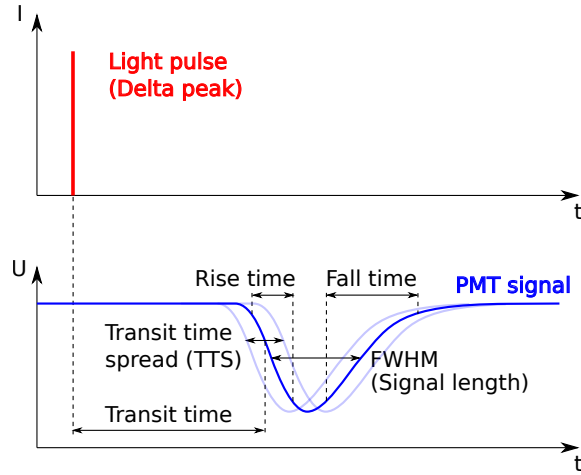


**Figure 1.10:** Illustration of the timing characteristics of the PMT output. Figure adapted from [48, 50, 51].

### 1.3.3.2 Quantum efficiency

As explained in Subsection 1.3.1, a photoelectron can be produced when light impinges on the PMT photocathode. During this process, the photon is absorbed and its energy  $E = h \cdot c / \lambda$  is transferred to an electron in the valence band of the photocathode material. To be emitted from the photocathode to the vacuum, the electron has to overcome a certain potential barrier which is called photoemission threshold  $W_{\text{ph}}$ . For metals, the photoemission threshold equals the thermionic work function  $W_{\text{th}}$  [47]:

$$W_{\text{ph}} = W_{\text{th}} = E_0 - E_{\text{F}}, \quad (1.10)$$

which is the difference of the potential energy  $E_0$  of an electron in vacuum and the Fermi level  $E_{\text{F}}$ .

Not every incident photon generates a photoelectron. The ratio of photoelectrons  $N_{\text{e,ph}}$  to the number of incident photons  $N_{\gamma}$  is called quantum efficiency (QE):

$$\text{QE} = \frac{N_{\text{e,ph}}}{N_{\gamma}} = \frac{h \cdot c}{\lambda \cdot e} \cdot \frac{I_{\text{k}}}{\Phi_{\gamma}}, \quad (1.11)$$

where  $h$  is the Planck constant,  $c$  the speed of light in vacuum,  $\lambda$  the wavelength of the incident light,  $e$  the electric constant,  $I_{\text{k}}$  the photocathode current, and  $\Phi_{\gamma}$  the flux of the incident light. Because the photon energy of the incident light depends on the wavelength, also the QE is wavelength-dependent. In fact, the QE is limited to longer wavelengths by the photoemission threshold which depends on the photocathode material. For the mDOM PMTs, the photocathode is made of a bialkali<sup>1</sup> material [52]. For bialkali materials, the maximal detectable wavelength is about 650 nm [48]. At short wavelengths, the transmission of the PMT window material typically limits the minimal detectable wavelength. The PMTs used for the mDOM have a window made of borosilicate glass [52]. Wavelengths below approximately 300 nm have a transmission close to zero and thus, cannot be detected by a PMT with a borosilicate glass window [48]. Typical values for the QE are between 0.15 and 0.4 [48].

<sup>1</sup>A combination of materials including two alkali metals.

### 1.3.3.3 Darkrate

A PMT produces signals even when no photons from a light source impinge on the PMT. The number of these signals per time is called darkrate. Four main causes contribute to the darkrate: Leakage current, thermionic emission, field effect, and background radiation.

In general, leakage current is a current which occurs when ideally no current should flow, for example, through an insulator. For a PMT, this current flows for instance through the electric connection between anode and last dynode (through the resistor chain shown in Figure 1.11). The leakage current is the only continuous component of the darkrate. In contrast to other darkrate contributions, the leakage current depends roughly linearly on the HV. Therefore, the leakage current dominates at low HVs (below approximately 750 V [48]) and at low temperatures.

As explained in Subsection 1.3.3.2, a photoelectron is produced only in case the energy of the incoming photon is larger than the thermionic work function of the metal-based photocathode. A similar energy threshold also exists for the secondary electrons produced at the dynodes. However, the energy thresholds of photocathode and dynodes are typically so low (for example, approximately 2 eV for bialkali materials [48, 47]) that electrons can be emitted even at room temperature due to thermal excitation. These electrons are accelerated and multiplied exactly the same as a photoelectron generated by a photon or a secondary electron. Finally, the thermally generated electrons produce a PMT signal which looks like a photon-induced signal. Because the photocathode is much larger than the dynodes and because especially later dynodes stages contribute less to the anode current, the thermionic emission from the photocathode dominates over the emission from the dynodes. Mostly, the PMT signals from thermionic emission have a charge of 1 p.e. or 2 p.e. The darkrate caused by thermionic emission increases exponentially with the HV. At typical operating HVs between approximately 750 V and 1300 V, the thermionic emission is the dominant contribution to the darkrate. Moreover, the thermionic emission increases with the temperature. Therefore, cooling of the photocathode helps to reduce the darkrate.

For HVs above approximately 1300 V, field emission becomes the dominant contribution to the darkrate. Field emission occurs when the electric field between the dynodes becomes so strong that electrons are emitted. Similar to the thermionic emission, these electrons are accelerated in the multiplier system of the PMT and produce a signal at the anode which equals a PMT signal generated by an incident photon. The field emission increases mainly with the HV.

Finally, background radiation such as cosmic rays and radioactivity contributes to the darkrate. Cosmic rays can produce Cherenkov light while passing through the PMT glass. In addition to that, radioactive decays of materials near or in the PMT (for example, the potassium 40 isotope ( $^{40}\text{K}$ ) which most of the PMT glasses contain) can increase the darkrate. While thermionic emission produces PMT pulses of mostly 1 p.e., radioactivity can produce signals up to 15 p.e. Signals induced by cosmic rays typically reach pulse heights between 15 p.e. and 200 p.e. [50].

In addition to the previously described causes for a permanent increase of the darkrate, the exposure of the photocathode to light intensities visible for the human eye can lead to a temporary increase of the darkrate. This increase is caused by the excitation of the photocathode or the glass envelope. How large the darkrate increases depends on the wavelength, the incident flux and the duration of the exposure. However, in case the incident flux is about 10 000 lx or higher, the photocathode can be irreversibly damaged [48]. Photocathode and glass envelope are also excited when no HV is applied to the PMT during the exposure to large light intensities. To decrease the darkrate again, the PMT must stay several minutes to hours—dependent on the PMT type—in the dark and connected to the HV [48, 47].

### 1.3.3.4 Correlated noise

In contrast to the darkrate, which is an uncorrelated background noise to the PMT signal, the correlated noise is correlated in time to a “normal” PMT signal (main pulse). Three different correlated noise types can be distinguished: Prepulsing, delayed pulsing, and afterpulsing. In the following, these three types are described in more detail.

#### Prepulsing

In some cases, the incident photon passes through the photocathode without producing a photoelectron. Instead, a photoelectron is created at the first dynode. Due to one missing amplification stage, the resulting PMT pulse is smaller compared to a PMT signal produced by all amplification stages. Furthermore, the PMT pulse arrives earlier than the main pulse. Therefore, this type of correlated noise is called prepulsing. The time difference  $\Delta_{\text{Prepulse}}$  between prepulse and main pulse is the difference of the average time  $t_e$  a photoelectron needs to travel from photocathode to the first dynode and the time  $t_\gamma$  a photon needs for the same path:  $\Delta_{\text{Prepulse}} = t_e - t_\gamma$ . How large  $\Delta_{\text{Prepulse}}$  is depends on the PMT type. For a 3-inch PMT as used for the mDOM,  $\Delta_{\text{Prepulse}}$  is typically between 10 ns and 20 ns [52].

#### Delayed pulsing

On occasion, the photoelectron produced at the photocathode scatters elastically at the first dynode and is backscattered towards the photocathode. In case this photoelectron is reaccelerated towards the first dynode and produces secondary electrons, the resulting PMT pulse is delayed in time compared to the main pulse. Thus, this correlated noise type is called delayed pulsing. Because the photoelectron travels a part of the distance between photocathode and first dynode three times instead of one time, the delayed pulse can arrive up to roughly  $2t_e$  later than the main pulse. Typical values for a 3-inch PMT are 15 ns up to about 80 ns [52].

#### Afterpulsing

Although the PMT is evacuated, some gas atoms remain inside the tube. With a certain probability, the secondary electrons from the main pulse can hit one of those gas atoms and ionize it. As a result, a positive ion is generated. This positive ion is accelerated towards the photocathode which is called ion feedback. When the ion hits the photocathode, it typically generates several photoelectrons which in turn produce a PMT signal following the main pulse. This pulse arriving after the main pulse is called an afterpulse. For a 3-inch PMT, afterpulses arrive typically between 100 ns and about  $10\ \mu\text{s}$  after the main pulse [52].

Table 1.2 shows an overview of the three correlated noise types. Each noise type has its own time and charge characteristic which helps to distinguish them. Prepulses arrive about 10–20 ns earlier than the main pulse and are smaller than a normal pulse. Delayed pulses, in contrast, are about 15–80 ns delayed compared to the main pulse, but have the same charge as normal. Prepulses as well as delayed pulses are a shift of the main pulse. Different from that, afterpulses occur in addition to the main pulse about 100 ns to  $10\ \mu\text{s}$  later than the main pulse [52] and have a significantly higher charge up to about 15 p.e. [50].

**Table 1.2:** Overview of the three correlated noise types: Prepulsing, delayed pulsing, and afterpulsing. Timing and probability values taken from [52].

	Prepulsing	Delayed pulsing	Afterpulsing
<b>Cause</b>	Photoelectron produced at first dynode	Elastic scattering of photoelectron at first dynode	Ion generates photoelectrons at photocathode
<b>Timing characteristics</b>	10–20 ns before main pulse	15–80 ns after main pulse	100 ns–10 $\mu$ s after main pulse
<b>Pulse characteristics</b>	Shift of main pulse	Shift of main pulse	Following main pulse
<b>Charge</b>	Less than normal	Same as normal	1–15 p.e.
<b>Typical probabilities</b>	0.1–1 %	3.5–5 %	5–15 %
<b>Schematic waveform</b>	<p>The schematic waveform diagram illustrates the timing of different noise events relative to the main pulse. The horizontal axis represents time <math>t</math> with key markers at -20 ns, 0, 40 ns, and 1 <math>\mu</math>s. A vertical line at <math>t=0</math> is labeled 'Main pulse arrival time'. The waveform shows four distinct events: a 'Prepulse' at -20 ns, the 'Main pulse' at 0, a 'Delayed pulse' at 40 ns, and an 'Afterpulse' at 1 <math>\mu</math>s. A '+' sign is positioned between the main pulse and the delayed pulse.</p>		

### 1.3.4 Technical aspects

In this subsection, some technical aspects of the PMT operation are explained. Subsection 1.3.4.1 focuses on two base types which are both used for the measurements described in this thesis. In Subsection 1.3.4.2, the two alternatives of HV polarity are described. Finally, Subsection 1.3.4.3 discusses two PMT operation modes which are both used in this thesis.

#### 1.3.4.1 Base types

To operate a PMT, a HV of about 1000 V is needed. This HV is applied to the PMT photocathode, the dynodes, and the anode of the PMT. In general, the HV is provided by an electric circuit

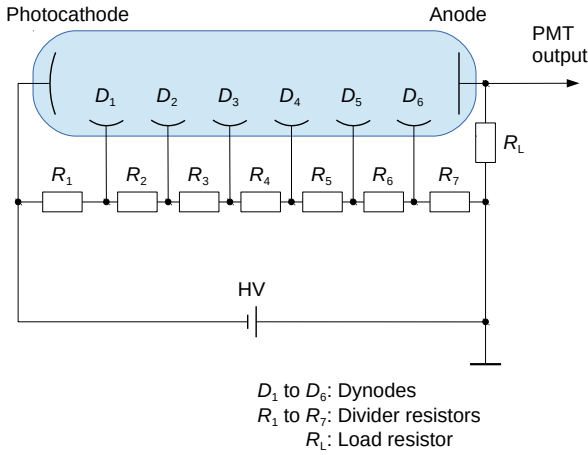


**Figure 1.11:** Schematic drawing of a voltage-divider circuit. Figure modified from [48].

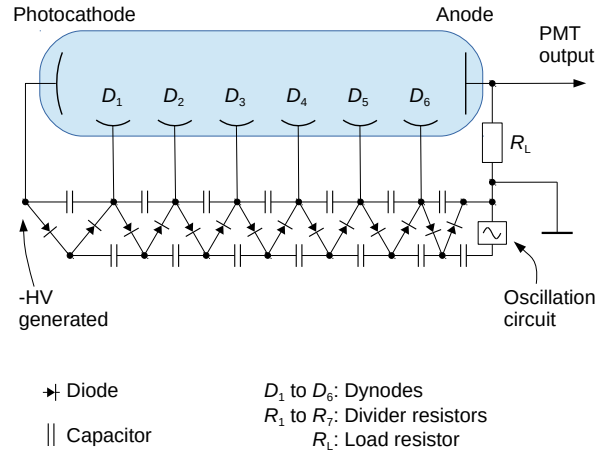


**Figure 1.12:** Schematic drawing of a Cockcroft-Walton circuit. Figure modified from [48].

which is connected to the PMT pins. This circuit is called PMT base. The PMT bases can be classified into passive and active bases. Passive bases consist only of passive electrical components such as resistors. In contrast, active bases additionally contain components which can actively increase the supply voltage, for example diodes. In the following, the two base types used in this thesis are described.

### Voltage-divider circuit

The voltage-divider circuit belongs to the passive bases. Figure 1.11 shows a schematic drawing of a typical voltage-divider circuit. All components of the multiplier process inside the PMT (photocathode, the dynodes, and the anode) are connected to a resistor chain consisting of the resistors  $R_1$  to  $R_7$ . Typical resistor values are between  $100\text{ k}\Omega$  and  $1\text{ M}\Omega$  [48]. A single HV supply providing the  $1000\text{ V}$  is connected to the resistor chain. Thus, the applied HV is divided such that each component in the multiplier process has a higher potential than the previous one. Between photocathode and anode, the undivided HV of the power supply is applied. At the PMT output, the voltage signal is picked up.

### Cockcroft-Walton circuit

The Cockcroft-Walton circuit is a voltage multiplier circuit converting a comparatively low (for example,  $5\text{ V}$  amplitude) alternating voltage into a high (for instance,  $1000\text{ V}$ ) direct current voltage. This circuit type is an active circuit forming an active PMT base. In Figure 1.12, a schematic drawing of a Cockcroft-Walton circuit is shown. A sequence of diodes and capacitors replaces the resistor chain used for the voltage-divider circuit. An oscillation circuit feeds a comparatively low alternating voltage into the Cockcroft-Walton circuit. Due to the switching between positive and negative input voltage  $U_{\text{in}}$ , the voltage at each dynode stage  $n$  is increased by a factor of  $2n \cdot U_{\text{in}}$ . Thus, each stage is supplied with a successively increased voltage. In contrast to the voltage-divider circuit, the Cockcroft-Walton circuit generates the necessary HV for each stage up to the maximal HV between photocathode and anode. The advantage of the Cockcroft-Walton

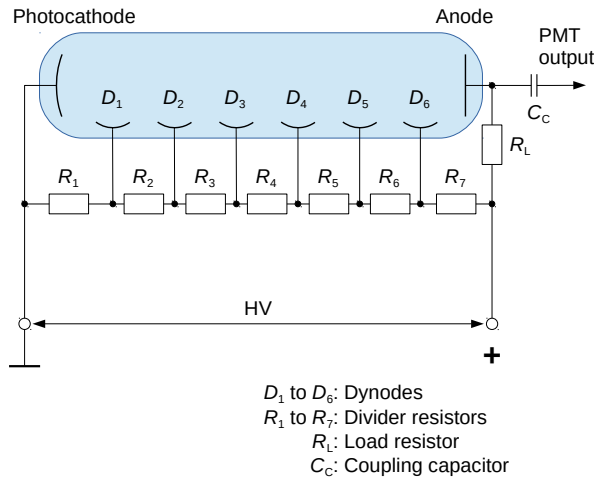


**Figure 1.13:** Schematic circuit diagram of a voltage-divider circuit using a positive HV (photocathode on ground potential). Figure modified from [47].

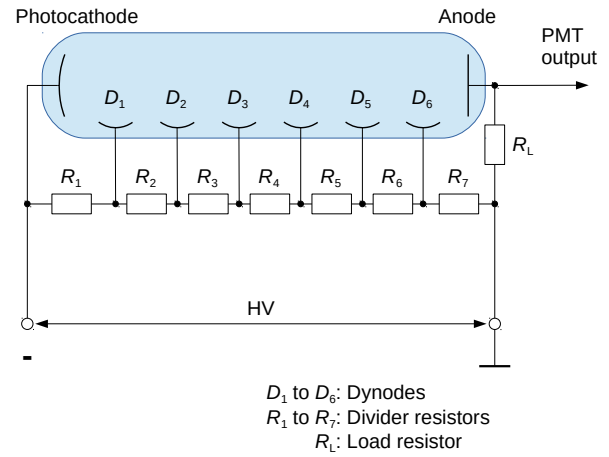


**Figure 1.14:** Schematic circuit diagram of a voltage-divider circuit using a negative HV (anode on ground potential). Figure modified from [47].

circuit is its low power consumption. For instance, while requiring an input of 6–12 V, the power consumption of commercial devices is about 0.1 W [53].

### 1.3.4.2 High voltage polarity

The applied PMT HV can be either positive or negative. Which HV polarity is chosen depends on the application. In the following, the two HV alternatives are explained on the basis of the voltage-divider circuit.

#### Positive HV

Figure 1.13 shows a schematic circuit diagram of a PMT using a circuit with a positive HV. In this case, the photocathode is kept at ground potential whereas the anode is at a high positive potential. Using this HV polarity makes the PMT less prone to disturbances of the electron paths inside the PMT which can increase the darkrate (see increasing darkrate for negative HV in Paragraph 1.3.4.2) during operation. To separate the output signal from the HV at the anode, a coupling capacitor  $C_c$  is used. Due to the time constant of the capacitor in combination with the resistance of the cable, however, the PMT signal is broadened which reduces the time resolution.

#### Negative HV

In Figure 1.14, a schematic circuit diagram for a PMT using a negative HV is shown. The negative HV is applied to the photocathode while the anode stays on ground potential. In this case, no coupling capacitor is needed and the output signal can be picked up directly from the PMT output. Thus, the PMT signal is not reshaped and maintains its timing information. Therefore, a negative HV is often used for applications which need a fast timing [54]. However, operating the photocathode at a high negative potential can increase the PMT darkrate. Grounded metal (for example, a PMT mounting) near the glass tube can attract electrons from the multiplier cascade. When the electrons hit the glass, they can cause scintillation light. In addition, leakage current

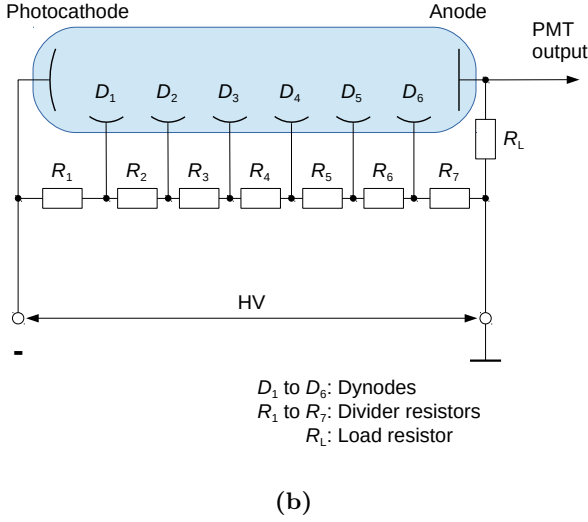
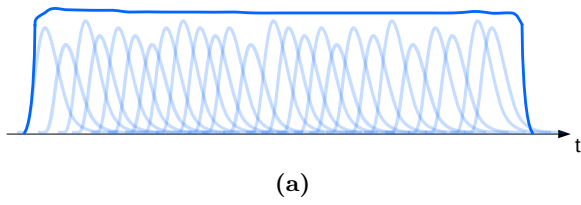


**Figure 1.15:** (a) Illustration of the PMT output for current mode. (b) Schematic circuit diagram for a PMT operated in current mode. Figures modified from [49].

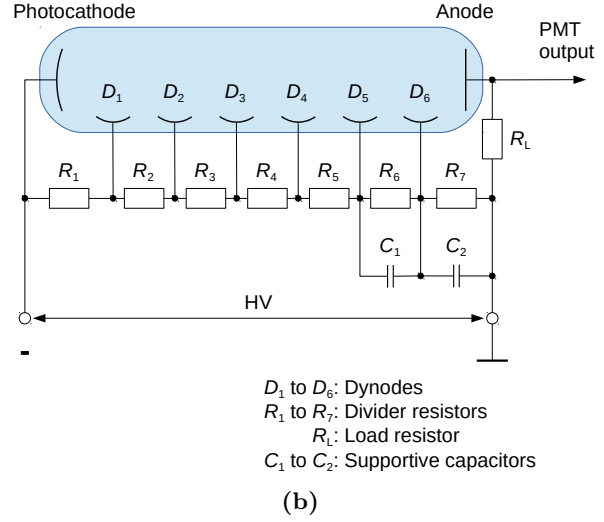
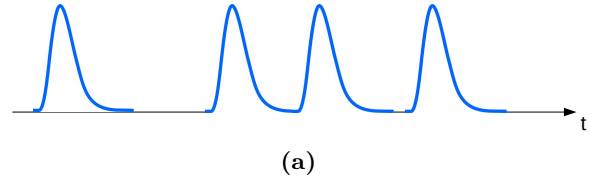


**Figure 1.16:** (a) Illustration of the PMT output for pulse mode. (b) Schematic circuit diagram for a PMT operated in pulse mode. Figures modified from [49].

between the photocathode and the glass can occur when the glass close to the photocathode is on ground potential. Both scintillation as well as leakage current lead to an increase of the darkrate. To neutralize the potential gradients and avoid these effects, the glass tube can be coated with a conductive layer which is connected to photocathode potential. The conductive layer, in turn, is covered by an insulating coating with a high insulation resistance.

### 1.3.4.3 PMT operation modes

A PMT can be operated in current mode or in pulse mode depending on the application. In the following, both operation modes are explained by reference to the voltage-divider circuit.

#### Current mode

As explained in Subsection 1.3.3.1, the illumination of a PMT with a delta peak causes a short voltage pulse at the PMT output. In case the PMT is illuminated with many light pulses in quick succession (or continuous light), the output pulses add up to a continuous signal as shown in Figure 1.15a. In current mode, this continuous output current is measured. Therefore, a circuit as shown in Figure 1.15b is used for the PMT base. A negative HV with the anode on ground potential has to be used, because the coupling resistor used for positive HV and shown in Figure 1.13 would block the continuous current signal.

**Pulse mode**

Operating a PMT in pulse mode means using a pulsed light source. Consequently, the PMT output is not continuous, but consists of short voltage pulses as shown in Figure 1.16a. Furthermore, the used light intensities are often so small that each pulse refers to one detected photon. Both a positive and a negative HV can be used to operate a PMT in pulse mode. In Figure 1.16b, a schematic circuit diagram for a negative HV is shown. When a PMT is operated in pulse mode, high peak currents, especially between the last dynode stages, can occur (up to approximately 200 mA [50]). Such high currents can lead to an additional release of electrons (field emission, see Subsection 1.3.3.3) because of the strong electric fields, or to saturation of the dynodes. For such cases, additional capacitors  $C_1$  to  $C_2$  are connected in parallel to the resistors. During the electron cascade, the capacitors provide an additional charge, thus helping to maintain linearity and avoid saturation effects [50]. All measurements described in this thesis, except the QE measurements described in Subsection 3.3.2, were performed in pulse mode.

## Chapter 2

# The multi-PMT Digital Optical Module for the IceCube Upgrade

---

<b>2.1</b>	<b>Challenges and advantages of the mDOM . . . . .</b>	<b>23</b>
<b>2.2</b>	<b>Design . . . . .</b>	<b>25</b>
<b>2.3</b>	<b>Working principle . . . . .</b>	<b>27</b>
<b>2.4</b>	<b>Components relevant for this work . . . . .</b>	<b>29</b>
2.4.1	Photomultiplier tubes . . . . .	29
2.4.2	PMT base . . . . .	29
2.4.3	Analog front end . . . . .	31
2.4.4	Mainboard . . . . .	32
<b>2.5</b>	<b>Data acquisition and operation in ice . . . . .</b>	<b>35</b>

---

In this chapter, the multi-PMT Digital Optical Module (mDOM), which will be used for the IceCube Upgrade among other sensor types (see Table 1.1), will be introduced. The first section (Section 2.1) gives an overview of the challenges as well as the advantages of the mDOM. Section 2.2 focuses on the mechanical design with the main components. Afterwards, Section 2.3 explains the working principle of the mDOM. In Section 2.4, the mDOM components relevant for this work are described in more detail: photomultiplier tube (PMT), PMT base, analog front end (AFE), and mainboard. Finally, Section 2.5 focuses on the data acquisition.

### 2.1 Challenges and advantages of the mDOM

The installation of the IceCube Upgrade leads to several challenges which result in certain requirements the mDOM has to fulfill. Apart from that, the special design of the mDOM has a few advantages compared to other DOM designs such as the PDOM. Both aspects are discussed in the following in more detail.

## Challenges and resulting requirements for the mDOM

As described in Subsection 1.2.2, more than 400 mDOMs will be installed in the glacier of Antarctica as part of the IceCube Upgrade project. This isolated detector location leads to several challenges which have to be taken into account in the mDOM design. In the following list, these challenges are explained in more detail.

**Low temperatures** The environmental temperatures in the region where the mDOMs will be installed and are later operating is between approximately  $-27^{\circ}\text{C}$  and  $-19^{\circ}\text{C}$  (installation depths taken from [7], ice temperatures taken from [55]). All components including the electronics must work at these temperatures reliably. In addition to that, the switched off mDOMs must sustain even more extreme temperatures during the installation (Using the hot-water drilling method [19], a borehole filled with water is drilled in the glacier. The modules are placed inside the water and the borehole refreezes afterwards.). Within seconds, the environmental mDOM temperature changes from approximately  $-50^{\circ}\text{C}$  at the glacier surface up to about  $0^{\circ}\text{C}$  [56] when the mDOM is placed inside the borehole filled with water. Similar to the above mentioned operation temperature, the mDOM must resist this temperature change during installation.

**Limited space** Due to the drill costs, the borehole diameter is restricted. Therefore, the overall mDOM diameter is limited which limits the entire available space inside one mDOM. To fit in all components nevertheless, the mDOM is not a sphere, but extended in the middle with a cylindrical part (see Section 2.2). Additionally, the used PMTs are custom designed for the mDOM space requirements. Thus, the PMTs are about 6 mm shorter than the PMTs used for the KM3NeT experiment in [29].

**High pressure** When the IceCube DOMs were installed, pressure peaks up to about 550 bar were measured [57]. Including a safety margin, the mDOM is required to withstand external pressures of about 690 bar [57]. Furthermore, the mDOMs have to withstand (stay closed) the—compared to normal pressure—lower pressure in an airplane. The mDOM must be designed such that it resists these pressure characteristics.

**Limited power supply** Due to the isolated location in Antarctica deep in the glacier ice, the available power supply is limited. Therefore, a requirement of the entire module is a low power consumption (during normal operation, an mDOM consumes a total power of about 9 W, see Figure 5.9). This limitation applies to all electronic components such as the PMT base and the mDOM mainboard.

**Faint signals** Neutrinos are detected by measuring the Cherenkov light produced by the secondary particles which the neutrinos generate. In ice, the typical number of produced Cherenkov photons is in the order of few hundred photons per centimeter. However, the distances of the different modules is in the order of few meters. For a reconstruction as good as possible, the PMTs must be able to detect small photon numbers, in effect, single photons.

**Limited transmission bandwidth** Last, the bandwidth of the data transfer from the mDOM to the surface is limited. This issue comes from the cables which are used for the modules in the glacier. In effect, each cable behaves like a bandpass filter. Signals with low frequencies (low data transfer rate) can pass almost unchanged whereas signals with high frequencies (high data transfer rates) are attenuated. Thus, the maximum data transfer rate of one cable is about 1.5 Mb/s [58]. On the one hand, the limited bandwidth imposes a limit on the overall background noise. For instance, not all neutrino signals might be transferred to the surface in case the background noise is too high. Thus, not only the noise of the PMTs themselves

must be as low as possible (in this thesis, the measured darkrate is typically around 70 Hz at  $-20^{\circ}\text{C}$ , see Figure 3.13), but also the radioactivity of the used components—which would increase the noise of the integrated PMTs—such as pressure vessel glass and optical gel must be low (the radioactivities of pressure vessel and optical gel were measured in [59], see page 40, Table 6.3). Besides, the limited bandwidth influences the data processing inside the mDOM. In essence, only the charge and the time is transferred (see Section 2.5) in most cases and not the raw signal.

**Reliability** After the installation of the mDOMs in the glacier ice, it is no longer possible to recover the mDOMs, for instance in case of a failure. Therefore, it is required that at least 95 % of the mDOMs have to operate reliably for ten years [57].

### Advantages of the mDOM

Compared to the PDOM, some design improvements were made which lead to several advantages of the mDOM compared to the PDOM. In the following, these advantages of the mDOM are presented.

**Large sensitive area** An mDOM uses 24 small (3-inch) PMTs instead of one large 10-inch PMT as the PDOM. Thus, the sensitive area of an mDOM is about two times the sensitive area of a PDOM.

**$4\pi$ -angular acceptance** The PMTs of an mDOM are angled in different directions, thus covering an angular acceptance of  $4\pi$ . Compared to that, the PMT of a PDOM is directed downwards having an angular acceptance of roughly  $2\pi$ .

**Directional resolution** The sensitive area of an mDOM is segmented into 24 (independent) sensitive areas (each PMT). This segmentation leads to an intrinsic directional resolution of the mDOM.

**Background suppression** The use of several individual PMTs allows to eliminate a certain type of background noise. Coincident noise hits detected by different PMTs can be suppressed by reconstruction algorithms such as used in [25].

**Photon counting** The reconstruction of the number of detected photons and their respective arrival time is more precise when using several small PMTs instead of one large PMT. For one large PMT, the number of photons and the arrival time has to be reconstructed from a multi-photon event. In case of the mDOM, however, each PMT has its own data readout which has to process less photons at a time.

## 2.2 Design

The design idea of the mDOM was inspired by the multi-PMT design used for the KM3NeT DOM which is described in [29]. For the IceCube Upgrade, however, the KM3NeT design was adapted and optimized for a maximum effective area and a minimized diameter due to the limited borehole diameter. An overview of the mDOM design can be found in [30]. Figure 2.1 shows two schematics of the mDOM design. In the left schematic, a closed mDOM is shown. The mDOM consists of a 13 mm thick pressure vessel made of borosilicate glass protecting the inner components from the environmental pressure (can be up to approximately 700 bar [19]) and containing 24 PMTs as well as further parts. To be exact, the pressure vessel consists of two half spheres with a cylindrical extension in the middle. Thus, the closed pressure vessel has a diameter of 356 mm and a height of

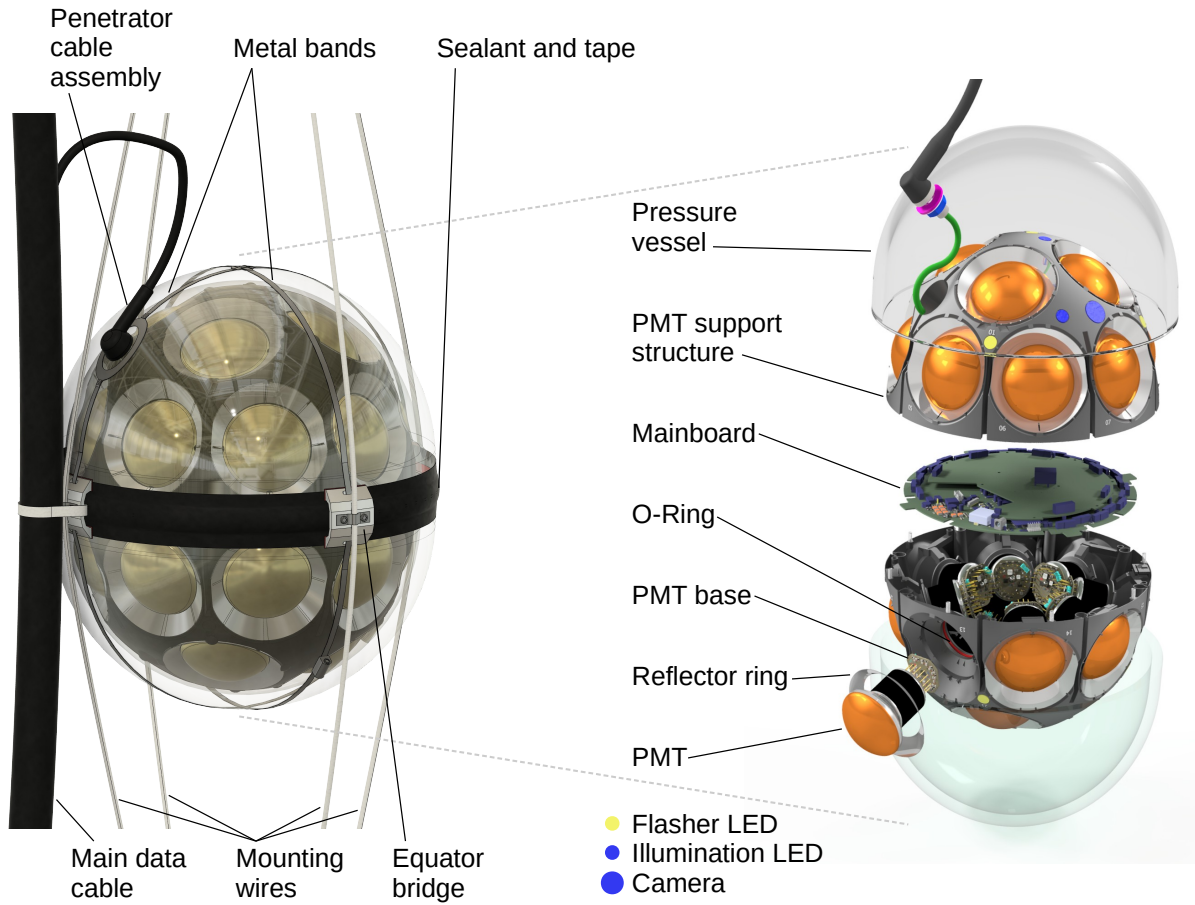


**Figure 2.1:** Schematics of the mDOM. Left picture: Modified from [60]. Right picture: Modified from [25].

410 mm [30]. The two half spheres of the pressure vessel are held together by two crossed metal bands. To prevent the mDOM from leakage, a sealant covered by a tape seals the interface of the two hemispheres. Four equator bridges are glued to the outer pressure vessel surface. A mounting wire is fixed to each equator bridge. Together with the bridges, the mounting wires hold the mDOM in place. The penetrator cable assembly is connected to the main data cable.

The right schematic of Figure 2.1 shows an exploded view of the mDOM with a focus on the inner parts. The entire communication with the mDOM as well as its power supply is guided inside and outside the mDOM through the penetrator cable assembly. This special cable is directed through a borehole in the upper hemisphere of the pressure vessel. Sealings and insulations around the cable prevent the cable as well as the glass from possible damages. The cable is also guided through the PMT support structure which holds the PMTs in place. Between pressure vessel and PMT support structure, an approximately 4 mm thick layer (in the center of the PMT photocathode [61]) of a silicone-based two-component optical gel is poured. On the one hand, the optical gel has a refractive index close to the glass of the pressure vessel and thus, minimizes the refraction loss of incident light at the boundary surface between optical gel and pressure vessel glass. On the other hand, the optical gel serves as cushion between pressure vessel glass and the PMTs. The mainboard is attached to the top margin of the PMT support structure of the lower

hemisphere such that the mainboard is located in the middle of the two mDOM hemispheres. Each of the two hemispheres of the support structure has twelve holes for the PMTs. An O-Ring clipped into a notch in the PMT support structure prevents the optical gel from flowing into the inside of the mDOM during the pouring process of the gel. The PMT holes are arranged in two rows. Each hemisphere contains four PMTs close to the respective up- or downside of the mDOM and eight PMTs close to the middle. Altogether, 24 PMTs are contained inside the mDOM. Moreover, the photocathode of each PMT is surrounded by a reflector ring made from a 0.5 mm thick coated aluminum sheet. Furthermore, each PMT has its own base which is soldered to the pins at the backside of the PMT. Additionally, three further devices are introduced in the PMT support structure: Flasher LED, illumination LED, and camera. Their respective position is indicated by a colored circle in Figure 2.1. A more detailed overview of this positioning is shown in Figure 2.4. One mDOM contains three cameras, four illumination LEDs and ten flasher LEDs. The inner volume of the mDOM which is surrounded by the two hemispheres of the PMT support structure is filled with gaseous nitrogen. The gas pressure is about 480 mbar. Using nitrogen ensures a clean and dry atmosphere which is important for the electronics. Besides, the low pressure prevents the mDOM from opening during transport with an airplane or at the South Pole.

## 2.3 Working principle

Basically, the mDOM works as follows. Light—produced either by a neutrino or by calibration devices—impinges on the mDOM. First, the light has to pass the pressure vessel which has a transmittance close to 100 % [62] for wavelengths above approximately 350 nm up to at least 700 nm<sup>1</sup>. After that, the light passes the optical gel layer which has a transmittance of about 90 % for wavelengths between 350 nm and 750 nm [63]. Afterwards, the light (more precisely, light with wavelengths between approximately 275 nm and 700 nm, see Figure 3.12 and Figure 3.13) is detected by the PMTs. Each PMT is held in place by the PMT support structure which has extra holes for the PMTs, so that the photocathode is not covered by the structure itself. Next to the PMT photocathode, a reflector ring is glued onto the PMT support structure. Light which would otherwise be absorbed by the PMT support structure is reflected by the reflector ring towards the PMT photocathode and thus, can be detected nevertheless (for more information, see pages 166 to 174 in [51]). Each PMT is supplied with the necessary HV by its own base. The PMT base and with that, the PMT, is powered by the AFE. In addition, the AFE also processes the measured PMT signal. Each PMT has its own AFE circuit. While the PMT bases are soldered directly to the corresponding PMT pins, the AFE circuits are located on the mainboard. Besides, further environmental sensors such as an accelerometer, a magnetometer, a pressure sensor, a temperature sensor, and a light sensor are placed on the mainboard. Due to the limited space on the mainboard, another circuit board, the mDOM Adapter Board (mDAB), is stacked onto the mainboard. The mDAB powers the flasher LEDs, the cameras, and the illumination LEDs. In sum, ten flasher LEDs, each LED on a flasher board, are distributed inside one mDOM (see Figure 2.4 for the exact positions). The flasher LEDs [64] emit light at a wavelength of about 405 nm which is used to calculate the exact mDOM position in ice via trilateration. In addition, the ice properties of the glacier can be determined by using the flasher LEDs. However, the flasher LEDs are switched

<sup>1</sup>Wavelengths above 700 nm are not relevant for the mDOM, because the quantum efficiency of the PMT is close to zero at 700 nm and thus, light with such wavelengths cannot be detected by the PMT (see Figure 3.12 and Figure 3.13).

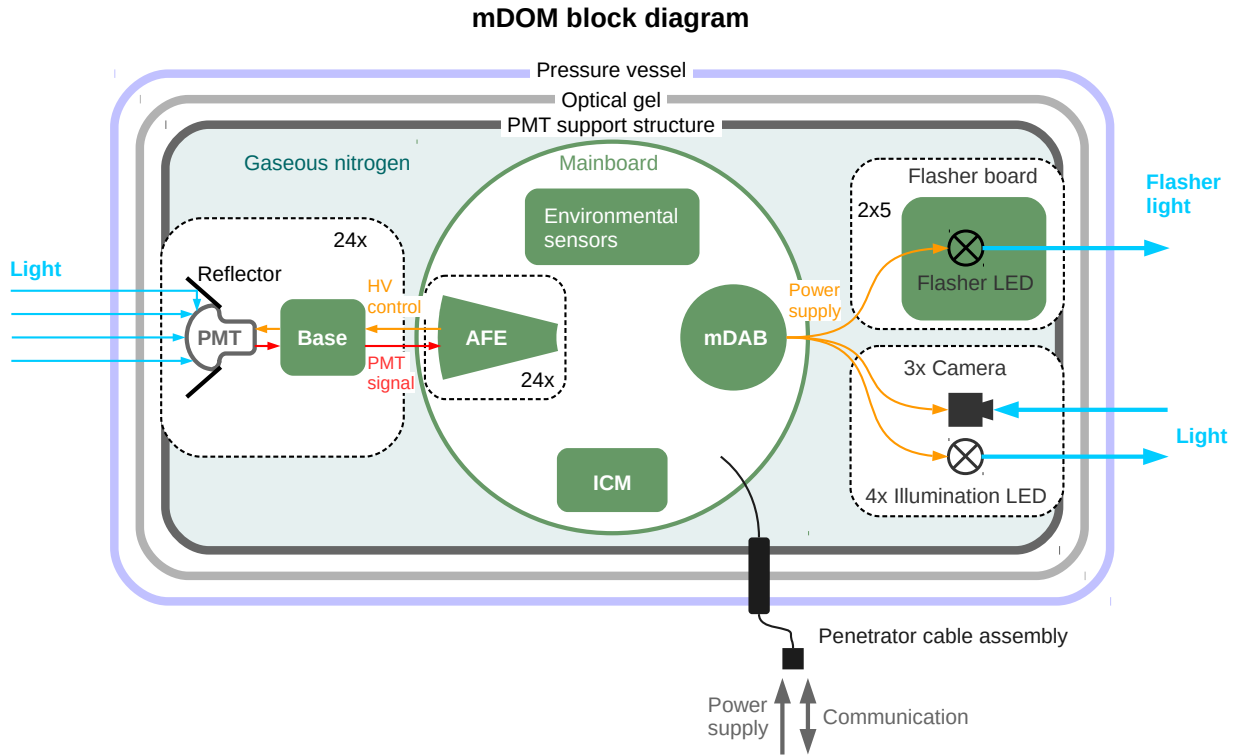


**Figure 2.2:** Block diagram of the mDOM with the main components.

on only for special calibration measurements and not during the normal operation of the detector. Likewise, the illumination LEDs are used only when the cameras are running. The illumination LEDs [65] emit light at a wavelength of about 465 nm illuminating the vicinity of the mDOM. Thus, the camera can take pictures of the otherwise dark surrounding ice. As a result, irregularities in the ice such as dust, bubbles, or the exact position of the main cable can be monitored. In addition, the scattering and absorption lengths of the ice can be measured. A more detailed introduction of the camera and the corresponding LED can be found in [66]. Inside the mDOM, the camera has an effective field of view of about  $90^\circ$  due to shadowing of the PMT support structure. To observe different directions, three cameras and four illuminating LEDs are located inside one mDOM. One camera is directed upwards, the second one downwards, and the third one to the side. In Figure 2.4, the positions of the cameras and the illuminating LEDs relative to the PMTs are shown. For an unobstructed view of cameras, flasher LEDs, and illumination LEDs, the devices are placed behind windows of the PMT support structure. The inside of the PMT support structure is filled with gaseous nitrogen at a pressure of about 480 mbar.

On the mainboard, the data of all electronic devices are processed. The entire communication of the mDOM with devices outside is performed by the IceCube Communication Module (ICM) which is another small circuit board stacked onto the mainboard. All communication and power supply cables are bundled together to the penetrator cable assembly which runs through the PMT support structure, the optical gel, and the pressure vessel.

## 2.4 Components relevant for this work

As visible in Figure 2.1, the mDOM contains many different components. In this section, the four components most relevant for this work are described in more detail: PMTs, PMT base, AFE, and mainboard.

### 2.4.1 Photomultiplier tubes

Compared to standard PMT types, the PMTs used for the mDOM have some features which are shown in Figure 2.3. First of all, the space inside the mDOM is limited so that the PMT tube length is shorter than for a usual PMT with the same photocathode area (about 91 mm instead of 97 mm as used in [29]). Second, also due to limited space reasons, a negative HV (see Subsection 1.3.4.2) is used so that the PMT signal can be picked up directly at the anode without any capacitors or large transformers needed. If not properly insulated, a negative HV can lead to higher darkrates of the PMT which is unpreferable (see Subsection 1.3.4.2). To reduce the darkrates, a conductive paint—called HA coating by Hamamatsu Photonics K.K. (see page 269 in [48])—together with an insulating cover above is applied around the PMT tubes [47, 48]. Third, a copper tape is used. As described in Section 2.2, an aluminum reflector surrounds the PMT’s photocathode to increase the effective area of the PMT. As stated in [47], metal in the vicinity of the photocathode can lead to an increased or unstable darkrate. In [67], three different scenarios were investigated: reflector at floating potential, reflector at ground, and reflector at cathode potential. It was found that the lowest darkrate is obtained when the reflector is set to the PMT’s photocathode potential. To achieve such an electrical connection, a copper tape should be used [68]. At one side, it is connected to the photocathode’s pin. Guided below the insulating cover of the HA coating, the copper tape can be connected to the reflector at the other side, thus, setting the reflector to the same potential as the PMT’s photocathode. Fourth, each PMT needs its individual HV which is supplied by a base connected to the PMT. Due to the limited space inside the mDOM, the base must be soldered to the pins as closely as possible to the PMT tube.

Figure 2.4 shows the configuration of the 24 PMTs inside the mDOM. The figure sketches the projection if the mDOM was flipped open. Each black circle describes one PMT while the number denotes the corresponding PMT position. The 24 PMTs are arranged such that eight PMTs are close to the equator (middle of the mDOM) and four PMTs are close to the poles of each hemisphere. In the middle between the two hemispheres, the mainboard is located. An alignment arrow on the mainboard points in the direction of the PMT at position eight. As a consequence, the mainboards are oriented in the same way for all mDOMs. On the upper hemisphere, the solid black circle denotes the penetrator cable assembly. Moreover, the ten light blue circles describe the positions of the flasher LEDs. Analogically, the four darkblue filled circles denote the positions of the illumination LEDs. Similarly, the three cameras are described by the darkblue open circles.

### 2.4.2 PMT base

The PMT base provides the PMT dynodes with the HV and picks up the PMT signal at the anode. Each PMT used for the mDOM needs an HV of about 1200 V. For the IceCube Upgrade, such an HV cannot be supplied by an HV device using a passive PMT base. Instead, an active base (see Subsection 1.3.4.1) is used. In the following, the active PMT base for the mDOM is called microbase. Because each PMT has its own microbase, each mDOM has 24 microbases.

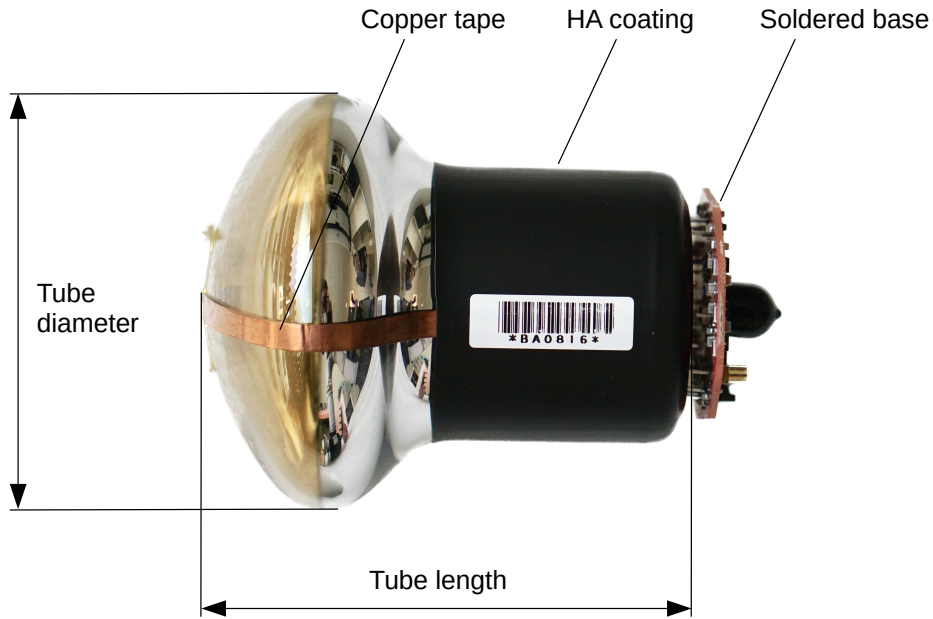


**Figure 2.3:** Features of the PMTs used for the IceCube Upgrade. Furthermore, tube length and diameter are defined. Photograph of the PMT type R15458-20 from Hamamatsu Photonics K.K.

The microbase has to fulfill the following requirements. First, the power consumption must be as low as possible due to the overall power consumption limitations of the mDOM. The final mDOM microbase consumes a power of less than 10 mW [30]. Second, the microbase circuit must fit into the limited space inside the mDOM. Due to the special requirements for the mDOM application, the microbase is custom-designed for the mDOM PMT. The final microbases are assembled and soldered to the PMTs by the PMT manufacturer Hamamatsu Photonics K.K.

The working principle of the microbase is shown in the block diagram of Figure 2.5. A microcontroller controls a rectangle wave driver which generates a rectangular wave with a minimum at 0 V and a maximum at 3.3 V. The necessary wave frequency is typically between 100 kHz and 110 kHz. This rectangular wave is fed into an LC resonator. The LC circuit outputs a sine wave with a peak-to-peak amplitude between 75 V and 150 V. Afterwards, the sine wave is directed to a 13-stage Cockcroft-Walton multiplier (see Paragraph 1.3.4.1 for information about the working principle of Cockcroft-Walton multipliers). Not only is the alternating voltage multiplied by the Cockcroft-Walton multiplier, but also changed from an alternating voltage into a direct voltage. By picking up the voltage at different stages of the Cockcroft-Walton multiplier, the different dynodes can be supplied with their corresponding HVs. From anode to cathode, the inter-dynode voltages have approximately the ratios 1:1:1:1:1:1:1:1:3. At the cathode, a negative HV of about  $-1200$  V is applied. The exact HV is adjusted for each PMT individually by using a fixed frequency close to the resonance frequency of the LC circuit and varying the duty cycle<sup>2</sup> of the rectangular wave. After the amplification by the Cockcroft-Walton multiplier, the direct current voltages for the dynodes are smoothed by an RC filter. These resulting dynode voltages are applied to the corresponding PMT pins. The measured PMT signal, in turn, is picked up at the anode and directed to the mainboard for further data processing (see Subsection 2.4.3). A

<sup>2</sup>The duty cycle is the fraction of the width of the positive half cycle and the period of a rectangular wave.

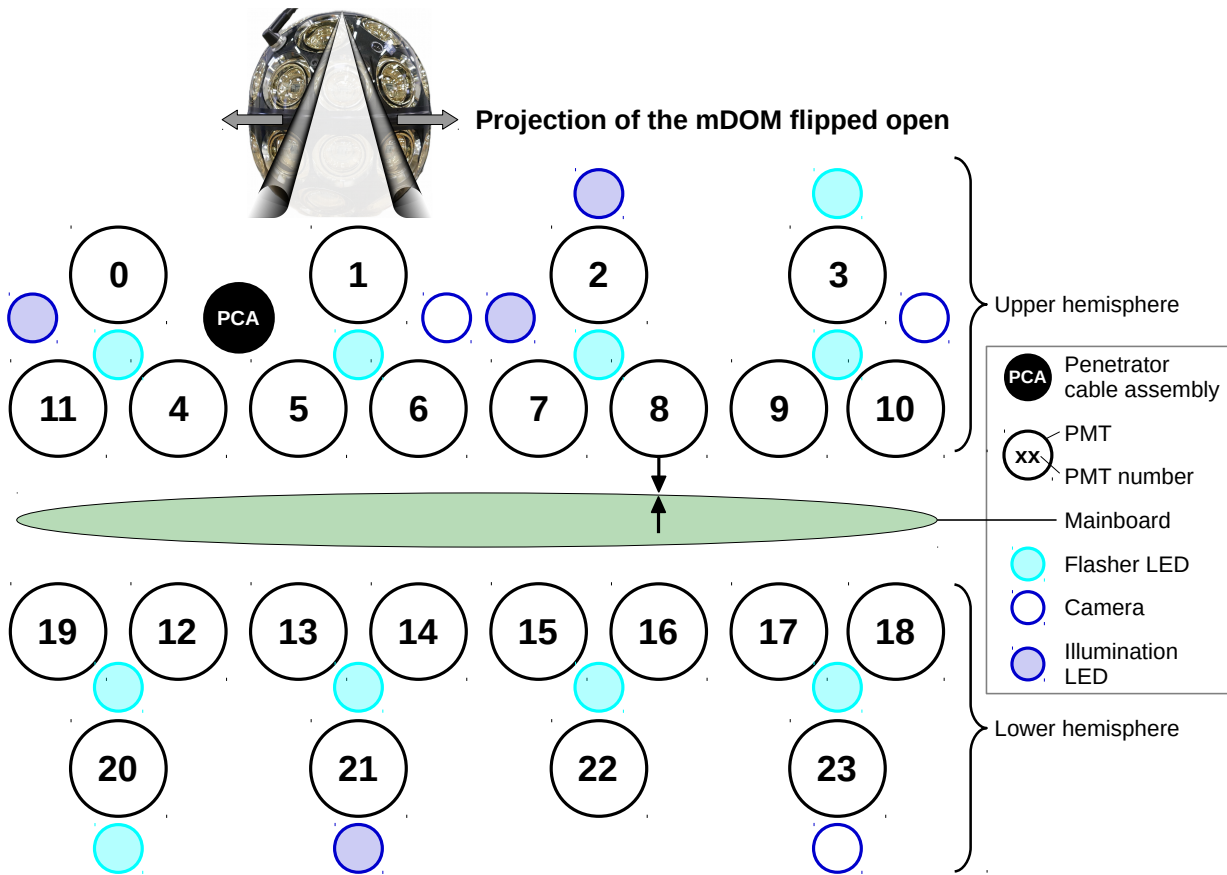


**Figure 2.4:** Schematic of the PMT ordering inside the mDOM. Besides, the positioning of the cameras, flasher LEDs, and illumination LEDs is shown. Adapted from [69].

more detailed description of the microbase can be found in Subsection “2.2 Active PMTs Bases” in the proceedings [30].

### 2.4.3 Analog front end

The AFE is the part of the electronics which processes the analog PMT signal before it is digitized by the analog-to-digital converter (ADC). For the mDOM, the AFE is custom-built. Figure 2.6 shows a block diagram of the main components of the AFE used on the mDOM mainboard. The negative PMT signal is first split up. One part is used as an input for the discriminator which converts the PMT pulse into a rectangular pulse. This pulse (discriminator signal) serves as a trigger input and is directed to the field programmable gate array (FPGA). The trigger threshold of the discriminator is adjusted by a digital-to-analog converter (DAC). Furthermore, the discriminator signal is used for the leading edge time determination. The second part of the PMT signal is directed to a preamplifier where the signal is not only amplified but also inverted. Afterwards, the signal is fed into a low pass filter broadening the PMT signal for a better digitizing resolution. Subsequently, the signal is amplified and inverted by another amplifier. After that, the signal (amplifier signal) is digitized by a 12-bit ADC. The baseline of the ADC is also adjusted by the DAC. Only in case the discriminator is triggered, the digitized amplifier and discriminator

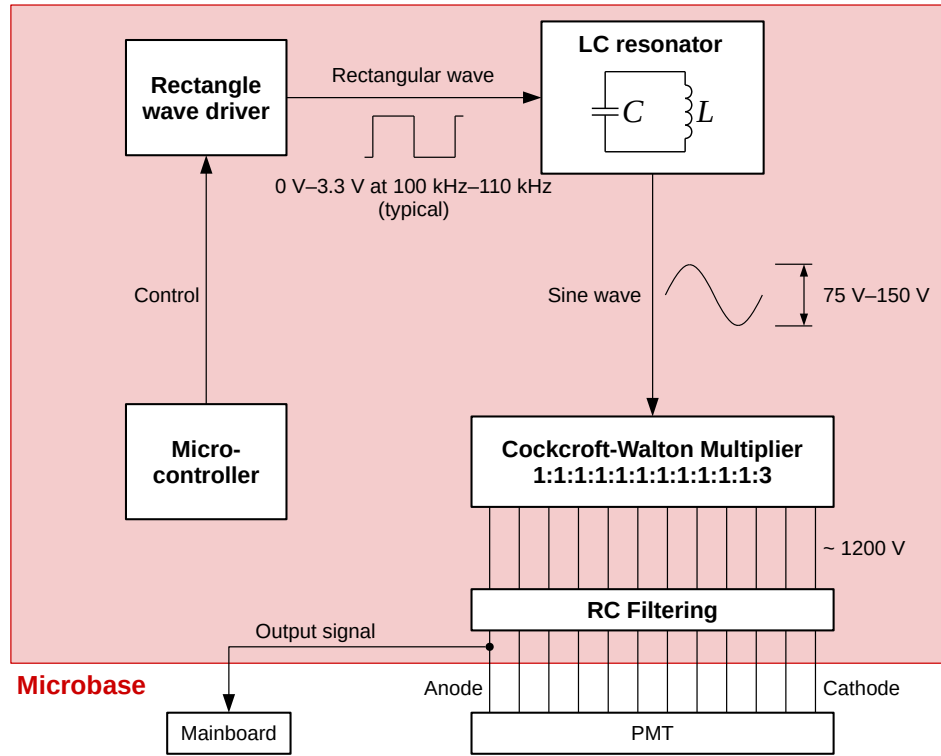


**Figure 2.5:** Block diagram of the mDOM PMT microbase. Adapted from [30].

signals are stored by the FPGA for further processing. Splitting the signal allows to optimize for the time resolution as well as for the energy resolution. The arrival time of a PMT pulse is sampled eight times faster by the discriminator than by the ADC (960 MHz compared to 120 MHz). The trigger accuracy of 1 ns is an important requirement for the mDOM, because it improves the quality of the event reconstruction [70]. By picking up the PMT signal before the preamplifier for the discriminator input, no additional noise from the preamplifier is added and a better triggering on 0.2 p.e. can be achieved. With the amplifier signal, on the other hand, the charge and with that, the energy, of the PMT pulse can be extracted.

Analogically to the microbase, each PMT with microbase is connected to its own AFE. Therefore, 24 AFE channels are placed on the mainboard.

#### 2.4.4 Mainboard

Similar to microbase and AFE, the mainboard is custom-designed for the mDOM application. The mainboard provides power to the different electrical devices as for example the PMTs, it processes the measured data and communicates with devices outside the mDOM. In fact, three different circuit boards exist: The actual mainboard, the ICM, and the mDAB. Figure 2.7 shows all three circuit boards and their placement relative to each other. Most components are located directly on the mainboard. In contrast, the ICM is a piggyback circuit board stacked onto the mainboard and responsible for the communication with devices outside the mDOM. Moreover, the ICM has an internal system clock which provides the mDOM with a synchronized internal time. For a standardized read-out and communication, each module deployed in ice for the IceCube Upgrade

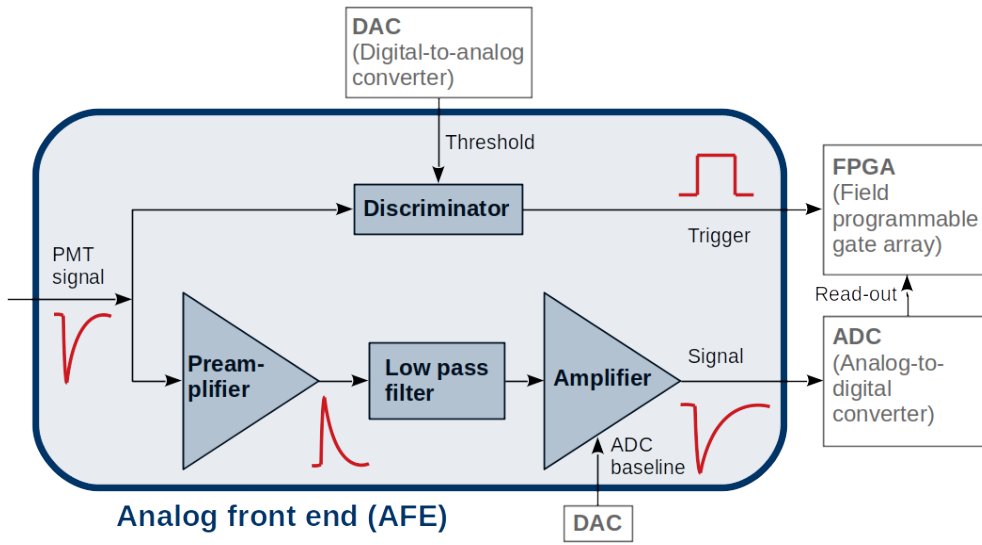


**Figure 2.6:** Block diagram of the main components of the AFE.

(mDOM, D-Egg, and so on) uses an ICM. Because not enough space is available on the mainboard itself, another piggyback circuit board—the mDAB—almost as large as the mainboard is stacked onto the mainboard above the ICM. All ten flasher LEDs, four illumination LEDs, and three cameras are controlled as well as read-out by the mDAB. In the left picture of Figure 2.7, the main components of the mainboard are shown. The FPGA is placed in the middle of the mainboard. A hit buffer, a microcontroller, six ADCs, and nine DACs surround the FPGA. Together with the ICM, 24 AFE channels encircle the middle area of the mainboard. Furthermore, the mainboard contains a primary as well as a secondary DC-to-DC converter. Finally, each mainboard has an alignment arrow to orient the mainboard towards the PMT position 8 (see Figure 2.4).

The functional interaction of all those components is shown in the block diagram in Figure 2.8. All data as well as the supplied voltage of 96 V have to pass the penetrator cable assembly. After that, data and supply voltage are separated by a bias tee. Whereas input and output data are transferred via the ICM, the 96 V supply voltage is converted into 5 V by the primary DC-to-DC converter. On the one hand, the 5 V serves as supply voltage for the ICM. On the other hand, the 5 V is divided into four different power rails by the secondary DC-to-DC converter: 1.0 V, 1.35 V, 1.8 V, and 3.3 V. All other electronic devices on the mainboard such as the microcontroller are supplied by these power rails. The microcontroller reads out the environmental sensors which are an accelerometer, a magnetometer, a pressure sensor, a temperature sensor, and a light sensor. Moreover, the microcontroller reads out and controls the mDAB which, in turn, reads out and controls the flasher LEDs, the illumination LEDs, and the cameras. In addition, the microcontroller controls the microbases and reads back the adjusted HVs. Furthermore, the values for the ADC baselines and the DAC thresholds are passed from the microcontroller to the FPGA. The main task of the FPGA is to control the 24 AFE channels. Additionally, the FPGA controls the DACs which adjust both the ADC baselines and the DAC thresholds of the different AFE channels. Powered by the corresponding AFE channel, the microbases supply the respective PMTs with the necessary HVs. The measured PMT signal, in turn, is picked up by the microbase and passed to the AFE channel where the signal is split up and further processed (see Subsection 2.4.3). After

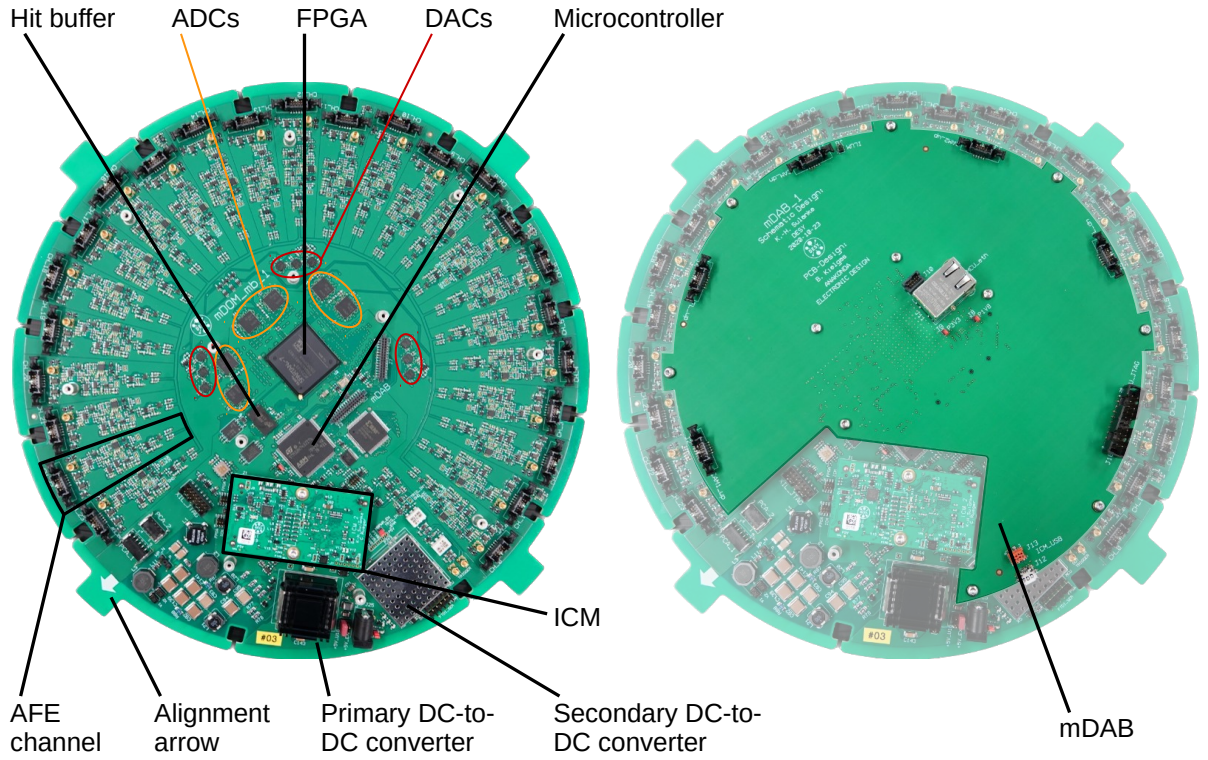


**Figure 2.7:** Pictures of the mDOM mainboard. Left picture: Mainboard together with the ICM. Right picture: mDAB stacked onto the mainboard. Modified from [71].

the amplification by the AFE, the amplifier signal is digitized by the ADC. Both the digitized amplifier signal as well as the discriminator signal are passed to the FPGA which saves the data on the 2 Gbit hit buffer. After that, the microcontroller sends the data to the ICM which passes the data through the bias tee and the penetrator cable assembly to further devices outside the mDOM (see Section 2.5 for a description of the data taking). A more detailed description of the mDOM mainboard can be found in [72].

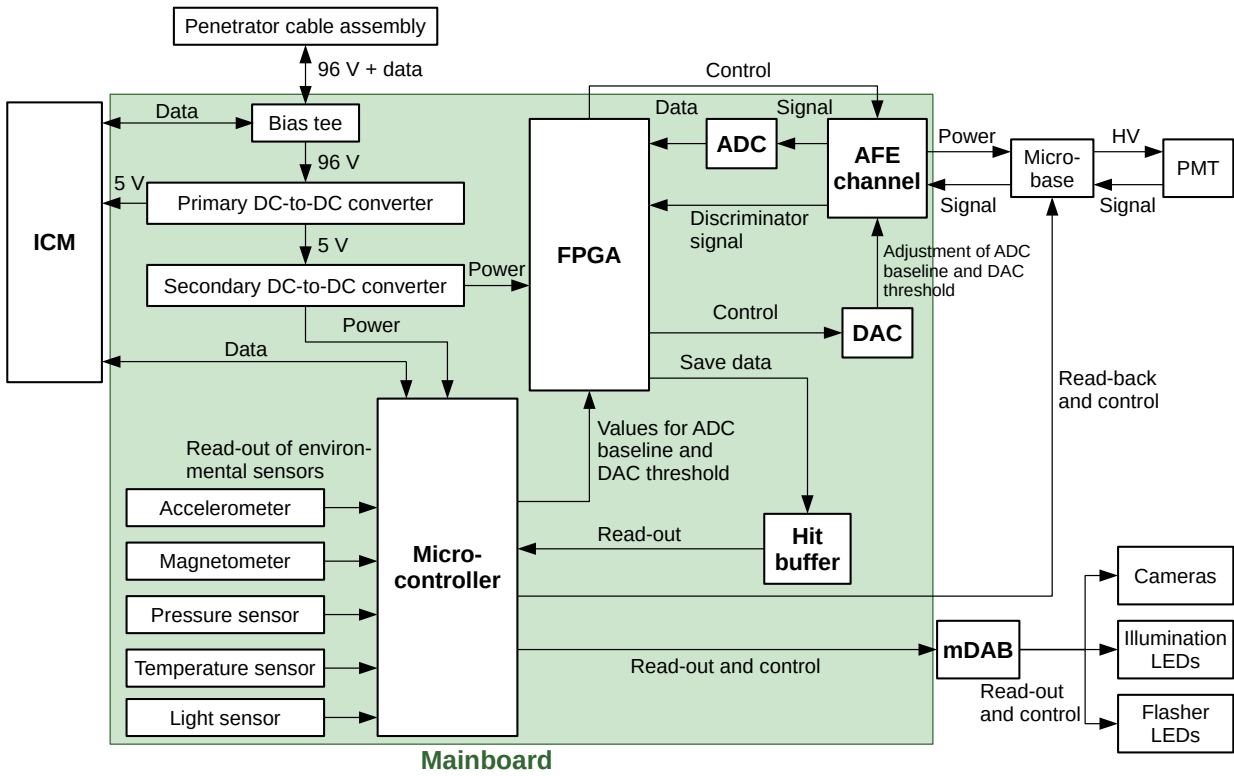
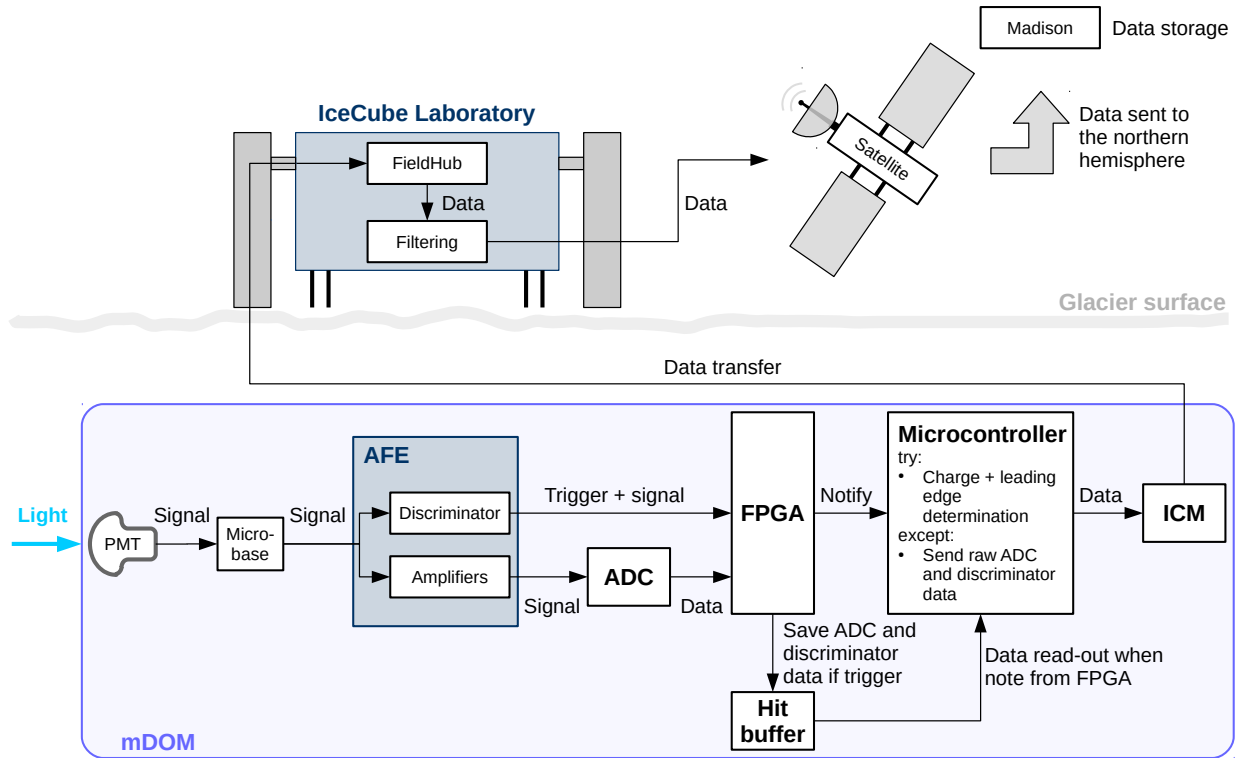


Figure 2.8: Block diagram of the mDOM mainboard.

## 2.5 Data acquisition and operation in ice

The data acquisition of the mDOM works as follows. Incoming light is measured by a PMT which produces a signal as explained in Subsection 1.3.1. This signal is picked up by the respective microbase of the PMT and passed to the corresponding AFE where the signal is processed (see Subsection 2.4.3). The electronic circuit of the AFE splits the signal into a discriminator signal and an amplifier signal. The amplifier signal is used to determine the charge of the signal. In contrast, the discriminator signal is used to determine the time of the signal as well as to trigger the FPGA. Before the amplifier signal is passed to the FPGA, it is sampled with 120 MHz by a 12-bit ADC (ADC data). Differently, the discriminator signal is digitized by the FPGA and sampled with 960 MHz (discriminator data). In case the discriminator triggers the FPGA, both the digitized discriminator data as well as the ADC data are saved on the hit buffer. At the same time, the FPGA notifies the microcontroller that data have been saved on the hit buffer. Subsequently, the microcontroller reads the previously saved data from the hit buffer. From the discriminator data, the microcontroller tries to determine the leading edge of the measured PMT signal. From the ADC data, on the other hand, the microcontroller tries to determine the charge. If these determinations work, only the charge and the leading edge time information is sent to the ICM. If the determinations fail, the raw discriminator and ADC data are passed to the ICM. On the ICM, a system clock is placed which distributes the times to FPGA and microcontroller. From the ICM, the data are transferred to a so-called FieldHub which is placed inside the IceCube laboratory on the glacier surface. One FieldHub manages one IceCube Upgrade string. Thus, seven FieldHubs



**Figure 2.9:** Block diagram of the data-taking procedure with the mDOM.

exist. Three tasks are accomplished by the FieldHub. First, the FieldHub supplies all modules on a string with the necessary power. Second, the entire communication with the modules on the string is performed by the FieldHub. Third, the FieldHub determines the correct leading edge time of the mDOM data. Therefore, each FieldHub has an internal clock which is synchronized with the global positioning system (GPS) time. By using the IceCube procedure RAPCal (see Section 3.3 in [19]), the times determined by the mDOM via the ICM are converted to GPS time. Afterwards, the data are filtered and sent via satellite to the University of Madison on the northern hemisphere where the data are stored for further data analysis.

## Chapter 3

# PMT characterization measurements

---

<b>3.1</b>	<b>Overview of investigated PMT types . . . . .</b>	<b>38</b>
<b>3.2</b>	<b>PMT calibration . . . . .</b>	<b>39</b>
3.2.1	Setup . . . . .	39
3.2.2	Gain calculation . . . . .	39
3.2.3	HV calibration . . . . .	42
<b>3.3</b>	<b>Determination of the PMT characteristics . . . . .</b>	<b>43</b>
3.3.1	Transit time spread (TTS) . . . . .	43
3.3.2	Quantum efficiency . . . . .	44
3.3.3	Darkrate . . . . .	46
3.3.4	Correlated noise . . . . .	47
3.3.4.1	Prepulsing . . . . .	48
3.3.4.2	Delayed pulsing . . . . .	48
3.3.4.3	Afterpulsing . . . . .	49
<b>3.4</b>	<b>Comparison of Hamamatsu and HZC PMT types . . . . .</b>	<b>51</b>
<b>3.5</b>	<b>Characterization of the final PMT type . . . . .</b>	<b>54</b>
<b>3.6</b>	<b>Summary . . . . .</b>	<b>56</b>

---

The PMTs detect the Cherenkov light induced by the neutrinos and the PMT characteristics limit the energy resolution as well as the directional resolution of the IceCube Upgrade detector. Moreover, the PMTs contribute to the overall noise which limits the performance of reconstructing neutrino events. With regard to the final design of the mDOM, four different PMT types from two manufacturers were characterized. The results were the basis for the selection process of the final PMT type for the mDOM. In addition, some of the parameters measured in Section 3.5 are used as input in simulations of the IceCube Upgrade detector.





In the first section, the features of the PMT necessary for a good mDOM performance are explained. Section two gives an overview of the different PMT types investigated in this chapter. The third section describes the process of the calibration of the PMTs nominal HV which includes the measurement setup as well as the analysis methods. After that, the fourth section explains how the different PMT characteristics were determined from the measurements. In the fifth section, the results of a PMT type from Hamamatsu Photonics K.K. and a PMT type from HZC Photonics

are compared. Afterwards, section six presents the characterization results of the final PMT type. The last section summarizes the chapter.

### 3.1 Overview of investigated PMT types

Because no standard PMT type fulfilled the requirements mentioned in Subsection 2.4.1, new PMT types were introduced by the manufacturers. By constantly giving feedback to the manufacturers, the PMT types could be improved such that they fulfill the requirements described in Subsection 2.4.1.

**Table 3.1:** Overview of all PMT types investigated in this thesis. Numbers were taken from [73], [74], [75], [76]. The diameter is the diameter of the entrance window of the PMT as shown in Figure 2.3. Similarly, the tube length corresponds to the length of the glass tube without pins or evacuation port.

	R12199-01 HA	XP82B2F	R15458-02	R15458-20
				
Company	Hamamatsu Photonics K.K.	HZC Photonics	Hamamatsu Photonics K.K.	Hamamatsu Photonics K.K.
Diameter	80.5 mm	87.5 mm	80 mm	80 mm
Tube length	93 mm	94.5 mm	91 mm	91 mm
HA coating	✓	✓	✓	✓
Copper Tape	-	-	✓	✓
Soldered base	-	-	-	✓

In this thesis, four PMT types shown in Table 3.1 were investigated (R15458-02 and R15458-20 are actually the same PMT type, the only difference between the two is the soldered base). PMTs from Hamamatsu Photonics K.K. [77] and HZC Photonics [78] were characterized. While the PMT types R12199-01 HA, R15458-02, and R15458-20 from Hamamatsu Photonics K.K. have a similar tube diameter of 80.5 mm and 80 mm, respectively, the XP82B2F from HZC Photonics has a larger diameter of 87.5 mm. Moreover, earlier PMT types such as the R12199-01 HA and the XP82B2F still have longer tubes whereas the R15458-02 and R15458-20 have a short tube length of 91 mm. All investigated PMT types have an HA coating. The copper tape was introduced later so that only the PMT types R15458-02 and R15458-20 have one. The last step was the production of PMTs

with a soldered PMT base which was only done for PMT type R15458-20. The characterization of more than 150 PMTs was distributed between the author, Jonas Reubelt and student assistants.

## 3.2 PMT calibration

The first step in the characterization process of a PMT is the calibration of the nominal HV. For the mDOMs in the IceCube Upgrade, each PMT should be operated at a gain of  $5 \cdot 10^6$ . To reach this gain number, the PMT must be operated at a certain HV called nominal HV. It is different for each PMT and must be determined at first. Therefore, the HV calibration was performed for each PMT individually. In the following, the procedure of the HV calibration process is explained.

### 3.2.1 Setup

To determine the nominal HV, a special setup shown in Figure 3.1 was used. The PMT was placed into a darkbox and connected to a passive base which distributed the voltage of the HV supply to the PMT dynodes. Only the PMT type measured in Section 3.5 was characterized with an active base—in the following called microbase—instead. The development of the microbase has been independent of the PMT characterization at first, but in the end, the system PMT + microbase must work together. Therefore, the final PMT design was tested with the designated microbase design instead of a passive base. The PMT signal was read out by an oscilloscope [79]. A pulsed LED (PLS 450 from PicoQuant [80]) illuminated the photocathode area of the PMT. For this purpose, a function generator located outside of the darkbox sent a trigger signal with a repetition frequency of 1 kHz simultaneously to the oscilloscope and to a picosecond LED driver [81]. The LED driver shortened the signal to a pulsewidth of about 800 ps and drove the pulsed LED which has a peak wavelength of 470 nm. The light output of the LED was coupled into an optical fiber which was guided into the darkbox. A diffusor inside the darkbox generated a homogeneous illumination of the PMT's photocathode area. The intensity of the LED was adjusted such that the average charge measured by the PMT was about 0.1 p.e. The simultaneous trigger of LED and oscilloscope ensured that PMT signals were only processed when the PMT was illuminated by the LED. In the end, the PMT data were saved to a hard drive. All HV calibration measurements were performed at room temperature in air.

### 3.2.2 Gain calculation

The data acquired as described in Subsection 3.2.1 were saved as voltage over time values, so-called waveforms. Each waveform is 200 ns long and contains one trigger event. In total, 50 000 waveforms were saved in one measurement and each waveform was processed as follows. At first, the mean baseline  $U_0$  was subtracted such that its mean value centers on 0 mV. The baseline window was set before the signal window (see left plots of Figure 3.2) because the probability of a PMT pulse after the signal window is higher than before. Afterwards, a signal window (40 ns–80 ns) was defined. All PMT pulses generated from the LED output appear roughly at the same position within the

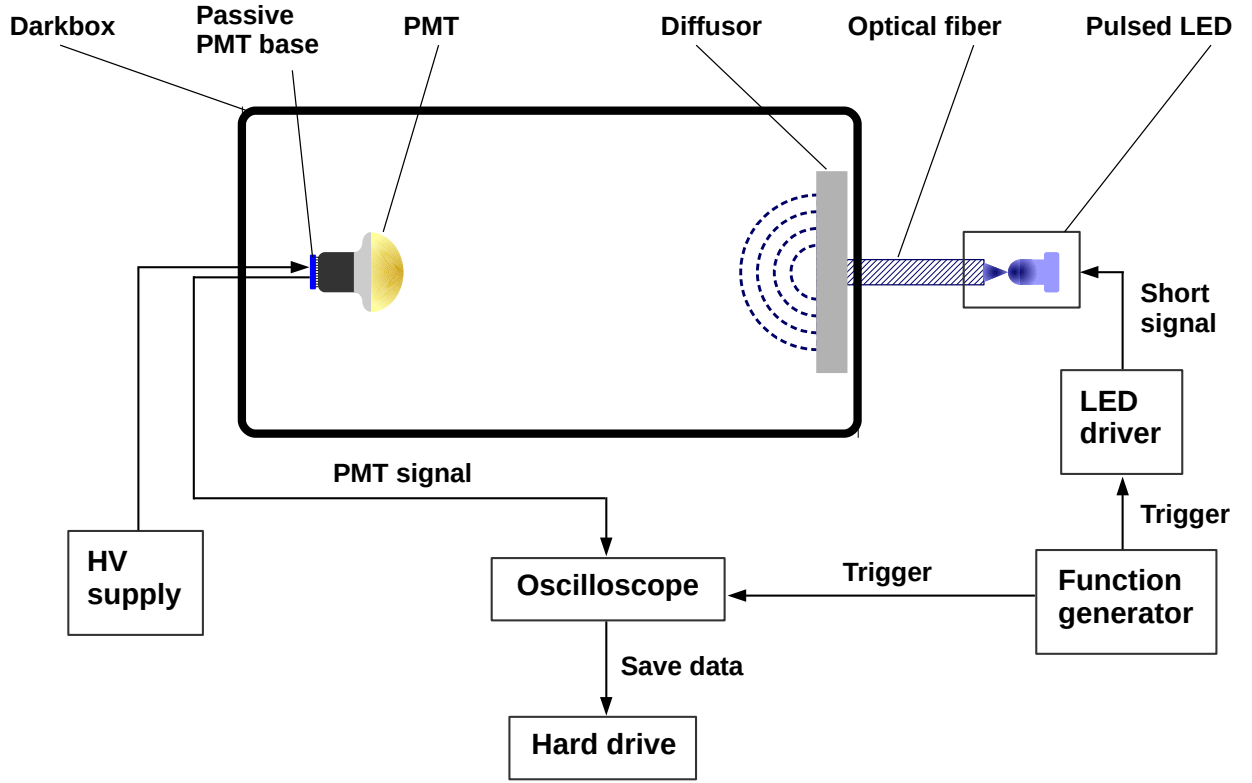


**Figure 3.1:** Schematic of the setup used for the calibration of the PMTs.

waveform. Thus, the signal window could be defined such that all PMT pulses were included. The charge of each waveform can be calculated as:

$$\text{charge} = \int I(t) dt = \int \frac{U(t)}{50 \Omega} dt \stackrel{\text{discrete voltage}}{=} \sum_t \frac{U(t)}{50 \Omega} \cdot \Delta t \quad (3.1)$$

$$\stackrel{\text{in this thesis}}{=} \sum_{\text{signal window}} \frac{U(t) - U_0}{50 \Omega} \cdot \Delta t. \quad (3.2)$$

In principle, the charge can be calculated by integrating the time-dependent current over time (see Equation 3.1). By using the input impedance of the measurement device ( $50 \Omega$  in case of the oscilloscope), the current can be expressed via the measured voltage. Because the time is measured in discrete datapoints, the integral is changed to a sum with  $\Delta t$  as the time between two succeeding voltage values. In this specific case, the charge is calculated according to Equation 3.2 with the baseline subtracted voltage values.

The charges of all waveforms yield the charge distribution. Because the measurement was performed at very low light intensities and therefore, the charge of a single photoelectron is dominant compared to higher charges, this type of charge distribution is also called single photoelectron (SPE) spectrum. Figure 3.2 illustrates how the specific shape of the SPE spectrum results from the data. During the measurement, two different signals occur: Electronic noise and PMT pulses. Because the average charge measured by the PMT is 0.1 p.e., most of the time, a charge of 0 p.e. is detected. This charge corresponds to a signal with only electronic noise and contributes to the so-called

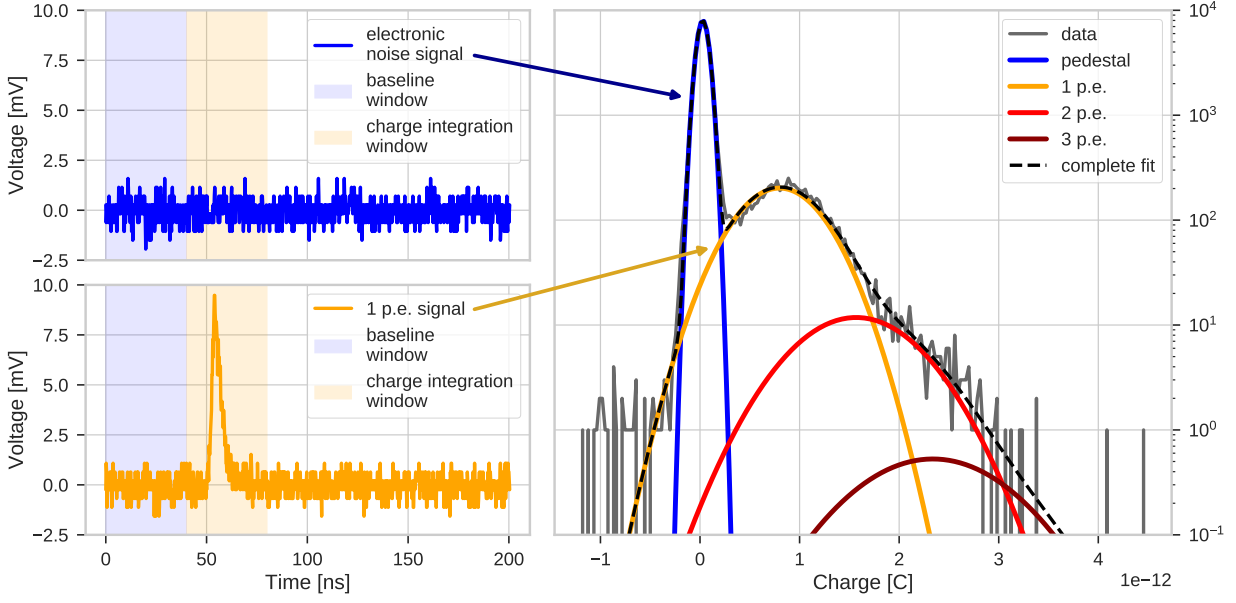


**Figure 3.2:** Illustration of the single components of the SPE spectrum. Charge is given in arbitrary units (a.u.). Exemplarily shown for the PMT DM00021 of the PMT type R15458-20 from Hamamatsu Photonics K.K. at room temperature.

pedestal in the SPE spectrum. In some cases, however, a PMT signal is detected. The signal has a nonzero charge and yields Gaussian peaks with a mean of 1 p.e., 2 p.e., and so on. Together, the electronic noise and the different charges of the PMT pulses result in the SPE spectrum. A valley is located between pedestal and the Gaussian with a mean charge of 1 p.e. The Gaussians of 1 p.e., 2 p.e., and so on, however, cannot be distinguished visually.

The gain  $G$  is the multiplication factor of the PMT. A photoelectron coming from the photocathode is multiplied by  $G$  when arriving at the anode (see Subsection 1.3.2). From the distance of pedestal and the 1 p.e. distribution,  $G$  can be calculated as:

$$G = \frac{Q_{\text{spe}} - Q_{\text{ped}}}{e}, \quad (3.3)$$

with the mean charge of the 1 p.e. distribution  $Q_{\text{spe}}$  and the mean charge of the pedestal  $Q_{\text{ped}}$ , and the elementary charge  $e$ . To determine  $Q_{\text{spe}}$  and  $Q_{\text{ped}}$ , a fit was performed. Because the assumption is made that the photons emitted by the light source are Poisson distributed, a Poisson distribution is convoluted with Gaussian distributions representing the different charge multiplicities (see [82]). Altogether, the distribution  $f(q)$  of the PMT response can be approximated as:

$$f(q) \propto G(q, Q_{\text{ped}}, \sigma_{\text{ped}}) + \sum_{n=1}^{\infty} \frac{\mu^n \cdot e^{-\mu}}{n!} \cdot G_n(q, Q_{\text{spe}}, \sigma_{\text{spe}}), \quad (3.4)$$

where  $q$  is the charge,  $G(q, Q_{\text{ped}}, \sigma_{\text{ped}})$  a Gaussian distribution describing the pedestal,  $\sigma_{\text{ped}}$  the standard deviation of the pedestal,  $n$  the number of photoelectrons,  $\mu$  the mean number of photoelectrons collected by the first dynode,  $G_n(q, Q_{\text{spe}}, \sigma_{\text{spe}})$  a Gaussian distribution describing the charge multiplicity, and  $\sigma_{\text{spe}}$  the standard deviation of the 1 p.e. distribution. Figure 3.3 shows a typical fit of the PMT response function (red line) to the SPE spectrum using Equation 3.4.

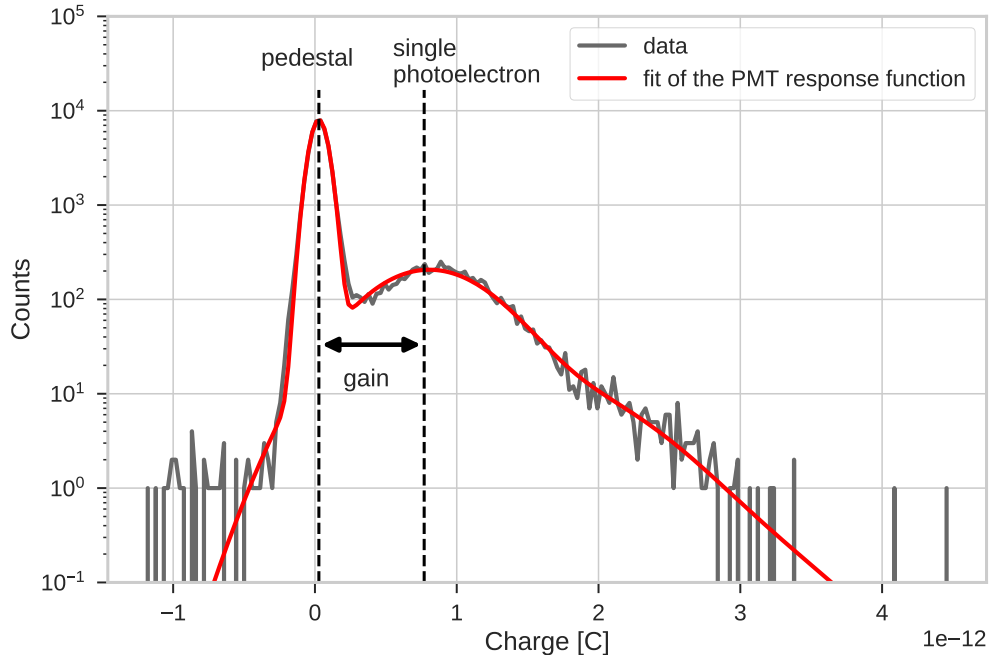


**Figure 3.3:** Typical fit of the PMT response function to the charge spectrum shown for the PMT DM00021 of the PMT type R15458-20 from Hamamatsu Photonics K.K. at room temperature.

The black dashed line to the left indicates the mean charge of the pedestal whereas the black dashed line to the right indicates the mean charge of the single photoelectron peak. From the fit of Equation 3.4 to the SPE spectrum, the fit parameters  $Q_{\text{spe}}$  and  $Q_{\text{ped}}$  were extracted. Inserting them into Equation 3.3 yielded the gain of the PMT. For the data shown in Figure 3.3, the calculated gain is  $4.8 \cdot 10^6$ .

### 3.2.3 HV calibration

For the calibration of the nominal HV, the PMT was placed into the setup described in Subsection 3.2.1. After adjusting the HV, a measurement was performed. Subsequently, the data were processed as explained in Subsection 3.2.2. A fit of the PMT response function (Equation 3.4) was performed to the data and the gain was calculated using Equation 3.3. This procedure was performed for at least three different HV values between 900 V and 1500 V starting with the nominal HV value measured by the manufacturer. The relative statistical error of the gain originates from the fit of the PMT response function and is in the order of 2%. Systematic errors originate from the temperature dependence of the PMT HV, fluctuations of the PMT HV, and deviations between reality and PMT response function. None of these systematic errors was monitored. When the decimal logarithm of the gain is plotted against the decimal logarithm of the HV as shown in Figure 3.4, a linear fit (blue line) can be performed to describe the datapoints (red dots). The dashed horizontal black line indicates the gain of  $5 \cdot 10^6$ . The x-value of the intersection with the fit line gives the nominal HV for the gain of  $5 \cdot 10^6$  and is shown as dashed vertical black line. Finally, this nominal HV was supplied to the PMT and another measurement was performed with setup and procedure described in Subsections 3.2.1 and 3.2.2. With this measurement at nominal gain, the HV calibration of the PMT was completed and the PMT characteristics could be investigated.

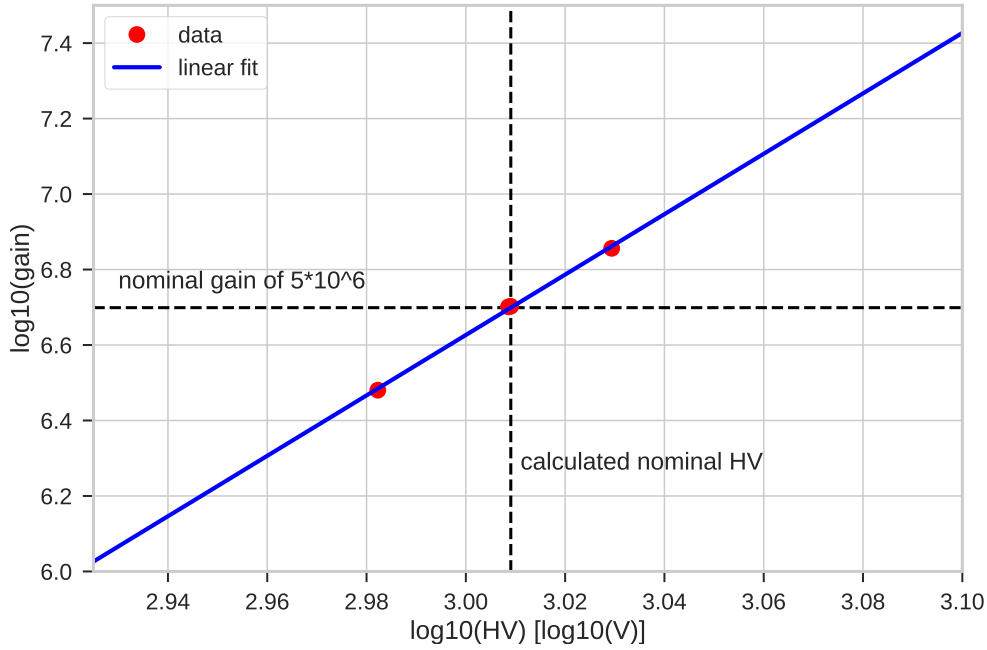


**Figure 3.4:** Typical fit for the determination of the nominal HV shown for the PMT DM00021 of the PMT type R15458-20 from Hamamatsu Photonics K.K. at room temperature.

### 3.3 Determination of the PMT characteristics

Several PMT characteristics were investigated such as transit time spread, quantum efficiency, darkrate at  $-20^{\circ}\text{C}$ , prepulsing, delayed pulsing, and afterpulsing. For each characteristic, the setup as well as the measurement procedure and analysis method are explained in the following. Unless stated differently, this approach was used for all PMT types.

#### 3.3.1 Transit time spread (TTS)

As explained in Subsection 1.3.3.1, the TTS is a measure of the time resolution of the PMT. Because the directional information of a neutrino event is extracted from the different arrival times of the Cherenkov light at the different mDOMs or PMTs, respectively, the TTS of the PMTs directly constrains the directional resolution of the IceCube Upgrade detector.

To determine the TTS, the data of the measurement with the nominal gain of Subsection 3.2.3 were used. The waveforms of these measurements had been saved and could be reused for the TTS determination. First of all, the transit times had to be calculated. Technically speaking, the transit time—also referred to as absolute transit time in the following—is the time difference between the occurrence of a light pulse and the corresponding PMT pulse crossing a certain threshold (see Figure 1.10). Because the absolute transit time is also a property of the setup and will be characterized in the final mDOM, it was not of interest in this measurement. It was sufficient to determine the time difference of the waveform start time, which has a defined time difference to the trigger, and the first PMT pulse crossing a certain threshold. In the following, this time difference is called relative transit time. For the mDOM in the IceCube Upgrade detector, the trigger threshold will be the average voltage value a PMT pulse with a charge of 0.2 p.e. would

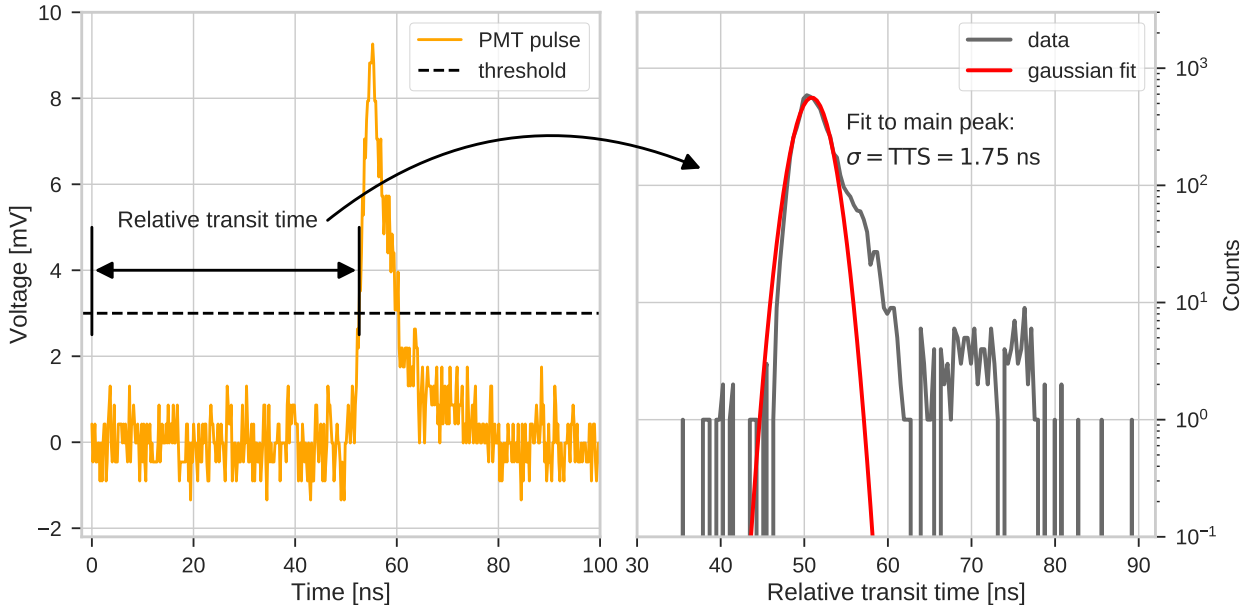


**Figure 3.5:** Illustration of the TTS determination shown for the PMT DM00002 of the PMT type R15458-20 from Hamamatsu Photonics K.K. at room temperature.

have. With the setup used in this thesis, however, only a voltage threshold corresponding to a charge of about 0.44 p.e. was possible due to electronic noise. Figure 3.5 shows how the TTS was calculated from the waveforms. A voltage threshold of 3 mV was used. For each waveform containing a PMT pulse crossing the threshold, the relative transit time was determined. After that, all relative transit times were filled into a histogram. A Gaussian function was fitted to the main peak. The sigma of the fit was defined as the TTS which is required to be less than 2 ns. The relative statistical error of the TTS originates from the fit error which is typically less than 1 %. Because the light pulse of the LED has a finite width  $T_{\text{pulse}}$  and therefore, the photons of the LED were emitted throughout the pulse width, the TTS values should be corrected for the LED's pulse width:

$$\text{TTS}_{\text{PMT}} = \sqrt{\text{TTS}^2 - T_{\text{pulse}}^2}. \quad (3.5)$$

For the LED used in this measurement,  $T_{\text{pulse}}$  is about 340 ps [80]. In this case, a typical TTS of 1.50 ns would be corrected to approximately 1.46 ns. Due to this small contribution, the TTS values are shown without this correction in the following.

### 3.3.2 Quantum efficiency

A larger QE results in a larger number of detected photons which in turn leads to a larger measured charge. Because the neutrino energy is determined by the detected charge, the energy resolution of the detector increases with a larger QE of the PMTs. Thus, lower limits for the QE were defined at three different wavelengths: 0.07 at 325 nm, 0.25 at 380 nm, and 0.15 at 500 nm.

A special setup shown in Figure 3.6 was used to determine the QE of each PMT. Connected to an HV supply, the PMT was placed into a dark box. Because the QE measurements were performed in current mode (see Paragraph 1.3.4.3) without an additional amplification at the

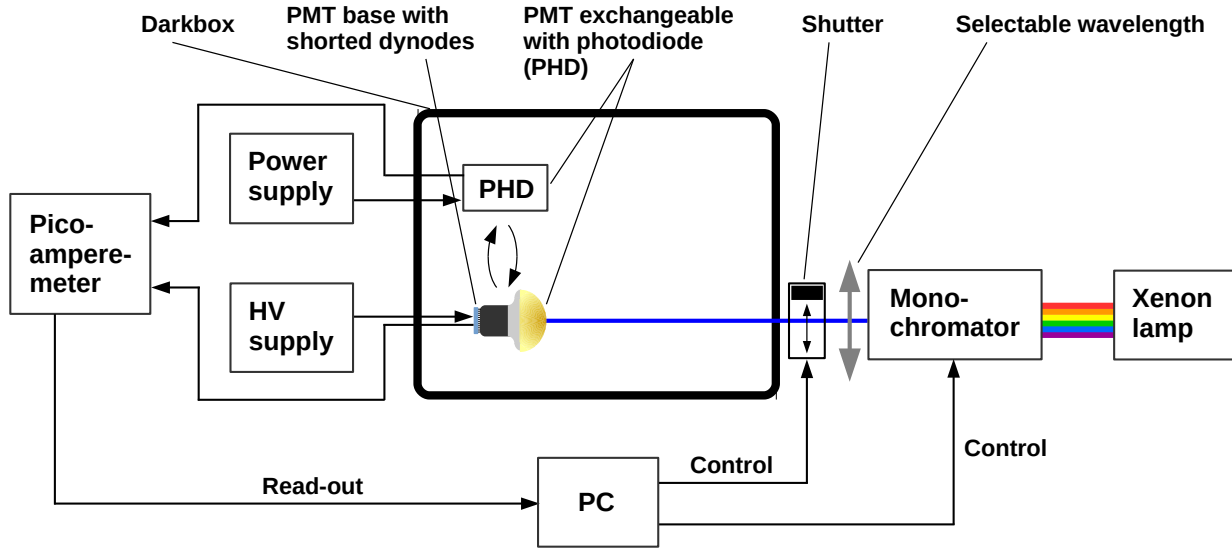


**Figure 3.6:** Schematic of the setup used for the measurements of the quantum efficiency. PHD and PMT are exchangeable.

dynodes, a special base was used. All dynodes of the PMT were at the same potential with a voltage of about 300 V—corresponding to the average voltage between photocathode and first dynode in pulse mode—applied between photocathode and the dynodes. This electrical connection ensured that only the QE of the photocathode was measured without any additional effects of the dynodes. The output current  $I_{\text{PMT}}$  of the PMT was read out by a picoamperemeter connected to a computer (PC). A Xenon lamp [83] with a spectrum ranging from ultraviolet to visible light [84] was used as a light source. With a precision  $< 2$  nm, an MSH301 monochromator from LOT Oriel selected a wavelength segment of the spectrum. The light of this wavelength segment was then directed to the PMT. A shutter at the darkbox could be opened and closed, letting the light beam from the monochromator either pass or not. Both monochromator and shutter were controlled by the PC. Because the QE is wavelength-dependent, the wavelength  $\lambda$  was scanned in steps of 5 nm between 245 nm and about 700 nm and the corresponding QE of the PMT was calculated. For that, reference measurements were needed. A photodiode (PHD) ([85]) with a known quantum efficiency  $\text{QE}_{\text{PHD}}$  calibrated by the manufacturer could be placed instead of the PMT at the same position. With an independent measurement, it was shown that the light output of the Xenon lamp stays constant during the time between reference and PMT measurements. Both photodiode and PMT were measured with closed shutter (dark) and open shutter scanning different wavelengths. Finally, the QE of the PMT could be calculated out of the measurements as:

$$\text{QE}_{\text{PMT}}(\lambda) = \frac{I_{\text{PMT}}(\lambda) - I_{\text{PMT}}(\text{dark})}{I_{\text{PHD}}(\lambda) - I_{\text{PHD}}(\text{dark})} \cdot \text{QE}_{\text{PHD}}(\lambda), \quad (3.6)$$

with the current  $I_{\text{PHD}}$  of the photodiode. In principle, all parameters in Equation 3.6 can contain errors. The values for  $\text{QE}_{\text{PHD}}(\lambda)$  were determined by the manufacturer with no information about any statistic or systematic errors. In addition, the intensity of the light source can vary over time. Between 300 nm and 500 nm, the relative error due to the light intensity variation is typically between 0.3 % and 2 %. The statistical error of the current measurements is much smaller than the

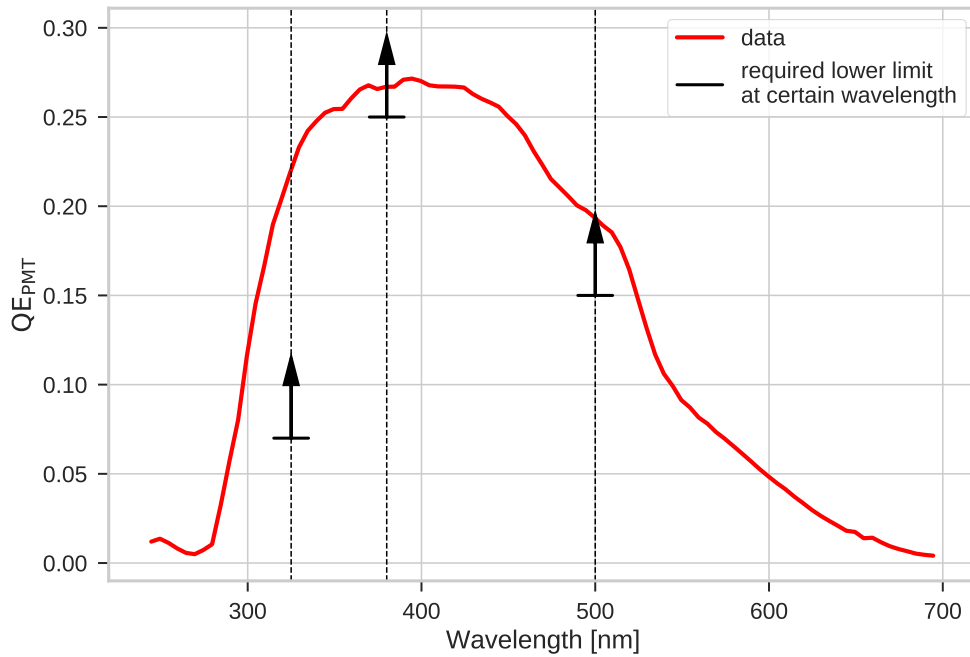


**Figure 3.7:** QE at different wavelength for the PMT BA0806 of the PMT type R15458-02 from Hamamatsu Photonics K.K. at room temperature.

error from the stability of the light source. All measurements were performed at room temperature. In Figure 3.7, a typical QE measurement is shown. The QE shows a peak at about 400 nm and a sharp edge towards the ultraviolet to the left whereas the decrease to the right of the QE spectrum after 500 nm is less sharp. The basis of the black arrows indicates the required lower limit at the specific wavelength which is always exceeded for the PMT shown in Figure 3.7.

### 3.3.3 Darkrate

Different from TTS and QE, the darkrate is a background. The darkrate of each PMT contributes to the overall noise of the mDOM which is why the PMT's darkrate is desired to be less than 150 Hz at  $-20^{\circ}\text{C}$ . High darkrates reduce the reconstruction performance of neutrino events. Furthermore, the bandwidth of the data cable at South Pole is limited to 1.4 Mb/s for three modules on a 2.8 km cable [86]. In case the noise of the mDOMs exceeded the bandwidth limit, not all data could be transferred to the IceCube Laboratory at the South Pole which would lead to data loss of neutrino events.

The darkrate was measured with the setup shown in Figure 3.8. The PMT connected to its passive base was put into a darkbox which in turn was placed in a freezer. A power supply was connected to the passive base of the PMT and the PMT signal was read out by an oscilloscope [79]. The data were saved to a hard drive. A temperature sensor [87] close to the PMT's photocathode and read out by a PC monitored the temperature in the darkbox.

First of all, the PMT was switched on. Therefore, the nominal HV determined in Subsection 3.2.3 was used. This HV value was not changed during the measurement, although the temperature changes throughout the measurement and the nominal HV decreases with lower

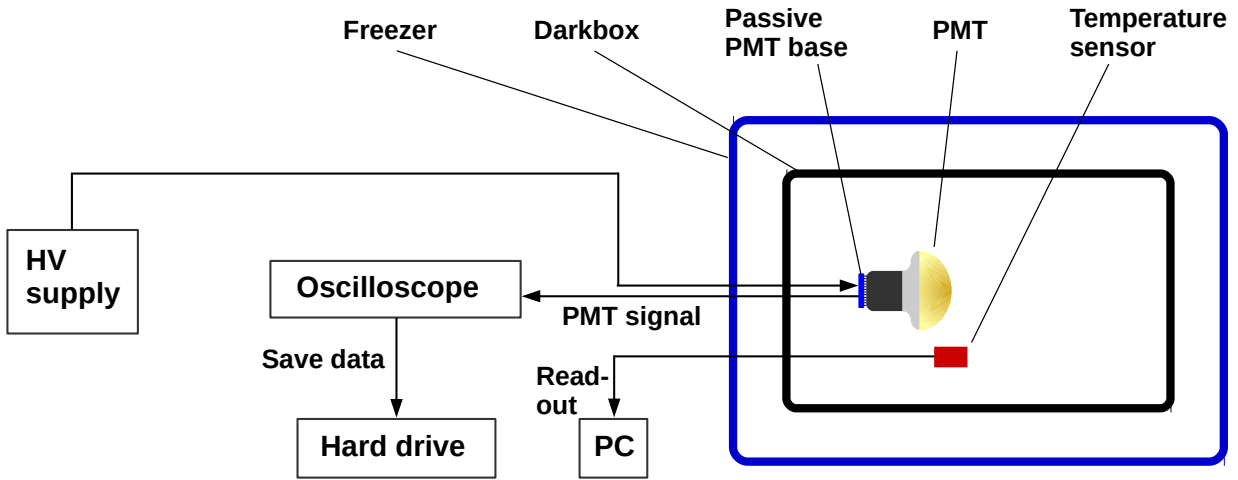


**Figure 3.8:** Schematic of the setup used for the darkrate measurements.

temperatures by few volts. This effects leads to a higher gain at lower temperatures for the same high voltage value. Thus, the darkrate was slightly overestimated in the measurements.

The data of darkrate, temperature and time were saved from the beginning. To determine the darkrate, a trigger threshold of 4 mV was adjusted at the oscilloscope. Ideally, the threshold should be the voltage value a PMT pulse with a charge of 0.2 p.e. would have which would be about 1.4 mV. Due to electronic noise, such a small threshold was not possible with this setup and the lowest possible threshold of 4 mV was used. Only PMT pulses crossing this threshold were processed. This trigger mode is called selftrigger. An oscilloscope math function measured the time between 101 threshold crossings (it was not possible to measure the time between two threshold crossings, because the oscilloscope cannot measure such high rates). This time was divided by 100 and the reciprocal value was taken. The mean of 100 such measurements yielded the darkrate. Further investigations of this method were made by Anna Eimer in her bachelor thesis [88]. Using this method, the relative statistical error of the darkrate measurements results from event counting and is in the order of 1 %.

After the PMT was powered, the freezer was switched on cooling to  $-20^{\circ}\text{C}$ . Two effects reduce the darkrate. First, the thermal excitation decreases with lower temperatures. Second, free electrons in the PMT previously knocked out of the photocathode by exposure to light (see Subsection 1.3.3.3) are transported out of the PMT due to the applied HV. Both effects lead to a decrease of the darkrate with time. Several hours were measured until the PMT was in thermal equilibrium and the darkrate stable. The darkrate was measured after the PMT was at least 5 h in the dark. A typical measurement is shown in Figure 3.9. After cooling down to  $-20^{\circ}\text{C}$ , the darkrate is stable. The mean of all darkrate values marked with a black line yields the darkrate at  $-20^{\circ}\text{C}$ .

### 3.3.4 Correlated noise

Similar to the darkrate, the correlated noise is an unwanted background process changing the timing of the detector and possibly reducing the reconstruction performance. Therefore, the exact probabilities are measured to include them in a later simulation. Different from the uncorrelated

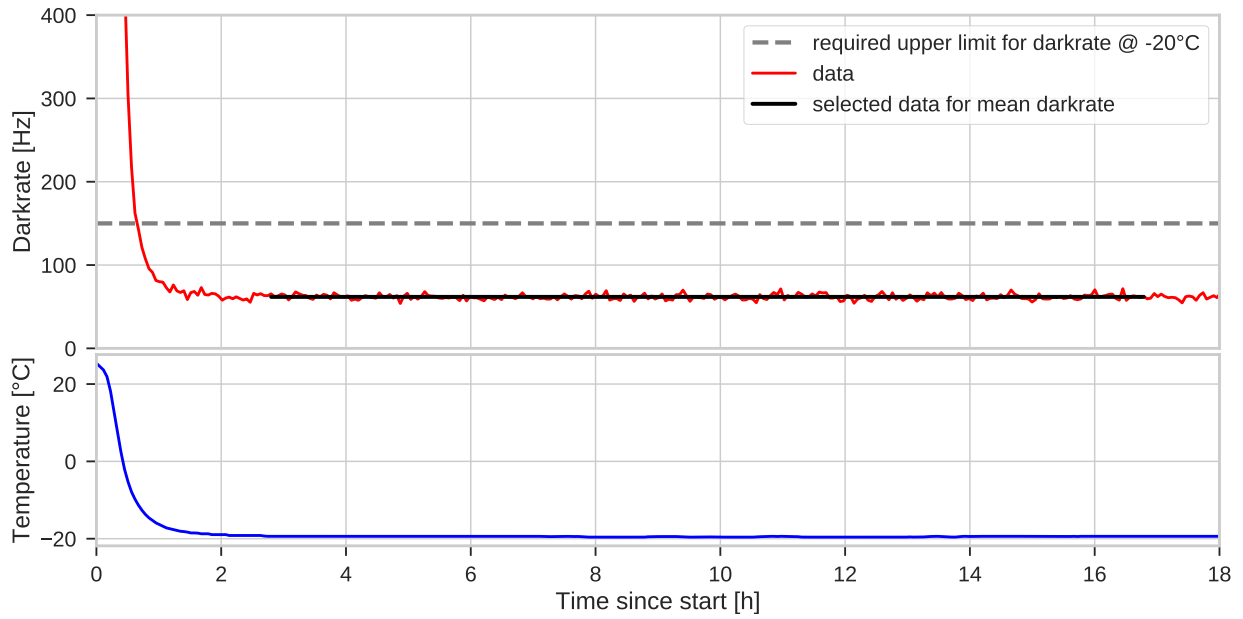


**Figure 3.9:** Darkrate over time at  $-20^{\circ}\text{C}$  for the PMT DM00002 of the PMT type R15458-20 from Hamamatsu Photonics K.K. using a trigger threshold of 4 mV.

darkrate, the correlated noise occurs correlated in time with respect to the main pulse. The different timing characteristics of the correlated noise help to classify them into prepulsing, delayed pulsing, and afterpulsing.

#### 3.3.4.1 Prepulsing

The prepulsing probability is the probability that the transit time of a PMT pulse is significantly shorter than normal (see Paragraph 1.3.3.4). For the mDOM, all pulses arriving 10 ns to 20 ns before the main PMT pulse can be identified as prepulses. Prepulsing can be measured together with the TTS. The histogram of the relative transit times already used for the determination of the TTS is shown in Figure 3.10. In Subsection 3.3.1, the main peak was used. For the prepulsing probability, all entries between 10 ns to 20 ns (prepulsing window) before the main peak were counted and divided by the total number of entries. For the PMTs from Hamamatsu Photonics K.K., the number of prepulses is mostly 0, 1, or 2. According to [89] (Table II), the 68.27% confidence interval when assuming a background of 0 ranges from 0.00 to 1.29 for a mean of 0 counts, from 0.37 to 2.75 for a mean of 1 count, and from 0.74 to 4.25 for a mean of 2 counts. For the PMTs from HZC Photonics, a typical number of prepulses is 13. This number yields a 68.27% confidence interval from 9.28 to 17.30 according to [89] when assuming a background of 0. For the mDOM, the requirement is a prepulsing probability of less than 0.01.

#### 3.3.4.2 Delayed pulsing

Delayed pulses are pulses that occur shortly after the main pulse. For the mDOMs, the time window for delayed pulses was set to 15 ns to 80 ns after the main pulse. Because of the short time after the main pulse, the delayed pulse probability could be extracted from the same measurement

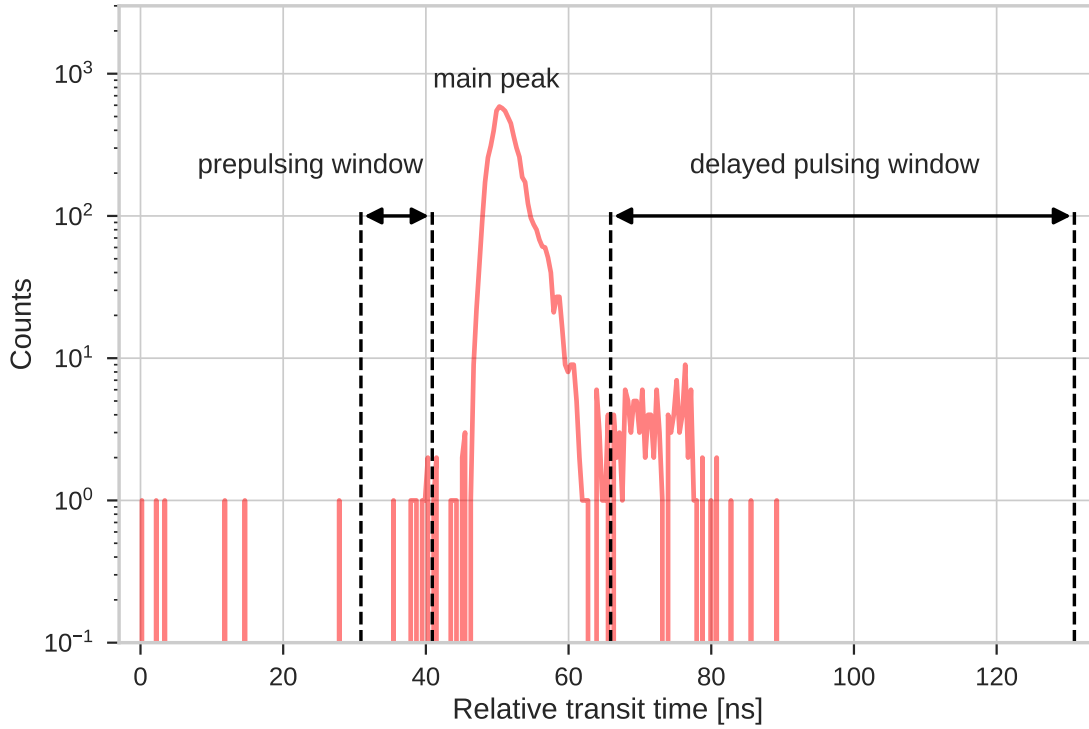


**Figure 3.10:** Histogram of the relative transit time shown for the PMT DM00021 of the PMT type R15458-20 from Hamamatsu Photonics K.K. at room temperature.

as the TTS. Similar to the determination of the prepulse probability, the histogram of the relative transit times was used. All pulses arriving 15 ns to 80 ns after the main peak (see Figure 3.10) were counted and divided by the total number of entries. The ratio is the probability of a delayed pulse which is required to be less than 0.05. The statistical error of the delayed pulse probability originates from event counting. With approximately 5000 signals and a typical delayed pulse probability of 2 %, the number of delayed pulses is about 100 with an absolute statistical error of  $\pm\sqrt{100} = \pm 10$ .

### 3.3.4.3 Afterpulsing

Other than prepulses and delayed pulses, afterpulses occur not instead of but additionally to their main pulse. Moreover, afterpulses occur not within nanoseconds but within microseconds after the main pulse. Thus, an extra measurement with a larger time window was needed.

For the measurement of afterpulses, 50 000 waveforms, each with a length of  $20\ \mu\text{s}$ , were recorded. Next, the relative transit time was calculated for each pulse in one waveform crossing a threshold of 3 mV. This calculation was done for all waveforms. A histogram of the relative transit time is shown in Figure 3.11. The dominant peak at  $1.95\ \mu\text{s}$  is the main peak whereas the broad band at the bottom is the homogeneously distributed darkrate. For the afterpulse probability, all peaks inside the time window between 100 ns and  $12\ \mu\text{s}$  after the main peak (afterpulse window) were counted. After that, the number was corrected for the darkrate. For this purpose, another time window before the prepulsing window was defined (darkrate window). All peaks inside this

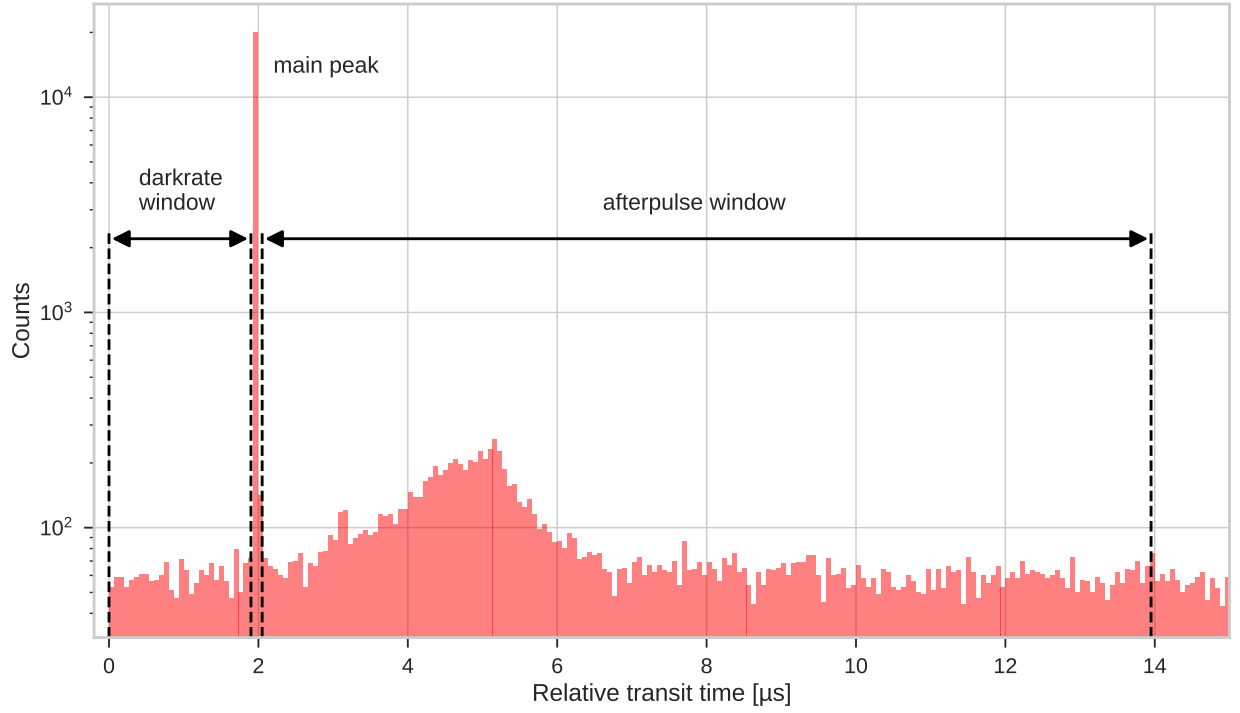


**Figure 3.11:** Histogram of the relative transit time for the determination of the afterpulsing probability shown for the PMT DM00059 of the PMT type R15458-20 from Hamamatsu Photonics K.K. at room temperature.

window were counted, corrected for the length of the afterpulsing window and its number was subtracted from the counts of the afterpulsing window. The remaining counts were afterpulses. Divided by the total number of entries, the probability of afterpulsing was calculated which must be less than 0.15. This method yields a relative statistical error from event counting of less than 3 %. Table 3.2 shows a summary of the requirements of the PMT characteristics investigated in this thesis as well as the physical motivation.

**Table 3.2:** Overview of all PMT requirements investigated in this thesis. Requirements were taken from [68].

PMT characteristic	Requirement	Physical motivation
Transit time spread (TTS)	$< 2.0$ ns	SPE time resolution
Quantum efficiency (QE) at 325 nm	$> 0.07$	Energy resolution
Quantum efficiency (QE) at 380 nm	$> 0.25$	Energy resolution
Quantum efficiency (QE) at 500 nm	$> 0.15$	Energy resolution
Darkrate at $-20^{\circ}\text{C}$	$< 150$ Hz	Bandwidth limit, reconstruction performance
Prepulse probability $[-20\text{ ns}, -10\text{ ns}]$	$< 0.01$	Correct timing
Delayed pulse probability $[15\text{ ns}, 80\text{ ns}]$	$< 0.05$	Reconstruction performance
Afterpulse probability $[100\text{ ns}, 12\text{ }\mu\text{s}]$	$< 0.15$	Reconstruction performance
Mean amplitude of a 1 p.e. pulse	$> 6$ mV	Trigger above noise level

### 3.4 Comparison of Hamamatsu and HZC PMT types

At the beginning of the PMT mass characterization measurements, different nominal gain values such as  $3 \cdot 10^6$ ,  $5 \cdot 10^6$ , and  $1 \cdot 10^7$  were investigated. With a higher gain value, the TTS can be reduced whereas unwanted background processes such as darkrate increase. For optimal performance of the PMTs, a nominal gain of  $5 \cdot 10^6$  was chosen by the collaboration. Furthermore, PMT types from different manufacturers were characterized with mass testing measurements. In this chapter, 100 PMTs of the R12199-01 HA PMT type from Hamamatsu Photonics K.K. and 45 PMTs of the XP82B2F PMT type from HZC Photonics are compared. For simplification, the PMT types are referred to as Hamamatsu PMTs and HZC PMTs in this section.

Figure 3.12 shows the results for the Hamamatsu PMTs in red and for the HZC PMTs in blue. The required upper or lower limit is shown as a dashed black line. Investigated parameters were TTS, QE, darkrate at  $-20^{\circ}\text{C}$ , prepulsing probability, delayed pulse probability, and afterpulse probability. All measurements except darkrate were performed at room temperature.

Concerning the TTS, the Hamamatsu PMTs show significantly better results than the HZC PMTs. The mean TTS of the Hamamatsu PMTs is 1.49 ns whereas the mean of the HZC PMTs is 1.91 ns. Moreover, 36 % of the HZC PMTs do not fulfill the TTS requirement of less than 2 ns.

Plotting QE versus wavelength, both PMT types show a similar shape with a maximum at around 380 nm. However, the cutoff of the HZC PMTs at the left side of the spectrum starts at larger wavelengths than for the Hamamatsu PMTs. This behavior can also be seen in the histogram of the QE at 325 nm. The QEs of all Hamamatsu PMTs clearly exceed the requirement of 0.07 with a mean of 0.22. Also all HZC PMTs fulfill the requirement, but are closer to the required lower limit with a mean QE of 0.13. This QE requirement at 325 nm is important, because more Cherenkov photons are emitted for smaller wavelength. At 380 nm, both PMT types have similar mean QE values with 0.27 for the Hamamatsu PMTs and 0.26 for the HZC PMTs. Two of the

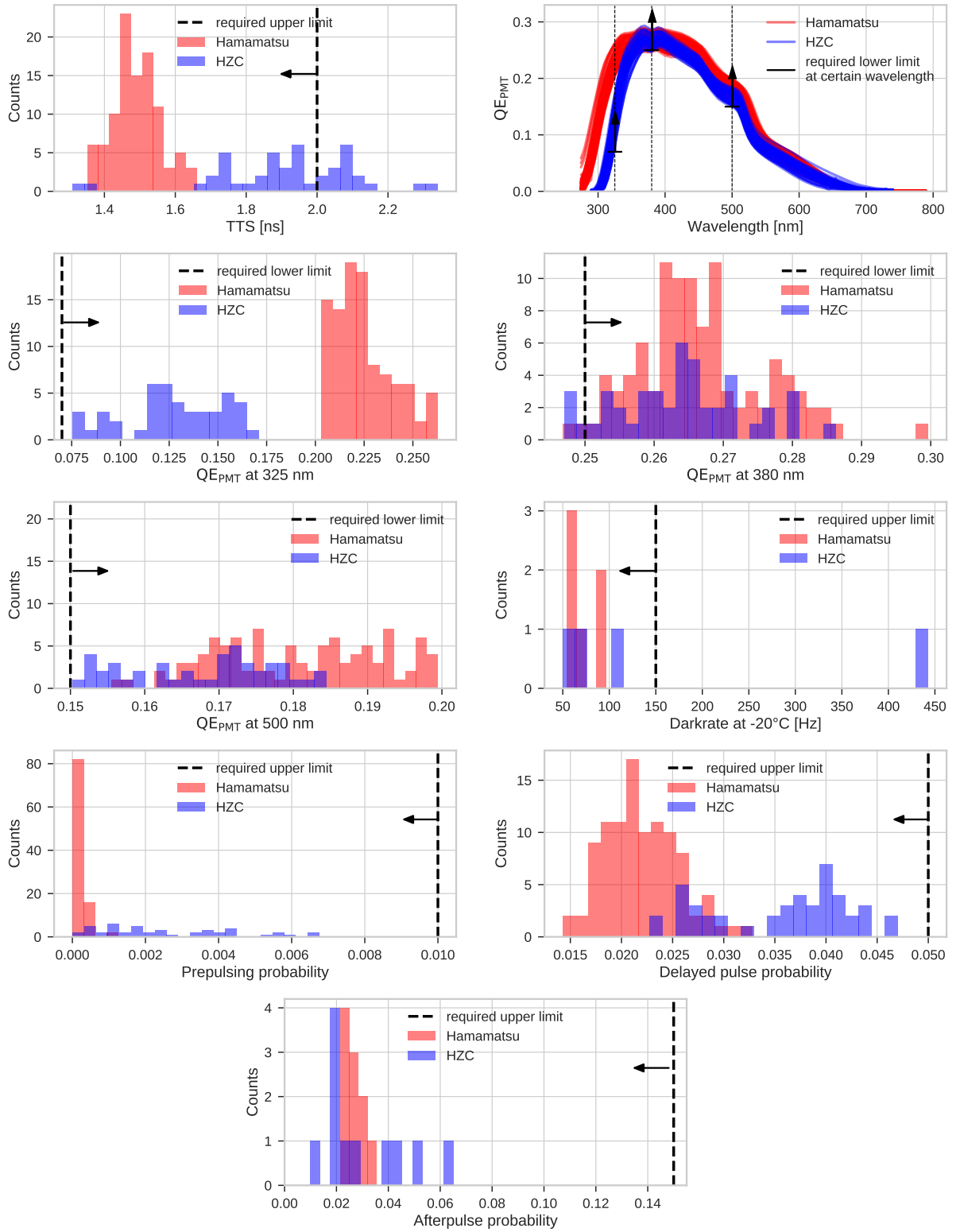


**Figure 3.12:** Comparison of TTS, QE, darkrate at  $-20^{\circ}\text{C}$ , prepulsing probability, delayed pulse probability, and afterpulse probability for the Hamamatsu R12199-01 HA PMT type (red) and the HZC XP82B2F PMT type (blue).

Hamamatsu and four of the HZC PMTs have a minimum QE of 0.25. At 500 nm, all PMTs fulfill the requirement. The mean QE of the Hamamatsu PMTs is 0.18 and 0.17 for the HZC PMTs.

For the Hamamatsu and the HZC PMT types investigated in this section, the darkrate at  $-20^{\circ}\text{C}$  was determined different than described in Subsection 3.3.3. The PMTs were cooled down to  $-50^{\circ}\text{C}$  and then warmed up to room temperature again. To obtain the darkrate at  $-20^{\circ}\text{C}$ , the first temperature on the cooling curve falling below  $-20^{\circ}\text{C}$  was taken. For this temperature, the darkrate was extracted. The same was done for the first temperature on the warming curve above  $-20^{\circ}\text{C}$ . The final darkrate at  $-20^{\circ}\text{C}$  was determined as mean value of the two darkrate values on warming and cooling curve. With this method, the deviation of measured temperature by the temperature sensor and true temperature at the photocathode should be minimized. When the PMT was cooled down and the temperature sensor showed  $-20^{\circ}\text{C}$ , the photocathode of the PMT was most likely warmer. Similarly, the photocathode was still cooler than  $-20^{\circ}\text{C}$  when the PMT was warmed up and the temperature sensors showed  $-20^{\circ}\text{C}$ . All PMTs were at least 5 h in the dark before the darkrate was determined unless the darkrate was smaller than 150 Hz before 5 h. Due to the long measurement time, the darkrate at  $-20^{\circ}\text{C}$  was not measured for all PMTs. Only six Hamamatsu and four HZC PMTs were characterized. All PMTs have a darkrate smaller than 150 Hz at  $-20^{\circ}\text{C}$  except one HZC PMT exceeding the upper limit of more than a factor of two.

In contrast to that, all Hamamatsu as well as all HZC PMTs have a lower prepulsing probability than the required upper limit of 0.01. The mean prepulsing probability of the Hamamatsu PMTs is 0.00015 whereas the mean of the HZC PMTs is 0.0026 and with that, one order of magnitude larger than the mean of the Hamamatsu PMTs.

Likewise, all tested PMTs fulfill the required maximal delayed pulse probability as well as the afterpulse probability. The Hamamatsu PMTs have a mean probability for a delayed pulse of 0.022 while the HZC PMTs have a mean of 0.036. Similar to the darkrate measurements, the afterpulsing probability was measured for only ten Hamamatsu and twelve HZC PMTs due to the long measurement time. Both Hamamatsu and HZC PMTs have a mean afterpulse probability of 0.027. It has to be taken into account, however, that the intensity of the incident light was low for the HZC PMTs leading to a low statistic for the determination of the afterpulse probability for each PMT. All mean values and failures are summarized in Table 3.3. The corresponding errors are discussed in the respective subsection of Section 3.3.

All in all, the Hamamatsu PMTs show a better performance than the HZC PMTs. Except two PMTs slightly deceeding the QE requirement at 380 nm, the Hamamatsu PMTs always fulfill the requirements whereas 36 % of the HZC PMTs exceed the TTS requirement, 9 % deceed the QE requirement at 380 nm, and 25 % exceed the darkrate requirement. In addition to that, the Hamamatsu PMTs almost always have a larger reserve to the limit than the HZC PMTs. Finally, it was decided to use Hamamatsu PMTs for the mDOMs.

**Table 3.3:** Overview of the measured characteristics of the Hamamatsu R12199-01 HA PMT type and the HZC XP82B2F PMT type. If not stated otherwise, 100 Hamamatsu PMTs and 45 HZC PMTs were measured.

Characteristic	Hamamatsu R12199-01 HA			HZC XP82B2F			Requirement
	Mean		Failed	Mean		Failed	
TTS	1.49	ns	-	1.91	ns	36 %	< 2.0 ns
QE at 325 nm	0.22		-	0.13		-	> 0.07
QE at 380 nm	0.27		2 %	0.26		9 %	> 0.25
QE at 500 nm	0.18		-	0.17		-	> 0.15
Darkrate $-20^{\circ}\text{C}$	72	Hz	-	165	Hz	25 %	< 150 Hz
			(0 of 6)			(1 of 4)	
Prepulsing	0.000 15		-	0.0026		-	< 0.01
Delayed pulsing	0.022		-	0.036		-	< 0.05
Afterpulsing	0.027		-	0.027		-	< 0.15
			(0 of 10)			(0 of 12)	

### 3.5 Characterization of the final PMT type

In this section, the final PMT type used in the mDOMs is characterized. This PMT type is a successor PMT type of the R12199-01 HA from Hamamatsu Photonics K.K. called R15458-20 which is 2 mm shorter and has a copper tape between HA coating and glass tube. The copper tape can be connected to the reflector in the PMT support structure of the mDOM (see Figure 2.1 for the mDOM setup) and with that, the reflector is set to the potential of the PMT's photocathode. Studies made by [67] show that this reflector configuration yields the lowest PMT darkrate. Another difference is that the microbase is already soldered to the PMT pins. This soldering was directly done by Hamamatsu Photonics K.K. The basic idea of this characterization was to show that the final PMT design including the microbase still fulfills all requirements. For this purpose, a small sample of 19 PMTs was sent to Erlangen for testing.

In Figure 3.13, the same characteristics as in Section 3.4 are shown such as TTS, QE, darkrate at  $-20^{\circ}\text{C}$ , prepulsing probability, delayed pulse probability, and afterpulse probability. Moreover, the mean amplitude of a 1 p.e. pulse is shown. This amplitude must be larger than 6 mV so that it is possible to trigger on 0.2 p.e. signals without capturing electronic noise. The relative statistical error of the mean amplitude originating from the error of the mean is typically 0.04 %. For the other parameters, the errors are discussed in the respective subsection of Section 3.3, where the method to determine the respective parameter is introduced. The requirements are shown as dashed black lines. All measurements except darkrate were performed at room temperature. All 19 PMTs have a TTS smaller than 2 ns. Because a special base is necessary for the QE measurements to apply the same potential on all dynodes (see Subsection 3.3.2) which is not possible with an already soldered microbase on the PMTs, the PMT type R15458-02 is used for the QE measurements. This type is the same PMT type as the R15458-20, but without microbase. Except four PMTs at 380 nm, all

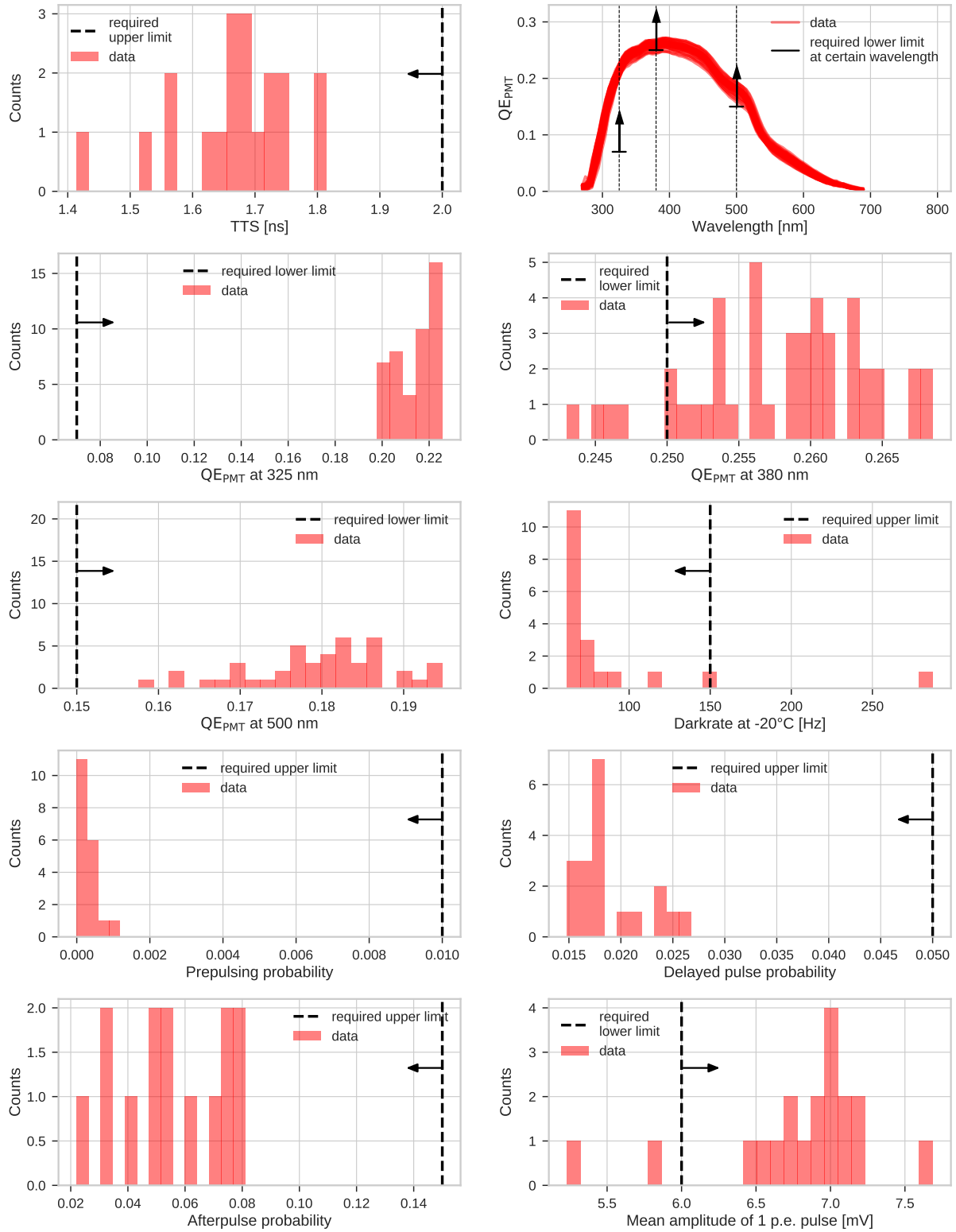


**Figure 3.13:** Results of TTS, darkrate at  $-20^{\circ}\text{C}$ , prepulsing probability, delayed pulse probability, afterpulse probability, and mean amplitude of a 1 p.e. pulse for the PMT type R15458-20 and the results of QE for the PMT type R15458-02 from Hamamatsu Photonics K.K.

**Table 3.4:** Overview of the measured characteristics of the R15458-20 (\*QE for R15458-02) PMT type from Hamamatsu Photonics K.K. Altogether, 19 (\*45) PMTs were measured, except for afterpulsing (14 PMTs).

Characteristic	Hamamatsu R15458-20 (R15458-02*)		Requirement
	Mean	Failed	
TTS	1.67 ns	-	< 2.0 ns
QE at 325 nm*	0.21	-	> 0.07
QE at 380 nm*	0.26	21 %	> 0.25
QE at 500 nm*	0.18	-	> 0.15
Darkrate $-20^{\circ}\text{C}$	87 Hz	11 %	< 150 Hz
Prepulsing	0.000 28	-	< 0.01
Delayed pulsing	0.019	-	< 0.05
Afterpulsing	0.055	-	< 0.15
1 p.e. amplitude	6.80	11 %	> 6 mV

PMTs fulfill the requirements for the QE. Two PMTs exceed the required darkrate of smaller than 150 Hz. While one of those two PMTs is close to the requirement, the other PMT has a darkrate of almost two times the requirement which is why this PMT was sent back to Hamamatsu Photonics K.K. On the other hand, all PMTs fulfill the requirements of prepulse probability, delayed pulse probability, and afterpulse probability. In contrast to that, two PMTs have a mean amplitude of a 1 p.e. signal smaller than 6 mV. An overview of all mean numbers and failures is given in Table 3.4. Except for the one PMT strongly exceeding the darkrate requirement, these results of the Hamamatsu PMT type R15458-20 were acceptable for the collaboration.

To sum up, most of the PMT type R15458-20 from Hamamatsu Photonics K.K. fulfill the requirements. Only one PMT with a too high darkrate was returned to the manufacturer. Before being integrated in an mDOM, all PMTs are characterized concerning nominal HV, TTS, photo-detection efficiency, charge response linearity (see Subsection 4.3.2.3 for information about linearity), darkrate, probability of prepulsing, delayed pulsing, and afterpulsing at mass testing facilities in Aachen and Dortmund [90]. All measurements are performed at  $-20^{\circ}\text{C}$ . PMTs not fulfilling the requirements are rejected.

### 3.6 Summary

Four PMT types of two manufacturers were investigated with regard to different requirements the PMT used for the mDOMs in the IceCube Upgrade have to fulfill. These requirements include TTS, QE, darkrate at  $-20^{\circ}\text{C}$ , prepulse probability, delayed pulse probability, and afterpulse probability. For the final PMT type, also the mean amplitude of a 1 p.e. signal was measured. In three setups, the different characteristics were measured. All measurements except the darkrate were performed at room temperature. Each PMT was calibrated to the nominal HV before the characterization

measurements. First, 100 PMTs of the PMT type R12199-01 HA from Hamamatsu Photonics K.K. and 45 PMTs of the PMT type XP82B2F from HZC Photonics were compared. While the R12199-01 HA PMTs—except two PMTs with a QE of 0.25 at 380 nm—always fulfilled the requirements, 16 of the XP82B2F PMTs missed the TTS requirement, 9 XP82B2F PMTs did not fulfill the required QE at 325 nm, and 1 of 4 tested XP82B2F PMTs had a too high darkrate. Moreover, the R12199-01 HA PMTs showed an overall better performance than the XP82B2F PMTs. Therefore, it was decided to use PMTs from Hamamatsu Photonics K.K. for the mDOMs. Before the PMT mass production for the mDOMs started, a test batch of 19 PMTs of the final PMT type R15458-20 had been characterized. Except for one PMT strongly exceeding the darkrate requirement, no serious problems were found and the results were satisfying for the collaboration so that the PMT mass production could start. Before being integrated into an mDOM, all PMTs are measured with regard to nominal HV, TTS, photo-detection efficiency, charge response linearity, darkrate, probability of prepulsing, delayed pulsing, and afterpulsing at  $-20^{\circ}\text{C}$  at the mass testing facilities in Aachen and Dortmund. In case a PMT does not pass the tests, it is sorted out.



## Chapter 4

# Measurements with the analog front end (AFE)

---

<b>4.1</b>	<b>AFE configuration</b>	<b>60</b>
<b>4.2</b>	<b>Investigated AFE requirements for the mDOM</b>	<b>60</b>
<b>4.3</b>	<b>Characterization of different AFE channel designs</b>	<b>61</b>
4.3.1	Measurement setup and calibration	61
4.3.2	Investigated parameters	63
4.3.2.1	Signal-to-noise ratio (SNR)	63
4.3.2.2	Dynamic range	65
4.3.2.3	Linearity	74
4.3.3	Comparison of channel characteristics	79
4.3.4	Problems	80
4.3.4.1	Mismatch in charge calibration	80
4.3.4.2	Deformation of charge histograms	82
<b>4.4</b>	<b>Characterization of the AFE channel design of the revision 1 mainboard</b>	<b>84</b>
4.4.1	Measurement setup	84
4.4.2	Functionality test	85
4.4.3	Investigated parameters	87
4.4.3.1	Signal-to-noise ratio (SNR)	87
4.4.3.2	Dynamic range	87
4.4.3.3	Linearity	91
4.4.3.4	Discriminator threshold stability	92
4.4.4	Conclusion	94
<b>4.5</b>	<b>Summary</b>	<b>95</b>

---

Similar to the PMTs, the AFE is tested during development before it is used for the mDOM. Thus, the AFE design was modified throughout the whole testing process. This chapter concentrates on characterization measurements of different AFE parameters. In the first section, the basic

working principle of the AFE is explained. The second section describes the AFE requirements which are investigated in this chapter. Different AFE designs are characterized in the third section. The designs are measured in view of different requirements and are compared to each other. Section four focuses on measurements with the final AFE design used for the revision 1 mainboard. In section five, a summary is given.

## 4.1 AFE configuration

As explained in Subsection 2.4.3, the AFE is the part of the electronics which processes the analog PMT signal before it is digitized by the ADC. The AFE designs characterized in this thesis are predecessor designs of the AFE design used for the mDOMs. In contrast to Figure 2.6 describing the mDOM AFE design, these predecessor AFE designs split the PMT signal after the preamplifier in discriminator signal and amplifier signal and not before the preamplifier. Splitting the PMT signal before the preamplifier, however, leads to a faster trigger and no additional noise from the preamplifier, which is why these changes were implemented later for the mDOM AFE.

The AFE itself fits on a small segment of a printed circuit board. Normally, the AFE is operated by further electronics on the mainboard. Because the mainboard was not ready at that time, a mainboard testboard (mDOT) was used instead. The mDOT is a circuit board with the same dimensions as the mainboard and similar electronic components with some differences. Compared to the mainboard, which is described in Subsection 2.4.4, the mDOT has neither a microcontroller nor a hit buffer. Using a special firmware, all functions of the microcontroller are performed by the FPGA instead. Furthermore, the ADC on the mDOT samples with 100 MHz (in contrast to the sampling rate of 120 MHz used for the mainboard). Besides, no mDAB is included on the mDOT. Moreover, only four AFE channels are located on the mDOT.

## 4.2 Investigated AFE requirements for the mDOM

The following AFE requirements are investigated in this thesis: Signal-to-noise ratio, dynamic range, linearity, and discriminator threshold stability. Because it should be possible to trigger on single photons, the root mean square (RMS) of the noise as measured in the ADC after pulse shaping is required to be less than or equal to  $1/25$  of the amplitude of an average SPE. In other words, the ratio of signal height and noise—called signal-to-noise ratio (SNR)—is required to be more than 25. As described in Subsection 1.2.2, the IceCube Upgrade will cover a neutrino energy range between approximately 1 GeV and 10 GeV [7]. Simulations performed by the IceCube collaboration [91] revealed that for this purpose, each PMT + microbase + AFE (= PMT channel) should be capable of triggering on as well as recording PMT signals with a charge ranging from 0.2 p.e. to not less than 50 p.e. per 10 ns. For the calibration of the charge calculation, the linearity of the system PMT + microbase + AFE is required. To be exact, the amplitude of the mean output signal should be proportional within 10 % to the amplitude of the input signal up to an input signal charge of 50 p.e. For the mDOMs in the IceCube Upgrade, the threshold of 0.2 p.e. is set to each discriminator. In case the threshold drifts, it either drifts towards smaller voltages and it is possible to trigger on noise, or the threshold drifts towards larger voltages so that some signals are lost. This inaccuracy of the discriminator threshold leads to an error in the photo-detection efficiency. To control this systematic error, the threshold of each discriminator should not drift more than

0.05 mean p.e. per week. All requirements are taken from [70]. An overview of the investigated AFE requirements, their exact wording, and their physical motivation is given in Table 4.1.

**Table 4.1:** Overview of the investigated AFE characteristics. Requirements are taken from [70].

AFE characteristic	Requirement	Physical motivation
Signal-to-noise ratio	“RMS noise as measured in the ADC after pulse shaping shall be less than or equal to 1/25 of the amplitude of an average SPE.”	Trigger on single photons
Dynamic range	“Each PMT channel shall be capable of triggering on and recording PMT signals ranging from 0.2 p.e./10 ns to not less than 50 p.e./10 ns.”	Covering relevant energy range
Linearity	“The amplitude of the mean output signal of the system shall be proportional within 10 % to the amplitude of the input signal up to an input signal charge of 50 p.e.”	Calibration of charge calculation
Discriminator threshold stability	“Each discriminator threshold shall not drift more than 0.05 mean p.e. per week.”	Controlled systematic error on photo-detection efficiency

### 4.3 Characterization of different AFE channel designs

Before the first mainboard was developed, different AFE channel designs existed. It was not clear which channel design should be used for the mDOM mainboard. Therefore, characterization measurements of the different AFE designs were performed.

#### 4.3.1 Measurement setup and calibration

A special setup shown in Figure 4.1 was used to characterize the different AFE channel designs. Four AFE channels (ch 0, ch 1, ch 2, ch 3) with different designs are placed directly on the mDOT. The channels use different resistor and capacitor values resulting in different amplification factors. Moreover, the inputs of channel 0 and channel 1 are DC coupled whereas the inputs of channel 2 and channel 3 are AC coupled (the different input coupling influences for example the baseline fluctuation). While the circuits of channel 1, channel 2, and channel 3 are directly integrated on the mDOT, channel 0 is a piggyback circuit board which was developed later and can be exchanged or modified independently of the mDOT. Because channel 1 was only developed to test the DC coupling and is not optimized for mDOM operation, it was used as a trigger channel. For the AFE characterization and comparison, channel 0, channel 2, and channel 3 were used. These three AFE channels were connected to a PMT each. The upper PMT was connected to channel 2, the middle PMT to channel 3 and the lower PMT to channel 0. The AFE channel supplied the PMT microbase with voltage and also processed the PMT signals. Due to the different designs of the AFE, the processed signals have different characteristics. Because the final PMT design did not

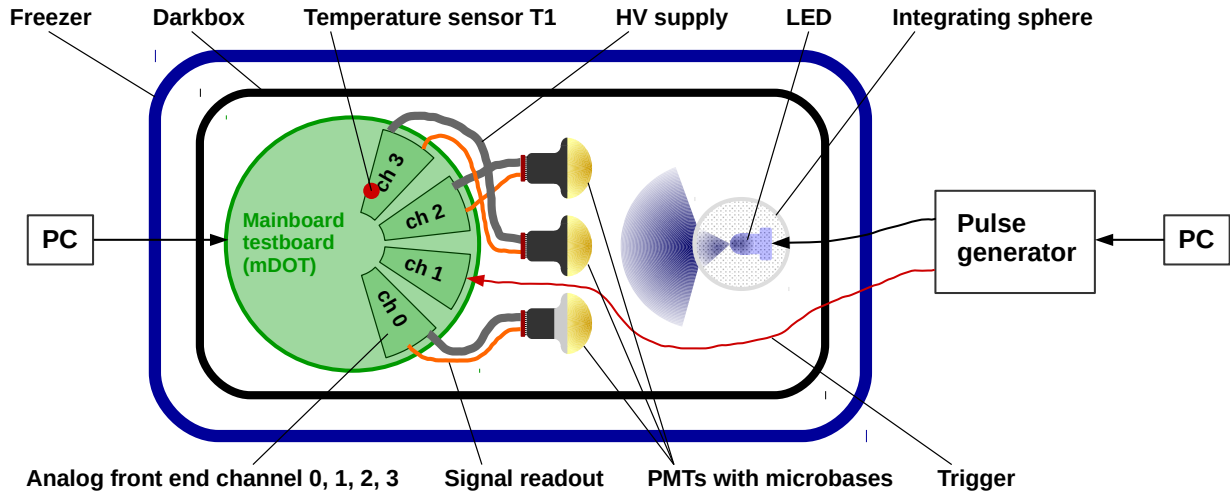


**Figure 4.1:** Measurement setup for the characterization of different AFE channel designs.

exist at that time, the predecessor PMT types were used. For the lower PMT, a R15458-02 type was used, and for the other two PMTs, the R12199-01-HA type. Because all PMTs were operated at nominal gain, it is not expected that the PMT types behave differently for the parameters investigated in this section. Different from the final design, the microbases were not soldered to the PMT pins but only plugged. To test the response of the AFE to different light intensities, a LED [92] with 370 nm wavelength was placed in front of the PMTs. To obtain a PMT illumination as homogeneous as possible, the LED was placed into an integrating sphere which was the same as used for the POCAM described in [93]. The LED was driven by a pulse generator using a repetition frequency of 1 kHz and a pulse width of 20 ns. To cover the light output for the entire required dynamic range, the pulse amplitude was varied (For example, the pulse amplitude was varied between 3.44 V and 3.75 V at room temperature for the setup described in Section 4.4; at m38C, the pulse amplitude was varied between 3.70 V and 3.96 V.). A trigger pulse was sent from the pulse generator to channel 1 of the mDOT. When channel 1 was triggered, the data of all four channels were read out. To minimize disturbances of external light, LED, integrating sphere, PMTs with their microbases, as well as the mDOT were placed into a darkbox. In order to control the ambient temperature during the measurements, the darkbox was put into a freezer. A temperature sensor T1 [94] integrated in the circuit of channel 3 (see Figure 4.1) was used to monitor the temperature inside the darkbox. The pulse generator as well as the mDOT were controlled and read out by a computer (PC).

Before a measurement was performed, PMTs and microbases were calibrated. Therefore, the PMT outputs as well as the trigger signal were connected to a calibrated ADQ14-DC-4C-VG digitizer [95] instead of the mDOT. As explained in Subsection 2.4.2, the input voltage of the Cockcroft-Walton multiplier is directed through an LC circuit first. Thus, the output voltage of the Cockcroft-Walton multiplier reaches its maximum at the resonant frequency of the LC circuit. To generate a sufficient HV for the PMTs, a suitable frequency had to be chosen for the Cockcroft-Walton multiplier on the microbase of each PMT. A frequency scan was performed scanning different frequencies and outputting the maximum voltage measured by the microbase for each frequency. After that, a frequency close to the resonance frequency was adjusted. Afterwards,

the PMTs were calibrated according to the PMT calibration procedure described in Section 3.2 and using the setup shown in Figure 4.1. Different from Section 3.2, only 20 000 waveforms were taken and saved directly on the PC controlling the digitizer. Both resonance frequency of the microbases as well as the nominal gain of the PMTs were calibrated and adjusted for each measured temperature range anew. The characterization measurements of the three different AFE channels were performed at two temperature ranges. The first range is between  $+17.0^{\circ}\text{C}$  and  $+18.5^{\circ}\text{C}$  and is referred to as measurement at  $+17^{\circ}\text{C}$ . The second temperature ranges from  $-43.2^{\circ}\text{C}$  to  $-41.2^{\circ}\text{C}$  is called measurement at  $-42^{\circ}\text{C}$ . These large temperature ranges are on the one hand caused by the temperature variations on short time scales (1 h) of about 1 K due to the hysteresis of the freezer, and on the other hand caused by external temperature changes resulting in changes of the mean temperature of less than 1 K over large time scales (days). Both temperature fluctuations are relevant for the measurements, because each measurement at one temperature lasted about one to two weeks. Between the calibration with the digitizer at a certain temperature and the measurement with the mDOT at the same temperature, the freezer was warmed up to room temperature to reconnect the PMT outputs to the mDOT. After that, the freezer was cooled down again to the same target temperature.

### 4.3.2 Investigated parameters

For the three different AFE designs, three parameters were investigated: SNR, dynamic range, and linearity. The dynamic range is subdivided in the capability of triggering on 0.2 p.e. and the capability of recording large pulses without saturation effects. Because it was less relevant for the AFE development during that time, the discriminator threshold stability was not investigated in this section. In the following, the procedure to determine these parameters and the results for the different AFE channels are discussed.

#### 4.3.2.1 Signal-to-noise ratio (SNR)

The first investigated parameter is the SNR. The output of the AFE consists of the baseline and the superimposed PMT signal. Ideally, the fluctuations of the baseline around the mean would be 0 V. In reality, however, the electronic noise leads to a nonzero fluctuation of the baseline. Different capacitor and resistor values result in different gain factors of each AFE design which leads to different output amplitudes and with that, also to different SNRs of the different AFE designs. The ratio of the signal amplitude and the fluctuation of the baseline is the SNR. For the signal amplitude, the mean amplitude of a 1 p.e. signal was used and the fluctuation of the baseline is described by the RMS of the baseline. In the following, the RMS of the baseline is called baseline RMS.

To determine the SNR, a measurement with a pulsed LED (called LED measurement in the following) was performed with the setup shown in Figure 4.1. The intensity of the LED was adjusted so that the mean number of detected photoelectrons at the PMTs was about 0.1. After that, 20 000 waveforms were acquired for each channel. This measurement was done for different LED voltages, because the mean number of photoelectrons is different for each PMT when using one LED voltage. Channel 1 served as trigger channel and all waveforms of all channels were saved when channel 1 was triggered. Figure 4.2 shows the method used in this thesis to determine the SNR from the described measurement. First of all, the charge of each waveform was calculated. This calculation was done in the same way as in Section 3.2 except that the charge is given in a.u.

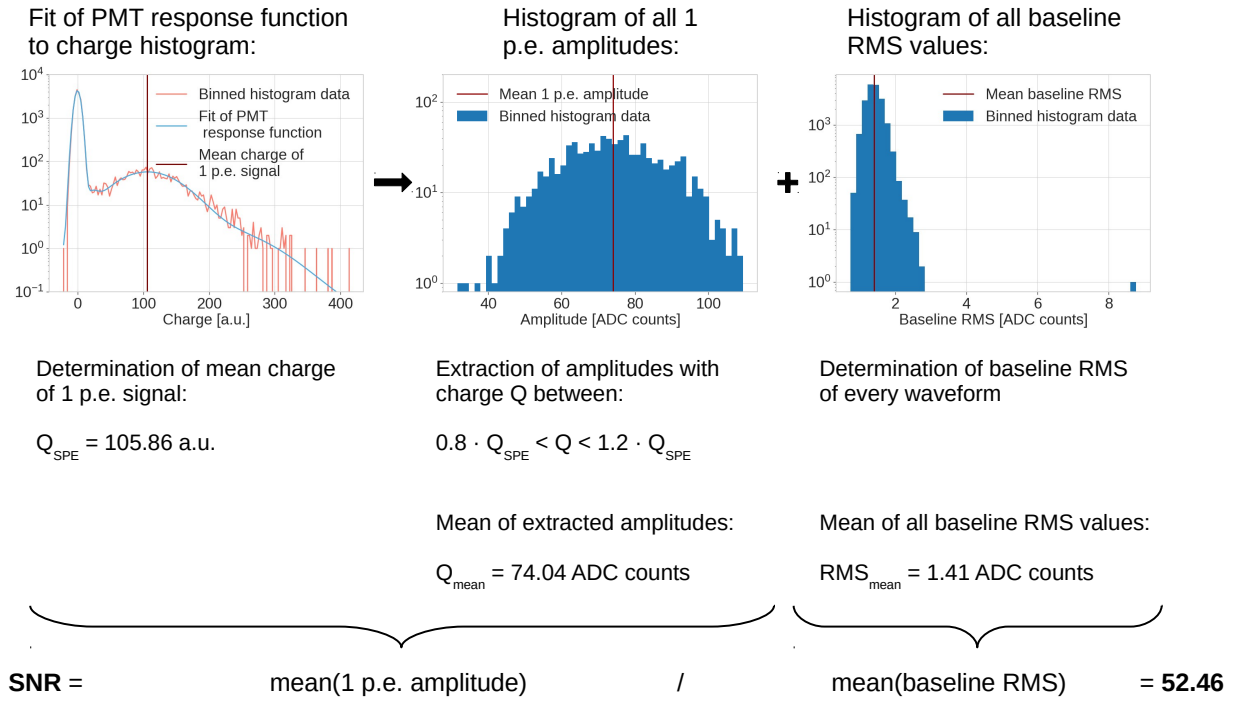


**Figure 4.2:** Illustration of the determination of the SNR shown for channel 3 at  $+17^\circ\text{C}$ .

The PMT response function was fitted to the charge spectrum in the same way as in Section 3.2. One of the fit parameters is the mean charge  $Q_{\text{SPE}}$  of a 1 p.e. signal. From this number, the mean amplitude of a 1 p.e. signal was determined. Therefore, all amplitudes with a charge  $Q$  between  $0.8 \cdot Q_{\text{SPE}} < Q < 1.2 \cdot Q_{\text{SPE}}$  were used and plotted in a histogram. The average of all those amplitudes gives the mean amplitude of a 1 p.e. signal. For the fluctuation of the baseline, the standard deviation of all values inside the baseline window (the first 30 voltage values of the waveform) was determined for each waveform. The right plot in Figure 4.2 shows a histogram of all those baseline RMS values. The mean of all the baseline RMS values gives the mean baseline fluctuation. Finally, the SNR was calculated as:

$$\text{SNR} = \frac{\text{mean}(1 \text{ p.e. amplitude})}{\text{mean}(\text{baseline RMS})}. \quad (4.1)$$

The SNR was calculated for  $+17^\circ\text{C}$  and  $-42^\circ\text{C}$  for all three channels. Table 4.2 shows an overview of all calculated values. With about 70 ADC counts, channel 3 has the largest mean amplitude of a 1 p.e. signal whereas channel 2 has the smallest mean amplitude of about 50 ADC counts. However, channel 3 also has the largest mean baseline RMS of about 1 ADC count. Compared to that, channel 0 is the channel with the lowest mean baseline RMS of about 0.6 ADC counts for both temperatures. Thus, channel 0 has the largest SNR of more than 100. However, all channels have a SNR of more than 25 at both temperatures. Except for channel 2, the mean baseline RMS decreases for the lower temperature which is expected. As a result, the SNR is larger at  $-42^\circ\text{C}$ . To sum up, all three channels fulfill the SNR requirement.

**Table 4.2:** Calculated SNR for all three channels at  $+17^\circ\text{C}$  and  $-42^\circ\text{C}$ .

Temperature	Parameter	channel 0	channel 2	channel 3	Requirement
$+17^\circ\text{C}$	Mean amplitude of a 1 p.e. signal [ADC counts]	65.59	53.39	74.04	-
	Mean baseline RMS [ADC counts]	0.60	0.69	1.41	-
	Signal-to-noise ratio	109.66	77.04	52.46	$> 25$
$-42^\circ\text{C}$	Mean amplitude of a 1 p.e. signal [ADC counts]	63.26	52.97	70.55	-
	Mean baseline RMS [ADC counts]	0.55	0.79	1.05	-
	Signal-to-noise ratio	114.88	66.83	67.39	$> 25$

#### 4.3.2.2 Dynamic range

To record neutrinos with energies between approximately 1 GeV and 10 GeV, the AFE has to process signals with mean charges between 0.2 p.e. and 50 p.e. [91]. In this subsection, both ends of the dynamic range are investigated. Paragraph 4.3.2.2.1 focuses on the capability of triggering on small signals with a mean charge of 0.2 p.e., while Paragraph 4.3.2.2.2 investigates from which charge on the AFE is saturated.

##### 4.3.2.2.1 Capability of triggering on 0.2 p.e.

It is required that the system PMT + microbase + AFE is able to trigger on pulses with a charge of 0.2 p.e. while at the same time, as little noise as possible is included. For simplification, the wording is trigger on 0.2 p.e. in the following, even though it is technically an amplitude trigger. Trigger on 0.2 p.e. means triggering on pulses with a mean charge of 0.2 p.e. The procedure described in the following was performed for each AFE channel separately. The basic measurement idea was to set the trigger threshold of the AFE channel to 0.2 p.e and record waveforms using this trigger threshold (selftrigger). As mentioned in Subsection 4.3.1, a PC was used to communicate with the mDOT. A threshold was set at the PC and the DAC adjusted the threshold to the discriminator of the channel (see Figure 2.6). The threshold had to be set in DAC counts while the recorded waveform was outputted in ADC counts. So the first step was to convert the adjusted trigger threshold from DAC counts into ADC counts.

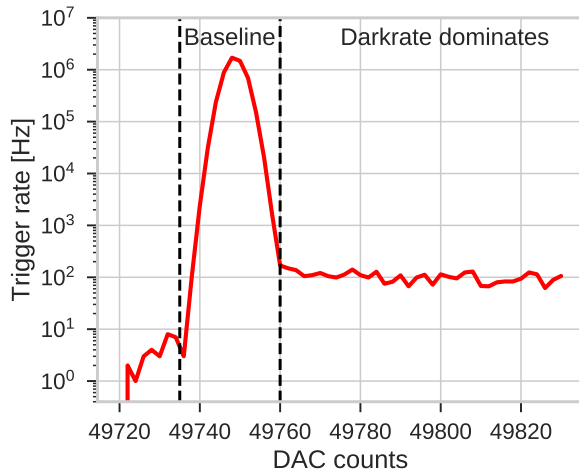


**Figure 4.3:** Typical threshold scan shown for channel 3 at +17°C.

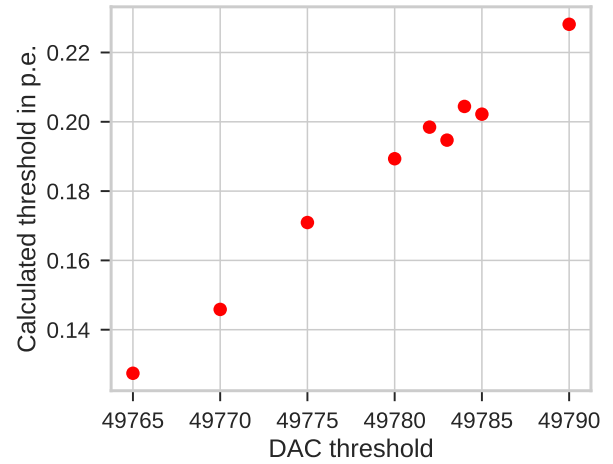


**Figure 4.4:** Calculated trigger threshold in p.e. versus adjusted trigger threshold in DAC counts shown for channel 3 at +17°C.

#### Determination of the trigger threshold in ADC counts

First, a threshold scan was performed to find the location of the baseline in DAC counts. The FPGA counts the threshold crossings within 1 s for different DAC thresholds and outputs the resulting trigger rate. Figure 4.3 shows an exemplary threshold scan for channel 3 at +17°C. Next, a threshold with few DAC counts above the baseline was adjusted, for example 49 780 DAC counts in case of Figure 4.3. After that, 20 000 waveforms were recorded for the channel using this threshold with selftrigger. For this measurement, no light source was needed and it was sufficient to use the PMT darkrate (selftrigger measurement in the dark). Figure 4.5 illustrates how the threshold in ADC counts was determined from the selftrigger measurement shown for channel 3 at +17°C. The first step was to determine the maximum of each waveform. This maximum has the unit ADC counts and is called amplitude. The left plot of Figure 4.5 shows a histogram of all these amplitudes. Basically, the left edge of the histogram is the trigger threshold in ADC counts. Only amplitudes close to the left cut were selected (middle plot in Figure 4.5) and an error function was fitted to the histogram of these selected amplitudes (right plot in Figure 4.5). The error function was used because the amplitude histogram is actually distributed according to a Gaussian function while the threshold cuts into the histogram as a Heaviside step function. The convolution of Gaussian and Heaviside step function results in an error function. One fit parameter is the x-value at half the height of the edge marked with a red point in the right plot of Figure 4.5. This fit value  $p1$  is considered as trigger threshold in ADC counts. This conversion of DAC into ADC thresholds was performed for several adjusted DAC thresholds.

#### Determination of the trigger threshold in p.e.

After the trigger threshold has been determined in ADC counts, it could be converted into units of p.e. Therefore, an additional measurement with a pulsed LED was needed. The same LED measurement and procedure used for the calculation of the SNR in Subsection 4.3.2.1 was taken. Figure 4.6 shows the different steps to determine the trigger threshold in p.e. shown for channel 3 at +17°C. The selftrigger measurement in the dark with a certain DAC threshold yields the

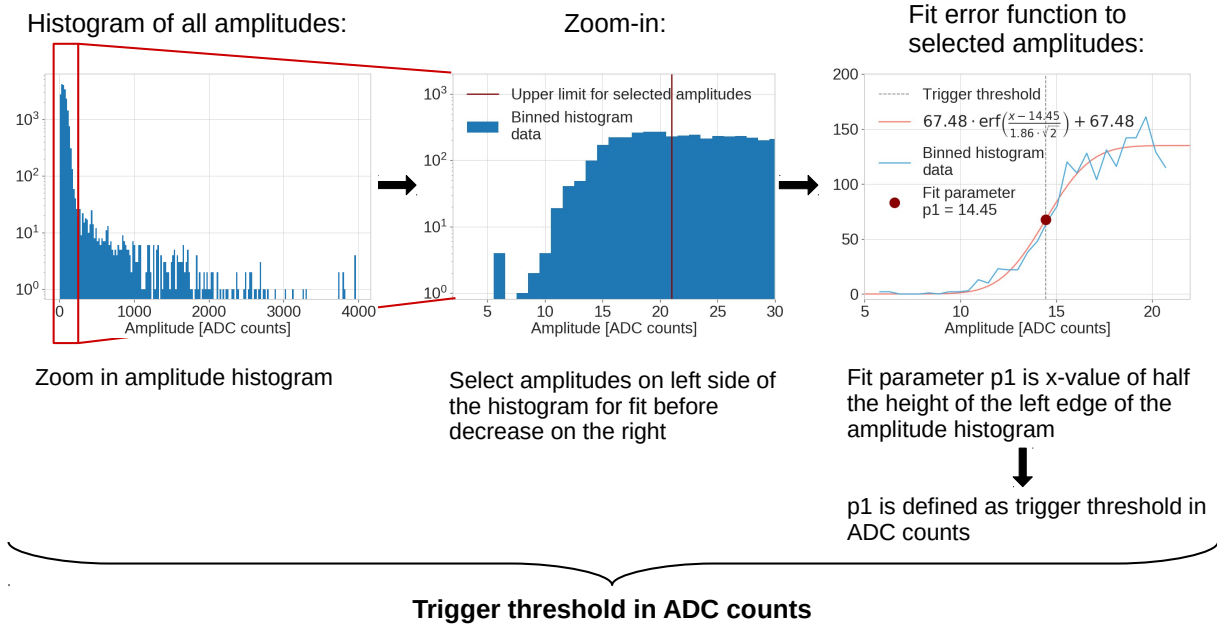


**Figure 4.5:** Illustration of the determination of the trigger threshold in ADC counts shown for channel 3 at +17°C.

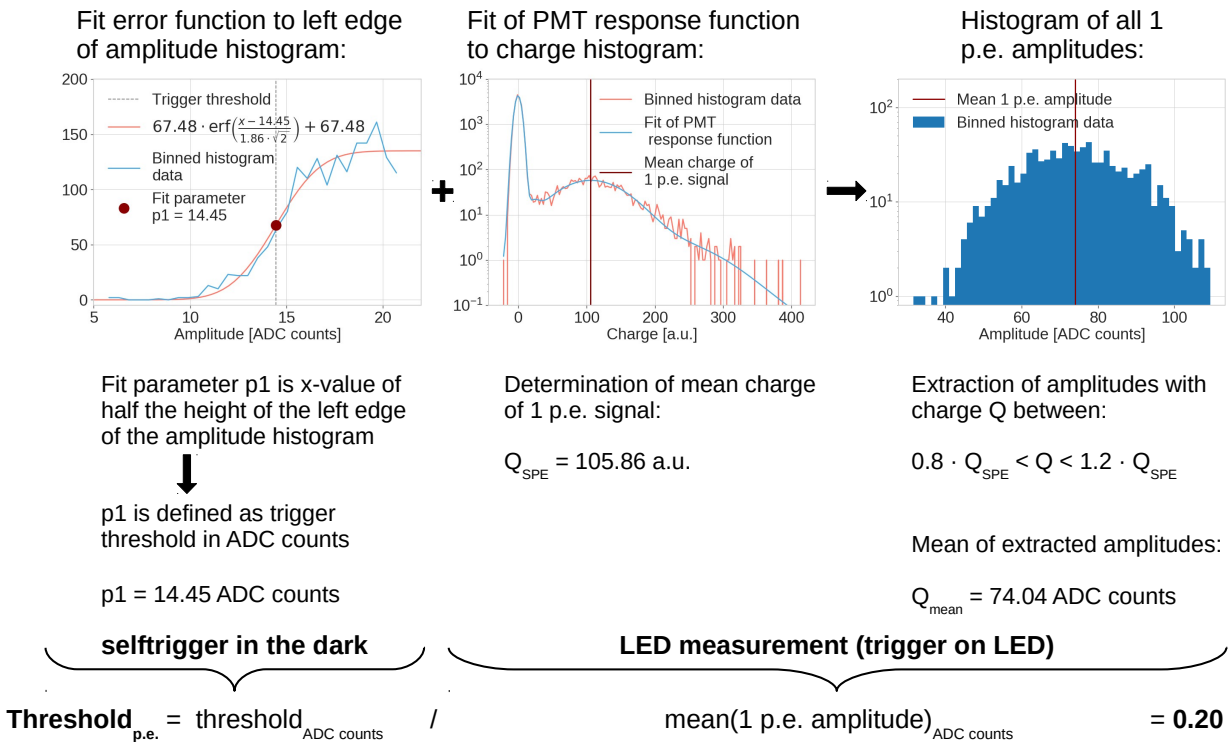


**Figure 4.6:** Illustration of the determination of the trigger threshold in p.e. shown for channel 3 at +17°C and a threshold of 0.2 p.e.

trigger threshold in ADC counts (left plot in Figure 4.6). From the LED measurement, the mean amplitude of a 1 p.e. signal in ADC counts can be extracted. The ratio of both parameters results in the trigger threshold in p.e.:

$$\text{Threshold}_{\text{p.e.}} = \frac{\text{threshold}_{\text{ADC counts}}}{\text{mean}(1 \text{ p.e. amplitude})_{\text{ADC counts}}} . \quad (4.2)$$

The conversion of all measured trigger thresholds in p.e. yields a correlation curve of the threshold in p.e. and the threshold in DAC counts. Figure 4.4 shows an exemplary correlation curve for channel 3 at  $+17^\circ\text{C}$ . The curve shows approximately the expected linear behavior (The fluctuations around 0.20 p.e. are less than 0.004 p.e. which is a sufficient precision.). This calculation of the threshold in p.e. is performed for all three channels at  $+17^\circ\text{C}$  and  $-42^\circ\text{C}$ . The datapoint closest to 0.2 p.e. is interpreted as selftrigger measurement at 0.2 p.e. yielding the DAC trigger threshold at 0.2 p.e.

These selftrigger measurements at 0.2 p.e. for each channel were used to investigate the capability of triggering on 0.2 p.e. Figure 4.7 shows the charge histograms in p.e. of the selftrigger measurements at 0.2 p.e. for all three channels at  $+17^\circ\text{C}$  and  $-42^\circ\text{C}$  in blue. In the background of each selftrigger measurement, the corresponding LED measurement with a measured mean charge of 0.1 p.e. from Subsection 4.3.2.1 is shown in red. To convert the calculated charge in a.u. into charge in p.e., all charge values were divided by  $Q_{\text{SPE}}$  which was already determined in Subsection 4.3.2.1. This conversion into p.e. allows a direct comparison of the histograms from the selftrigger measurements and the histograms from the LED measurements. Each LED measurement shows the position of the pedestal as well as the position of the 1 p.e. peak. The dashed black line indicates 0.2 p.e. Ideally, all histogram data of the selftrigger measurements in blue should have a charge larger than 0.2 p.e. and no noise should be included. However, all selftrigger histograms include some charges with  $Q < 0.2 \text{ p.e.}$ . As described in Figure 4.5, the left edge of the histogram of the amplitudes of the selftrigger measurements can be described by an error function. The x-value of half the height of the left edge of the histogram is defined as the threshold. So by definition, a small fraction of amplitudes falls below the threshold. Nevertheless, most data should lie above the threshold.

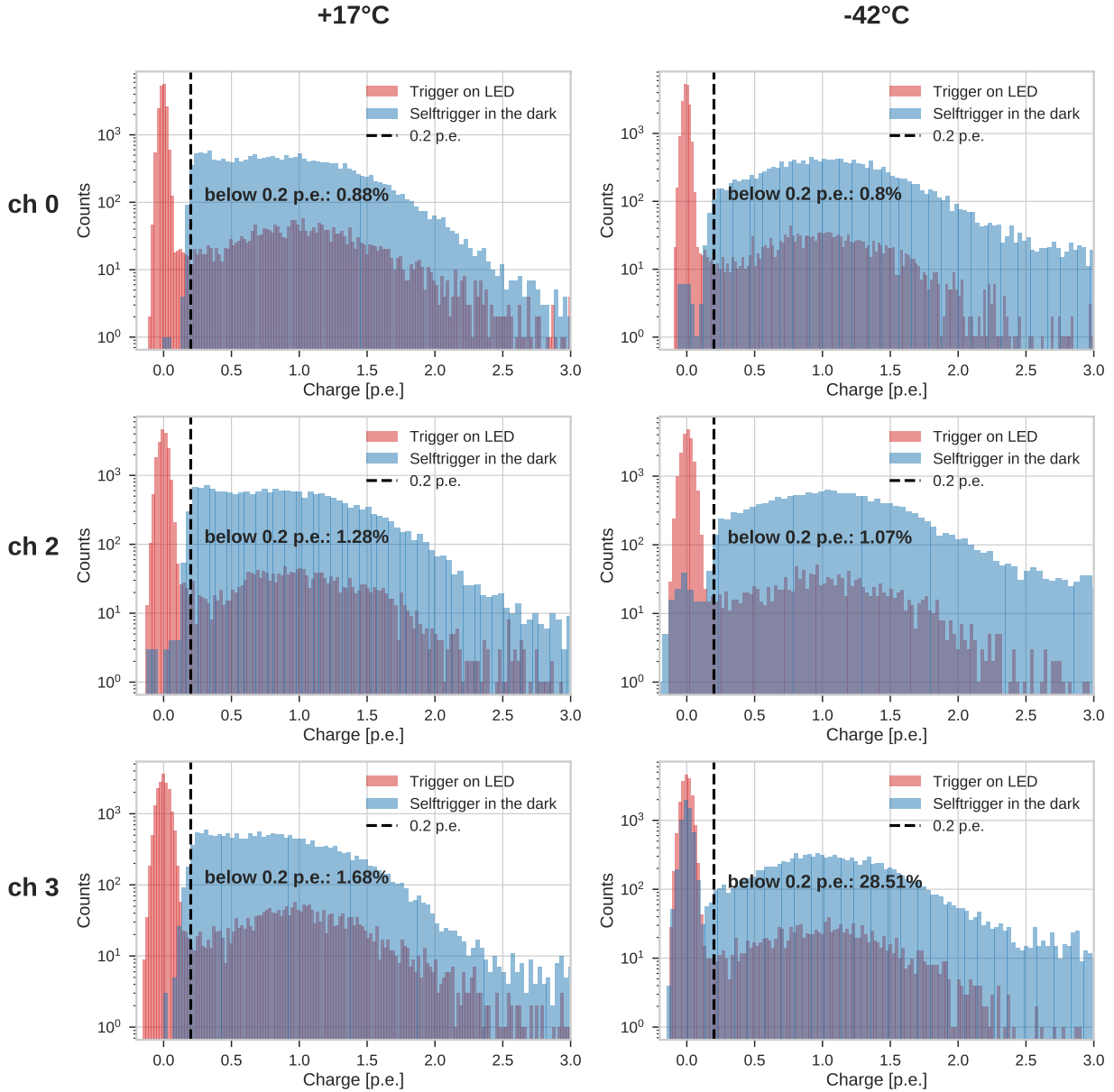


**Figure 4.7:** Comparison of the SPE spectra from measurements with trigger on LED and selftrigger measurements at 0.2 p.e. level in the dark at  $+17^{\circ}\text{C}$  and  $-42^{\circ}\text{C}$  for all three channels.

For channel 0, less than 1% of the triggered data have a charge smaller than 0.2 p.e. at both temperatures. Similarly, the fraction is about 1% for channel 2 at both temperatures. While channel 3 has a similar small fraction of 1.68% at  $+17^{\circ}\text{C}$ , about 29% of the triggered data have a charge smaller than 0.2 p.e. at  $-42^{\circ}\text{C}$ . A known problem were large bipolar signals induced by the freezer which have a small charge but a large amplitude. To verify large bipolar signals as reason for the large fraction of triggered pulses with a charge smaller than 0.2 p.e., the charges with  $Q < 0.2$  p.e. were investigated in a two-dimensional histogram. Figure 4.8 shows the baseline-subtracted amplitude in ADC counts versus the charge in p.e. The dark red dashed horizontal line

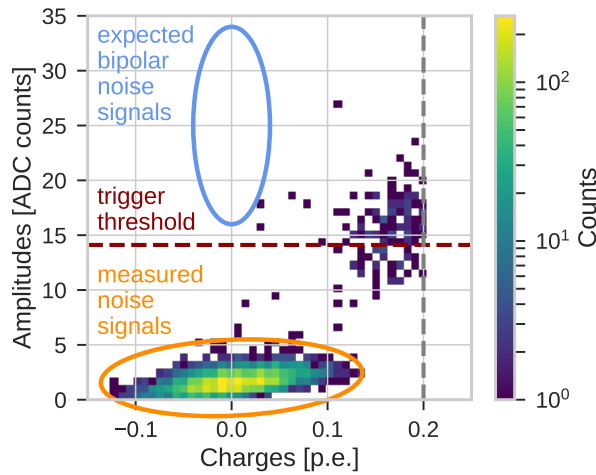


**Figure 4.8:** Two-dimensional histogram of amplitude in ADC counts versus charges in p.e. of the selftrigger measurement for channel 3 at  $-42^{\circ}\text{C}$ . Only charges with  $Q < 0.2$  p.e. are considered.

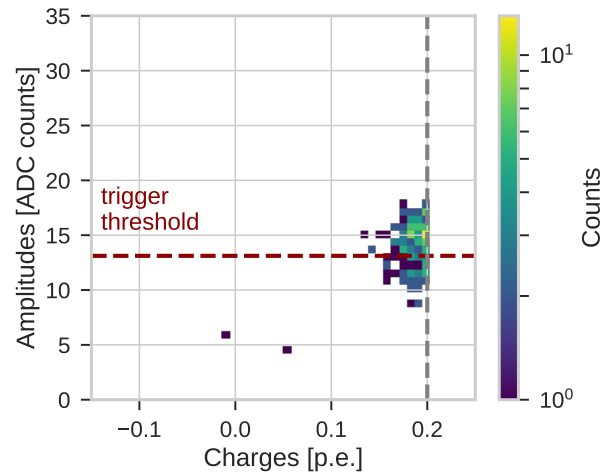


**Figure 4.9:** Typical two-dimensional histogram of amplitude in ADC counts versus charges in p.e. of the selftrigger measurement. Shown for channel 0 at  $17^{\circ}\text{C}$ . Only charges with  $Q < 0.2$  p.e. are considered.

indicates the used trigger threshold of this measurement. The gray dashed vertical line marks 0.2 p.e. Close to the intersection of both lines, a cluster of few datapoints is formed. These data are expected because the trigger operates as an error function and is not completely sharp. Large bipolar noise signals are expected within the blue circled area. These signals have a charge of almost 0 p.e., but an amplitude above the trigger threshold. However, no such data were observed and thus, could be excluded as origin of the large fraction of triggered pulses with a charge below 0.2 p.e. Instead, most measured data concentrate in a second cluster—circled in orange—having a charge of approximately 0 p.e. as well as an amplitude close to 0 ADC counts. Because the amplitude of these triggered signals is significantly lower than the trigger threshold, the discriminator should not trigger on such waveforms at all. In contrast to that, Figure 4.9 shows the expected distribution of the same parameters for channel 0 at  $17^{\circ}\text{C}$ . The first cluster close to the trigger threshold is also visible, but the second cluster is missing. A closer investigation of the waveforms from the second cluster—circled in orange in Figure 4.8—reveals that the waveforms consist of electronic noise. A wrongly adjusted trigger threshold within the electronic noise would lead to a trigger of only noise-related waveforms and a temporary change of the baseline could also be excluded. Finally, the discriminator circuit of channel 3 could be identified as the reason of the problem. All three channels use the same comparator type ADCMP600 [96] for the discriminator, but for channel 3, the comparator is connected in a different way so that also PMT signals at the lower end of the investigated spectrum trigger the discriminator. In the normal case, the comparator toggles to 1 and the ADC signal is read out by the FPGA when the discriminator is triggered. Afterwards, the comparator changes back to 0. For channel 3, however, the comparator does not change back to 0. Thus, the FPGA records data again after a certain dead time. Mostly, these data consist of electronic noise. This issue is shown in Figure 4.10 for two succeeding trigger events. Only after another signal crosses the threshold, the comparator of channel 3 changes back to 0. This circuit characteristic of channel 3 leads to 29 % of triggered electronic noise signals at  $-42^{\circ}\text{C}$ . Such a high

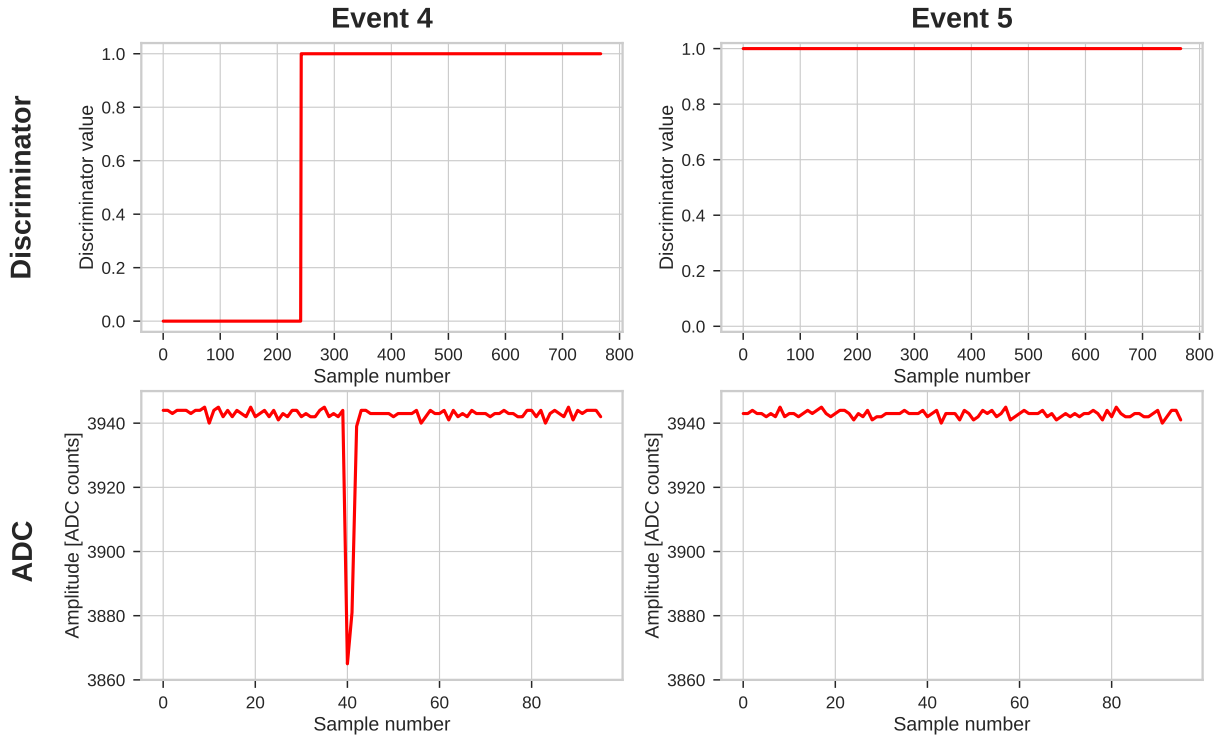


**Figure 4.10:** Exemplary waveforms of discriminator and ADC for two succeeding events. The discriminator toggles to 1 for a normal PMT signal (left) and stays at 1 afterwards. For the succeeding event (right), the discriminator is still at 1 and the ADC waveform contains only electronic noise.

trigger fraction on noise is not compatible with the analog signal electronic noise requirement<sup>1</sup>. To sum up, triggering on 0.2 p.e. works for all three channels at both  $+17^{\circ}\text{C}$  and  $-42^{\circ}\text{C}$  except for about 29 % of the waveforms of channel 3 at  $-42^{\circ}\text{C}$ .

#### 4.3.2.2.2 Capability of recording large pulses

The second part of the dynamic range requirement is the capability of recording pulses up to 50 p.e. without saturating. This upper limit of the dynamic range originates from simulations performed by the IceCube collaboration [91]. Because the dynamic range of PMT and microbase extends to about 500 p.e. (investigated in Subsection 4.3.2.3), the entire system PMT + microbase + AFE could be used to investigate the saturation behavior of the AFE. It is expected that the AFE saturates earlier than PMT and microbase. A 12-bit ADC is used to digitize the AFE signal, so that in total, 4096 ADC counts are available for a corresponding voltage of 2 V. To maximize the usable output range of the ADC and avoid artificial saturation (left plot in Figure 4.11), the baseline of the ADC output is shifted towards its upper edge (right plot in Figure 4.11). This baseline shift is achieved by adjusting the DAC parameters accordingly.

Figure 4.12 shows the setup used to investigate the saturation behavior of the AFE. As described in Figure 4.1, PMTs, AFE, and mDOT were in a darkbox which was put into a freezer. For simplification, darkbox and freezer are excluded in Figure 4.12. In principle, the same setup

<sup>1</sup> “Triggers due to any electronic noise ((non-Gaussian) noise floor + periodic, spiky noise) shall be not more than  $5\sigma$  fluctuations.” [70]

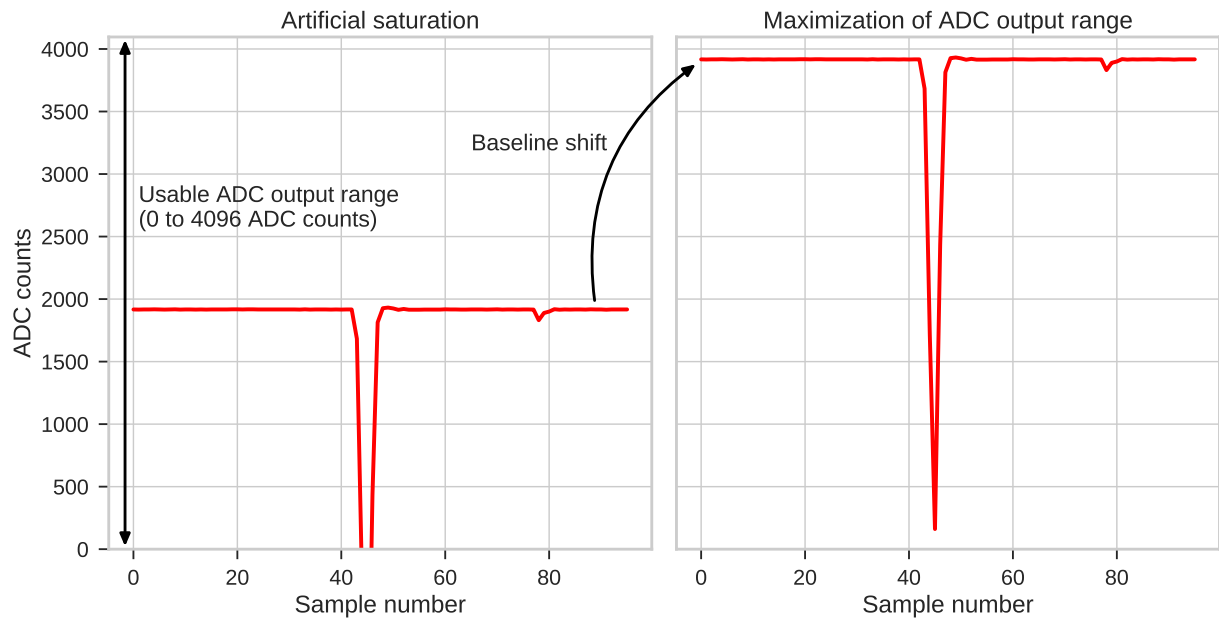
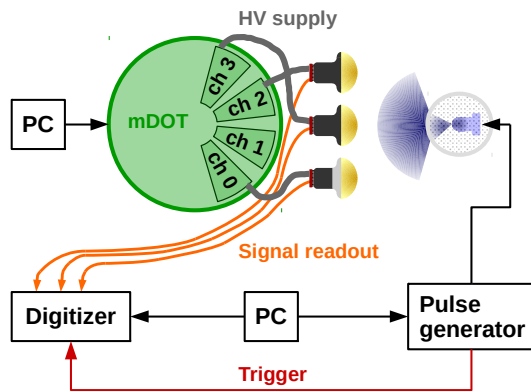


**Figure 4.11:** Illustration of the maximization of the ADC output range by shifting the baseline to the upper edge in case of negative signals (right plot) to avoid artificial saturation (left plot).

#### Measurement 1:

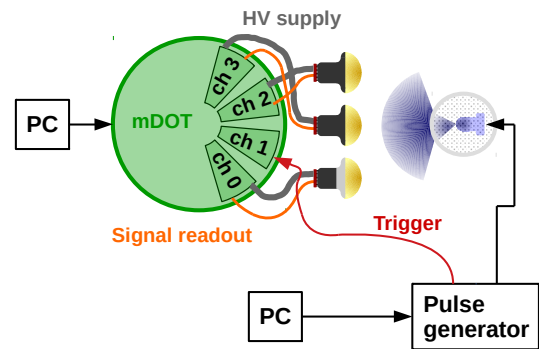
PMT signal output connected to digitizer



- Calibration of LED
- Measurement with different supply voltages of LED
- Determination of respective charge in p.e.

#### Measurement 2:

PMT signal output connected to respective mDOT channel



- Measurement with the same LED supply voltages as for measurement 1
- Determination of respective charge for each mDOT channel in a.u.

mDOT charge in a.u. versus input charge in p.e.

**Figure 4.12:** Illustration of the used setup and measurement procedure to investigate the AFE response to large input signals.

as described in Figure 4.1 was used. However, two measurements were needed. With a reference measurement (measurement 1), the LED was calibrated. The PMTs were powered by the AFE channels of the mDOT which was controlled by a PC, but the PMT output was connected to the calibrated digitizer used in Subsection 4.3.1. The digitizer was triggered by the pulse generator which also drove the pulsed LED. When the digitizer was triggered, all four channels of the digitizer were read out and the data were saved. Both digitizer and pulse generator were controlled by a PC. Different supply voltages of the LED were adjusted and a measurement with trigger on the pulse generator was performed for each LED voltage. By summing up the voltage values inside the signal window of each waveform according to Equation 3.2, the charge of each waveform was calculated. Afterwards, the mean charge was determined for each LED voltage out of 20 000 waveforms. With the nominal PMT gain  $G_{\text{nom}}$ , the number of photoelectrons can be calculated as:

$$\text{p.e.} = \frac{\text{charge}}{e \cdot G_{\text{nom}}} . \quad (4.3)$$

Using Equation 4.3, the charge was converted into units of p.e. This charge is referred to as input charge. These LED calibration measurements were performed in the course of the PMT and microbase calibration described in Subsection 4.3.1. Afterwards, the freezer was warmed up and the PMT outputs were connected to their respective AFE channel (measurement 2) while channel 1 was connected to the pulse generator. After that, the freezer was cooled down to the same temperature as before. For each signal generated by the pulse generator, channel 1 was triggered and all four channels of the AFE were read out and the data were saved. The same LED voltages as for measurement 1 were adjusted and a measurement performed. For each adjusted LED voltage, the mean charge in a.u. of each AFE channel was determined out of 20 000 waveforms. This charge is called mDOT charge. Combining both measurements results in a correlation of mDOT charge in a.u. and input charge in p.e. Both measurements were performed at  $+17^\circ\text{C}$  and at  $-42^\circ\text{C}$  <sup>2</sup>.

In Figure 4.13, the mDOT charge in a.u. is shown versus the input charge in p.e. for all three channels at  $+17^\circ\text{C}$  and at  $-42^\circ\text{C}$ . The gray shaded area indicates the required dynamic range from 0.2 p.e. up to 50 p.e. Saturation would be expressed by flattening of the linear curves in Figure 4.13, which is at the beginning barely visible for the charge values but can be seen in the amplitude histograms. Figure 4.14 exemplarily shows an amplitude histogram where saturation is visible as a cut at the right of the histogram. For most channels, the saturation starts beyond 70 p.e. Only channel 0 at  $+17^\circ\text{C}$  is already saturated at about 48 p.e. which can be explained by the large amplification factor of channel 0 compared to the other AFE channels. Saturation means that the ADC output signal exceeds the available 4096 ADC counts. To sum up, all channels except channel 0 at  $+17^\circ\text{C}$  are capable of recording PMT signals up to 50 p.e.

<sup>2</sup>However, this method to determine the input charge yields large systematic errors. This issue will be discussed in Subsection 4.3.4.1 in more detail and might be the reason for the nonlinear behavior in Figure 4.26. An improved method will be introduced in Paragraph 4.4.3.2.2.

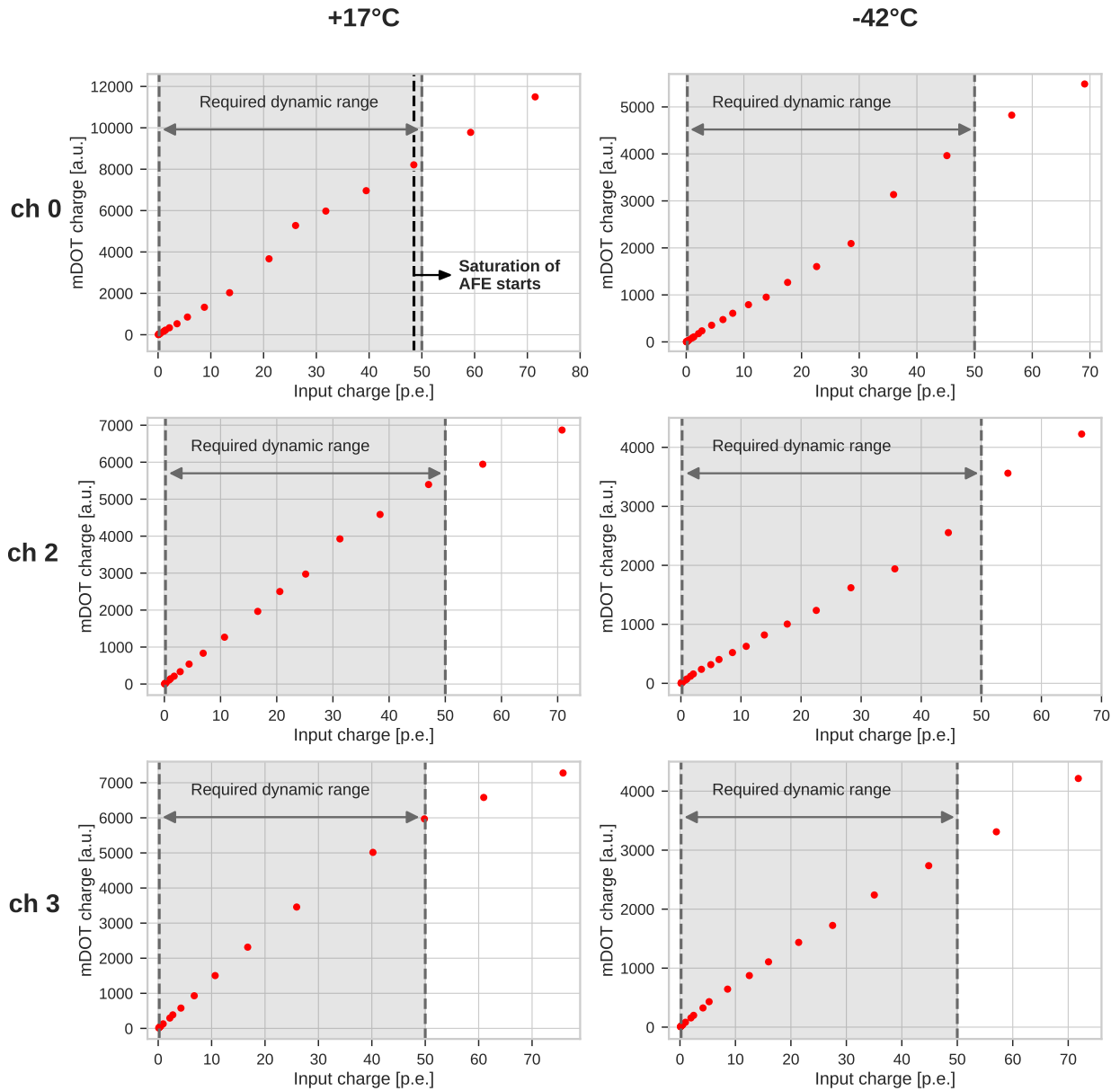


**Figure 4.13:** Dynamic range measurements focusing on large pulses for all channels at +17°C and at -42°C.

#### 4.3.2.3 Linearity

To calibrate the charge calculation for each PMT in the mDOM, the AFE is required to behave linearly. In fact, the entire system PMT + microbase + AFE should behave linearly. To exclude a possible impact of PMT and microbase during the AFE linearity measurements, the behavior of PMT and microbase was investigated separately at first. For the PMTs, the following is required: “The amplitude of the anode signal shall be linear to the number of photoelectrons

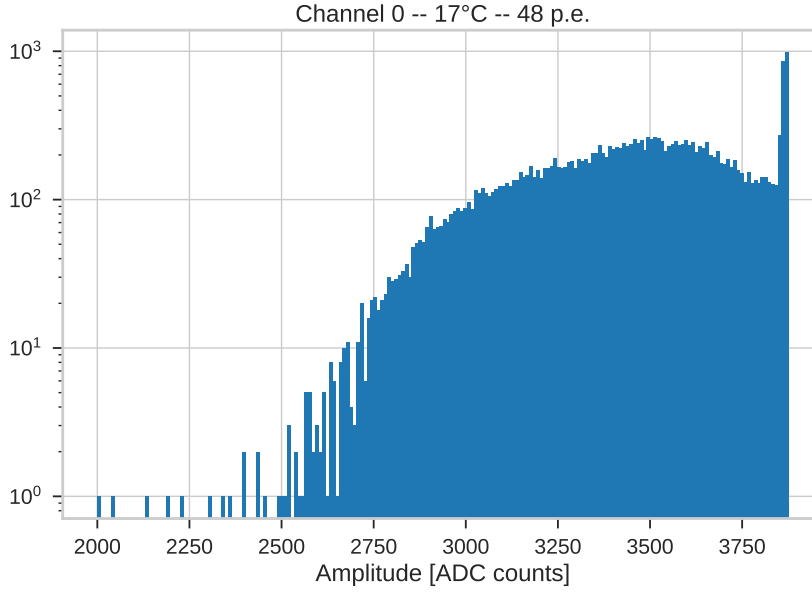


**Figure 4.14:** Amplitude histogram exemplarily shown for channel 0 at +17°C and a mean charge of 48 p.e. Saturation of the channel is expressed by the cut at the right of the histogram.

(10 ns pulse width) within 10 % up to 100 photoelectrons.” [68]. Two configurations were studied: PMT + passive base and PMT + microbase.

Figure 4.15 shows the block diagram of the setup used for these linearity measurements. For reference, a photodiode [98] connected to a power supply and read out by a picoamperemeter is used. The photodiode can be placed at the same position as the PMT. In case the PMT is connected to a passive base, the PMT is powered by an HV supply. When connected to the microbase, a 5 V power supply is sufficient. A pulse generator [99] triggers a laser driver [100] which shortens the pulse signal to less than 1 ns. The output is fed into a 375 nm laser diode head (LDH-P-C-375 [101]). To vary the light intensity, the laser beam is directed to a continuous neutral density filter wheel [102]. A step motor controlled by a PC rotates the filter wheel in different positions. Each position results in a different transparency of the filter wheel. The attenuated laser beam is directed to a diffusor ensuring a homogeneous illumination of the entire PMT photocathode or the photodiode, respectively. The oscilloscope [79] is triggered by the pulse generator simultaneously to the laser driver so that the data are saved to a hard drive only when a laser pulse arrived at the PMT. In contrast to that, the photodiode is read out continually.

At first, the filter wheel was calibrated. Therefore, a fixed laser output was adjusted and the intensity of different filter wheel positions were measured with the photodiode. Afterwards, the PMT was calibrated by using the same filter wheel positions, but at reduced laser intensity to compensate the different light sensitivities of PMT and photodiode. This measurement procedure was performed for a PMT of the type R15458-02 with a passive base and a PMT of the type R15458-20 with a soldered microbase, where both PMT types are from Hamamatsu Photonics K.K. All measurements were performed at room temperature. For each filter wheel position, the mean photocurrent of the photodiode and the mean charge as well as the mean amplitude of the PMT were determined. Both PMT amplitude and PMT charge were—at least in a certain range—linear

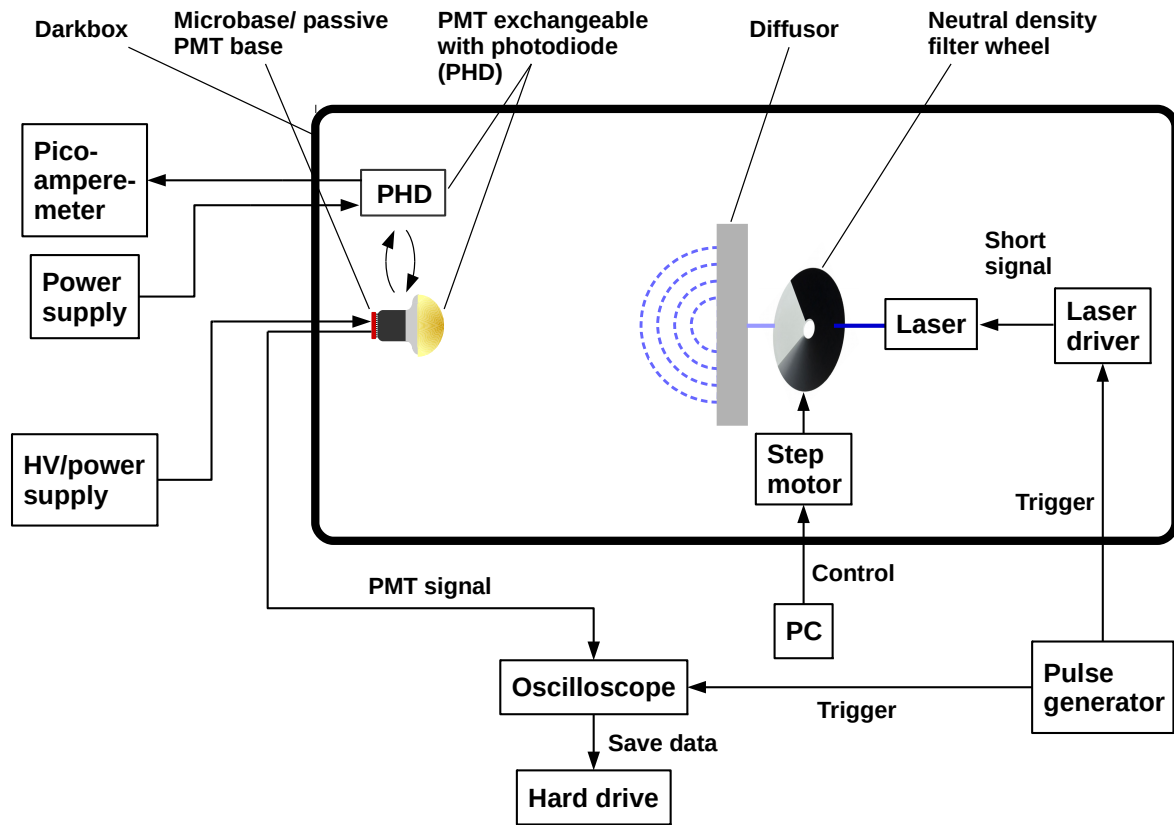


**Figure 4.15:** Block diagram of the setup used for the linearity measurements of PMT + passive base and PMT + microbase. Photodiode and PMT are exchangeable. Picture of filter wheel modified from [97].

to the photocurrent of the photodiode for both PMT types. Thus, PMT amplitude and PMT charge should have a linear dependence to each other.

In Figure 4.16, the linearity behavior of PMT BA0796 connected to a passive base is shown. The last three datapoints were excluded from the linear fit. The green shaded area indicates the region of  $\pm 10\%$  of the fit in which linearity is required. The PMT + passive base behaves linearly until saturation starts at approximately 550 p.e. Figure 4.17 shows the linearity behavior of PMT DM00471 with a microbase. The system PMT + microbase behaves linearly up to approximately 500 p.e. Both linearity measurements start at about 10 p.e. To sum up, both PMT and microbase are capable of recording charges up to approximately 500 p.e. without significant saturation.

For the AFE, linearity is required up to 50 p.e.: “The amplitude of the mean output signal of the system shall be proportional within 10 % to the amplitude of the input signal up to an input signal charge of 50 p.e.” [70]. To investigate the AFE linearity, real PMT pulses from the system PMT + microbase were used. The linearity data were extracted from the same measurements as the dynamic range described in Paragraph 4.3.2.2.2 and Figure 4.12<sup>3</sup>. In contrast to the dynamic range measurements, where the charge was the investigated parameter, for the linearity, the amplitude is relevant. Figure 4.18 illustrates how the relevant parameters were extracted from the linearity

<sup>3</sup>However, this method to determine the input charge yields large systematic errors. This issue will be discussed in Subsection 4.3.4.1 in more detail and might be the reason for the nonlinear behavior in Figure 4.19. An improved method will be introduced in Paragraph 4.4.3.2.2.

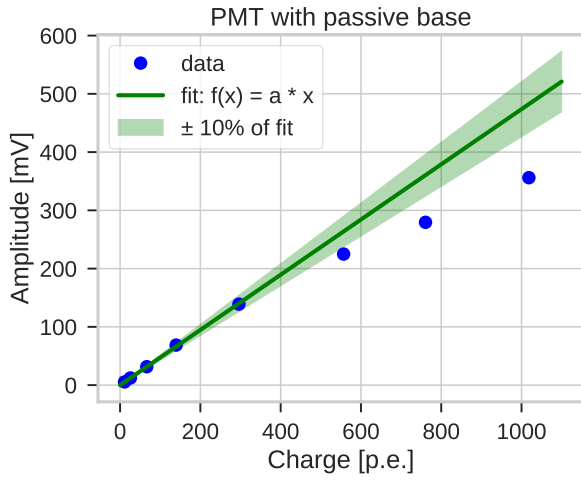


**Figure 4.16:** Linearity of amplitude versus charge for the PMT BA0796 of the PMT type R15458-02 from Hamamatsu Photonics K.K. The measurement was performed with a passive base. The last three datapoints were excluded from the fit. Saturation starts at approximately 550 p.e.

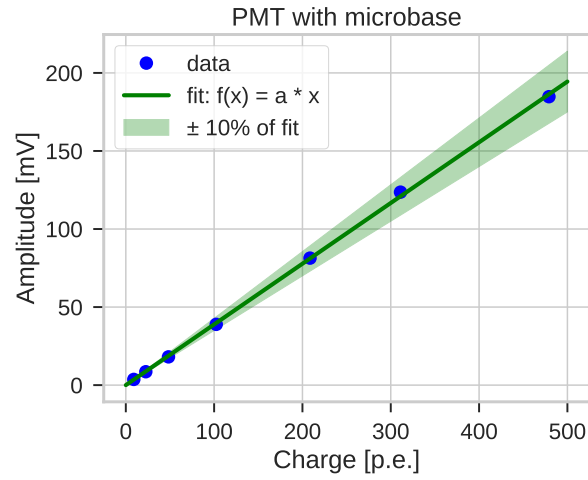
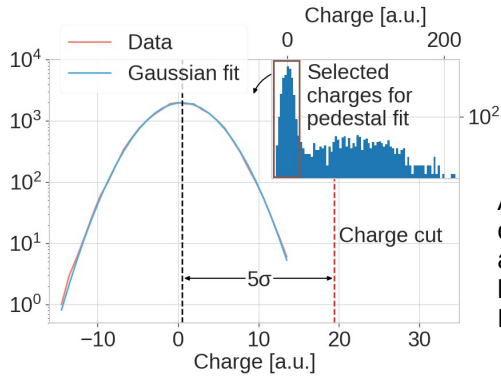


**Figure 4.17:** Linearity of amplitude versus charge for the PMT DM00471 of the PMT type R15458-20 from Hamamatsu Photonics K.K. The measurement was performed with a microbase. Linearity is given up to approximately 500 p.e.

Charge histogram for lowest light intensity:

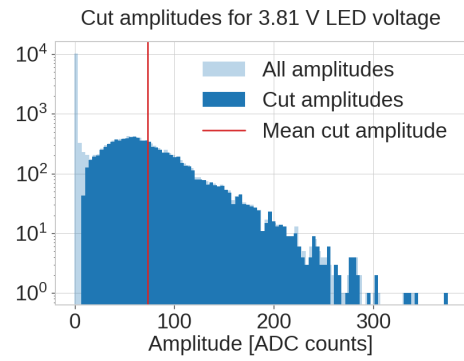


- Selection of pedestal charges
- Gaussian fit to pedestal charges
- Determination of charge cut:

$$\text{charge cut} = \text{mean} + 5\sigma$$

Application of charge limit to amplitude histograms of all LED voltages

For each LED voltage:



- For waveforms with charge > charge cut:
- Determination of the amplitude = cut amplitude
- Histogram of cut amplitudes
- Mean of cut amplitudes = mean cut amplitude

**= Output amplitude (for mDOT) or Input amplitude (for digitizer)**

**Figure 4.18:** Illustration of the determination of input and output amplitude for the AFE linearity investigations. Exemplarily shown for channel 2 at  $-42^{\circ}\text{C}$ .

measurements. For each measured LED voltage, the following procedure was performed for the measurements with the digitizer as well as for the measurements with the mDOT. First, a Gaussian was fitted to the pedestal of the charge histogram from the measurement with the lowest LED voltage, because the pedestal did not shift and the fit could be performed best for the lowest light intensity. The mean of the Gaussian plus  $5\sigma$  was determined as charge cut which was applied to all LED voltages. Only waveforms with a charge larger than this charge cut were considered for the analysis. For the waveforms surviving the charge cut, the amplitude (cut amplitude) was determined. Afterwards, the mean cut amplitude was calculated. The mean cut amplitude measured by the digitizer is called input amplitude and the mean cut amplitude measured by the mDOT channel is called output amplitude. For the digitizer measurements, the charge cut was also applied to the charges to obtain the corresponding mean charge to the respective input amplitude. Due to the pedestal cut, the smallest measured charge is 1 p.e. This procedure was performed for all three channels at  $+17^\circ\text{C}$  and at  $-42^\circ\text{C}$ .

Figure 4.19 shows the results of the AFE linearity measurements. The gray shaded area describes the fit range. Only datapoints at the lower end of the investigated charge range were included in the linear fit. The green shaded area indicates  $\pm 10\%$  of the fit in which linearity is required. The left dashed black lines describes the limit up to which linearity was measured. The right dashed black lines is the amplitude corresponding to 50 p.e. which is the upper end of the linearity requirement. No AFE channel is linear up to 50 p.e. For  $+17^\circ\text{C}$ , channel 0 is linear up to 14 p.e. and for  $-42^\circ\text{C}$ , it is linear up to 29 p.e. Channel 2 is linear up to 21 p.e. at  $+17^\circ\text{C}$  and up to 28 p.e. at  $-42^\circ\text{C}$ . For channel 3, linearity is given up to 17 p.e. at  $+17^\circ\text{C}$  and up to 21 p.e. at  $-42^\circ\text{C}$ . However, later measurements revealed that the input amplitude and charge were not calculated properly. This problem will be discussed in Subsection 4.3.4.1. A mismatch in the charge calibration could also explain the linearity to seemingly higher p.e. numbers for the measurements at  $-42^\circ\text{C}$ . All in all, none of the mDOT channels fulfills the linearity requirement at first view.

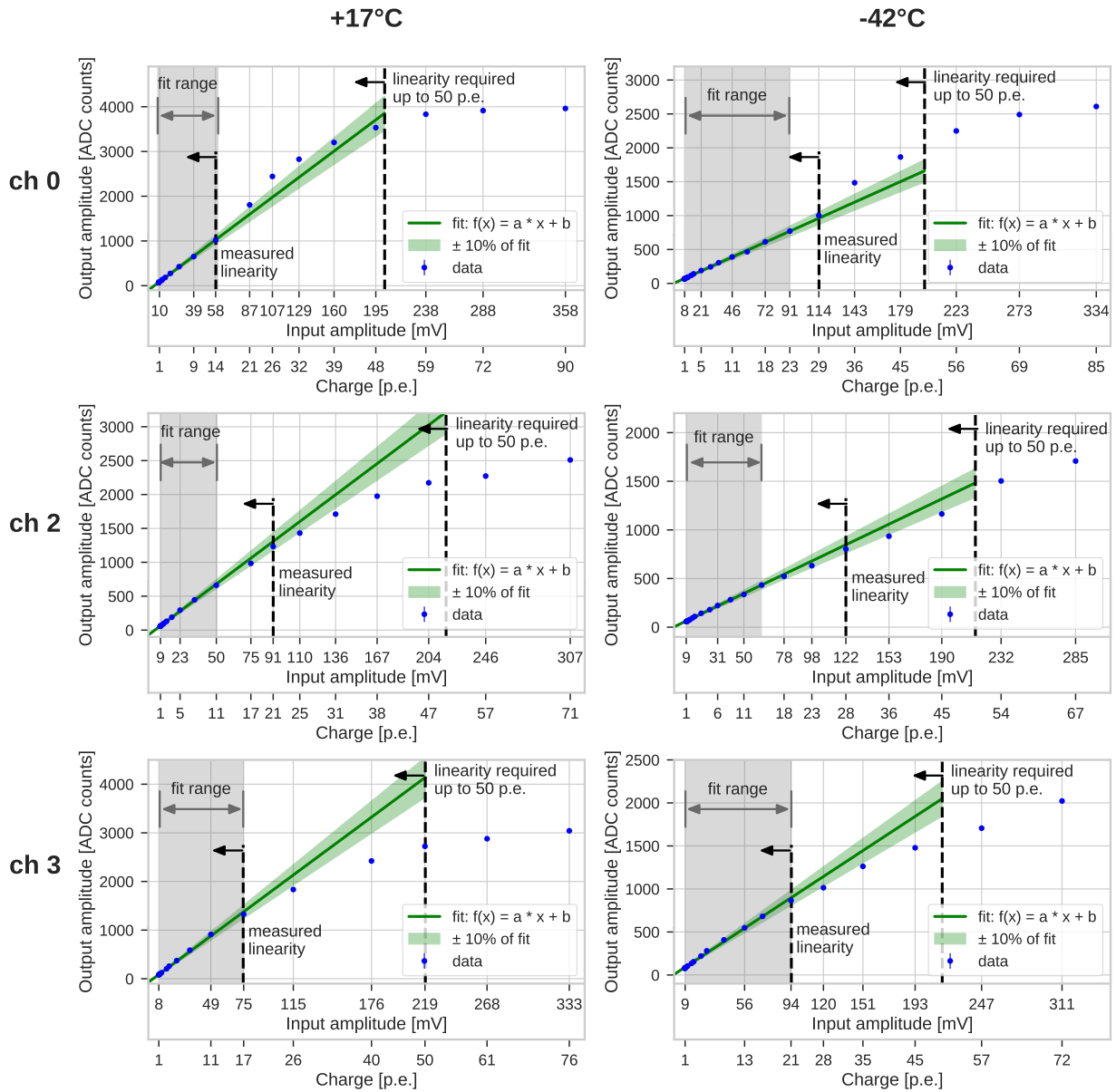


**Figure 4.19:** Linearity measurements for all three channels at +17°C and at -42°C.

### 4.3.3 Comparison of channel characteristics

Three different AFE channel designs have been investigated at +17°C and at -42°C. The investigated parameters were SNR, the lower as well as the upper end of the required dynamic range, and the linearity. Table 4.3 gives an overview of the results. The cellcolor indicates whether the requirement is fulfilled or not. Green signifies fulfilled, red failed, and yellow indicates a problem which is no direct fail of the requirement or a marginal fail. All three channels fulfill the SNR requirement at both temperatures. Thereby, channel 0 has the largest SNR of all channels. In principle, all channels are capable of triggering on 0.2 p.e. pulses, but during the measurement, a problem was found for channel 3 at -42°C. Due to the different discriminator circuit of channel 3,

29 % of the triggered pulses are only electronic noise. All channels are capable of recording signals up to more than 50 p.e. except channel 0 at  $+17^\circ\text{C}$  which saturates at 48 p.e. In contrast, no channel fulfills the linearity requirement.

**Table 4.3:** Comparison of the measured characteristics for all three channels at  $+17^\circ\text{C}$  and  $-42^\circ\text{C}$ . For channel 3 at  $-42^\circ\text{C}$ , the triggering on 0.2 p.e. is basically fulfilled, but a problem with noise was discovered during the measurements.\*

Temperature	Characteristic	channel 0	channel 2	channel 3	Requirement
$+17^\circ\text{C}$	Signal-to-noise ratio	109.66	77.04	52.46	$> 25$
	Dynamic range	$\geq 0.2$ p.e.	$\geq 0.2$ p.e.	$\geq 0.2$ p.e.	Trigger on 0.2 p.e.
		$< 48$ p.e.	$> 71$ p.e.	$> 76$ p.e.	Up to 50 p.e.
	Linearity	$\leq 14$ p.e.	$\leq 21$ p.e.	$\leq 17$ p.e.	Up to 50 p.e.
$-42^\circ\text{C}$	Signal-to-noise ratio	114.88	66.83	67.39	$> 25$
	Dynamic range	$\geq 0.2$ p.e.	$\geq 0.2$ p.e.	$\geq 0.2$ p.e.*	Trigger on 0.2 p.e.
		$> 85$ p.e.	$> 67$ p.e.	$> 72$ p.e.	Up to 50 p.e.
	Linearity	$\leq 29$ p.e.	$\leq 28$ p.e.	$\leq 21$ p.e.	Up to 50 p.e.

Due to the high trigger rate of channel 3 on electronic noise at  $-42^\circ\text{C}$  (see Figure 4.7), channel 3 is not well suited for the mDOM application. Furthermore, channel 3 has the highest mean baseline RMS or baseline fluctuation, respectively. Because channel 0 and channel 2 have a similar circuit and differ only by the signal amplification factor, it was decided to use channel 0 with the higher SNR as baseline channel for the mDOM.

#### 4.3.4 Problems

During the measurements with the setup and procedure described in Figures 4.1 and 4.12, two problems were discovered. The following subsections explain the issues in more detail.

##### 4.3.4.1 Mismatch in charge calibration

For the dynamic range and linearity measurements (see Figure 4.12), the LED was first calibrated with a digitizer (digitizer measurement). After that, the freezer was warmed up to room temperature

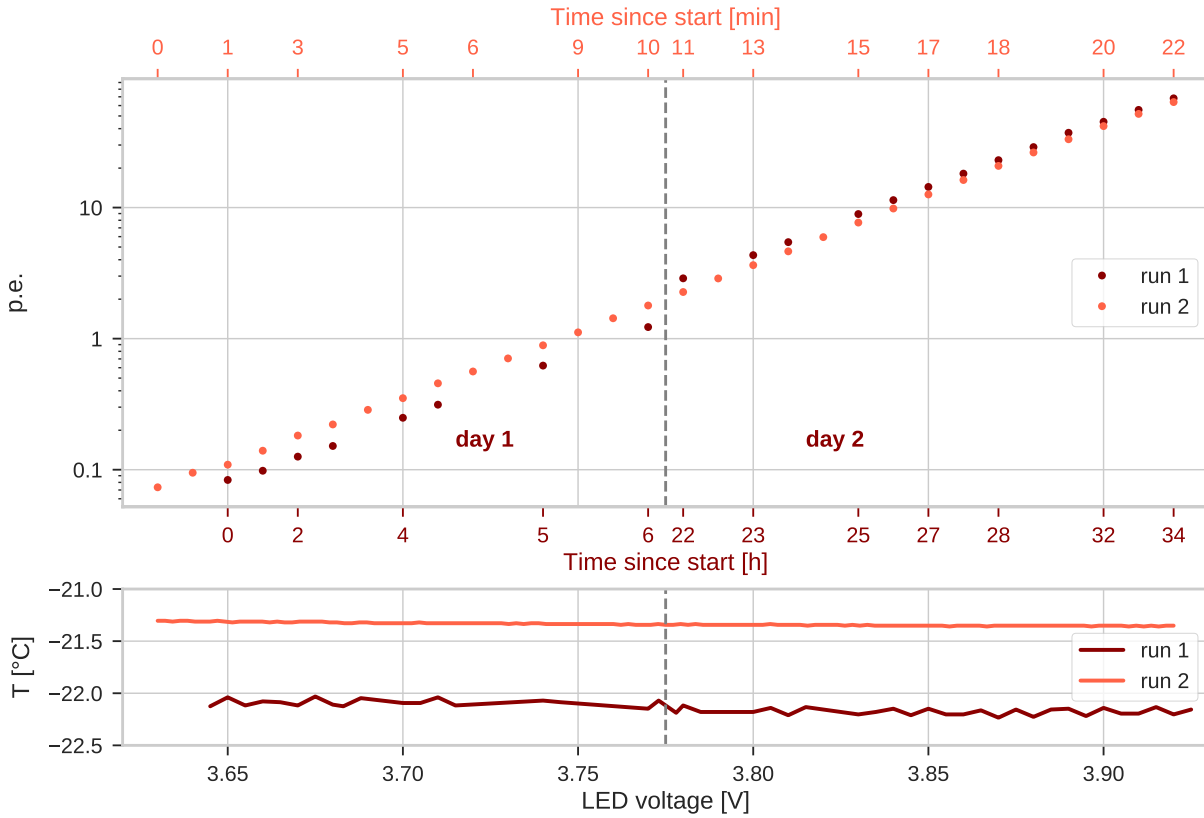


**Figure 4.20:** Comparison of two measurement runs of the mean p.e. number of the PMT versus the LED voltage. Run 1 was performed within two days with a total measurement time of 34 h whereas run 2 was performed during 22 min at one day. The LED output seems to vary with temperature and time. The measurements were made with channel 3 at approximately  $-20^{\circ}\text{C}$ .

and the PMT signal cables were reconnected to the mDOT AFE circuits. Afterwards, the freezer was cooled down again to the same temperature as for the digitizer measurement and the measurement was repeated for the same LED voltages, but the signal was read out by the AFE channels instead (mDOT measurement). However, this LED calibration method does not work properly. The two measurements with digitizer and mDOT are several days apart. In addition to that, the mDOT measurements themselves had to be extended over few days because of the low data transfer rate of the mDOT. During this time, the LED supply voltage necessary to obtain a certain p.e. number changes even when no temperature change was observed. This issue is shown in Figure 4.20. The upper plot shows the measured p.e. number versus the adjusted LED voltage for two measurement runs with the digitizer. The lower x-axis in dark red shows the time since the first measurement (run 1) has been started. The upper x-axis in bright red refers to the time since the second measurement has been started (run 2). Run 1 imitates the low data transfer rate of an mDOT measurement. For this reason, not all LED voltages were measured. Run 2 was performed with the normal data transfer rate of the digitizer. Run 1 extended over two days while run 2 was completed within about 20 min. In the lower plot, the temperature measured by the temperature sensor on the mDOT (see Figure 4.1) during the two measurement runs is shown. For run 2, the temperature was monitored continually during the measurement. In case of run 1, only one

temperature datapoint was taken before, after, and in the middle of one LED voltage measurement because an mDOT channel was read out at the same time and simultaneous channel read-out and temperature monitoring is not possible for the mDOT. The temperature difference of about 0.8 K between the two runs results in a different measured p.e. number for the same LED supply voltage which could be expected. Because the measured charge depends exponentially on the adjusted LED supply voltage and the y-axis is plotted logarithmically, a linear curve is expected such as visible for run 2. Almost no temperature change is visible between day 1 and day 2 for run 1. Nevertheless, a significant increase of the measured p.e. number is visible in the curve of run 1 between the two days. This behavior indicates that the LED output is not only highly temperature dependent, but the LED output also seems to vary over time. So two measurements performed at two days even at exactly the same temperature could yield different p.e. numbers for the same LED supply voltage.

As a result, the p.e. number determined for the dynamic range (Figure 4.13) and linearity measurements (Figure 4.19) yield large systematic errors (estimated charge offset can be more than 20 p.e.). This mismatch in the charge calibration could explain the large differences in the measured mDOT charge for the same p.e. number at  $+17^\circ\text{C}$  and at  $-42^\circ\text{C}$  in Figure 4.13. At  $-42^\circ\text{C}$ , the measured mDOT charge is about half the charge compared to the measurements at  $+17^\circ\text{C}$  for all three channels. A small difference might be expected because most electronic components are temperature dependent. However, such a large deviation should not occur. In addition to that, the measurements with the mDOT channels have been spread over more than one day. The measurements at different days might be the reason for the steps and the nonlinear behavior during one temperature measurement shown in Figure 4.19.

To conclude, the LED was not properly calibrated for the dynamic range and linearity measurements. For the following measurements, a different LED calibration method will be used which will be described in Subsection 4.4.1.

#### 4.3.4.2 Deformation of charge histograms

The second problem is an observed deformation of the charge distributions for the mDOT measurements. This deformation occurs with increasing light intensity for all three AFE channels at both temperatures. An example of the deformation behavior is shown in Figure 4.21 for channel 0 at  $17^\circ\text{C}$ . For different mean p.e. numbers, the measured charge histograms of digitizer and mDOT are compared. Because the digitizer is calibrated and outputs a voltage, the mean charge can be calculated using Equation 4.3. In case of the mDOT, the measured charge in a.u. was divided by the mean charge of  $Q_{\text{SPE}}$  which was determined in the SNR measurements in a.u. (Figure 4.2). As a consequence, the mean charge values differ from the mean charge shown in Figure 4.13 for the same dataset (for example 72 p.e. for channel 0 at  $17^\circ\text{C}$  instead of 48 p.e.). For all digitizer and mDOT measurements, the charge histograms were determined from 20 000 waveforms each. To compare the histogram shapes, a digitizer histogram with a similar charge was assigned to each mDOT histogram (the mean charge of digitizer histogram and mDOT histogram differ by few p.e. because the environmental conditions changed; this mismatch leads to a shift of the histograms). The digitizer histograms are red and the mDOT histograms are blue. The digitizer histograms look as expected. With increasing light intensity, the shape of the histograms resemble more and more a Gaussian distribution. For the mDOT, the shape is completely different. While for about 8 p.e., the shape of the mDOT histogram is very similar to the digitizer histogram, the shapes of the mDOT histogram deviate more and more from the digitizer histograms for

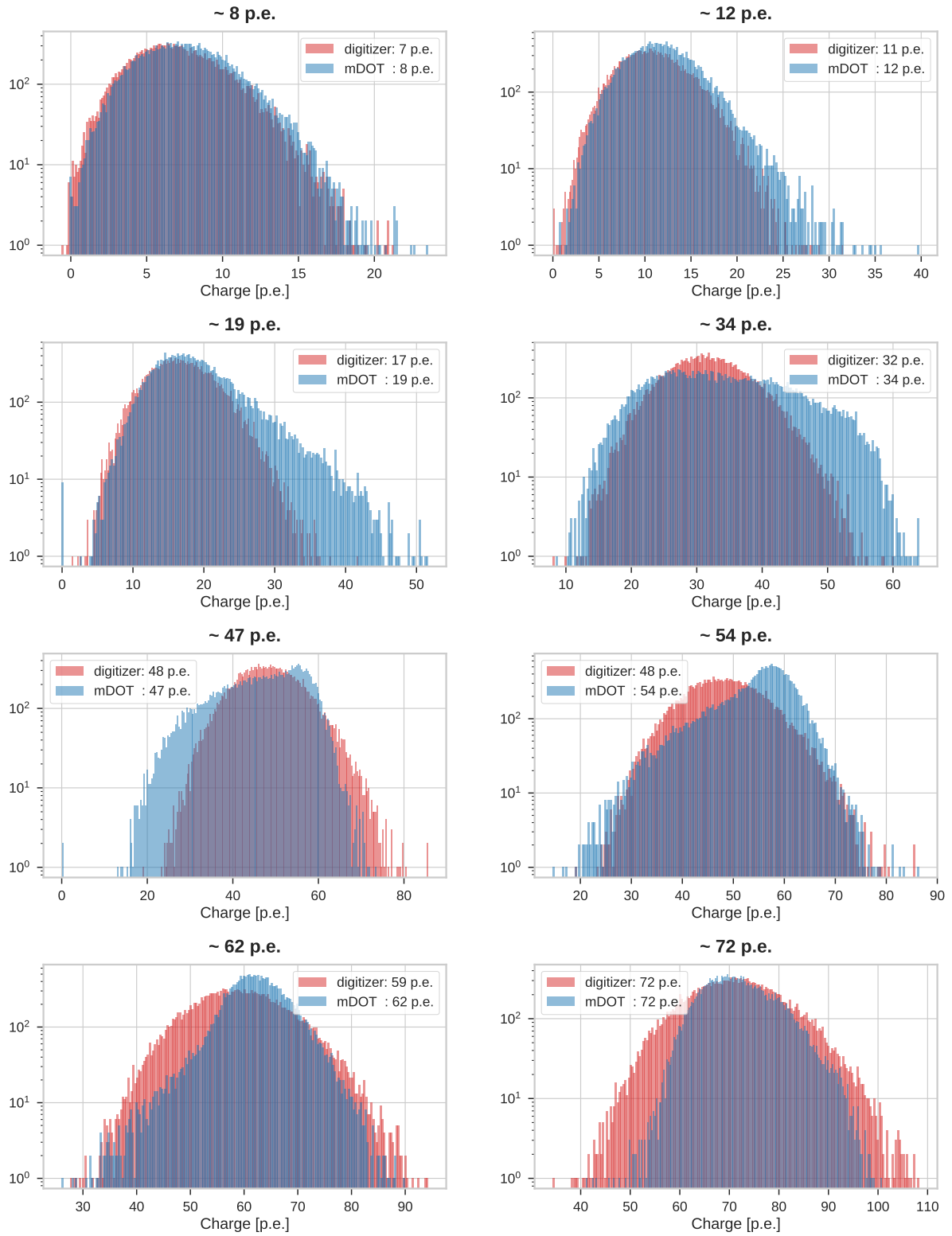


**Figure 4.21:** Exemplary comparison of charge histograms for measurements with digitizer (red) and mDOT (blue) of similar mean charge shown for different mean p.e. numbers. The measurements were made with channel 0 at 17°C. Deformations of the charge histograms appear for the measurements with the mDOT for mean charges larger than 8 p.e.

higher light intensities. For about 34 p.e., the mDOT histogram is no longer Gaussian shaped, but deformed. Starting at 19 p.e., the mDOT histograms become broader with a kind of shoulder, while they become more narrow and skew at about 54 p.e. compared to the digitizer histograms. For small light intensities with measured charges below 8 p.e., this deformation is not visible. It only occurs for larger light intensities. However, the light intensity is still low enough to not saturate the AFE. Because the data taken by the digitizer look normal and with that, the PMTs seem to behave normal, the results indicate that it is most likely an issue of the AFE. Measurements with a pulse generator confirmed that the problem is caused by the AFE.

Finally, it turned out that the deformations of the charge histograms shown in Figure 4.21 are most likely a bandwidth problem. By changing the preamplifier, the amplification factor was increased which reduced the bandwidth (old gain-bandwidth product: 300 MHz [103]; new gain-bandwidth product: 110 MHz [104]). Furthermore, the new preamplifier stays linear for larger input signals. The change of the preamplifier lead to a redesign of channel 0 which shows no deformations of the charge histograms (see Figure 4.23 in comparison to Figure 4.21). This new channel design was used for the revision 1 mainboard and will be described in Section 4.4.

## 4.4 Characterization of the AFE channel design of the revision 1 mainboard

After channel 0 was redesigned, it was tested whether it fulfills the AFE requirements for the mDOM before it was used as the AFE channel design for the revision 1 mainboard. In the following, this new channel design is called channel 0b. As explained in Subsection 4.3.4.2, the main difference of channel 0b compared to channel 0 is a different preamplifier. In this section, the characteristics of channel 0b are investigated.

### 4.4.1 Measurement setup

For the characterization measurements of channel 0b, the setup shown in Figure 4.22 was used. The mDOT containing the AFE design of channel 0b and also other channel designs was placed into a darkbox which was put into a freezer. A R15458-02 PMT type was connected to channel 0b for the AFE characterization. The channel provided the voltage for the PMT as well as for the microbase and also processed the PMT signal. Optionally, the PMT signal could be read out by a digitizer [95]. Another PMT from the R12199-01-HA type was used as a reference PMT. It was powered by channel 3, but its signal was always read out by the digitizer. An LED [92] was placed into an integrating sphere as used in [93] to illuminate the PMTs. The LED was driven by a pulse generator with a repetition frequency of 1 kHz and a pulse width of 20 ns. Furthermore, the pulse generator triggered channel 1 of the mDOT as well as the digitizer. Pulse generator, digitizer, and mDOT were controlled by a PC. The temperature was monitored with the temperature sensor T1 [94]. The calibration of the setup was performed as described in Subsection 4.3.1. However, three temperature ranges were measured:  $[+25^{\circ}\text{C to } +28^{\circ}\text{C}]$ ,  $[-22.0^{\circ}\text{C to } -22.2^{\circ}\text{C}]$ , and  $[-37.8^{\circ}\text{C to } -38.2^{\circ}\text{C}]$ . In the following, the temperature ranges are referred to as temperatures at  $+25^{\circ}\text{C}$ ,  $-22^{\circ}\text{C}$ , and  $-38^{\circ}\text{C}$  for simplification.

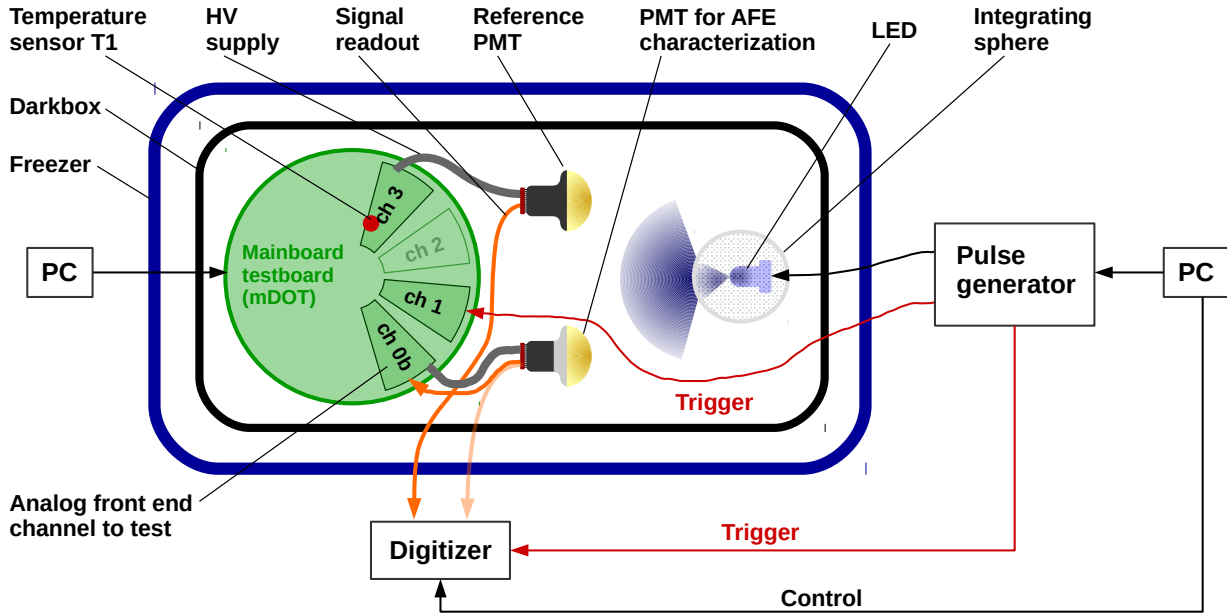


**Figure 4.22:** Measurement setup for the characterization of the AFE channel design of the revision 1 mainboard (ch 0b). The signal of the PMT for the AFE characterization can be read out optionally by the digitizer for calibration.

#### 4.4.2 Functionality test

The previously investigated AFE channel 0, channel 2, and channel 3 showed deformations in the charge histograms at  $+17^\circ\text{C}$  and at  $-42^\circ\text{C}$  (see Subsection 4.3.4.2). Examples of these deformations were shown in Figure 4.21. To confirm that these deformations are eliminated for the redesigned channel 0b, a similar comparison of the charge histograms from digitizer and AFE channel was made. For a meaningful comparison, all charge values were converted into p.e. Therefore, Equation 4.3 was used for the digitizer. In contrast to that, all mDOT charges were divided by the mean charge of  $Q_{\text{SPE}}$  which was determined before as described in Figure 4.2. Subsequently, each mDOT charge histogram was assigned to a digitizer histogram with a similar mean charge. Since the LED voltage could be adjusted only in discrete values, not any mean p.e. number could be characterized. Moreover, the LED output changed for a remeasurement with the same LED voltage, because the environmental conditions as for example the temperature changed. Therefore, the mean charges of mDOT charge histogram and digitizer charge histogram sometimes differ which leads to a shift of the two histograms. In Subsection 4.3.4.2, the deformations occurred for all charge histograms with a mean charge above 8 p.e. Figure 4.23 shows a representative selection of similar mean charge values for channel 0b at room temperature. The digitizer charge is shown in red and the mDOT charge is shown in blue. No deformations occur at all. Consequently, the issue with the deformations of the charge histograms is considered as fixed with the design of channel 0b.

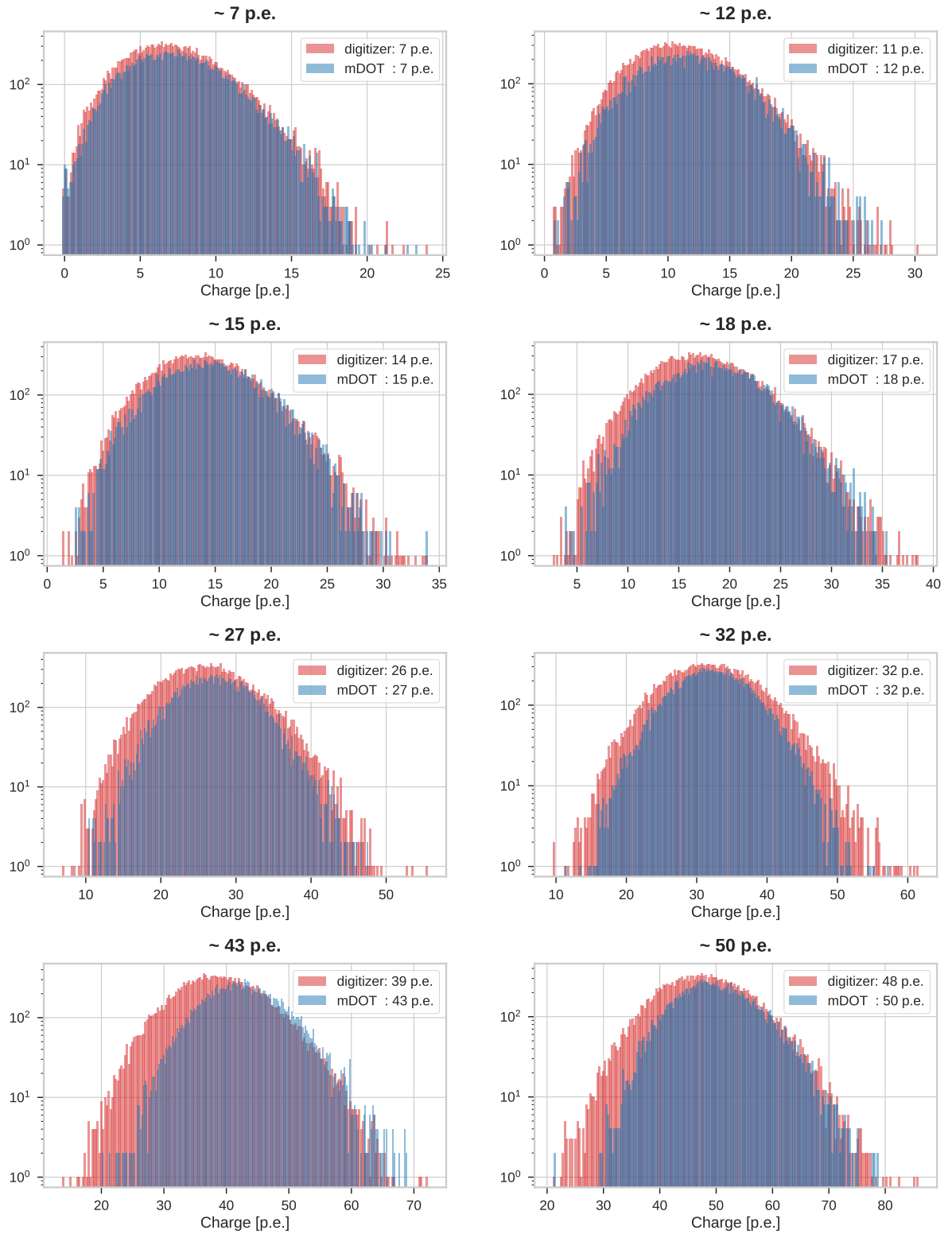


**Figure 4.23:** Comparison of charge histograms for measurements with digitizer (red) and mDOT (blue) of similar mean charge shown for different mean p.e. numbers. Exemplarily shown for room temperature. No deformations occur.

**Table 4.4:** Calculated SNR for channel 0b at  $+25^{\circ}\text{C}$ ,  $-22^{\circ}\text{C}$ , and  $-38^{\circ}\text{C}$ .

Parameter	$+25^{\circ}\text{C}$	$-22^{\circ}\text{C}$	$-38^{\circ}\text{C}$	Requirement
Mean amplitude of a 1 p.e. signal [ADC counts]	42.08	41.87	42.14	-
Mean baseline RMS [ADC counts]	0.72	0.69	0.68	-
Signal-to-noise ratio	58.09	60.27	61.73	$> 25$

### 4.4.3 Investigated parameters

The following parameters were investigated for the channel 0b AFE design: SNR, dynamic range, linearity, and discriminator threshold stability. As part of the dynamic range, the capability of triggering on 0.2 p.e. as well as the capability of triggering on large pulses is investigated. In this subsection, the results of the different measurements as well as the used analysis techniques are discussed.

#### 4.4.3.1 Signal-to-noise ratio (SNR)

Because the SNR is determined from one measurement at a low photon level and therefore, does not suffer from the mismatch in the charge calibration or the deformations of the charge histograms mentioned in Subsection 4.3.4, the SNR is determined as described in Subsection 4.3.2.1. A fit of the PMT response function to the charge histogram of the LED measurement yielded  $Q_{\text{SPE}}$ . Afterwards, the mean amplitude of a 1 p.e. signal was extracted. Additionally, the mean baseline RMS was determined from the values inside the baseline window. Finally, the SNR was calculated according to Equation 4.1 for  $+25^{\circ}\text{C}$ ,  $-22^{\circ}\text{C}$ , and  $-38^{\circ}\text{C}$ .

Table 4.4 shows an overview of the measured values. While the mean amplitude of a 1 p.e. signal is about 42 ADC counts for all three temperatures, the mean baseline RMS is always smaller than 1 ADC count and decreases with decreasing temperature. The measured SNR is more than twice as much as the required 25 for all temperatures.

#### 4.4.3.2 Dynamic range

The AFE is required to process signals with mean charges between 0.2 p.e. and 50 p.e. In Paragraph 4.4.3.2.1, the capability of triggering on 0.2 p.e. is investigated while in Paragraph 4.4.3.2.2, the capability of recording signals up to 50 p.e. is investigated.

##### 4.4.3.2.1 Capability of triggering on 0.2 p.e.

Because the relevant parameters extracted from the LED measurement—mean charge and mean amplitude of a 1 p.e. signal—do not depend on the temperature dependent LED output, the same

measurement and analysis procedure as described in Paragraph 4.3.2.2.1 was used to investigate the triggering on 0.2 p.e. of channel 0b. Nevertheless, all trigger thresholds were measured at one day and the corresponding LED measurement was performed shortly before the selftrigger measurements (one day before for  $-38^\circ\text{C}$  and immediately before for  $+25^\circ\text{C}$  and  $-22^\circ\text{C}$ ). First of all, it was determined which DAC threshold had to be adjusted to trigger on 0.2 p.e. Therefore, selftrigger measurements using different DAC thresholds were performed. For each measured DAC threshold, the trigger threshold in ADC counts was determined. By using the mean amplitude of a 1 p.e. signal extracted from the LED measurement as explained in Figure 4.6, the thresholds were calculated in units of p.e. After the selftrigger measurement at 0.2 p.e. had been extracted from the measurements at different thresholds, the selftrigger measurement was compared to the LED measurement at low p.e. level used for the determination of the SNR in Subsection 4.4.3.2. For that purpose, all measured charges were divided by  $Q_{\text{SPE}}$  which was determined in Subsection 4.4.3.2. Figure 4.24 shows the resulting histograms for  $+25^\circ\text{C}$ ,  $-22^\circ\text{C}$ , and  $-38^\circ\text{C}$ . The LED measurements are shown in red and the selftrigger measurements are shown in blue. The black dashed vertical line marks 0.2 p.e. For each selftrigger measurement, the fraction of recorded waveforms with a charge smaller than 0.2 p.e. was extracted. About 1 % of the measured waveforms have a charge smaller than 0.2 p.e. for all three temperatures. Thus, the triggering on 0.2 p.e. seems to work for channel 0b at all three temperatures.

#### 4.4.3.2.2 Capability of recording large pulses

In Subsection 4.3.4.1, it was shown that the LED calibration used for the dynamic range and linearity measurements performed in Paragraph 4.3.2.2.2 and Subsection 4.3.2.3 yielded large systematic errors. For this reason, a different approach was used for channel 0b. The linearity measurements of the PMT and microbase shown in Figure 4.16 and Figure 4.17 are not affected by the mismatch in the charge calibration discussed in Subsection 4.3.4, because a different setup was used. It was shown that the charge output of the system PMT + microbase is linear up to approximately 500 p.e. For the AFE measurements, the ADC baseline was shifted towards the upper edge of the usable ADC output range (see Figure 4.11) similar to Paragraph 4.3.2.2.2. To determine the correct p.e. number which was measured with the AFE, two measurements were needed: The reference measurement and the AFE measurement. Figure 4.25 illustrates the measurement procedure. For simplification, the darkbox and the freezer shown in Figure 4.22 are omitted although they are still part of the setup. First of all, the mDOT, the PMTs, and the LED were cooled down to the respective temperature. After that, the reference measurement was performed. During the reference measurement, the PMTs were powered by their respective AFE channel and both PMT outputs were read out by the digitizer. Different LED supply voltages were adjusted and—similar to Paragraph 4.3.2.2.2—20 000 waveforms were taken. Using the same procedure as described in Subsection 3.2.2, the charge was determined in units of p.e. according to Equation 4.3. The calculated charges are called  $\text{p.e.}_{\text{ch3 ref}}$  and  $\text{p.e.}_{\text{ch0b ref}}$  and are both a function of the LED voltage. After finishing the reference measurement, the setup was warmed up to room temperature. The output of the PMT powered by channel 0b was reconnected to the AFE channel 0b. Subsequently, the setup was cooled down to the same temperature as before. To ensure the same environmental conditions and prevent systematic errors, the measurement with the digitizer and the measurement with the mDOT should span the same time. Because the data processing of the digitizer is about 60 times faster than the data processing of the mDOT, the repetition frequency of the pulse generator was reduced to slow down the pulsing of the

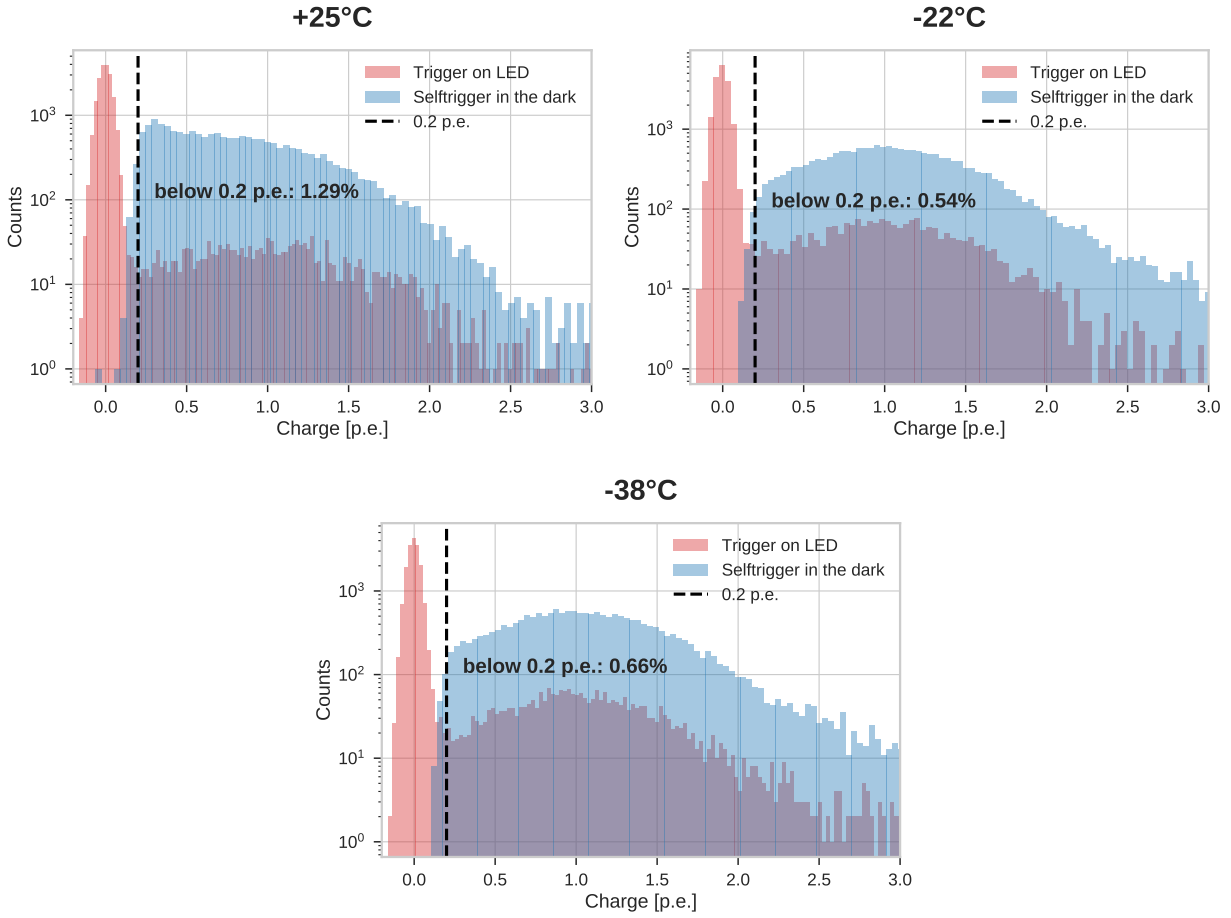


**Figure 4.24:** Comparison of the SPE spectra from measurements with trigger on LED and selftrigger measurements at 0.2 p.e. level in the dark for channel 0b at +25 °C, −22 °C, and −38 °C.

LED so that the readout of digitizer and mDOT last approximately the same time. For +25 °C, the repetition frequency was 6 Hz, and for −22 °C and −38 °C, the frequency was 10 Hz. For the AFE measurement, the voltage range was extended to both sides, because it was shown in Subsection 4.3.4.1 that the LED output varies over time. Thus, full coverage of the required charge range from 0.2 p.e. to 50 p.e. was ensured. The mean charges measured by digitizer and channel 0b were determined out of 20 000 waveforms in each case in units of p.e. for the digitizer and in a.u. for the mDOT. The mean charges are called  $\text{p.e.}_{\text{ch3 meas}}$  for the PMT powered by channel 3 and mDOT charge for the PMT powered and read out by channel 0b. From reference and AFE measurement,  $\text{p.e.}_{\text{ch0b meas}}$ —which is the correct p.e. value for channel 0b during data taking of the mDOT charge—can be determined to:

$$\text{p.e.}_{\text{ch0b meas}} = \frac{\text{p.e.}_{\text{ch0b ref}} \cdot \text{p.e.}_{\text{ch3 meas}}}{\text{p.e.}_{\text{ch3 ref}}}, \quad (4.4)$$

where  $\text{p.e.}_{\text{ch0b meas}}$  is the input charge. During the AFE measurement, the reference PMT monitors the LED output yielding  $\text{p.e.}_{\text{ch3 meas}}$ . In contrast to that,  $\text{p.e.}_{\text{ch3 ref}}$  and  $\text{p.e.}_{\text{ch0b ref}}$  from the reference measurement yield a geometric correction factor taking the different positions of the

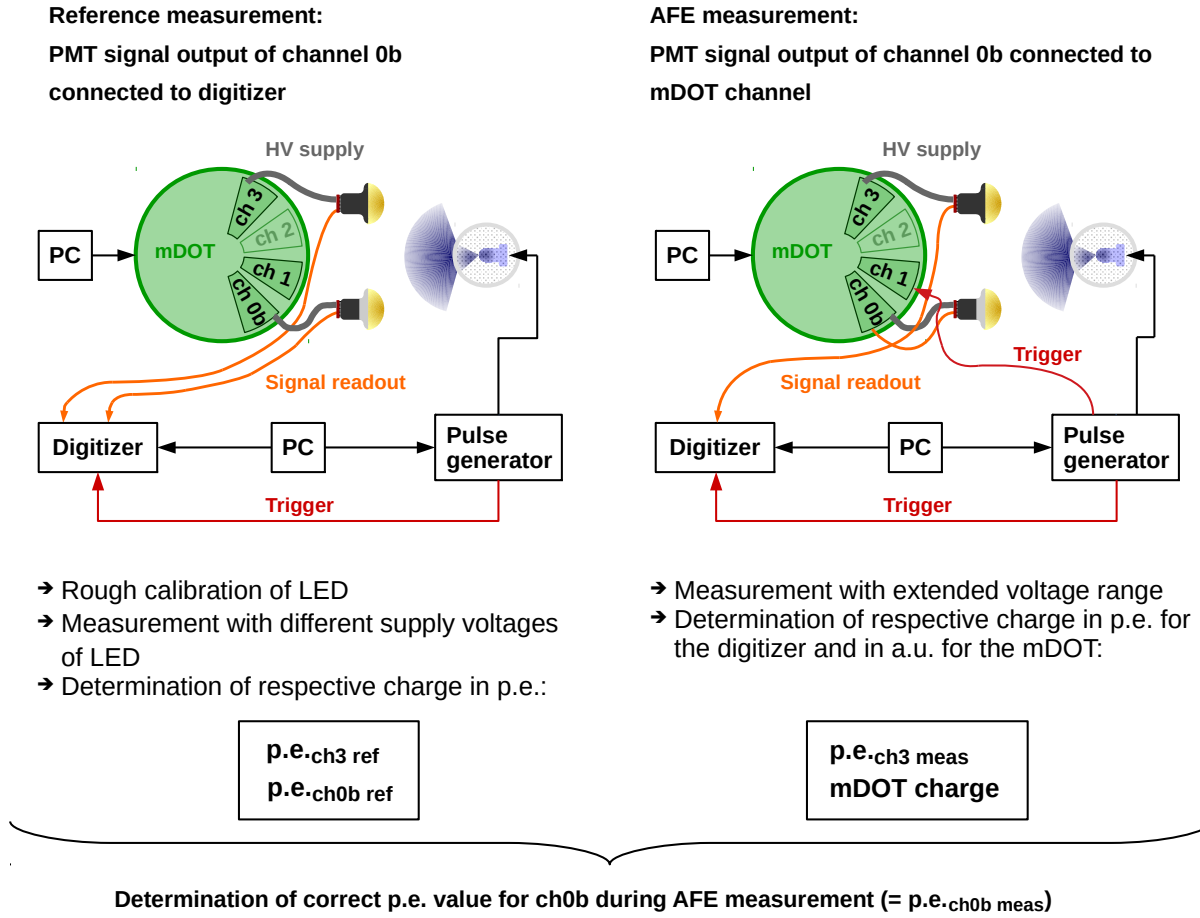


**Figure 4.25:** Illustration of the measurement procedure to determine the correct measured p.e. number for channel 0b during data readout with the AFE.

reference PMT and the PMT connected to channel 0b into account. Thus, the actual p.e. number during the AFE measurement can be determined according to Equation 4.4.

From these measurements, the dynamic range can be determined. Therefore, the mDOT charge in a.u. is plotted versus the input charge in p.e. Figure 4.26 shows the results of the dynamic range measurement for all three temperatures. The gray shaded area indicates the required dynamic range from 0.2 p.e. up to 50 p.e. For all three temperatures, the saturation starts beyond 80 p.e. and therefore, the dynamic range requirement is fulfilled for all three temperatures. In contrast to Figure 4.13 where the mDOT charge varied widely for the two measured temperatures at the same p.e. number because of the mismatch in the charge calibration described in Subsection 4.3.4.1, the datapoints for all three temperatures are located almost on one curve for channel 0b. This consistency of the three measurements indicates that the technique described in this paragraph to determine the input charge has smaller uncertainties.

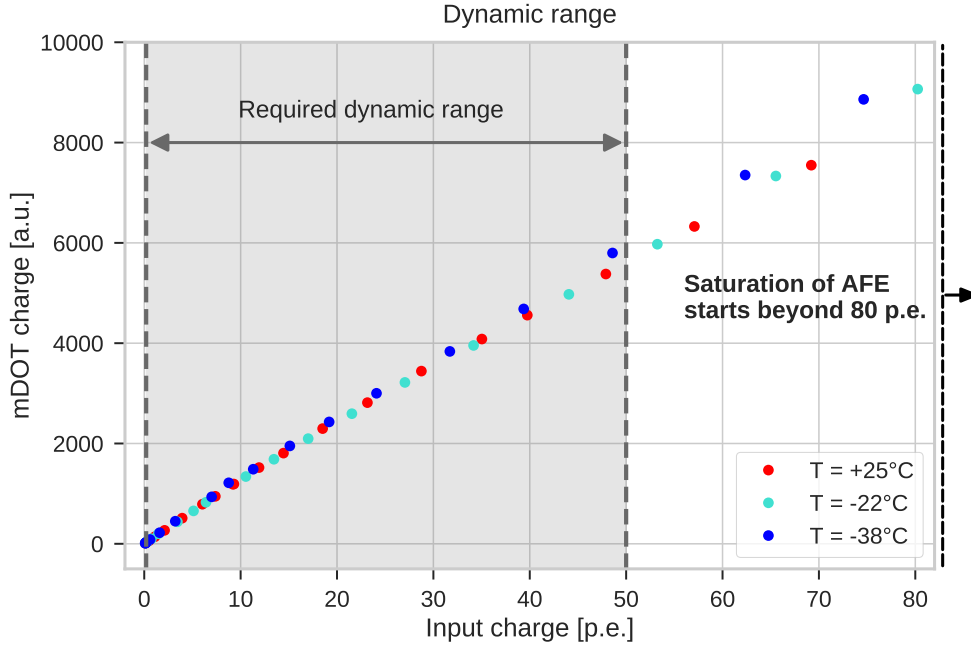


**Figure 4.26:** Dynamic range measurements focusing on large pulses for channel 0b at  $+25^\circ\text{C}$ ,  $-22^\circ\text{C}$ , and  $-38^\circ\text{C}$ .

#### 4.4.3.3 Linearity

To calibrate the charge calculation, the AFE is required to behave linearly. The same measurement as described in Paragraph 4.4.3.2.2 was used. In contrast, the amplitude instead of the charge was investigated. The procedure to determine the input and output amplitude was the same as described in Figure 4.18. Figure 4.27 shows the linearity measurements for channel 0b at  $+25^\circ\text{C}$ ,  $-22^\circ\text{C}$ , and  $-38^\circ\text{C}$ . The blue dots are the measured data. The gray shaded area describes the fit range of the linear function shown in green. The green shaded area represents  $\pm 10\%$  of the fit. The two black dashed lines indicate the measured and required linearity, respectively. At  $+25^\circ\text{C}$ , channel 0b is linear up to 48 p.e. marginally failing the linearity requirement. In contrast to that, channel 0b is linear up to 81 p.e. at  $-22^\circ\text{C}$ . Contrarily, channel 0b is linear up to 31 p.e. at  $-38^\circ\text{C}$ . A possible solution to still be able to calibrate the charge calculation is to fit a different function than a linear function to the data. All three curves show a linear behavior at first with a subsequent flattening to the end. Such a behavior was already described in [105] for the IceCube PMT. Based on the fit formula used in this article, the following modified fit function was used for the data shown in Figure 4.27:

$$A_{\text{out}} = s \cdot A_{\text{in}} \cdot \frac{\ln\left(1 + \frac{a}{A_{\text{in}}}\right)}{\ln\left(1 + \frac{a}{A_{\text{in}}}\right) + \frac{a}{c} \cdot e^{\left(\frac{-b}{A_{\text{in}}}\right)}}, \quad (4.5)$$

where  $A_{\text{out}}$  is the output amplitude,  $s$  a scaling factor,  $A_{\text{in}}$  the input amplitude,  $a$ ,  $b$ , and  $c$  further parameters. Figure 4.28 shows the fit of Equation 4.4 to the linearity measurements of channel 0b for  $+25^\circ\text{C}$ ,  $-22^\circ\text{C}$ , and  $-38^\circ\text{C}$ . The gray dashed line indicates the bisectrix multiplied by the scaling factor  $s$ . The fit describes the data deviating from the bisectrix  $\cdot s$ . In principle, this fit of

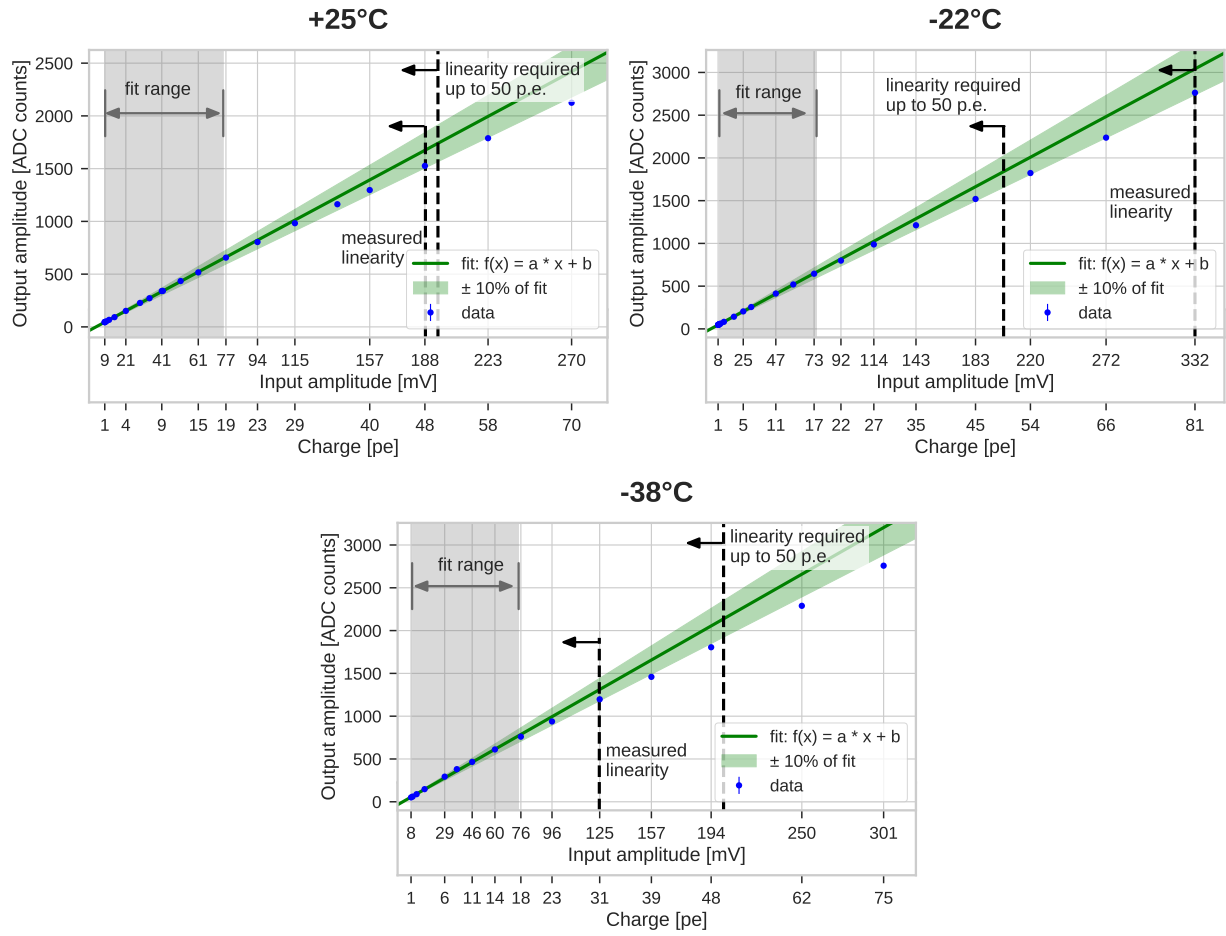


**Figure 4.27:** Linearity measurements for channel 0b at +25 °C, -22 °C, and -38 °C.

Equation 4.4 performed in Figure 4.28 can be used for the calibration of the charge calculation instead of a linear function. Thus, it was decided that the results of the linearity measurements shown in Figure 4.27 are acceptable for the mDOM AFE.

#### 4.4.3.4 Discriminator threshold stability

For the event reconstruction and detector calibration, it is important to have a controlled systematic error on the photo-detection efficiency. Therefore, the discriminator threshold should not drift more than 0.05 p.e. per week. To investigate the discriminator threshold stability, a long-term measurement was performed over approximately 26 days. Due to time constraints, the discriminator threshold was measured only at -38 °C. Before starting the long-term measurement, the threshold corresponding to 0.2 p.e. had to be calibrated first. The procedure was the same as described in Figure 4.6. An LED measurement was performed with triggering on the LED. This LED measurement yielded  $Q_{\text{SPE}}$ . After that, the mean amplitude of a 1 p.e. pulse was extracted from that LED measurement. Next, several selftrigger measurements at different DAC thresholds were taken. By fitting an error function to the amplitude histogram as described in Figure 4.6, the corresponding trigger threshold in ADC counts could be determined. Together with the LED

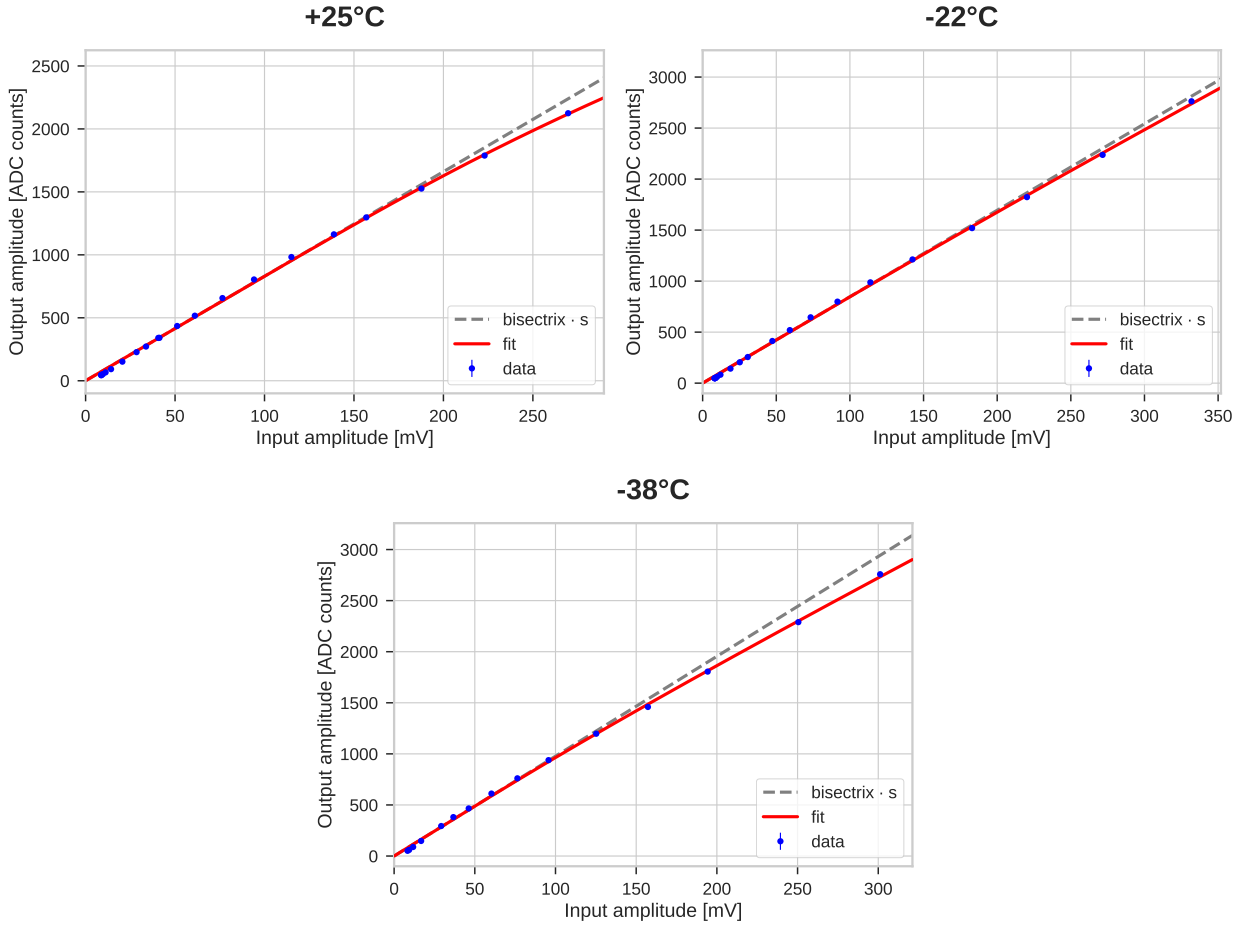


**Figure 4.28:** Fit describing the saturation behavior of the linearity measurements for channel 0b at +25°C, -22°C, and -38°C.

measurement, the trigger threshold was converted into units of p.e. resulting into a dependence as shown in Figure 4.4. Finally, the trigger threshold corresponding to 0.2 p.e. was adjusted in DAC counts. This threshold was adjusted once at the beginning of the long-term measurement and remained unchanged throughout the whole measurement. After adjusting the threshold, the long-term measurement was started. Approximately every 12 h, a selftrigger measurement with the adjusted DAC threshold was performed. Small pulses are necessary to perform the fit to the left edge of the amplitude histogram as shown in Figure 4.5. At lower temperatures and a certain time in the dark, the percentage of 1 p.e. pulses from darkrate events is drastically reduced. Therefore, the LED was powered with a voltage corresponding to a detected mean number of roughly 0.1 p.e. yielding mainly 1 p.e. pulses. To exclude a possible discriminator drift of the temperature dependent discriminator threshold due to temperature variations, the temperature was monitored during the whole long-term measurement by the temperature sensor T1 (see Figure 4.22). For every selftrigger measurement, an error function was fitted to the left edge of the amplitude histogram to extract the trigger threshold in ADC counts as described in Figure 4.5. Afterwards, each threshold was converted into units of p.e. according to Equation 4.2. Figure 4.29 shows the measured discriminator threshold stability. In the lower plot, the measured temperature is shown versus

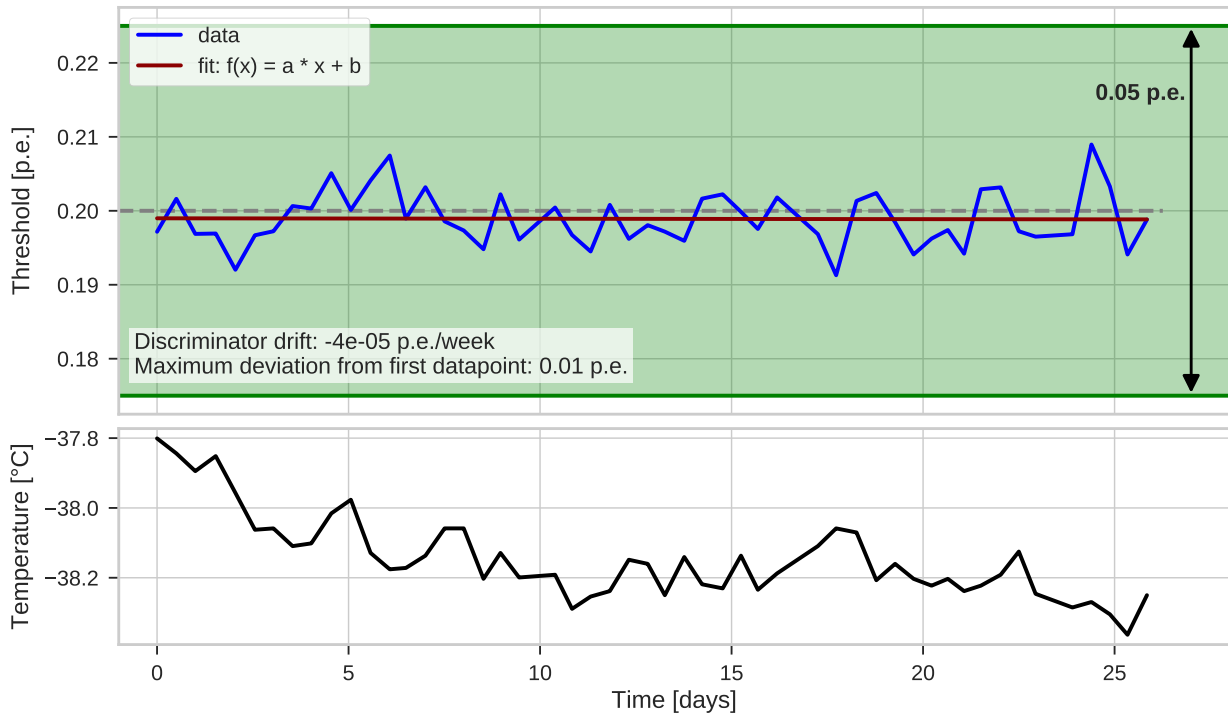


**Figure 4.29:** Discriminator threshold stability over 26 days for channel 0b at  $-38^{\circ}\text{C}$ .

time. In the upper plot, the measured threshold in p.e. is shown over time. The gray dashed horizontal line describes the threshold of 0.2 p.e. The green shaded area margined by the two green horizontal lines spans 0.05 p.e. The red line indicates the fit to the data in blue. A measured discriminator drift of  $-4 \cdot 10^{-5}$  p.e./week was determined from the slope of the fitted line. The maximum deviation from the first datapoint is 0.01 p.e. All in all, the measured discriminator drift of channel 0b at  $-38^{\circ}\text{C}$  is far lower than the required maximum drift of 0.05 p.e./week and thus, the requirement is fulfilled.

#### 4.4.4 Conclusion

After the measurements with the three different channel designs described in Section 4.3, a modified version of channel 0—called channel 0b—was chosen to be used for the revision 1 mainboard. The problems encountered during the measurements with the three different channel designs described in Subsection 4.3.4 could be solved. In Paragraph 4.4.3.2.2, it was shown that the corrected technique to determine the input charge works. Besides, a functionality test performed in Subsection 4.4.2 showed that no deformations in the charge histograms occur with the design of channel 0b. The SNR, the lower as well as the upper end of the required dynamic range, and the linearity were investigated at  $+25^{\circ}\text{C}$ ,  $-22^{\circ}\text{C}$ , and  $-38^{\circ}\text{C}$ . In addition, the discriminator threshold stability was measured at  $-38^{\circ}\text{C}$ . Table 4.5 summarizes the results. Whether the requirement is fulfilled or not is indicated by the cell color. Green marks fulfilled, red failed, and yellow indicates a fail of the requirement which can be accepted, though. The SNR is fulfilled for all three temperatures. Similarly, the triggering on 0.2 p.e. works for all three temperatures. Likewise, the measured dynamic range extends beyond the required 50 p.e. for all three temperatures. In contrast to that,

**Table 4.5:** Comparison of the measured characteristics for channel 0b at  $+25^\circ\text{C}$ ,  $-22^\circ\text{C}$ , and  $-38^\circ\text{C}$ . For  $+25^\circ\text{C}$  and  $-38^\circ\text{C}$ , the linearity requirement is actually missed, but it was decided that it is still acceptable.\*

Characteristic	$+25^\circ\text{C}$	$-22^\circ\text{C}$	$-38^\circ\text{C}$	Requirement
Signal-to-noise ratio	58.09	60.27	61.73	$> 25$
Dynamic range	$\geq 0.2 \text{ pe.}$	$\geq 0.2 \text{ pe.}$	$\geq 0.2 \text{ pe.}$	Trigger on 0.2 p.e.
	$> 69 \text{ p.e.}$	$> 80 \text{ p.e.}$	$> 75 \text{ p.e.}$	Up to 50 p.e.
Linearity	$\leq 48 \text{ p.e.*}$	$\leq 81 \text{ p.e.}$	$\leq 31 \text{ p.e.*}$	Up to 50 p.e.
Discriminator threshold stability	-	-	$-4 \cdot 10^{-5} \text{ p.e./week}$	drift $\leq 0.05 \text{ p.e./week}$

the linearity requirement is fulfilled only at  $-22^\circ\text{C}$ . For  $+25^\circ\text{C}$ , linearity was measured up to 48 p.e., which is slightly below 50 p.e. and thus, a marginal fail. At  $-38^\circ\text{C}$ , however, linearity was measured up to 31 p.e. Nevertheless, it was shown in Subsection 4.4.3.3 that a function describing the saturation behavior can be fitted to the data. As a consequence, the results of the linearity measurements are no reason to reject the channel design for the mDOM mainboard. The measured discriminator threshold stability, on the other hand, is far lower than the maximum allowed drift. All in all, it was shown that channel 0b, which is the design of the revision 1 mainboard, is well suited for the mDOM application.

## 4.5 Summary

In the scope of developing an AFE channel design which meets the requirements for the mDOM application, different AFE designs were investigated. Furthermore, the AFE was tested for the first time at cold temperatures and moreover, an environment close to the end application was used. Therefore, an extra setup was designed to test the AFE channels. In addition, special measurement and analysis techniques were developed to verify the requirements. For a start, three different AFE designs were compared (channel 0, channel 2, and channel 3) with regard to SNR, dynamic range, and linearity at  $+17^\circ\text{C}$  and at  $-42^\circ\text{C}$ . It was found that the SNR requirement is fulfilled for all channels at both temperatures. The same applies to the dynamic range, with two exceptions. Channel 0 saturates before the required 50 p.e. of the dynamic range at  $+17^\circ\text{C}$  due to the large SNR. Furthermore, channel 3 triggers on electronic noise with a probability of almost 30 % at  $-42^\circ\text{C}$ . The linearity requirement, however, is for none of the channels fulfilled. During the measurements, two problems were encountered. First, the output of the used LED varies between two days and thus, the technique to determine the mean input charge yielded large systematic errors. Second, all three channels show deformations in the charge histograms at

both temperatures starting at approximately 19 p.e. Both problems could be solved. The charge calibration technique was changed such that a reference PMT monitors the current p.e. number for each measurement. To eliminate the deformations in the charge histograms, the preamplifier was exchanged. A redesign of channel 0 lead to the AFE channel 0b which was tested at  $+25^{\circ}\text{C}$ ,  $-22^{\circ}\text{C}$ , and  $-38^{\circ}\text{C}$ . A functionality test proved that the deformation of the charge histograms were eliminated after the preamplifier change. While SNR, dynamic range, and linearity were measured at all three temperatures, the discriminator threshold stability was investigated only at  $-38^{\circ}\text{C}$ . Channel 0b fulfills all requirement except the linearity requirement at  $+25^{\circ}\text{C}$  and at  $-38^{\circ}\text{C}$ . However, it was shown that it is possible to fit a function describing the saturation behavior to the data. Thus, channel 0b was accepted as AFE design for the mDOM and was used for the revision 1 mainboard.

The setup as well as the measurement and analysis techniques developed in this thesis were reused to characterize SNR, dynamic range, linearity, and discriminator threshold stability of the mainboard. All four requirements were verified for the revision 1 as well as for the revision 2 mainboard. Together with other parameters, these requirements were verified in the final design review (results in [70]).

## Chapter 5

# Measurements with an integrated mDOM

---

<b>5.1</b>	<b>Setup . . . . .</b>	<b>97</b>
<b>5.2</b>	<b>Measurement procedure . . . . .</b>	<b>99</b>
<b>5.3</b>	<b>Temperature behavior of an mDOM . . . . .</b>	<b>100</b>
5.3.1	Simulation . . . . .	101
5.3.2	Power consumption . . . . .	104
5.3.3	Equilibrium temperatures . . . . .	105
5.3.4	Warm-up and cooling times . . . . .	111
<b>5.4</b>	<b>Further parameters . . . . .</b>	<b>114</b>
5.4.1	Pressure . . . . .	114
5.4.2	PMT high voltage . . . . .	115
<b>5.5</b>	<b>Summary and discussion . . . . .</b>	<b>116</b>

---

This chapter presents longterm measurements with an integrated mDOM. In the first section, the used setup for the measurements and in the second section, the measurement procedure is explained. The temperature behavior of the mDOM is investigated in the third section. Investigations include an attempt to simulate the temperature behavior of the mDOM as well as longterm measurements of different parameters. Power consumption, equilibrium temperature, as well as warm-up and cooling times are measured. Two further parameters—the pressure inside the mDOM and the PMT HV stability over time—are investigated in the fourth section. The last section summarizes the chapter and discusses the results.

### 5.1 Setup

This section explains the setup used for the measurements with an integrated mDOM. Figure 5.1 shows a schematic drawing. Since the mDOMs will be deployed in ice with typical temperatures between  $-27^{\circ}\text{C}$  and  $-19^{\circ}\text{C}$  (see Subsection 2.1), a freezer was used to emulate realistic thermal conditions. Two mDOMs were used for the measurements. Traditionally, all IceCube modules have nicknames. The local IceCube Upgrade group at DESY, Zeuthen Site, decided to name

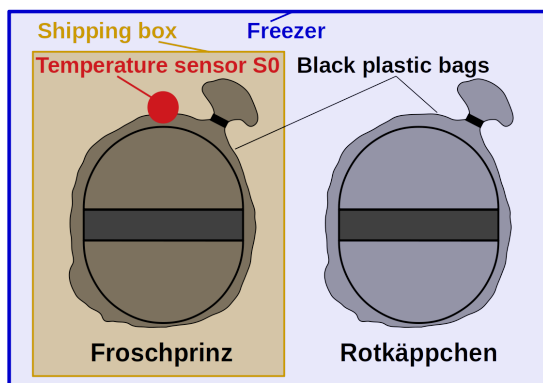


**Figure 5.1:** Schematic of the used setup. Two bagged mDOMs are put into a freezer. One mDOM is in a cardboard box, the other one not.

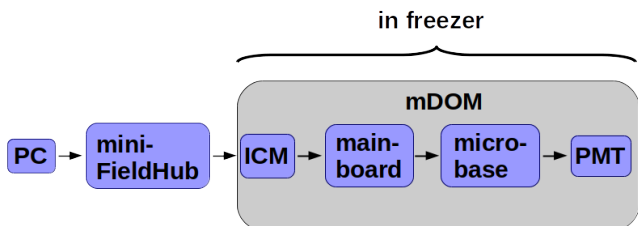


**Figure 5.2:** Schematic of the communication with the mDOM.

them according to german fairy tale characters. The nicknames of the two tested mDOMs are Froschprinz and Rotkäppchen. In the following, these names are used to specify the respective mDOM module. Although the freezer was located in a darkroom, both mDOMs were additionally put into black plastic bags (3M<sup>TM</sup> Conductive Drum Liner 2014 in [106]) to further shield them from environmental light exposure. In addition to that, Froschprinz was put into a shipping box made of cardboard. The main measurements were performed with Froschprinz while Rotkäppchen was used to crosscheck. To monitor the outside temperature of Froschprinz and the freezer temperature, a temperature sensor S0 was placed on top of the plastic bag housing Froschprinz.

As described in Section 2.2, a special cable guided through a hole in the upper hemisphere supplies the mDOM with power and also allows for communication with the mDOM. In Figure 5.2, a schematic block diagram shows the communication sequence. Running a special software on a computer (PC), commands could be sent to the mDOM and parameters of the mDOM could be read out. The computer was connected via USB to a miniFieldHub which is a prototype of the later used FieldHub (see Section 2.5). The miniFieldHub distributes the power to the connected mDOMs. Unlike the FieldHub, the miniFieldHub not only communicates with the mDOM, but also divides the input voltage—230 V from the socket—into 96 V. Both computer and miniFieldHub were outside the freezer in the darkroom. A cable was running from the miniFieldHub to the mDOM in the freezer. The first communication instance inside the mDOM is the ICM. It is responsible for the communication between miniFieldHub and mainboard and sends the mDOM data to the surface. Plugged on the mainboard, the ICM can be switched on independently of the mainboard. Every communication with further sensors such as camera, flasher, PMTs is running via the mainboard which also includes the readout of the PMTs and divides the incoming 96 V into different power rails (5 V, 3.3 V, 1.8 V, 1.35 V, and 1.0 V). A special circuit with a microcontroller (microbase) produces the HV for the PMT and distributes the different voltages to the dynodes of the PMT. The microbases are connected to the mainboard via cables.

## 5.2 Measurement procedure

In this section, the measurement procedure is described. Since the main measurements are performed with Froschprinz, the measurement procedure for Froschprinz is explained first.

Because the mDOMs will be deployed in ice and will be switched on after freezing in ice, Froschprinz underwent a cold start. Seven consecutive operation stages were investigated: “all off”, “ICM on”, “mb on”, “HV on”, “HV off”, “mb off”, and “all off”. An overview of the measurement procedure is shown in Figure 5.3 for both mDOMs. First of all, Froschprinz was switched off completely (operation stage “all off”). Computer and miniFieldHub were still running, but no voltage was applied to the mDOM. During this operation stage, no sensors of the mDOM could be read out. During the switch-off, wirepair current and wirepair voltage were saved. The wirepair values were measured by the miniFieldHub. Moreover, the absolute time in unix time was saved. Because it is independent of the mDOM electronics, the temperature sensor S0 in the shipping box of Froschprinz was running and read out. Absolute time, temperature of S0, wirepair current and wirepair voltage were continually recorded during the entire measurement. Froschprinz stayed at least two days in the operation stage “all off” so that all of its components could cool down to the freezer temperature.

In the next step, the ICM was switched on while the mainboard stayed switched off (“ICM on”). The FPGA on the ICM also has a temperature sensor which can be read out as soon as the ICM is powered. Together with the temperature sensor S0 in the shipping box, two temperature sensors were available during this operation stage.

Running only the ICM for some time and letting it warm-up, the mainboard was switched on after some hours (“mb on”). As soon as the mainboard was powered, all six temperature sensors of the mainboard and the pressure sensor became available. Enabling the HV interlock of the PMTs in the miniFieldHub provided 24 additional temperature sensors on the microbases without switching on the PMT HV. Only the microcontroller of the PMT microbase was powered and temperature as well as the HV at the tenth dynode—which is 0 V during this operation stage—were saved. All in all,  $8 + 24$  temperature sensors were read out in addition to the absolute time, wirepair current, wirepair voltage, pressure, power consumption and the PMT HVs.

Several hours were measured with the mainboard switched on but the PMT HVs switched off allowing the system inside the mDOM to reach a thermal equilibrium. Then, the HVs were switched on (“HV on”). Each PMT with its microbase had been calibrated at the PMT testing facility in Aachen (introduced in [90]) at  $-20^{\circ}\text{C}$ . The nominal HVs are uploaded in a global database and were used in this measurement. Changes in the nominal HV with temperature are of the order of few volts in the used temperature range and its contribution can be neglected with respect to the total power consumption. During the operation stage “HV on”, the same parameters as for “mb on” were available to be read out.

After some time, the HV was switched off (“HV off”). Still, all parameters were available. Similar to the operation stage “HV on”, the measurement ran several hours in the operation stage “HV off” before the HV interlock of the PMTs in the miniFieldHub was disabled.

As soon as the mainboard was switched off in the next operation stage (“mb off”), all microbase sensors—24 microbase temperatures and 24 PMT HVs of the tenth dynode—became unaccessible. Furthermore, the pressure sensor could not be read out any more. The same applies for the six temperature sensors of the mainboard. Because only the ICM was still running, the only remaining

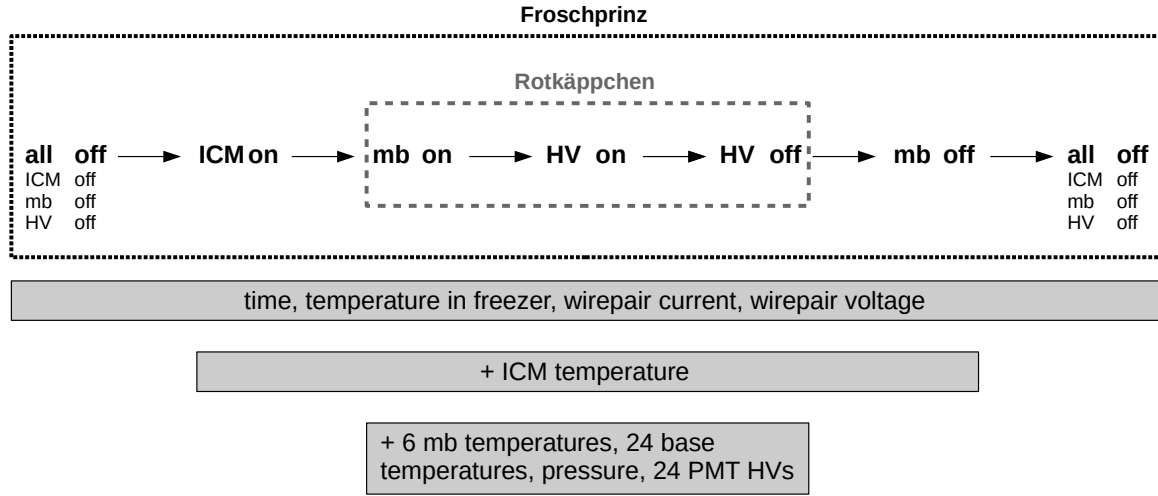


**Figure 5.3:** Schematic of the measurement procedure of Froschprinz (black dotted box) and Rotkäppchen (gray dashed box). The gray shaded boxes indicate which parameters are accessible in which operation stage.

active temperature sensor inside the mDOM was the one embedded in the ICM. Absolute time, temperature of the temperature sensor S0, wirepair current and voltage remained available.

In the last operation stage, the ICM was switched off. Thus, the entire mDOM was switched off again and therefore, the operation stage is called “all off”. Only absolute time, freezer temperature, wirepair current and voltage could be monitored. To investigate the cooling process after the ICM was switched off, all available parameters were monitored for a few hours in the operation stage “all off”.

The measurement procedure described above was performed for Froschprinz at  $-27^{\circ}\text{C}$  and at  $-49^{\circ}\text{C}$ . Both temperatures were also used for Rotkäppchen. However, the measurements of Rotkäppchen contain less measured operation stages than for Froschprinz, because Rotkäppchen was always running. In Figure 5.3, the gray dashed box indicates the performed operation stages for the measurements with Rotkäppchen. Investigating only the three operation stages “mb on”, “HV on” and “HV off”, all parameters were accessible during the entire measurement. To ensure that the temperature sensor S0 in Froschprinz’s box was not heated up and could be used as a reference for the freezer temperature, Froschprinz was switched off during the measurements with Rotkäppchen. Summing up, four measurements were performed which are referred to as follows: Froschprinz  $-49^{\circ}\text{C}$ , Rotkäppchen  $-49^{\circ}\text{C}$ , Froschprinz  $-27^{\circ}\text{C}$ , and Rotkäppchen  $-27^{\circ}\text{C}$ .

### 5.3 Temperature behavior of an mDOM

As described in Section 2.4, many electronic components are included in the mDOM. Each of these components produces heat which has to be dissipated to the outer surface of the mDOM. Glass vessel, optical gel, and PMT support structure are the outermost mDOM components resulting into approximately 15 mm of insulating material which complicates the heat transport. Although the mDOM is deployed in ice at temperatures between  $-27^{\circ}\text{C}$  and  $-19^{\circ}\text{C}$  (see Subsection 2.1), it is in question whether the outside temperature is able to cool the mDOM sufficiently. Some electronic

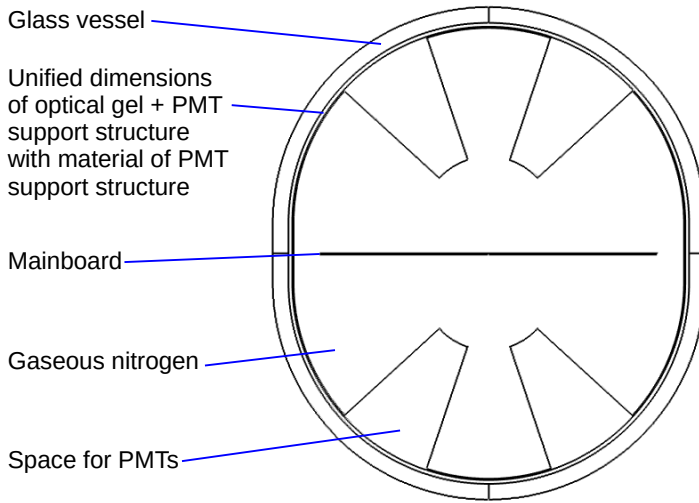


**Figure 5.4:** Cross-section of the 3D geometry used for the COMSOL Multiphysics simulation.

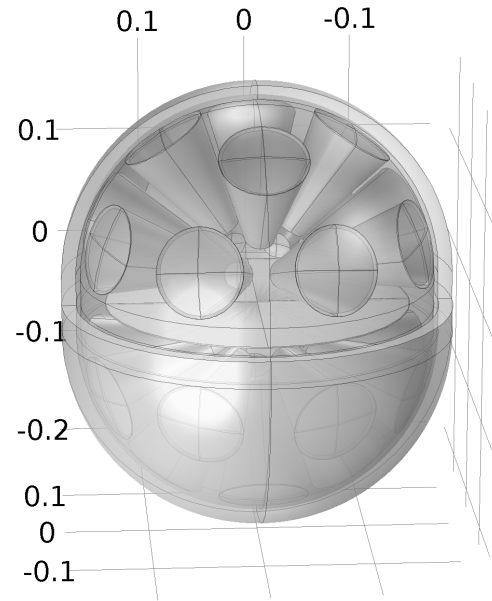


**Figure 5.5:** Used geometry for the COMSOL Multiphysics simulation.

parts might warm up above their specifications, which can impact the performance of electronic components or even result in failures. For example, higher temperatures of the photocathodes of the PMTs lead to higher darkrates (see Subsection 1.3.3.3). Contributing significantly to the overall noise background of the mDOM, too high darkrates can worsen the reconstruction of the measured neutrino signals. Moreover, the bandwidth of data transfer to the surface is limited. Therefore, as small PMT darkrates as possible are required. Once the first working mDOM was available, the temperature behavior of an mDOM could be measured.

### 5.3.1 Simulation

Before the first mDOM was produced, questions concerning the temperature behavior of an mDOM arose. The main question was whether the cooling of the electronic inside the mDOM works well enough with the current design or whether additional cooling elements such as used in the DOMs [29] of the KM3NeT experiment are necessary. Therefore, a simulation with COMSOL Multiphysics [107] was used to investigate the temperature behavior before the first prototype was available. It was planned to simulate the temperature behavior of an mDOM in air at first and compare it to later measurements in air. When simulation and measurement agree with each other sufficiently, a simulation in ice could be implemented. Measurements in ice, especially at the corresponding pressure, were not feasible.

Before a simulation run could be started, the mDOM geometry had to be defined. The material with characteristic properties such as thermal conductivity or thermal coefficients was assigned to each component. Afterwards, the entire geometry was meshed which means that all components were modelled with tetrahedrons. Next, the desired physical process, as for example heat conduction, was defined. After that, the simulation was started.

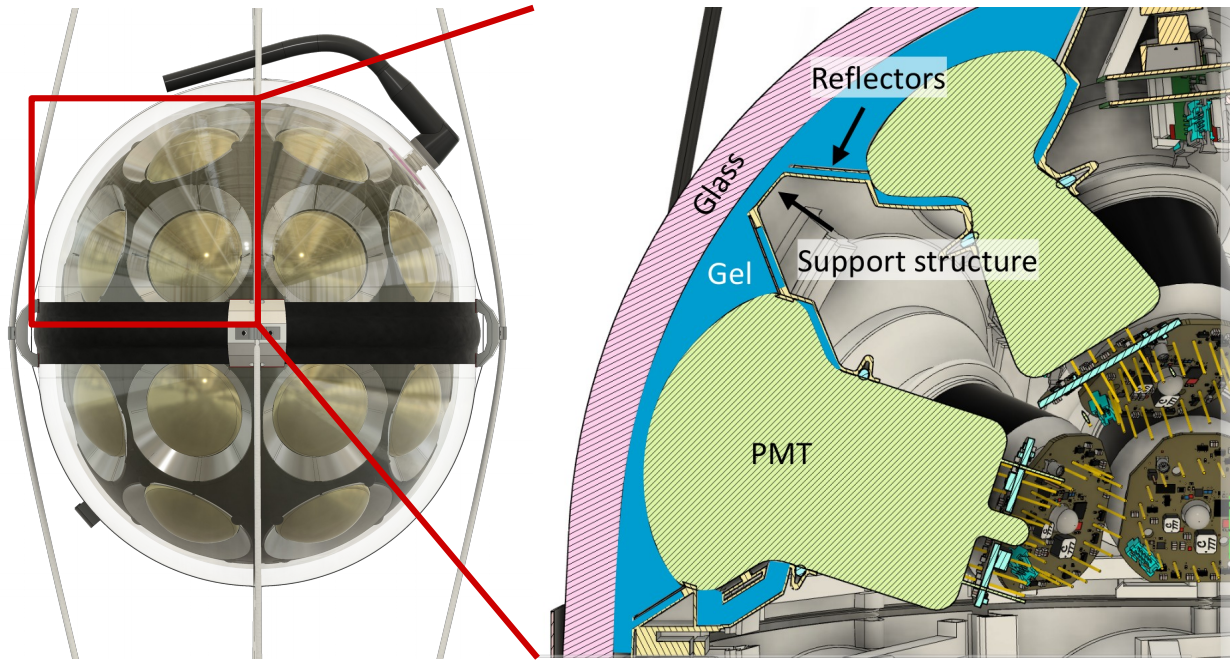


**Figure 5.6:** Technical drawing of the entire mDOM to scale (left). Cross-section to scale of an mDOM segment showing the areas filled with optical gel in blue (right). Pictures taken from [60] (left) and [108] (right).

In principle, it is possible to import the computer-aided design (CAD) step file with the mDOM geometry into COMSOL Multiphysics, but the geometry is too complex and contains too many fine structures. Instead, a simplified model of the mDOM geometry was built within COMSOL Multiphysics itself. Figure 5.4 shows a cross-section through the xy-plane. The outermost structure is the pressure vessel of 13 mm thickness and an outer diameter of 356 mm consisting of two hemispheres with a 50 mm cylindrical part in between (total outer dimensions: 356 mm width and 406 mm height). The mDOM pressure vessel consists of borosilicate glass. However, silica glass was used in the simulation, because no other option existed. The next component is the optical gel. In reality, the thickness of the optical gel varies depending on the position inside the mDOM. Figure 5.6 shows an enlarged section of the areas filled with optical gel near the PMTs. The thickest area of optical gel is where the PMT touches the reflector ring. In contrast, the optical gel is thinner in front of the PMTs and in front of the PMT support structure. For simplification, the optical gel has a constant thickness of  $3.18 \text{ mm} + 1 \text{ mm}$  in the simulation. Normally, the PMT support structure would be the third component. Being only 1 mm thick and therefore causing problems with the meshing, the PMT support structure was joint with the optical gel. Because the thermal conductivity of the optical gel (silicone) is smaller than those of the PMT support structure (polyamide), silicone was used as material for the joint component. This approach falsifies the results, but it prevents from underestimating the equilibrium temperature of the mDOM. Neglecting the electronic parts inside, a PMT basically consists of an evacuated borosilicate glass tube. Therefore, the PMTs were defined as hollow parts with no defined material. Thus, they do not contribute to the heat transport. Moreover, the microbase was incorporated into the PMT geometry which is a segment of a sphere with a length of 107 mm. This number corresponds

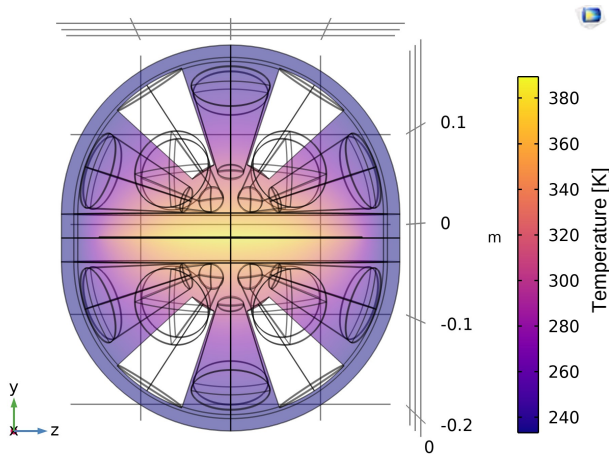


**Figure 5.7:** Temperature distribution inside the mDOM for the stationary solution. The only included heat transport is conduction while convection is not included.

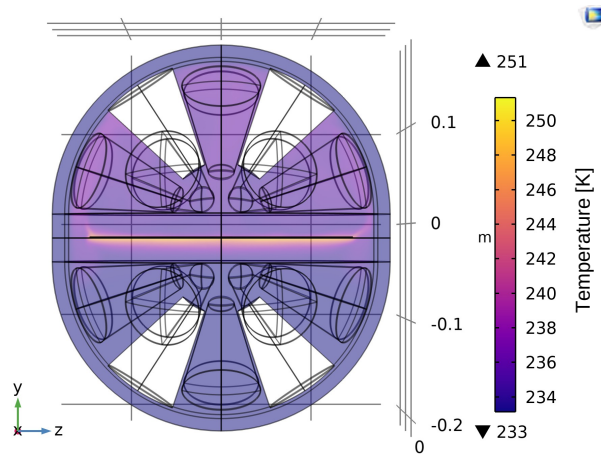


**Figure 5.8:** Temperature distribution inside the mDOM for the time dependent solution 10s after switch on of the electronics. Conduction and convection are both included.

to the length of PMT plus microbase. In Figure 5.4, only four polar PMTs and no equatorial ones are visible because no equatorial PMTs exist in the  $xy$ -plane. The three-dimensional (3D) geometry can be seen in Figure 5.5. In the middle of the mDOM, a copper disk of 277 mm diameter and 1 mm thickness represents the mainboard with no physical contact to the other components neglecting the mounts attaching the mainboard to the PMT support structure. The rest volume between mainboard, PMTs and PMT support structure was filled with gaseous nitrogen. On the first attempt, a pressure of 1 bar was used instead of 0.5 bar. All physical dimensions were adopted from the mDOM CAD drawing, up-to-date at the time the simulation was performed.

For the simulation of the thermal behavior of the mDOM, the mainboard was defined as a heat source with a power of 5 W which was switched on in the beginning of the simulation. The initial temperature of all components was  $-40^{\circ}\text{C}$ . The outer surface of the glass vessel was set to permanently  $-40^{\circ}\text{C}$  working as a perfect heat sink.

COMSOL Multiphysics uses differential equations to describe the physical processes. To learn about the temperatures in normal operation mode of the mDOM, it is necessary to find the thermal equilibrium of the system. Therefore, it was tried to find a solution that does not depend on time, in other words, a stationary solution. In a first simulation approach, the only included mode of heat transport was conduction. Figure 5.7 shows the stationary solution for this scenario. A cross-section of  $yz$ -plane of the mDOM is shown. The temperature is indicated by the color. Yellow indicates higher temperatures and blue lower temperatures. While glass vessel, optical gel + PMT-support-structure and the outer areas of the gas stay close to  $-40^{\circ}\text{C}$ , the gas in the vicinity of the mainboard is heated up to  $110^{\circ}\text{C}$ . Because convection can occur in gasses and can be the dominant heat transport, the scenario is unrealistic and a simulation including convection is necessary.

In a second approach, the same parameters were used as before, but this time, convection was included. First, it was tried to find a stationary solution similar to the scenario described before where convection was disabled. Unfortunately, such a solution was not found. For that reason, the differential equation describing the temperature evolution and the gas movement inside the

mDOM was calculated in discrete time intervals. The result of the first simulated interval was used as input for the simulation of the second time interval and so on. This procedure was repeated a certain number of times in order to evolve the simulation in time (time-dependent solution). The simulated time is 10 s which needs a computation time of about six days. Figure 5.8 shows a cross-section of the yz-plane and the temperature after 10 s in color scale. Again, glass vessel and optical gel + PMT-support-structure remain close to the mDOM surface temperature of  $-40^{\circ}\text{C}$  while mainly the gas is heated. In contrast to the stationary solution where the gas is equally heated around the mainboard, gravity leads to a difference between upper and lower hemisphere. Being the only heat source in the mDOM, the mainboard heats up the surrounding gas. Because the warm gas expands and is then lighter than the outer cooler gas, the warm gas layers in the upper hemisphere rise up and distribute over the entire gas volume above the mainboard. The situation in the lower hemisphere, however, is different. The heated gas is blocked by the mainboard and cannot propagate upwards. Therefore, it forms a layer of hot gas below the mainboard with temperatures up to  $-23^{\circ}\text{C}$ . The remaining gas of the lower hemisphere does not heat up.

Both simulation approaches have downsides. The first simulation neglects convection which is a relevant heat transfer for gasses and also for the mDOM. Using only conduction as heat transfer makes the simulation unrealistic. The second simulation is time-consuming. Simulating 10 s takes more than six days of computation time. Assuming the mDOM needs one day to reach equilibrium, a time-dependent simulation would run about 142 years<sup>1</sup>. The simpler the geometry, the shorter is the time needed for the simulation. Because the geometry in the simulation is already simplified compared to reality, further simplifications do not seem appropriate. The real mDOM has many fine structures as well as sharp edges which complicates the meshing process and increases the simulation time. Furthermore, thermal radiation should be included in the simulation for a complete description of the heat transfer inside the mDOM. Due to these simulation downsides, it was decided to focus on measurements.

### 5.3.2 Power consumption

As explained in Section 5.1, the miniFieldHub applies the voltage to the mDOM. Together with internal resistors, the applied voltage results into a current. By multiplying input current and input voltage, the total power consumption is calculated. In the following, it is assumed that the whole mDOM power consumption is converted into heat influencing warm-up and cooling times as well as the equilibrium temperature of the mDOM.

The miniFieldHub can read out wirepair current and wirepair voltage (see Section 5.2). The wirepair voltage is the voltage applied to the mDOM. Similarly, the wirepair current is the current directly going into the mDOM. Their product leads to the power consumption from the wirepair readouts. Because the miniFieldHub is always running, wirepair current and wirepair voltage are always accessible.

Figure 5.9 shows the power consumption over time for Froschprinz  $-27^{\circ}\text{C}$ . In bold red, the power consumption from the wirepair readouts is shown ranging over the entire measurement duration. The vertical dashed lines separate the seven operation stages of the mDOM: “all off”, “ICM on”, “mb on”, “HV on”, “HV off”, “mb off”, and “all off”. Below the operation stage, the mean power consumption from the wirepair readouts for the respective operation stage is written. Less than 1 W are consumed by the ICM and only about 0.17 W—low power consumption was a require-

<sup>1</sup>Measurements in Section 5.3.4 show that the time needed to reach equilibrium is about 28 h.

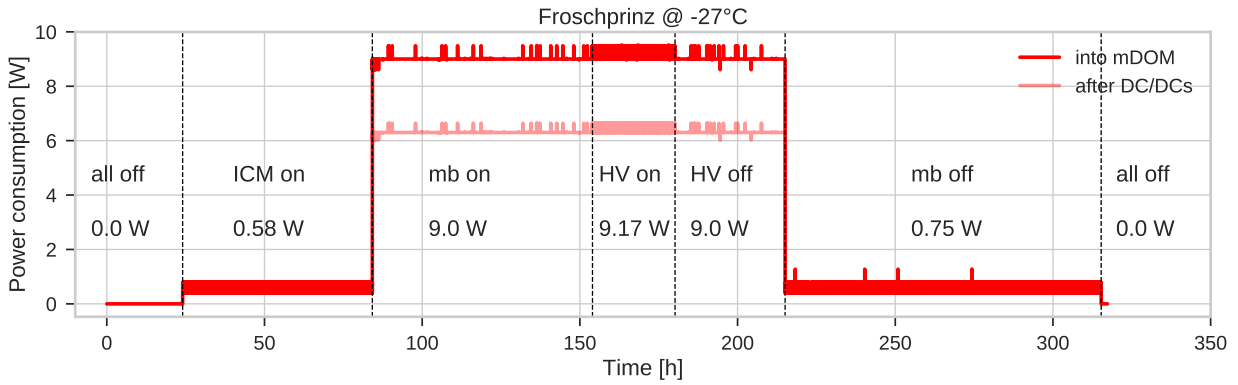


**Figure 5.9:** Power consumption of the mDOM for the different operation stages shown for Froschprinz at  $-27^{\circ}\text{C}$ .

ment—are consumed by all 24 PMTs together with their microbases. The main power—around 9 W—is consumed by the mainboard. Figure 5.9 indicates that the main temperature increase inside the mDOM is expected when the mainboard is switched on. Contributions of ICM and the PMTs to the overall temperature increase can be expected to be small.

Effectively, the mDOM mainboard needs only 6 W of power when it is running. However, about 9 W are supplied due to losses on the mainboard. Inside the mDOM, the 96 V from the miniFieldHub are divided into smaller voltages by two DC-to-DC converters (DC/DCs). Their efficiency is smaller than 100 %. About 1 W is lost by the first DC-to-DC converter and about 2 W are lost by the second DC-to-DC converter<sup>2</sup>. The available power after the two DC-to-DC converters—about 6 W when the mainboard is running—is shown in light red in Figure 5.9. Froschprinz  $-49^{\circ}\text{C}$ , Rotkäppchen  $-49^{\circ}\text{C}$ , and Rotkäppchen  $-27^{\circ}\text{C}$  show similar results.

Knowing the power consumption of the electronic components, the temperature behavior of the mDOM can be investigated. How the power consumption influences the temperature behavior of the mDOM is discussed in the following sections.

### 5.3.3 Equilibrium temperatures

Investigating the equilibrium temperatures inside an mDOM indicates whether the cooling of the mDOM works sufficiently or whether any components heat up to above their specified temperature. Therefore, the temperatures inside an mDOM were measured. As explained in Section 5.2 and Figure 5.3, several temperature sensors exist in the measurement setup. One temperature sensor is placed on top of Froschprinz and is always available regardless of the mDOM operation stage. For each PMT, the microcontroller’s temperature of the microbase can be read out. An overview of the other seven temperature sensors on the mainboard is given in Figure 5.10. Plugged onto the mainboard, the ICM includes an FPGA with an internal temperature sensor. Furthermore, the FPGA on the mainboard contains an internal temperature sensor. Accelerometer S1, magnetometer S2, and pressure sensor S3 also have a temperature sensor each. Additionally, two bare temperature sensors S4 and S6 are placed at two different positions on the mainboard.

<sup>2</sup>measured by Karl-Heinz Sulanke for a revision 2 mainboard, small differences to the revision 1 mainboard are expected.

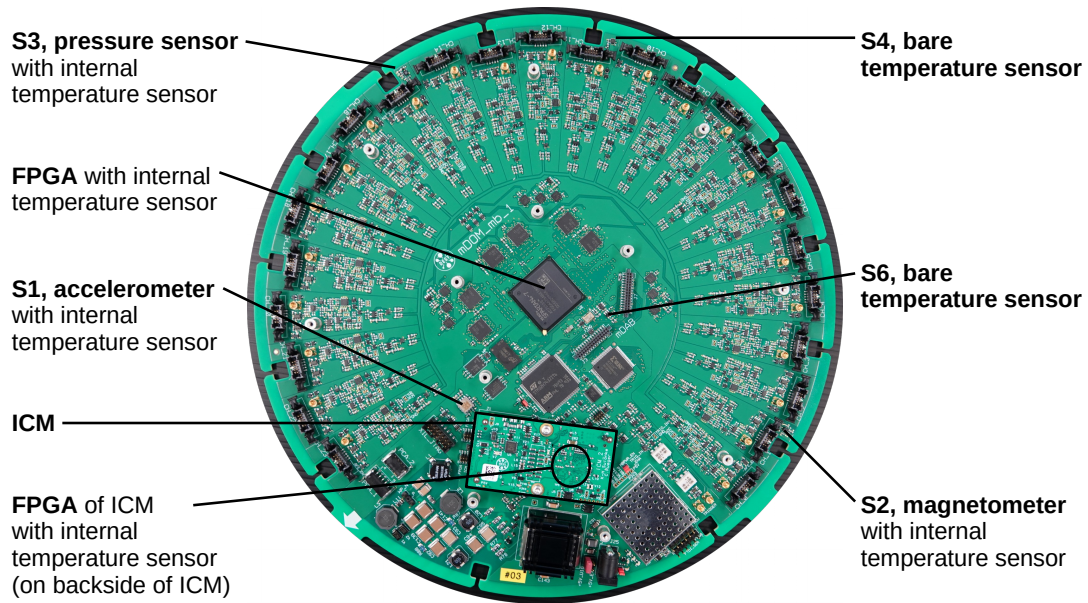


**Figure 5.10:** Photograph of the mainboard with the ICM and the location of the temperature sensors on the mainboard. Modified from [71].

The goal of this study was to operate an mDOM under almost in-ice conditions. Normal operation includes outside mDOM temperatures between  $-27^{\circ}\text{C}$  and  $-19^{\circ}\text{C}$  (see Subsection 2.1). Therefore,  $-27^{\circ}\text{C}$  was chosen as a typical in-ice temperature. Because low temperatures are critical for electronic parts and the ice can reach temperatures below  $-30^{\circ}\text{C}$ , further measurements were performed at  $-49^{\circ}\text{C}$ . For realistic conditions, the electronics were operated similarly to later in ice. A realistic scenario is an mDOM in the dark with the mainboard switched on and the PMTs running with their nominal HV. As explained in Section 5.2, a cold start was performed with Froschprinz to emulate start-up and operation in ice.

All temperature and other sensors were read out periodically as described in Section 5.2. Figure 5.11 shows the temperature distribution of Froschprinz over time at  $-27^{\circ}\text{C}$ . The upper plot shows the twelve microbase (uBase) temperatures of the upper hemisphere. The color indicates the PMT position of the PMT the microbase is connected to. Accordingly, the lower plot shows the microbase temperatures of the lower hemisphere. In the middle plot, the seven temperatures of the mainboard are shown as well as the temperature from the temperature sensor S0 on top of Froschprinz. The dashed lines mark the time stamps where the operation stage changes. For instance, the first dashed line is the time when the ICM was switched on. At the beginning of the measurement (0h), the mDOM was switched off for two days and only the temperature sensor S0 was read out. The mean temperature is  $-27^{\circ}\text{C}$ . When the ICM is switched on, the temperature readout of the FPGA on the ICM is working and the ICM temperature can be measured, too. Increasing steeply, the temperature curve flattens after a few hours. The moment the mainboard is switched on, all temperature sensors are available. All show a similar behavior. A steep increase is followed by a slow settling at a certain temperature. From investigations of the power consumption (see Figure 5.9), it is expected that the mainboard acts as the main heat source while ICM and HV have a smaller contribution. These assumptions are verified. Switching on the PMT HV leads

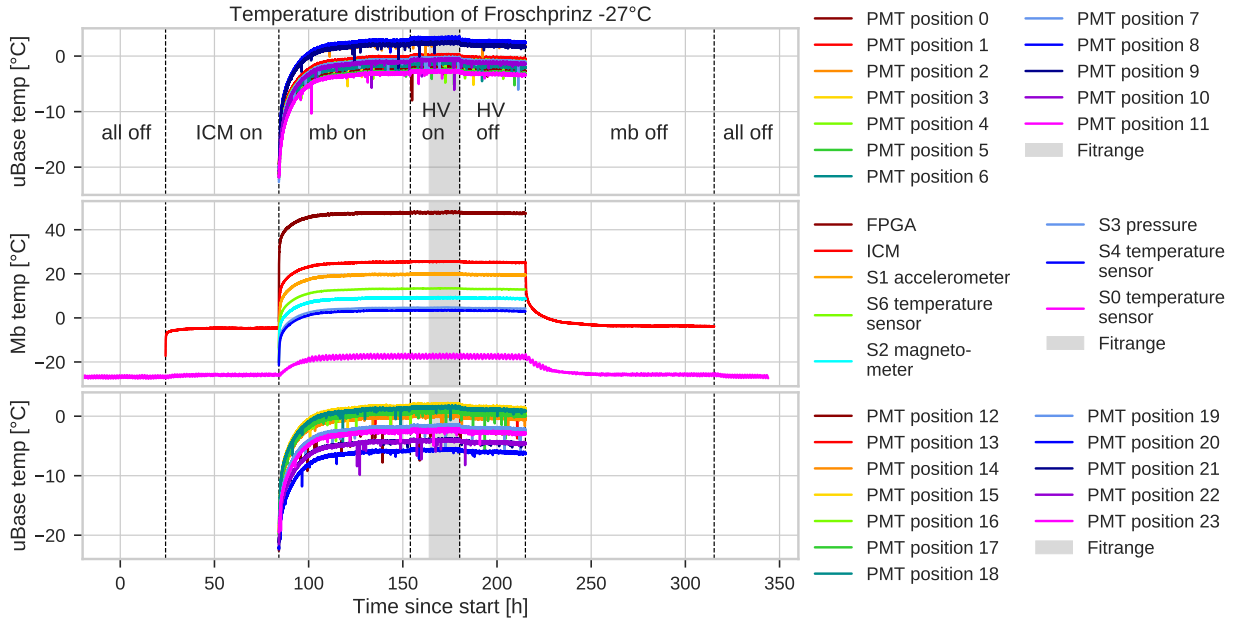


**Figure 5.11:** Temperature behavior over time of Froschprinz at  $-27^{\circ}\text{C}$ .

to a temperature increase of less than 1 K. Although the temperature of the ICM increases more than 10 K when the ICM is switched on, the outer mDOM temperature changes only by 1 K while it increases by 8 K when the mainboard is switched on. Furthermore, all temperature sensors except the ICM are still close to  $-20^{\circ}\text{C}$  when the mainboard is switched on. On the other hand, all temperatures inside the mDOM increase by more than 15 K after the mainboard is powered. The cold start of Froschprinz does not work without problems. When mainboard and ICM have been switched off for many hours or few days, respectively, and it was tried to switch on the ICM, communication failed at the first attempt. Investigations of the problem showed neither a significant dependence on the temperature nor on the time the mDOM was switched off. This behavior was observed for both Froschprinz and Rotkäppchen. However, the problem could always be solved by retrying the switch-on procedure. Later revisions of the mainboard will be tested with respect to this behavior.

The parts known to have the largest power consumption are located in the middle of the mainboard and in the segment around the ICM. Their placement explains the temperature distribution when the mainboard is on and in thermal equilibrium. Warming up to more than  $40^{\circ}\text{C}$ , the FPGA on the mainboard is the warmest measured part of the mDOM followed by the ICM, S1, and S6, which are all located close to parts consuming much power. Located at the outer edge of the mainboard, S2, S3, and S4 measured the lowest temperatures on the mainboard. With a low power consumption and a relatively large distance to the mainboard FPGA, the temperatures measured by the sensors on the microbases are the lowest of the mDOM. Why the temperatures of the microbases show sharp drops from time to time is not entirely understood. Most likely is a misreading of the ADC values from time to time [109]. Similar to switching on the PMT HVs, switching them off barely changes the temperature. As soon as the mainboard is turned off, only the ICM and S0 are available. Both slopes of the temperature change decrease steeply at first and

then flatten. They reach similar temperatures as before the mainboard is powered. When the ICM is switched off, the temperature outside the mDOM decreases to  $-27^\circ\text{C}$  again.

To analyze the data more quantitatively, the equilibrium temperatures for “HV on”—the realistic scenario in ice—were determined. Therefore, all data 10 h after the PMT HVs were switched on until they were switched off again were used. The corresponding area is called fit range and is shaded in gray in Figure 5.11. The length of the fit range varies between the four measurements: 7 h for Froschprinz  $-49^\circ\text{C}$ , 16 h Froschprinz  $-27^\circ\text{C}$ , 29 h for Rotkäppchen  $-49^\circ\text{C}$ , and 40 h for Rotkäppchen  $-27^\circ\text{C}$ . A linear fit was performed to all data inside the fit range for each curve separately and for each of the four temperature measurements. Being always smaller than  $0.01^\circ\text{C/h}$ , the slope is so small that thermal equilibrium is assumed. Mean value and standard deviation were determined by a `python` function. Ignoring the remaining slope, the statistical error  $\text{err}_{\text{stat}}$  was calculated as:

$$\text{err}_{\text{stat}} = \frac{\sigma}{\sqrt{n}}, \quad (5.1)$$

where  $\sigma$  is the standard deviation and  $n$  is the number of datapoints. For all measurements and curves, the statistical error is of the order of  $0.01^\circ\text{C}$ . With that, the statistical error is smaller than the accuracies of the temperature sensors which can be regarded as a systematic error. Table 2 in Appendix 1 contains all absolute mean values as well as the statistical errors. Moreover, Table 1 gives an overview of the accuracy of all temperature sensors. Typically, the accuracy is about  $\pm 1^\circ\text{C}$ , but it can also be  $\pm 2^\circ\text{C}$  or larger (mainboard FPGA:  $\pm 4^\circ\text{C}$  as a maximum). However, the temperature sensors can detect relative temperature changes. For comparisons between the four measurements (Froschprinz  $-49^\circ\text{C}$ , Rotkäppchen  $-49^\circ\text{C}$ , Froschprinz  $-27^\circ\text{C}$ , and Rotkäppchen  $-27^\circ\text{C}$ ), the temperature difference  $\Delta T$  is used instead of the absolute equilibrium temperature:

$$\Delta T = T_{\text{meas}} - T_{\text{ref}}, \quad (5.2)$$

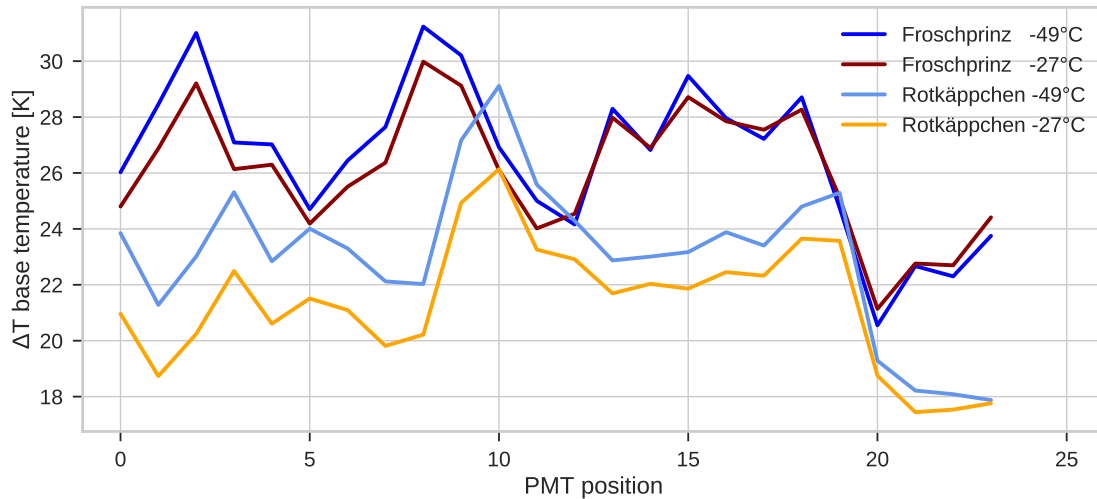
where  $T_{\text{meas}}$  is the measured absolute temperature of each temperature sensor and  $T_{\text{ref}}$  is the reference temperature of each measurement. The mDOM ambient temperature serves as the reference temperature. For Froschprinz, the reference temperature is the mean value of sensor S0 before the ICM is switched on and for Rotkäppchen, it is the mean value of sensor S0 in the time window of the fit range. These differences exist because the used temperature sensor was in Froschprinz’s box and was heated up when Froschprinz was running. During the measurements with Rotkäppchen, Froschprinz was switched off (see Section 5.2) and is not heating S0. In Table 5.1, the temperature differences to the reference temperature of the four measurements for all temperature sensors inside the mDOM are compared. In case of the microbase temperatures ( $\Delta T$  Bases), only the minimum and maximum temperatures are shown. As the hottest part in the mDOM, the FPGA on the mainboard is up to about 77 K warmer than the mDOM ambient temperature. The microbases only heat up to about 31 K above ambient temperature. For all temperature sensors, Froschprinz is always few degrees warmer than Rotkäppchen. Because Froschprinz is inside a shipping box and heats up the box as well as the air inside, this behavior is expected. In addition to that, the temperature differences at  $-27^\circ\text{C}$  are systematically smaller by few degrees than for  $-49^\circ\text{C}$ . This difference can be explained by the temperature dependence of the heat capacity. Because convection occurs in the mDOM, the heat capacity of the gas defines how fast the heat of the electronics is transported away. However, the heat capacity is larger for larger temperatures resulting in a better cooling and therefore a smaller temperature increase for larger ambient temperatures. Taking this correlation into account, smaller temperature differences are

**Table 5.1:** Temperature differences to the reference temperature for all four measurements.

		Froschprinz		Rotkäppchen	
		−49 °C	−27 °C	−49 °C	−27 °C
Reference temperature	[°C]	−49.06	−26.76	−49.19	−26.45
$\Delta T$ FPGA	[K]	76.78	74.59	73.24	69.95
$\Delta T$ ICM	[K]	54.003	52.33	51.03	48.52
$\Delta T$ S1 accelerometer	[K]	47.04	46.72	46.96	45.65
$\Delta T$ S6 temp. sensor	[K]	41.75	40.15	40.31	37.45
$\Delta T$ S2 magnetometer	[K]	38.22	35.93	36.08	32.47
$\Delta T$ S3 pressure sensor	[K]	33.57	31.44	29.89	26.86
$\Delta T$ S4 temp. sensor	[K]	31.55	30.25	29.95	27.37
$\Delta T$ Bases [min, max]	[K]	[20.55, 31.24]	[21.14, 29.98]	[17.88, 29.11]	[17.44, 26.14]

expected for larger ambient temperatures which is observed in Table 5.1. For later produced mDOMs, the mainboard FPGA is thermally coupled to the mDAB (a picture of the mDAB is shown in Figure 2.7). Thereby, the mDAB works as a cooling element for the FPGA. This thermal coupling extends the application range of the FPGA to higher ambient mDOM temperatures and ensures enough clearance especially for room temperature measurements. Measurements performed by Sarah Mechbal and presented in [110] showed that the measured temperature of the FPGA is about 10 K lower than without the coupling.

The temperature distribution of the microbases can be seen in Figure 5.12. The temperature difference of the microbases is plotted against the PMT position of the corresponding microbase for all four measurements (see Figure 2.4 for a visualization of the PMT position). For one mDOM, the two measurements at different temperatures show a similar behavior. For instance, the microbase of PMT position 10 of Rotkäppchen has the largest temperature at −49 °C and also at −27 °C. In

**Figure 5.12:** Temperature differences to the reference temperature for all microbases of all four measurements.

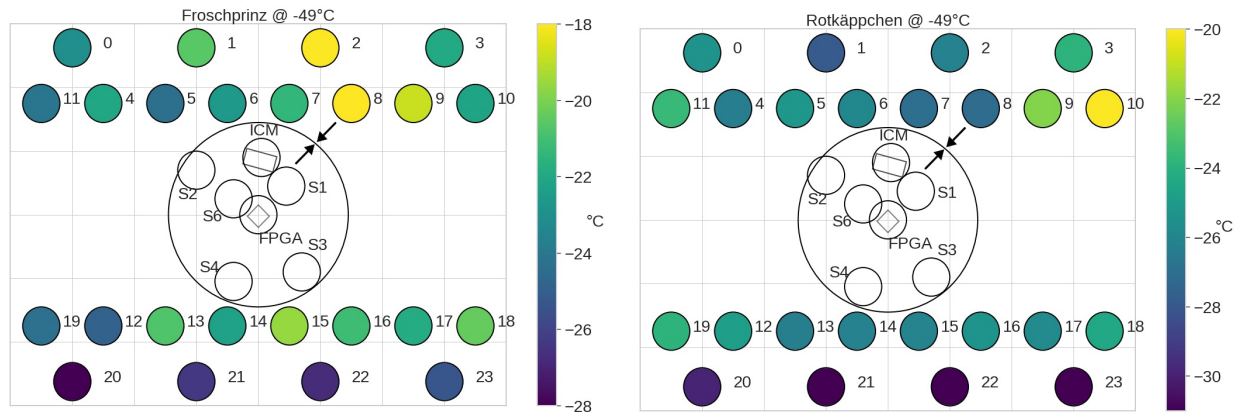


**Figure 5.13:** Absolute temperature distribution of the microbases at -49°C for Froschprinz (left) and Rotkäppchen (right).

contrast to that, differences occur between Froschprinz and Rotkäppchen. For Froschprinz, the microbases of PMT positions 2 and 8 are the hottest ones while for Rotkäppchen, the microbase of PMT position 10 has the largest temperature. However, the microbases at the PMT positions 20-23 always have the coldest temperatures in all measurements. A possible explanation for their temperature behavior is the location of the microbases with respect to the mainboard. Figure 5.13 shows a plot with the spatial distribution of the absolute microbase temperature at  $-49^{\circ}\text{C}$  for Froschprinz on the left and Rotkäppchen on the right. Each colored circle corresponds to one microbase. Next to the circle is the number of the PMT position the microbase is associated with. While 0-11 belong to the upper hemisphere, the numbers 12-23 correspond to the lower hemisphere. Each hemisphere has four polar PMTs with the largest distance to the mainboard and in another row, eight equatorial PMTs. PMT 8 is aligned to the arrow on the mainboard, which is drawn not to scale with the most important components of the mainboard. The color indicates the absolute temperature in  $^{\circ}\text{C}$ . As shown in Figure 5.12, the microbases at the PMT positions 20-23 are always the coldest ones. These microbases correspond to the polar PMTs of the lower hemisphere. The simulation results in Figure 5.8 indicate that almost no convection exists in the lower hemisphere. Therefore, the gas of the lower hemisphere is barely heated up in the simulation except for a thin, hot layer formed directly below the mainboard. In reality, the microbases generate some heat and are expected to cause convection also in the lower hemisphere. Though, with respect to the low power consumption of the microbases, their contribution is assumed to be small. To sum up, suppressed convection in the lower hemisphere can explain the low temperatures of the microbases at the PMT positions 20-23.

One might expect that the microbases directly above the warmest parts of the mainboard—the FPGA on the mainboard and the sector around the ICM—are heated up more than the other microbases. While position number 7 is located above the hottest parts, it has not the highest microbase temperature in the measurements. For Froschprinz, the microbases at the PMT positions 2 and 8 have the highest temperature and for Rotkäppchen, the hottest microbases are the ones at PMT positions 9 and 10. Different explanations exist for this behavior. To begin with, the accuracy of the temperature can be up to  $\pm 1^{\circ}\text{C}$  off. Another aspect is that the mDOMs are not aligned 100% vertically, but might be slightly tilted. This tilt can be different for Froschprinz and Rotkäppchen, which could explain the difference in the measurements. In addition to that, many

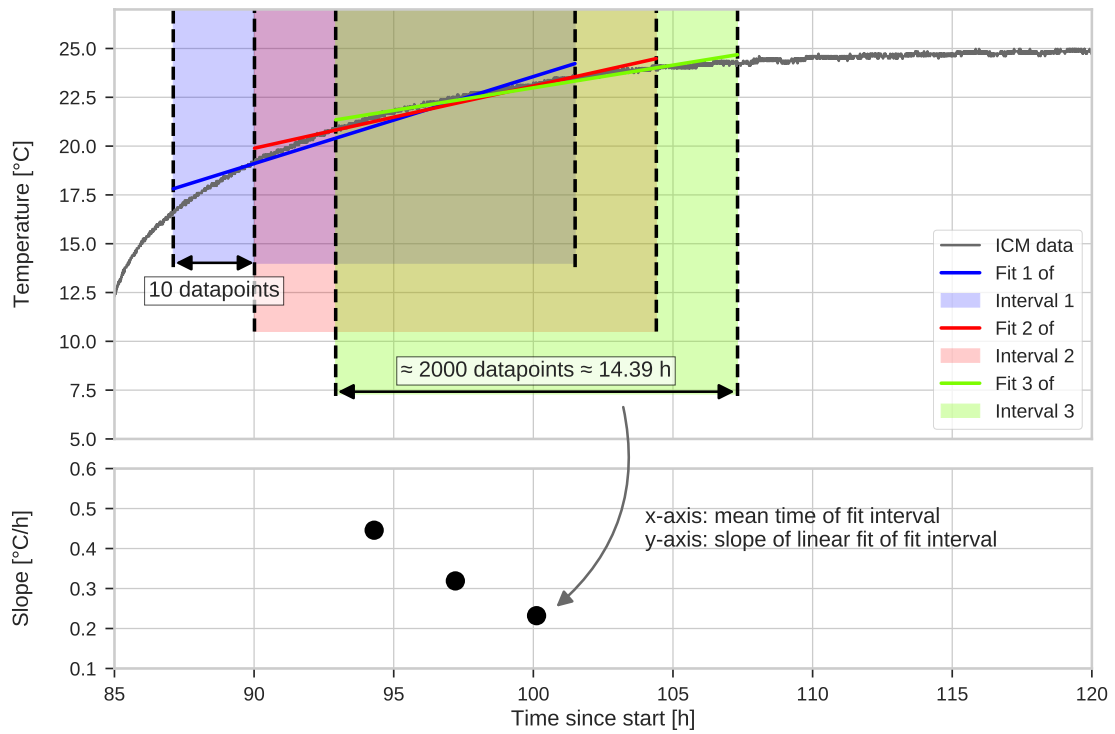
cables run through the gas volume of the mDOM. Each microbase is connected to its AFE channel on the mainboard by two cables of about 35 cm length. The cables do not lie in exactly the same position for each mDOM and influence the convection behavior, which can lead to temperature differences of the microbases between Froschprinz and Rotkäppchen.

All in all, the temperature behavior of the mDOM is as expected and the cooling works sufficiently. All electronic parts are cooled enough and no part runs outside its temperature specification. As the hottest part in the mDOM, the FPGA on the mainboard is about 70 K to 77 K hotter than the outside temperature. The microbases heat up to about 21 K to 31 K above ambient temperature. Some microbases in the upper hemisphere form hotspots, but their position is not the same for Froschprinz and Rotkäppchen. The four polar microbases of the lower hemisphere have the lowest measured temperatures in the mDOM.

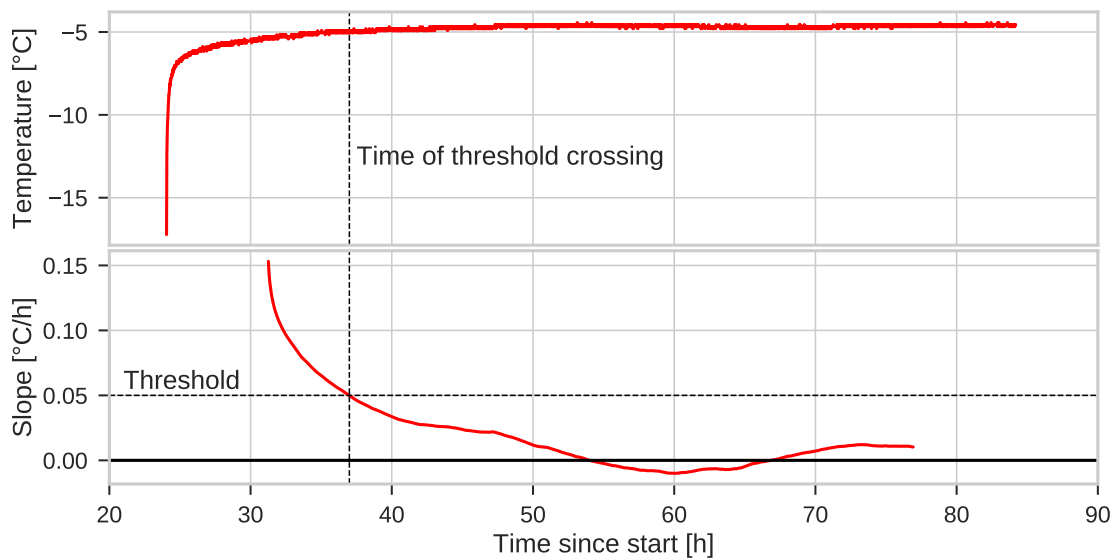
#### 5.3.4 Warm-up and cooling times

Not only the exact equilibrium temperature of an mDOM is part of the temperature behavior, but also the time needed to reach equilibrium. Of special interest for laboratory tests is the warm-up and cooling time. Ideally, thermal equilibrium is reached when the slopes of the warm-up or cooling curves are 0.

To investigate the warm-up and cooling times, the measurement Froschprinz  $-27^{\circ}\text{C}$  was used. First of all, the temperature measurement shown in Figure 5.11 was divided into five different fit regions: “ICM on”, “mb on”, “HV on”, “HV off”, and “mb off”. The data of the different temperature sensors were analyzed separately for all fit regions. During “ICM on” and “mb off”, only data from the temperature sensor on the ICM were recorded. In contrast, 24 temperature sensors on the microbases and 7 on the mainboard were available to record data during “mb on”, “HV on”, and “HV off”. Since it was not located inside the mDOM and its measured temperatures oscillated with a large amplitude around the mean value, sensor S0 was not included in the analysis. In total,  $(24 + 7) \cdot 3 + 2$  temperature data sets were recorded. Next, the recorded temperature values of all data sets were plotted over time and the slope of each temperature curve was determined. In the following, a linear approximation was used to calculate warm-up and cooling times, since no suitable fit function was found. Figure 5.14 illustrates the basic procedure. Each of the  $(24 + 7) \cdot 3 + 2$  temperature data sets were divided into overlapping fit intervals. Each fit interval has a length of about 2000 datapoints corresponding to about 14.39 h. This interval length was chosen in order to average over the temperature variation caused by the permanent switch-on and switch-off of the freezer. Each fit interval was fitted with a line until the last interval extends to the last datapoint of the data set. The mean time of each interval is shown on the x-axis in the lower plot of Figure 5.14. On the y-axis, the corresponding slope is shown (slope curve). This procedure to approximate the slope can be regarded as sampling over the whole temperature curve which reduces the number of datapoints of the slope curve by a factor of ten compared to the temperature curve. The slope curve starts 1000 datapoints later and ends 1000 datapoints earlier than the temperature curve. This feature can be seen in the lower plot of Figure 5.15 compared to the associated temperature curve (upper plot). Over time, the temperature slowly reaches equilibrium. The slope decreases. It is not sure where the bumps in the slope between 45 h and 75 h come from. Their periodicity suggests that they may come from sunrise and sunset changing the temperature in the laboratory and the cooling behavior of the freezer. However, the variation of the bumps stays below the threshold and thus, was neglected.



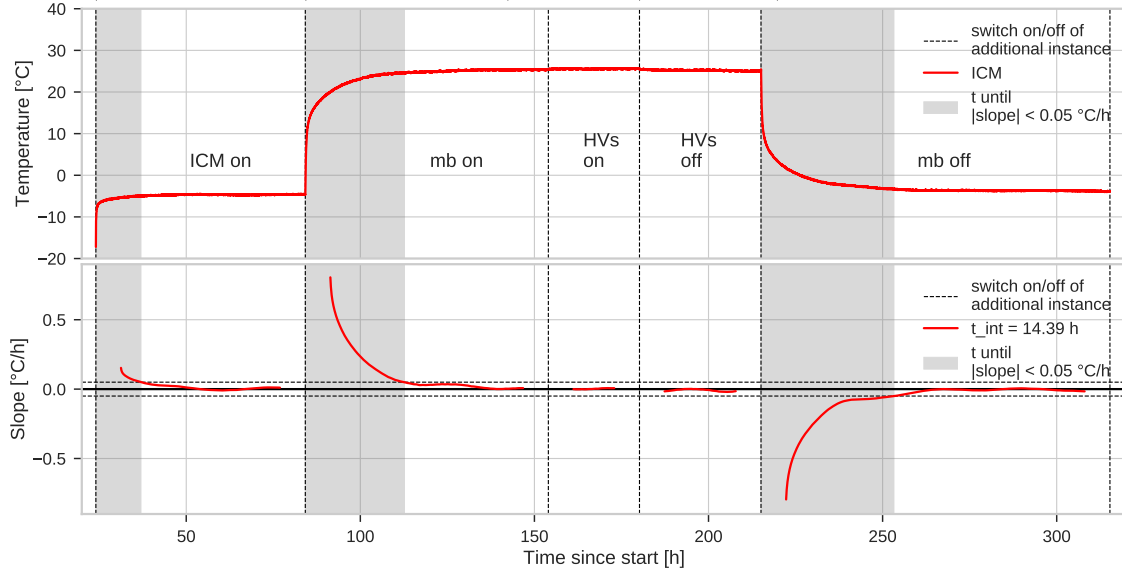
**Figure 5.14:** Illustration of the slope determination from the temperature data shown for the ICM temperature curve during the operation stage “mb on”. The distance of the fit intervals is not to scale. For illustration purposes, only three fit intervals are shown.



**Figure 5.15:** Example of a temperature curve and its calculated slope.

**Table 5.2:** Equilibrium times for each temperature sensor for each operation stage at  $-27^{\circ}\text{C}$  for Froschprinz.

		ICM on	Mb on	HV on	HV off	Mb off
FPGA	[h]	-	28.43	-	-	-
ICM	[h]	12.95	28.50	-	-	38.18
S1 acc	[h]	-	28.58	-	-	-
S6 T	[h]	-	28.29	-	-	-
S2 mag	[h]	-	27.86	-	-	-
S3 pres	[h]	-	28.29	-	-	-
S4 T	[h]	-	28.29	-	-	-
Bases	[h]	-	[27.35, 29.58]	-	-	-

**Figure 5.16:** Temperature curve of the ICM and its calculated slopes for all five operation stages.

For the measurements of this subsection, temperature equilibrium was defined when the temperature changed less than  $+0.05^{\circ}\text{C/h}$  for the warm-up curves and more than  $-0.05^{\circ}\text{C/h}$  for the cooling curves. The threshold is indicated by a dashed horizontal line in Figure 5.15. The vertical dashed line marks the point in time when the slope crosses the threshold or put another way, when equilibrium is reached. The time from changing the operation stage of the mDOM (for example “mb on”) until the temperature reaches the above defined equilibrium state is called equilibrium time. This time is calculated for each of the  $(24 + 7) \cdot 3 + 2$  temperature data sets and the results are shown in Table 5.2.

It takes roughly 13 h after the cold start until the ICM is warmed up. After the mainboard is switched on, it takes almost 30 h until thermal equilibrium is reached. All temperature sensors behave similarly. For the microbases (Bases), only minimum and maximum values are shown. Because the change in temperature is less than 1 K for “HV on” and “HV off” and takes only about 1 h, the used method to determine the slope is not appropriate in this case. When the mainboard is switched off, it takes almost 40 h for the mDOM to cool down again. In Figure 5.16, the corresponding data are shown for the ICM as an example. The upper plot shows the entire

temperature curve for all five operation stages. In the lower plot, the corresponding slope is shown. The vertical dashed lines indicate when the operation stage changed and an additional instance is switched on or off, respectively. The time to reach equilibrium of each operation stage is shaded in gray. For other ambient temperatures than  $-27^\circ\text{C}$ , the equilibrium times might slightly differ. However, the calculated equilibrium times can be used as rough guidelines for other laboratory measurements when it is important to know when the system is in thermal equilibrium.

## 5.4 Further parameters

Besides the temperature behavior of an mDOM, also other parameters are important for the mDOM. In the following, the pressure inside the mDOM and the PMT HV are investigated.

### 5.4.1 Pressure

For optimal operation in ice, the mDOM is filled with gaseous nitrogen at underpressure. The nitrogen atmosphere prevents water from condensating on electronic parts inside the mDOM. Underpressure is used so that the two hemispheres of an mDOM stay together at South Pole and in the airplane during transport. In these situations, ambient pressures down to 600 mbar can occur which would cause the two hemispheres to open up in case of a pressure of 1 bar inside the mDOM.

The mDOMs are filled with gaseous nitrogen, stored, shipped to pole and finally deployed. The whole process from filling until deployment lasts roughly between one to three years. During this time, the mDOM must stay leak-proof. From experience with the first few mDOM modules, it is known that a leakage occurs most likely during the first few days. To monitor the leakproofness, a pressure sensor is located on the mainboard (see Figure 5.10). For all four measurements described in Section 5.2, the pressure was monitored when the mainboard was running. Figure 5.17 shows two scatterplots of the pressure versus the temperature for Froschprinz on the left and for Rotkäppchen on the right. Because it is more accurate, the temperature of S4 was chosen for the scatterplots and not the pressure sensor. According to Table 5.1, their absolute values differ only by few degrees which was neglected. In both plots, the blue datapoints correspond to the measurement at  $-49^\circ\text{C}$  and the red datapoints correspond to the measurements at  $-27^\circ\text{C}$ . For Froschprinz, the pressure was monitored for about 80 h to 150 h for each temperature measurement and the two temperature measurements are about 1 month apart. In contrast, the measurements with Rotkäppchen are 65 h to 100 h long and about 2 month apart. If the mDOM stays leak-proof, a linear behavior according to  $pV = nk_{\text{B}}T$  between temperature and pressure is expected. To verify this linear relation, a linear fit was performed to the joint data of both temperatures shown as an orange line. For Froschprinz, some datapoints deviate from the linear curve. The deviation occurs for the temperature range in which the mDOM was not yet in thermal equilibrium. Consequently, not all datapoints of Froschprinz were included in the fit. Only the datapoints lying in the shaded fit regions were used. They show a linear behavior. Because the filling pressure and with that, the particle number density can vary from mDOM to mDOM, Rotkäppchen was fitted separately. Rotkäppchen was running all the time and no cold start was performed. Therefore, all datapoints cluster around the two measurement temperatures. All in all, the results confirm the linear behavior according to  $pV = nk_{\text{B}}T$  and the leakproofness of Froschprinz and Rotkäppchen during the time of 1 month and 2 months, respectively.

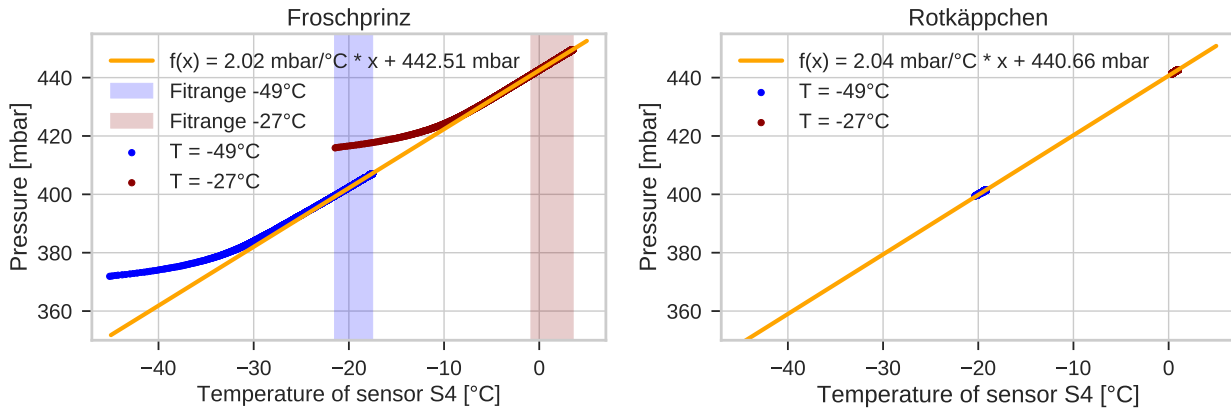


**Figure 5.17:** Pressure versus temperature of the temperature sensor S4 for Froschprinz (left) and Rotkäppchen (right).

### 5.4.2 PMT high voltage

The last investigated parameter is the PMT HV. As discussed in Chapter 3, each PMT will be operated at a gain of  $5 \cdot 10^6$ . To reach this gain number, a certain PMT HV is needed. The exact HV value is different for each PMT. The PMT HV is directly produced on the microbase (see Subsection 2.4.2). One can set the nominal HV value—or, more precise, the value at the tenth dynode—for each PMT and the microcontroller on the microbase adjusts this value. Furthermore, the microcontroller permanently reads back the applied HV value. The microcontroller measures the voltage at the tenth dynode of the PMT and directly readjusts the voltage in case it is not correct. Ideally, the measured voltage at the tenth dynode should not only be always constant, but should also equal the nominal HV value.

To check the HV stability, the voltage at the tenth dynode is read out and saved during the operation stage “HV on” for all four measurements described in Section 5.2. In Figure 5.18, the data of the quotient of the measured voltage at the tenth dynode and the nominal voltage at the tenth dynode is plotted over time for all four measurements. The dashed horizontal line indicates the target value. Each of the 24 colored lines represents a different PMT. As already mentioned in Section 5.2, the nominal HV from the database calibrated in Aachen is used. Most values deviate by 0.05 % from the target value. The maximum deviation is about 0.12 % during 17 h to 50 h. Thus, the PMT HV can be considered as stable.

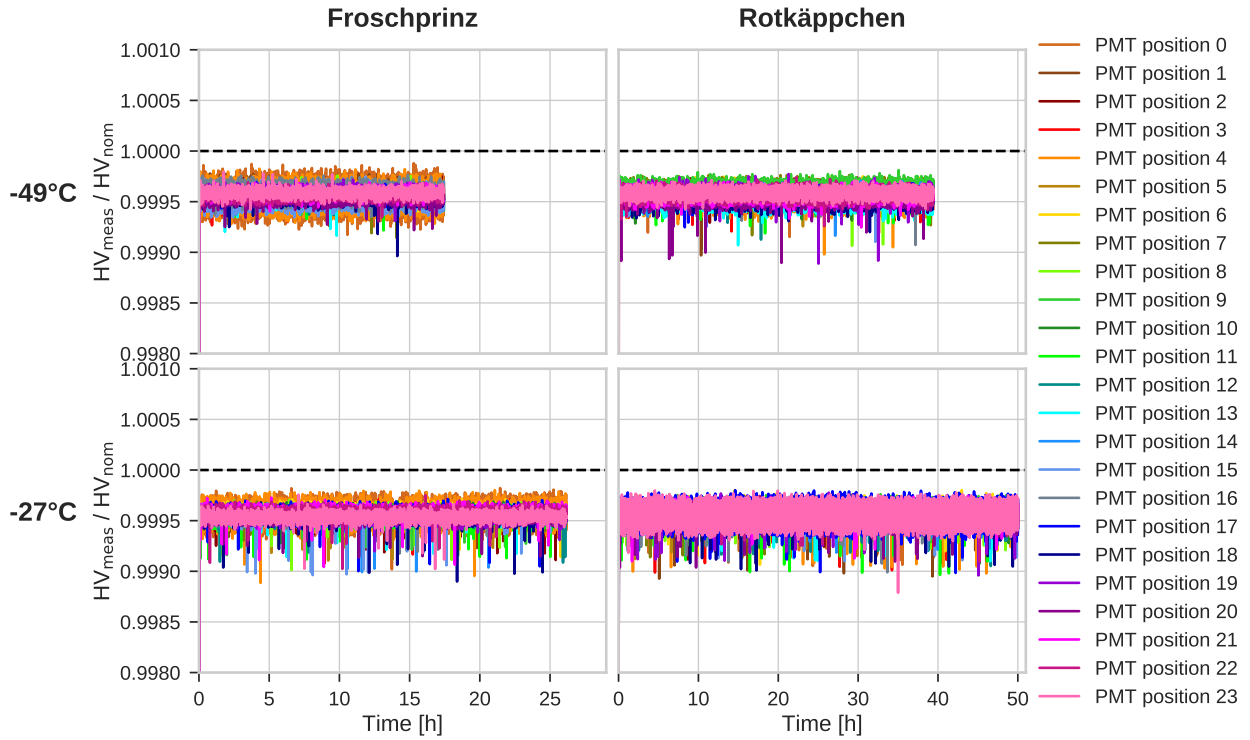


**Figure 5.18:** Measured voltage at the tenth dynode divided by nominal voltage at the tenth dynode over time for all four measurements.

## 5.5 Summary and discussion

A time-dependent measurement was performed with the two mDOMs Froschprinz and Rotkäppchen at  $-27^{\circ}\text{C}$  and at  $-49^{\circ}\text{C}$ . While Rotkäppchen was always running, Froschprinz underwent a cold start. Different parameters were monitored such as the temperature at different positions in the mDOM, absolute time, power consumption, pressure, and the PMT HVs. In addition, the temperature behavior was investigated with a COMSOL Multiphysics simulation. A simplified model of the mDOM geometry was built and material properties as well as physical properties were assigned to the different components. First, a stationary solution was investigated. However, a stationary solution was only found if thermal conduction was included and convection not. However, convection is expected to occur in the mDOM and therefore, could not be neglected. To include convection, a time-dependent simulation was used. Although this approach worked and delivered useful results, the time-dependent simulation appeared so time consuming that it was decided to stop the simulation efforts and focus on measurements.

Mainly, the temperature behavior of the mDOMs was investigated. Thereby, the power consumption worked as heat source of the mDOM. The overall power consumption in a typical situation in ice was about 9 W. Most power was consumed by the mainboard while ICM and PMTs needed only a small fraction. The temperature behavior of an mDOM was as expected. The largest temperature increase was caused by the mainboard while ICM and PMTs produced smaller temperature increases. The hottest part inside the mDOM was the FPGA on the mainboard. It warmed up to about 70 K to 77 K above ambient temperature. The larger the distance to the FPGA

and ICM, the smaller were the measured temperature differences to the ambient temperature. The coldest measured parts inside the mDOM were the microbases ranging from 17 K to 31 K above ambient temperature. The cold start of Froschprinz did not work without problems, but they could be circumvented. Furthermore, the time needed to reach equilibrium was investigated with a linear approximation for Froschprinz  $-27^{\circ}\text{C}$ . It took about 13 h after the ICM was switched on, about 28 h after the mainboard was switched on, and about 38 h after the mainboard was switched off to reach equilibrium. Temperature changes caused by the PMT HVs were so small and short that they were not visible with this method. Measurements of the pressure confirmed the linear behavior of pressure versus temperature and proofed that the mDOM was not leaking gas within 1 month and 2 months, respectively. Moreover, the PMT HV deviated less than 0.2 % from the nominal HV during 17 h to 50 h.

All in all, both mDOMs behaved as expected concerning temperature, pressure, and PMT HV. The cooling inside the mDOM worked sufficiently and no part was running outside its specifications.

In future measurements, the influence of the tilt on the temperature distribution of the microbases in the upper hemisphere can be investigated further. After an offset calibration of the accelerometer, the mDOM could be differently tilted. For each tilt configuration, the temperature distribution of the microbases could be investigated. With these measurements, it can be checked whether always the same microbases are heated up most independent of the tilt or whether the tilt indeed influences the temperature distribution measured by the microbases. Furthermore, other parameters should be investigated in a longterm measurement concerning stability such as PMT HV, trigger threshold, and darkrate of the PMTs over at least one week at temperatures of about  $-27^{\circ}\text{C}$ . For these measurements, calibration measurements inside the mDOM are necessary. Part of the calibration is a fit of the PMT response function. Because the automatization of these measurements was not yet implemented, these parameters were not investigated in this thesis. Moreover, a revision 1 mainboard was used for all measurements in this chapter. In the final design, a higher mainboard revision will be used. Although it is expected that the temperature features will most likely not change, the temperature behavior of the final design should be checked.

Another aspect is the temperature of the photocathodes of the PMTs. Because the thermal darkrate of the mDOM PMTs increases for temperatures above  $0^{\circ}\text{C}$ , the photocathode temperatures should be kept below  $0^{\circ}\text{C}$ . The temperatures of the microbases cannot be taken as a reference for the PMT temperature because the temperature sensor is located directly at the part of the microbase producing the heat. Furthermore, the photocathode of a PMT is about 10 cm closer to the outer surface than the microbase. To get a better estimate of the temperature of the photocathode, a possible solution would be to tape temperature sensors on the outer surface of the glass vessel.

Further possible measurements aim for the temperature distribution of an mDOM frozen in ice. In case the mDOM is surrounded by air—like for the measurements presented in this thesis—the mDOM is cooled via the convection in the air. In contrast to that, the mDOM will later be frozen in ice where no convection occurs. In addition to that, ice is an insulator. Therefore, the temperature distribution inside an mDOM surrounded by ice could differ from an mDOM surrounded by air for the same ambient temperature. Given that a measurement with additional temperature sensors taped onto the outer surface of the glass vessel as described above was already performed, these measured temperatures could serve as input parameters for a simplified simulation. A geometry with only the glass vessel and the surface temperatures from the measurement could be used. Then one would simulate the temperature behavior with convection in surrounding air and the behavior

with surrounding ice to compare the cooling behavior of the two situations. Another possibility would be a direct measurement of the mDOM in ice.

## Chapter 6

# Summary & Outlook

This thesis concentrates on characterization measurements of different hardware components of the multi-PMT Digital Optical Module (mDOM), which is one of the novel modules developed for the future low energy extension of IceCube, the IceCube Upgrade. To sum up, three different hardware systems were characterized in this thesis: photomultiplier tubes (PMTs), analog front end, and an integrated mDOM.

In total, four different PMT types of the two manufacturers Hamamatsu Photonics K.K. and HZC Photonics were investigated. By continually giving feedback to the manufacturers, the PMT design was improved to meet the requirements for the mDOM, which guarantees an excellent directional and energy resolution of the IceCube Upgrade as well as a good reconstruction performance of neutrino events. The following characteristics of about 150 PMTs were measured: Transit time spread, quantum efficiency, darkrate, and correlated noise (prepulsing, delayed pulsing, afterpulsing). In comparison, the PMTs from Hamamatsu Photonics K.K. showed an overall better performance than the PMTs from HZC Photonics. Based on the measurements shown in this thesis, the IceCube collaboration decided to use PMTs from Hamamatsu Photonics K.K. for the mDOM to ensure an excellent time resolution, maximize the amount of detected light, and minimize the overall background. After slight modifications of the previously tested PMT types, a test batch of 19 PMTs from the final PMT type R15458-20 was characterized. It was found that the performance of these 19 PMTs satisfies the requirements. Only one PMT was returned to the manufacturer, because it strongly exceeded the darkrate requirement. In addition to the verification of the requirements for the mDOM, the fit parameters of the PMT linearity fits of the final PMT type were inputted into the simulation of the IceCube Upgrade detector.

Similar measurements were performed with the analog front end to ensure the ability of single photon counting and the coverage of the relevant neutrino energy range for the IceCube Upgrade. To investigate different analog-front-end designs, a dedicated setup was built. Furthermore, special measurement and analysis techniques were developed to investigate the following characteristics: Signal-to-noise ratio, dynamic range, and linearity. All parameters were measured at room temperature as well as at temperatures between  $-20^{\circ}\text{C}$  and  $-42^{\circ}\text{C}$ . These temperatures below  $0^{\circ}\text{C}$  are typical for the operation of the IceCube Upgrade. At first, three different analog-front-end channel-designs using different signal-amplification factors were compared to find the channel which covers the relevant neutrino energy range best. During these measurements, two problems were found. First, the measurement technique used to determine the dynamic range and linearity yields large systematic errors due to temperature changes during the measurements which led

to changes in the LED output intensity and thus, yielded no reliable results. Second, the PMT-charge distributions above approximately 19 p.e. were deformed which was caused most likely by a bandwidth issue of the analog front end. Both problems could be solved. The measurement technique was adapted by using a reference PMT which allowed to monitor the LED output intensity. Moreover, the preamplifier was changed by the electronics engineer leading to the analog-front-end channel-design called channel 0b. For this design, the signal-to-noise ratio, dynamic range, and linearity were tested at  $+25^{\circ}\text{C}$ ,  $-22^{\circ}\text{C}$ , and  $-38^{\circ}\text{C}$  as well as the discriminator threshold stability at  $-38^{\circ}\text{C}$ . Channel 0b fulfills all requirements specified by the IceCube Upgrade except the linearity requirement at  $+25^{\circ}\text{C}$  and at  $-38^{\circ}\text{C}$ . However, the performance of channel 0b was found to be sufficient to be used for the mDOM application in the IceCube Upgrade. Thus, channel 0b was used for the revision 1 mainboard.

Last, two integrated mDOMs were investigated in a time-dependent study at  $-27^{\circ}\text{C}$  and at  $-49^{\circ}\text{C}$ . In the IceCube Upgrade, the mDOMs will be operated in the ice at similar temperatures and will be switched on only after the ice refroze after the installation process. For the first time, a cold start of an mDOM was performed. For both mDOMs, the temperature at different positions in the mDOM, power consumption, pressure, and the PMT high voltage were monitored over the absolute time. In thermal equilibrium and during normal operation, the hottest part inside the mDOM (the FPGA on the mainboard) warmed up to about 70 K to 77 K above ambient temperature. Furthermore, the overall power consumption was about 9 W. Moreover, no gas leakage was found during the pressure measurements and the PMT high voltage remained stable. In addition, the time needed to reach thermal equilibrium was determined for one mDOM at  $-27^{\circ}\text{C}$ . While it took about 30 h after the mainboard was switched on to reach thermal equilibrium, about 40 h were needed to cool down after the mainboard was switched off. Both mDOMs worked as expected. No electronic component was running outside of its specifications and the cooling inside the mDOM worked sufficiently.

To conclude, this thesis contributed to develop a successful mDOM design so that fully functional mDOMs could be built for the IceCube Upgrade. Their proper performance was confirmed during extensive design verification tests realized by different people. Moreover, every produced mDOM undergoes thorough final acceptance tests which have already started. In August 2024, the first 117 mDOMs will be shipped to the South Pole, followed by the remaining 288 mDOMs one year later. In the Antarctic summer season 2025/26, all 405 mDOMs will be installed in the glacier together with 279 D-Eggs, 14 PDOMs, and several calibration devices in a denser instrumented volume than the existing IceCube detector. With the IceCube Upgrade, the sensitivity to tau neutrino appearance measurements can be improved, thus improving the sensitivity to neutrino oscillation parameters and serving as a probe of the unitarity of the PMNS matrix. Furthermore, the optical glacier ice properties will be measured in detail, which will be used to considerably improve the directional reconstruction performance of IceCube.

# Additional material

**Table 1:** Accuracies of the used temperature sensors according to the datasheets.

Temperature sensor	Accuracy according to datasheet
FPGA	$\pm 4^{\circ}\text{C}$ maximum error [111]
ICM	-
S1 accelerometer	$\pm 0.7^{\circ}\text{C}$ maximum error [112]
S6 temperature sensor	$\pm 1^{\circ}\text{C}$ (typical) from $-55^{\circ}\text{C}$ to $125^{\circ}\text{C}$ , $\pm 2^{\circ}\text{C}$ (maximum) from $-55^{\circ}\text{C}$ to $125^{\circ}\text{C}$ [113]
S2 magnetometer	-
S3 pressure sensor	$\pm 1.5^{\circ}\text{C}$ (typical) for $T = 0^{\circ}\text{C}$ to $65^{\circ}\text{C}$ [114]
S4 temperature sensor	$\pm 0.25^{\circ}\text{C}$ (typical) from $-55^{\circ}\text{C}$ to $+125^{\circ}\text{C}$ , $\pm 1^{\circ}\text{C}$ (maximum) from $-40^{\circ}\text{C}$ to $+110^{\circ}\text{C}$ , $\pm 2^{\circ}\text{C}$ (maximum) from $-55^{\circ}\text{C}$ to $+125^{\circ}\text{C}$ [115]
Bases	$\pm 1^{\circ}\text{C}$ maximum error, checked at room temperature with thermometer [116]
S0 temperature sensor	Absolute accuracy between $-40^{\circ}\text{C}$ and $-20^{\circ}\text{C}$ is typically $\pm 1.5^{\circ}\text{C}$ [117]

**Table 2:** Absolute temperatures and the corresponding statistical error according to equation 5.1 from all mainboard temperature sensors and S0 for all four temperature measurements.

	Froschprin		Rotkäppchen	
	−49 °C	−27 °C	−49 °C	−27 °C
Reference temperature	−49.06 °C	±0.017 °C	−26.76 °C	±0.016 °C
FPGA	27.72 °C	±0.003 °C	47.83 °C	±0.003 °C
ICM	4.94 °C	±0.002 °C	25.56 °C	±0.002 °C
S1 accelerometer	−2.02 °C	±0.003 °C	19.95 °C	±0.002 °C
S6 temperature sensor	−7.31 °C	±0.0003 °C	13.39 °C	±0.001 °C
S2 magnetometer	−10.84 °C	±0.003 °C	9.17 °C	±0.002 °C
S3 pressure sensor	−15.49 °C	±0.0003 °C	4.68 °C	±0.001 °C
S4 temperature sensor	−17.51 °C	±0.0006 °C	3.48 °C	±0.001 °C
S0 temperatures sensor	−39.54 °C	±0.020 °C	−17.39 °C	±0.027 °C

**Table 3:** Absolute temperatures and the corresponding statistical error according to equation 5.1 of the 24 microbases for all four temperature measurements.

PMT position	Froschprinz			Rotkäppchen		
	−49 °C	−27 °C	−49 °C	−49 °C	−27 °C	−27 °C
0	−23.03 °C	±0.002 °C	−1.96 °C	±0.002 °C	−25.34 °C	±0.002 °C
1	−20.61 °C	±0.003 °C	0.11 °C	±0.002 °C	−27.91 °C	±0.002 °C
2	−18.05 °C	±0.003 °C	2.44 °C	±0.002 °C	−26.17 °C	±0.002 °C
3	−21.97 °C	±0.002 °C	−0.63 °C	±0.002 °C	−23.87 °C	±0.002 °C
4	−22.04 °C	±0.003 °C	−0.47 °C	±0.003 °C	−26.35 °C	±0.001 °C
5	−24.36 °C	±0.002 °C	−2.57 °C	±0.002 °C	−25.18 °C	±0.001 °C
6	−22.62 °C	±0.002 °C	−1.25 °C	±0.002 °C	−25.89 °C	±0.001 °C
7	−21.41 °C	±0.003 °C	−0.39 °C	±0.003 °C	−27.07 °C	±0.002 °C
8	−17.82 °C	±0.003 °C	3.22 °C	±0.002 °C	−27.16 °C	±0.001 °C
9	−18.85 °C	±0.003 °C	2.36 °C	±0.002 °C	−22.02 °C	±0.001 °C
10	−22.14 °C	±0.002 °C	−0.66 °C	±0.003 °C	−20.07 °C	±0.002 °C
11	−24.06 °C	±0.004 °C	−2.75 °C	±0.002 °C	−23.61 °C	±0.002 °C
12	−24.90 °C	±0.003 °C	−2.22 °C	±0.002 °C	−24.90 °C	±0.001 °C
13	−20.76 °C	±0.003 °C	1.22 °C	±0.002 °C	−26.32 °C	±0.001 °C
14	−22.24 °C	±0.004 °C	0.14 °C	±0.003 °C	−26.18 °C	±0.002 °C
15	−19.59 °C	±0.006 °C	1.95 °C	±0.002 °C	−26.02 °C	±0.002 °C
16	−21.10 °C	±0.003 °C	1.09 °C	±0.002 °C	−25.30 °C	±0.002 °C
17	−21.84 °C	±0.002 °C	0.78 °C	±0.003 °C	−25.78 °C	±0.001 °C
18	−20.35 °C	±0.004 °C	1.50 °C	±0.002 °C	−24.39 °C	±0.002 °C
19	−24.30 °C	±0.002 °C	−1.63 °C	±0.003 °C	−23.90 °C	±0.002 °C
20	−28.51 °C	±0.004 °C	−5.62 °C	±0.002 °C	−29.90 °C	±0.001 °C
21	−26.39 °C	±0.002 °C	−4.00 °C	±0.002 °C	−30.97 °C	±0.002 °C
22	−26.76 °C	±0.003 °C	−4.07 °C	±0.002 °C	−31.10 °C	±0.002 °C
23	−25.31 °C	±0.003 °C	−2.35 °C	±0.003 °C	−31.31 °C	±0.002 °C



# List of Abbreviations

<b>3D</b>	three-dimensional
<b>ADC</b>	analog-to-digital converter
<b>AFE</b>	analog front end
<b>AGN</b>	active galactic nucleus
<b>CAD</b>	computer-aided design
<b>CMB</b>	cosmic microwave background
<b>DAC</b>	digital-to-analog converter
<b>DC</b>	direct current
<b>D-Egg</b>	Dual optical sensors in an Ellipsoid Glass for Gen2
<b>DESY</b>	Deutsches Elektronen-Synchrotron DESY
<b>DOM</b>	Digital Optical Module
<b>EBL</b>	extragalactic background light
<b>FPGA</b>	field programmable gate array
<b>FWHM</b>	full width at half maximum
<b>GPS</b>	global positioning system
<b>GRB</b>	gamma-ray burst
<b>HV</b>	high voltage
<b>IceCube</b>	IceCube Neutrino Observatory
<b>ICEHAP</b>	International Center for Hadron Astrophysics, Chiba University
<b>ICM</b>	IceCube Communication Module
<b>LED</b>	light-emitting diode
<b>mDAB</b>	mDOM Adapter Board
<b>mDOM</b>	multi-PMT Digital Optical Module
<b>mDOT</b>	mainboard testboard
<b>MSU</b>	Michigan State University
<b>PDOM</b>	PINGU Digital Optical Module
<b>p.e.</b>	photon equivalent
<b>PHD</b>	photodiode
<b>PINGU</b>	Precision IceCube Next Generation Upgrade
<b>PMNS</b>	Pontecorvo-Maki-Nakagawa-Sakata
<b>PMT</b>	photomultiplier tube
<b>POCAM</b>	Precision Optical Calibration Module
<b>QE</b>	quantum efficiency
<b>RAPCal</b>	Reciprocal Active Pulsing Calibration
<b>RMS</b>	root mean square

<b>SNR</b>	signal-to-noise ratio
<b>SPE</b>	single photoelectron
<b>TTS</b>	transit time spread
<b>UV</b>	ultraviolet
<b>WIPAC</b>	Wisconsin IceCube Particle Astrophysics Center

# Bibliography

- [1] Wolfgang Pauli. *Offener Brief an die Gruppe der Radioaktiven bei der Gauvereins-Tagung zu Tübingen (Open letter to the group of radioactive people at the Gauverein meeting in Tübingen)*. 1930.
- [2] C. L. Cowan et al. “Detection of the free neutrino: A Confirmation”. In: *Science* 124 (1956), pp. 103–104. DOI: 10.1126/science.124.3212.103.
- [3] IceCube collaboration. *IceCube web pages*. URL: <https://icecube.wisc.edu/> (visited on 12/19/2023).
- [4] IceCube Collaboration\*. “Evidence for High-Energy Extraterrestrial Neutrinos at the IceCube Detector”. In: *Science* 342.6161 (2013), p. 1242856. DOI: 10.1126/science.1242856. eprint: <https://www.science.org/doi/pdf/10.1126/science.1242856>. URL: <https://www.science.org/doi/abs/10.1126/science.1242856> (visited on 02/12/2024).
- [5] The IceCube Collaboration et al. “Multimessenger observations of a flaring blazar coincident with high-energy neutrino IceCube-170922A”. In: *Science* 361.6398 (2018), eaat1378. DOI: 10.1126/science.aat1378. eprint: <https://www.science.org/doi/pdf/10.1126/science.aat1378>. URL: <https://www.science.org/doi/abs/10.1126/science.aat1378> (visited on 02/13/2024).
- [6] IceCube Collaboration\*† et al. “Evidence for neutrino emission from the nearby active galaxy NGC 1068”. In: *Science* 378.6619 (2022), pp. 538–543. DOI: 10.1126/science.abg3395. eprint: <https://www.science.org/doi/pdf/10.1126/science.abg3395>. URL: <https://www.science.org/doi/abs/10.1126/science.abg3395> (visited on 02/12/2024).
- [7] Aya Ishihara. “The IceCube Upgrade - Design and Science Goals”. In: *Proceedings of 36th International Cosmic Ray Conference — PoS(ICRC2019)*. Vol. 358. 2019, p. 1031. DOI: 10.22323/1.358.1031.
- [8] Edoardo Vitagliano, Irene Tamborra, and Georg Raffelt. “Grand unified neutrino spectrum at Earth: Sources and spectral components”. In: *Rev. Mod. Phys.* 92 (4 Dec. 2020), p. 045006. DOI: 10.1103/RevModPhys.92.045006. URL: <https://link.aps.org/doi/10.1103/RevModPhys.92.045006> (visited on 02/07/2024).
- [9] U.F. Katz and Ch. Spiering. “High-energy neutrino astrophysics: Status and perspectives”. In: *Progress in Particle and Nuclear Physics* 67.3 (2012), pp. 651–704. ISSN: 0146-6410. DOI: <https://doi.org/10.1016/j.ppnp.2011.12.001>. URL: <https://www.sciencedirect.com/science/article/pii/S0146641011001189> (visited on 02/07/2024).

- [10] Tsvi Piran. “Gamma-ray bursts and the fireball model”. In: *Physics Reports* 314.6 (1999), pp. 575–667. ISSN: 0370-1573. DOI: [https://doi.org/10.1016/S0370-1573\(98\)00127-6](https://doi.org/10.1016/S0370-1573(98)00127-6). URL: <https://www.sciencedirect.com/science/article/pii/S0370157398001276> (visited on 02/07/2024).
- [11] E. Troja et al. “A nearby long gamma-ray burst from a merger of compact objects”. In: *Nature* 612.6 (2022), pp. 228–231. DOI: 10.1038/s41586-022-05327-3. URL: <https://www.nature.com/articles/s41586-022-05327-3.pdf> (visited on 03/01/2024).
- [12] Kenneth Greisen. “End to the Cosmic-Ray Spectrum?” In: *Phys. Rev. Lett.* 16 (17 Apr. 1966), pp. 748–750. DOI: 10.1103/PhysRevLett.16.748. URL: <https://link.aps.org/doi/10.1103/PhysRevLett.16.748> (visited on 02/07/2024).
- [13] G. T. Zatsepin and V. A. Kuzmin. “Upper limit of the spectrum of cosmic rays”. In: *JETP Lett.* 4 (1966), pp. 78–80.
- [14] Javier Tiffenberg. *UHE Neutrino searches with the Pierre Auger Observatory*. Talk at NuSky conference 2011. 2011.
- [15] R. L. Workman et al. “Review of Particle Physics”. In: *PTEP* 2022 (2022), p. 083C01. DOI: 10.1093/ptep/ptac097.
- [16] P. A. Čerenkov. “Visible Radiation Produced by Electrons Moving in a Medium with Velocities Exceeding that of Light”. In: *Phys. Rev.* 52 (4 Aug. 1937), pp. 378–379. DOI: 10.1103/PhysRev.52.378. URL: <https://link.aps.org/doi/10.1103/PhysRev.52.378> (visited on 02/07/2024).
- [17] Stephen G. Warren. “Optical constants of ice from the ultraviolet to the microwave”. In: *Appl. Opt.* 23.8 (Apr. 1984), pp. 1206–1225. DOI: 10.1364/AO.23.001206. URL: <https://opg.optica.org/ao/abstract.cfm?URI=ao-23-8-1206> (visited on 02/21/2024).
- [18] Albert Lehmann. *Detektoren für Teilchen und Strahlung*. Lecture. 2015/2016.
- [19] M.G. Aartsen et al. (IceCube Collaboration). “The IceCube Neutrino Observatory: instrumentation and online systems”. In: *Journal of Instrumentation* 12.03 (Mar. 2017), P03012. DOI: 10.1088/1748-0221/12/03/P03012. URL: <https://dx.doi.org/10.1088/1748-0221/12/03/P03012> (visited on 02/07/2024).
- [20] R. Abbasi et al. “The design and performance of IceCube DeepCore”. In: *Astroparticle Physics* 35.10 (2012), pp. 615–624. ISSN: 0927-6505. DOI: <https://doi.org/10.1016/j.astropartphys.2012.01.004>. URL: <https://www.sciencedirect.com/science/article/pii/S0927650512000254> (visited on 02/07/2024).
- [21] R. Abbasi et al. “IceTop: The surface component of IceCube”. In: *Nuclear Instruments and Methods in Physics Research Section A: Accelerators, Spectrometers, Detectors and Associated Equipment* 700 (2013), pp. 188–220. ISSN: 0168-9002. DOI: <https://doi.org/10.1016/j.nima.2012.10.067>. URL: <https://www.sciencedirect.com/science/article/pii/S016890021201217X> (visited on 02/07/2024).
- [22] Francis Halzen. “High-Energy Neutrinos from the Cosmos”. In: *Annalen der Physik* 533 (Sept. 2021). DOI: 10.1002/andp.202100309.

- 
- [23] R. Abbasi et al. “The IceCube data acquisition system: Signal capture, digitization, and timestamping”. In: *Nuclear Instruments and Methods in Physics Research Section A: Accelerators, Spectrometers, Detectors and Associated Equipment* 601.3 (2009), pp. 294–316. ISSN: 0168-9002. DOI: <https://doi.org/10.1016/j.nima.2009.01.001>. URL: <https://www.sciencedirect.com/science/article/pii/S0168900209000084> (visited on 02/07/2024).
  - [24] R. Abbasi et al. “Calibration and characterization of the IceCube photomultiplier tube”. In: *Nuclear Instruments and Methods in Physics Research Section A: Accelerators, Spectrometers, Detectors and Associated Equipment* 618.1 (2010), pp. 139–152. ISSN: 0168-9002. DOI: <https://doi.org/10.1016/j.nima.2010.03.102>. URL: <https://www.sciencedirect.com/science/article/pii/S0168900210006662> (visited on 02/07/2024).
  - [25] C.J. Lozano Mariscal et al. “Sensitivity of multi-PMT optical modules in Antarctic ice to supernova neutrinos of MeV energy”. In: *The European Physical Journal C* 81 (Dec. 2021), p. 1058. DOI: 10.1140/epjc/s10052-021-09809-y. URL: <https://doi.org/10.1140/epjc/s10052-021-09809-y> (visited on 02/08/2024).
  - [26] R. Abbasi et al. (IceCube Collaboration). “D-Egg: a dual PMT optical module for IceCube”. In: *Journal of Instrumentation* 18.04 (Apr. 2023), P04014. DOI: 10.1088/1748-0221/18/04/P04014. URL: <https://dx.doi.org/10.1088/1748-0221/18/04/P04014> (visited on 02/07/2024).
  - [27] PINGU Collaboration. *Letter of Intent: The Precision IceCube Next Generation Upgrade (PINGU)*. 2017. arXiv: 1401.2046 [physics.ins-det]. URL: <https://arxiv.org/pdf/1401.2046.pdf> (visited on 01/19/2024).
  - [28] KM3NeT collaboration. *KM3NeT web pages*. URL: <https://www.km3net.org/> (visited on 12/20/2023).
  - [29] E Leonora and on behalf of the KM3NeT Collaboration. “The Digital Optical Module of KM3NeT”. In: 1056.1 (July 2018), p. 012031. DOI: 10.1088/1742-6596/1056/1/012031. URL: <https://dx.doi.org/10.1088/1742-6596/1056/1/012031> (visited on 10/26/2023).
  - [30] R. Abbasi et al. (IceCube Collaboration) and Karl-Heinz Sulanke. “Design and performance of the multi-PMT optical module for IceCube Upgrade”. In: *Proceedings of 37th International Cosmic Ray Conference—PoS(ICRC2021)*. Vol. 395. 2021, p. 1070. DOI: 10.22323/1.395.1070.
  - [31] Kayla Leonard DeHolton. *Atmospheric neutrino oscillations with IceCube: Recent results with DeepCore and future potential with the Upgrade*. Talk at XX International Workshop on Neutrino Telescopes (Neutel 23). Version Final. Mar. 2024. DOI: 10.5281/zenodo.10579975. URL: <https://doi.org/10.5281/zenodo.10579975> (visited on 03/22/2024).
  - [32] K. Abe et al. “Measurements of neutrino oscillation parameters from the T2K experiment using  $3.6 \times 10^{21}$  protons on target”. In: *The European Physical Journal C* 83 (9), p. 782. DOI: 10.1140/epjc/s10052-023-11819-x. URL: <https://doi.org/10.1140/epjc/s10052-023-11819-x> (visited on 03/28/2024).
  - [33] P. Adamson et al. “Precision Constraints for Three-Flavor Neutrino Oscillations from the Full MINOS+ and MINOS Dataset”. In: *Phys. Rev. Lett.* 125 (13 Sept. 2020), p. 131802. DOI: 10.1103/PhysRevLett.125.131802. URL: <https://link.aps.org/doi/10.1103/PhysRevLett.125.131802> (visited on 03/21/2024).

- [34] M. A. Acero et al. “Improved measurement of neutrino oscillation parameters by the NOvA experiment”. In: *Phys. Rev. D* 106 (3 Aug. 2022), p. 032004. DOI: 10.1103/PhysRevD.106.032004. URL: <https://link.aps.org/doi/10.1103/PhysRevD.106.032004> (visited on 03/21/2024).
- [35] Volodymyr Takhistov. *Atmospheric Neutrino Oscillations with Super-Kamiokande*. Talk at ICHEP conference 2020. 2020. URL: [https://indico.cern.ch/event/868940/contributions/3817174/attachments/2082629/3498300/ICHEP2020\\_SK\\_Takhistov.pdf](https://indico.cern.ch/event/868940/contributions/3817174/attachments/2082629/3498300/ICHEP2020_SK_Takhistov.pdf) (visited on 03/21/2024).
- [36] R. Abbasi et al. “Measurement of atmospheric neutrino mixing with improved IceCube DeepCore calibration and data processing”. In: *Phys. Rev. D* 108 (1 July 2023), p. 012014. DOI: 10.1103/PhysRevD.108.012014. URL: <https://link.aps.org/doi/10.1103/PhysRevD.108.012014> (visited on 03/21/2024).
- [37] Fermi National Accelerator Laboratory managed by Fermi Research Alliance LLC for the U.S. Department of Energy Office of Science. *NOvA web pages*. URL: <https://novaexperiment.fnal.gov> (visited on 01/23/2024).
- [38] T2K Collaboration. *T2K web pages*. URL: <https://t2k-experiment.org> (visited on 01/23/2024).
- [39] Fermi National Accelerator Laboratory; Office of Science/U.S. Department of Energy; managed by Fermi Research Alliance LLC. *MINOS*. URL: <https://www.fnal.gov/pub/science/experiments/intensity/minos.html> (visited on 01/23/2024).
- [40] Nikhita Khara and Felix Henningsen. “POCAM in the IceCube Upgrade”. In: *Proceedings of 37th International Cosmic Ray Conference — PoS(ICRC2021)*. Vol. 395. 2021, p. 1049. DOI: 10.22323/1.395.1049.
- [41] M. Rongen, D. Chirkin, and on behalf of IceCube collaboration. “Advances in IceCube ice modelling & what to expect from the Upgrade”. In: *Journal of Instrumentation* 16.09 (Sept. 2021), p. C09014. DOI: 10.1088/1748-0221/16/09/C09014. URL: <https://dx.doi.org/10.1088/1748-0221/16/09/C09014> (visited on 02/08/2024).
- [42] Rasha Abbasi et al. “Operations plans and sensitivities of the IceCube Upgrade camera system”. In: *Proceedings of 38th International Cosmic Ray Conference — PoS(ICRC2023)*. Vol. 444. 2023, p. 1037. DOI: 10.22323/1.444.1037.
- [43] Wisconsin IceCube Particle Astrophysics Center (WIPAC) and the IceCube-Gen2 Collaboration. *IceCube-Gen2 web pages*. URL: <https://icecube-gen2.wisc.edu> (visited on 01/17/2024).
- [44] Rasha Abbasi et al. “The next generation neutrino telescope: IceCube-Gen2”. In: *Proceedings of 38th International Cosmic Ray Conference — PoS(ICRC2023)*. Vol. 444. 2023, p. 994. DOI: 10.22323/1.444.0994.
- [45] Rasha Abbasi et al. “Mechanical design of the optical modules intended for IceCube-Gen2”. In: *Proceedings of 38th International Cosmic Ray Conference — PoS(ICRC2023)*. Vol. 444. 2023, p. 979. DOI: 10.22323/1.444.0979.
- [46] Charlotte Benning et al. “Performance Studies of the Acoustic Module for the IceCube Upgrade”. In: *Proceedings of 38th International Cosmic Ray Conference — PoS(ICRC2023)*. Vol. 444. 2023, p. 241. DOI: 10.22323/1.444.0241.

- 
- [47] S.O. Flyckt and C. Marmonier. *Photomultiplier Tubes - Principles and Applications*. 2002. URL: [https://www2.pv.infn.it/~debari/doc/Flyckt\\_Marmonier.pdf](https://www2.pv.infn.it/~debari/doc/Flyckt_Marmonier.pdf) (visited on 11/21/2023).
  - [48] Hamamatsu Photonics K.K. - Editorial Committee. *Photomultiplier Tubes - Basics and Application*. 4th ed. Hamamatsu Photonics K.K. - Electron Tube Division, 2017. URL: [https://www.hamamatsu.com/content/dam/hamamatsu-photonics/sites/documents/99\\_SALES\\_LIBRARY/etd/PMT\\_handbook\\_v4E.pdf](https://www.hamamatsu.com/content/dam/hamamatsu-photonics/sites/documents/99_SALES_LIBRARY/etd/PMT_handbook_v4E.pdf) (visited on 10/30/2023).
  - [49] Hamamatsu Photonics K.K. *Photomultiplier tubes and related products*. 2020. URL: [https://www.hamamatsu.com/content/dam/hamamatsu-photonics/sites/documents/99\\_SALES\\_LIBRARY/etd/PMT\\_TPMZ0002E.pdf](https://www.hamamatsu.com/content/dam/hamamatsu-photonics/sites/documents/99_SALES_LIBRARY/etd/PMT_TPMZ0002E.pdf) (visited on 12/15/2023).
  - [50] ET Enterprises Limited. *Understanding Photomultipliers*. 2011. URL: [https://et-enterprises.com/images/brochures/Understanding\\_Pmts.pdf](https://et-enterprises.com/images/brochures/Understanding_Pmts.pdf) (visited on 12/13/2023).
  - [51] Lew Classen. “The mDOM - a multi-PMT digital optical module for the IceCube-Gen2 neutrino telescope”. Dissertation. Friedrich-Alexander-Universität Erlangen-Nürnberg (FAU), Feb. 2017. URL: [https://opus4.kobv.de/opus4-fau/files/8678/document\\_Classen.pdf](https://opus4.kobv.de/opus4-fau/files/8678/document_Classen.pdf) (visited on 10/18/2023).
  - [52] Hamamatsu Photonics K.K. *Technical information - R15458-02 (Hemispherical PMT with 80 mm in diameter)*. 2019.
  - [53] A. G. Wright. *The Photomultiplier Handbook*. Oxford University Press, June 2017. ISBN: 9780199565092. DOI: 10.1093/oso/9780199565092.001.0001. URL: <https://doi.org/10.1093/oso/9780199565092.001.0001> (visited on 02/08/2024).
  - [54] William R. Leo. *Techniques for Nuclear and Particle Physics Experiments*. 2nd ed. Springer Berlin, Heidelberg, 1994. DOI: <https://doi.org/10.1007/978-3-642-57920-2>.
  - [55] IceCube Collaboration. *South Pole ice temperature data*. May 14, 2020. DOI: 10.21234/sp-ice-temperature. URL: <https://icecube.wisc.edu/data-releases/2020/05/south-pole-ice-temperature/> (visited on 10/24/2023).
  - [56] L. Greenler et al. “Modeling hole size, lifetime and fuel consumption in hot-water ice drilling”. In: *Annals of Glaciology* 55.68 (2014), pp. 115–123. DOI: 10.3189/2014AoG68A033.
  - [57] IceCube Collaboration. *mDOM Engineering Requirements Document*. Unpublished internal document. URL: [https://uwprod.sharepoint.com/:x:/r/sites/icecubeupgrade/\\_layouts/15/Doc.aspx?sourcedoc=%7BA82231A1-50B3-4F73-977B-E4401BA26FB9%7D&file=mDOM%20ERD.xlsx&action=default&mobileredirect=true](https://uwprod.sharepoint.com/:x:/r/sites/icecubeupgrade/_layouts/15/Doc.aspx?sourcedoc=%7BA82231A1-50B3-4F73-977B-E4401BA26FB9%7D&file=mDOM%20ERD.xlsx&action=default&mobileredirect=true) (visited on 06/12/2023).
  - [58] IceCube Collaboration. *Ice Comms Module (ICM) Firmware Design Status and Notes*. Unpublished internal document. URL: [https://uwprod.sharepoint.com/:p:/r/sites/icecubeupgrade/\\_layouts/15/Doc.aspx?sourcedoc=%7BBBF2F65F-1FC9-4757-97DA-857F983385E4%7D&file=Ice%20Comms%20Module%20Firmware%20DSN.pptx&action=edit&mobileredirect=true](https://uwprod.sharepoint.com/:p:/r/sites/icecubeupgrade/_layouts/15/Doc.aspx?sourcedoc=%7BBBF2F65F-1FC9-4757-97DA-857F983385E4%7D&file=Ice%20Comms%20Module%20Firmware%20DSN.pptx&action=edit&mobileredirect=true) (visited on 11/07/2023).
  - [59] Martin Antonio Unland Elorrieta. “Studies on dark rates induced by radioactive decays of the multi-PMT digital optical module for future IceCube extensions”. Master thesis. Westfälische Wilhelms-Universität Münster, Dec. 2017. URL: [https://www.uni-muenster.de/imperia/md/content/physik\\_kp/agkappes/abschlussarbeiten/masterarbeiten/1712-ma\\_munland.pdf](https://www.uni-muenster.de/imperia/md/content/physik_kp/agkappes/abschlussarbeiten/masterarbeiten/1712-ma_munland.pdf) (visited on 10/25/2023).

- [60] Anna Pollmann. *Private communication*. Aug. 3, 2023.
- [61] Matthias Schust. *Private communication*. Oct. 20, 2023.
- [62] IceCube Collaboration. *mDOM Pressure vessel - Design, Status, and Notes*. Unpublished internal document. URL: [https://uwprod.sharepoint.com/:p:/r/sites/icecubeupgrade/\\_layouts/15/Doc.aspx?sourcedoc=%7BB47CFDA6-70EE-4354-87B6-D002E0F9C01C%7D&file=mDOM%20PV%20DSN.pptx&action=edit&mobileredirect=true](https://uwprod.sharepoint.com/:p:/r/sites/icecubeupgrade/_layouts/15/Doc.aspx?sourcedoc=%7BB47CFDA6-70EE-4354-87B6-D002E0F9C01C%7D&file=mDOM%20PV%20DSN.pptx&action=edit&mobileredirect=true) (visited on 11/18/2023).
- [63] Martin Unland Elorrieta. *Update on optical gel*. Unpublished internal document. mDOM Call, Nov. 27, 2020.
- [64] Roithner Lasertechnik GmbH. *XRL-400-50 Technical data*. 2012. URL: [http://www.roithner-laser.com/datasheets/led\\_div/xrl-400-50.pdf](http://www.roithner-laser.com/datasheets/led_div/xrl-400-50.pdf) (visited on 10/17/2023).
- [65] OSRAM Opto Semiconductors GmbH. *GB CS8PM1.13—OSLON® SSL 80*. 2020. URL: <https://look.ams-osram.com/m/9480b7e0a11ad95/original/GB-CS8PM1-13.pdf> (visited on 10/17/2023).
- [66] Woosik Kang, Christoph Tönnis, and Carsten Rott. “The camera system for the IceCube Upgrade”. In: *Proceedings of 36th International Cosmic Ray Conference — PoS(ICRC2019)*. Vol. 358. 2019, p. 928. DOI: 10.22323/1.358.0928. URL: <https://arxiv.org/pdf/1908.07734.pdf> (visited on 02/08/2024).
- [67] M.A. Unland Elorrieta et al. “Characterisation of the Hamamatsu R12199-01 HA MOD photomultiplier tube for low temperature applications”. In: *Journal of Instrumentation* 14.03 (Mar. 2019), P03015. DOI: 10.1088/1748-0221/14/03/P03015. URL: <https://dx.doi.org/10.1088/1748-0221/14/03/P03015> (visited on 02/08/2024).
- [68] IceCube Collaboration. *mDOM PMT Engineering Requirements Document*. Unpublished internal document. URL: [https://uwprod.sharepoint.com/:x:/r/sites/icecubeupgrade/\\_layouts/15/doc2.aspx?sourcedoc=%7BC6E9E890-1986-47FF-BC6A-40F4E3070FC8%7D&file=mDOM%20PMT%20ERD.xlsx&action=default&mobileredirect=true&cid=6ea64177-e953-4703-96c4-1f38b13bbb55](https://uwprod.sharepoint.com/:x:/r/sites/icecubeupgrade/_layouts/15/doc2.aspx?sourcedoc=%7BC6E9E890-1986-47FF-BC6A-40F4E3070FC8%7D&file=mDOM%20PMT%20ERD.xlsx&action=default&mobileredirect=true&cid=6ea64177-e953-4703-96c4-1f38b13bbb55) (visited on 06/12/2023).
- [69] S. Niedworok/Deutsches Elektronen-Synchrotron DESY. Jan. 2023.
- [70] IceCube Collaboration. *mDOM Mainboard Engineering Requirements Document*. Unpublished internal document. URL: [https://uwprod.sharepoint.com/:x:/r/sites/icecubeupgrade/\\_layouts/15/doc2.aspx?sourcedoc=%7BF6957087-B865-4241-8CCD-3EE37ACC04F2%7D&file=mDOM%20Mainboard%20ERD.xlsx&action=default&mobileredirect=true&cid=069dbdc9-2a10-495c-a018-6a54821c8420](https://uwprod.sharepoint.com/:x:/r/sites/icecubeupgrade/_layouts/15/doc2.aspx?sourcedoc=%7BF6957087-B865-4241-8CCD-3EE37ACC04F2%7D&file=mDOM%20Mainboard%20ERD.xlsx&action=default&mobileredirect=true&cid=069dbdc9-2a10-495c-a018-6a54821c8420) (visited on 06/12/2023).
- [71] Karl-Heinz Sulanke. *Private communication*. Feb. 22, 2022.
- [72] Tyler Anderson et al. (IceCube Collaboration). “Design and Performance of the mDOM Mainboard for the IceCube Upgrade”. In: *Proceedings of 38th International Cosmic Ray Conference — PoS(ICRC2023)*. Vol. 444. 2023, p. 967. DOI: 10.22323/1.444.0967.
- [73] Hamamatsu Photonics K.K. *Final test sheet photomultiplier tube type R12199-01 HA*. 2018.
- [74] HZC. *PMT final test sheet*. 2019.
- [75] Hamamatsu Photonics K.K. *Final test sheet photomultiplier tube type R15458-02*. 2020.

- 
- [76] Hamamatsu Photonics K.K. *Final test sheet photomultiplier tube type R15458-20*. 2020.
  - [77] Hamamatsu K.K. *MMC and MPPC module for precision measurement*. accessed: 4.10.2017. URL: [http://www.hamamatsu.com/resources/pdf/ssd/mppc\\_kapd0004e.pdf](http://www.hamamatsu.com/resources/pdf/ssd/mppc_kapd0004e.pdf).
  - [78] HZC Photonics. *HZC Photonics website*. site inactive on 2022-11-15. URL: [http://web.archive.org/web/20190816095709/http://www.hzcphotonics.com/en\\_index.html](http://web.archive.org/web/20190816095709/http://www.hzcphotonics.com/en_index.html) (visited on 11/15/2022).
  - [79] LeCroy Corporation. *WaveRunner 6000 Series*. 2004. URL: <https://www.valuetronics.com/pub/media/vti/datasheets/LeCroy%20WaveRunner%206000%20Series.pdf> (visited on 11/02/2022).
  - [80] PicoQuant GmbH. *PLS Series—Sub-nanosecond Pulsed LEDs for PDL 800-B/-D/828*. 2018. URL: [https://www.picoquant.com/images/uploads/downloads/pls\\_series.pdf](https://www.picoquant.com/images/uploads/downloads/pls_series.pdf) (visited on 11/02/2022).
  - [81] PicoQuant GmbH. *PDL 800-B Picosecond Pulsed Diode Laser Driver*. 2018. URL: <https://www.picoquant.com/images/uploads/downloads/pdl800-b.pdf> (visited on 11/02/2022).
  - [82] E. H. Bellamy et al. “Absolute calibration and monitoring of a spectrometric channel using a photomultiplier”. In: *Nuclear Instruments and Methods in Physics Research* 339.3 (1994), pp. 468–476. DOI: [https://doi.org/10.1016/0168-9002\(94\)90183-X](https://doi.org/10.1016/0168-9002(94)90183-X).
  - [83] LOT-QuantumDesign Europe. *Arc light sources 50 - 150 W arc light source*. URL: [https://qd-uki.co.uk/wp-content/uploads/2019/06/50-150W-arc-light-sourcesLQ\\_50\\_150\\_w\\_arc\\_light\\_source\\_eu.pdf](https://qd-uki.co.uk/wp-content/uploads/2019/06/50-150W-arc-light-sourcesLQ_50_150_w_arc_light_source_eu.pdf) (visited on 11/02/2022).
  - [84] LOT-QuantumDesign Europe. *Xenon arc light sources 75-150 W*. URL: [https://qd-europe.com/fileadmin/Mediapool/products/lightsources/en/Xenon\\_arc\\_light\\_sources\\_75\\_150\\_W.pdf](https://qd-europe.com/fileadmin/Mediapool/products/lightsources/en/Xenon_arc_light_sources_75_150_W.pdf) (visited on 11/23/2022).
  - [85] Hamamatsu Photonics K.K. *Si photodiode S6337-01—Large area photodiode for UV to IR, precision photometry*. 2004. URL: <https://s1.dtsheet.com/store/data/000749932.pdf?key=594169a02d47e415f1aa1ec3f9083cc6&r=1> (visited on 11/02/2022).
  - [86] IceCube Collaboration. *Ice Comms Module (ICM) Engineering Requirements Document*. Unpublished internal document. URL: [https://uwprod.sharepoint.com/:x:/r/sites/icecubeupgrade/\\_layouts/15/Doc.aspx?sourcedoc=%7BE5EA84F6-5D9B-4107-9C09-684924676DF4%7D&file=Ice%20Comms%20Module%20ERD.xlsx&action=default&mobileredirect=true](https://uwprod.sharepoint.com/:x:/r/sites/icecubeupgrade/_layouts/15/Doc.aspx?sourcedoc=%7BE5EA84F6-5D9B-4107-9C09-684924676DF4%7D&file=Ice%20Comms%20Module%20ERD.xlsx&action=default&mobileredirect=true) (visited on 06/12/2023).
  - [87] Phidgets Incorporated. *Precision Temperature Sensor 1124\_0*. 2022. URL: [https://www.phidgets.com/?tier=3&catid=14&pcid=12&prodid=95#Technical\\_Details](https://www.phidgets.com/?tier=3&catid=14&pcid=12&prodid=95#Technical_Details) (visited on 11/16/2022).
  - [88] A. Eimer. “Measurement of PMT dark rates for the IceCube mDOM”. Bachelor’s Thesis. Friedrich-Alexander-Universität Erlangen-Nürnberg, 2021. URL: [https://ecap.nat.fau.de/wp-content/uploads/2021/05/Bachelor\\_thesis\\_Anna\\_Eimer.pdf](https://ecap.nat.fau.de/wp-content/uploads/2021/05/Bachelor_thesis_Anna_Eimer.pdf) (visited on 11/02/2022).
  - [89] Gary J. Feldman and Robert D. Cousins. “Unified approach to the classical statistical analysis of small signals”. In: *Phys. Rev. D* 57 (7 Apr. 1998), pp. 3873–3889. DOI: 10.1103/PhysRevD.57.3873. URL: <https://link.aps.org/doi/10.1103/PhysRevD.57.3873> (visited on 04/16/2024).

- [90] Lasse Halve and Johannes Werthebach. *Design of an Efficient, High-Throughput Photomultiplier Tube Testing Facility for the IceCube Upgrade*. 2021. DOI: 10.48550/ARXIV.2107.09954. URL: <https://arxiv.org/abs/2107.09954> (visited on 02/08/2024).
- [91] IceCube Collaboration. *OM requirements task force*. Unpublished internal document. (Visited on 03/07/2023).
- [92] Roithner LaserTechnik GmbH. *XSL-370-TB-4 UV—LED, TO46 with glass ball lens*. 2010. URL: [http://www.roithner-laser.com/datasheets/led\\_div/xsl-370-tb-4.pdf](http://www.roithner-laser.com/datasheets/led_div/xsl-370-tb-4.pdf) (visited on 11/17/2022).
- [93] Christian Fruck, Felix Henningsen, and Christian Spannfellner. “The POCAM as self-calibrating light source for the IceCube Upgrade”. In: *Proceedings of 36th International Cosmic Ray Conference — PoS(ICRC2019)*. Vol. 358. 2019, p. 908. DOI: 10.22323/1.358.0908.
- [94] Texas Instruments Incorporated. *TMP116 High-Accuracy, Low-Power, Digital Temperature Sensor With SMBus- and I2C-Compatible Interface*. 2017. URL: <https://www.ti.com/general/docs/suppproductinfo.tsp?distId=26&gotoUrl=https://www.ti.com/lit/gpn/tmp116> (visited on 03/02/2023).
- [95] Teledyne Signal Processing Devices Sweden AB. *ADQ14 Datasheet*. 2021. URL: [https://www.spdevices.com/images/stories/data\\_sheets/14-1290-ADQ14-datasheet.pdf](https://www.spdevices.com/images/stories/data_sheets/14-1290-ADQ14-datasheet.pdf) (visited on 03/09/2023).
- [96] Analog Devices. *Rail-to-Rail, Very Fast, 2.5 V to 5.5 V, Single-Supply TTL/CMOS Comparators ADCMP600/ADCMP601/ADCMP602*. 2006-2011. URL: [https://www.analog.com/media/en/technical-documentation/data-sheets/adcmp600\\_601\\_602.pdf](https://www.analog.com/media/en/technical-documentation/data-sheets/adcmp600_601_602.pdf) (visited on 02/15/2023).
- [97] Thorlabs incorporated. *NDC-50C-4 - Unmounted Continuously Variable ND Filter, Ø50 mm, OD: 0.04 - 4.0*. 2004. URL: <https://www.thorlabs.com/thorproduct.cfm?partnumber=NDC-50C-4> (visited on 02/23/2023).
- [98] Thorlabs incorporated. *Mounted Si Photodiode SM1PD2A*. 2017. URL: <https://www.thorlabs.com/drawings/f5cec17d1816a25a-57DF1DD9-F5BE-DEAB-D663D1BC52E6663D/SM1PD2A-SpecSheet.pdf> (visited on 02/15/2023).
- [99] RIGOL TECHNOLOGIES GmbH. *DG1000Z Series—Function/Arbitrary Waveform Generator*. 2016. URL: [https://cdn-reichelt.de/documents/datenblatt/D100/DG1000Z\\_DS-EN.pdf](https://cdn-reichelt.de/documents/datenblatt/D100/DG1000Z_DS-EN.pdf) (visited on 02/15/2023).
- [100] PicoQuant GmbH. *PDL 800-D Picosecond Pulsed Diode Laser Driver*. 2018. URL: <https://www.picoquant.com/images/uploads/downloads/pdl800-d.pdf> (visited on 02/15/2023).
- [101] PicoQuant GmbH. *LDH Series—Picosecond Laser Diode Heads for PDL 800-D/PDL 828*. 2022. URL: [https://www.picoquant.com/images/uploads/downloads/17-ldh\\_series\\_3.pdf](https://www.picoquant.com/images/uploads/downloads/17-ldh_series_3.pdf) (visited on 02/15/2023).
- [102] Thorlabs incorporated. *Continuously variable ND filter*. 2014. URL: <https://www.thorlabs.com/drawings/f5cec17d1816a25a-57DF1DD9-F5BE-DEAB-D663D1BC52E6663D/NDC-50C-4-A-AutoCADPDF.pdf> (visited on 02/15/2023).
- [103] Texas Instruments. *OPA838 1-mA, 300-MHz Gain Bandwidth, Voltage-Feedback Op Amp*. 2023. URL: <https://www.ti.com/lit/gpn/opa838> (visited on 03/06/2024).

- 
- [104] Texas Instruments. *OPA836 Very-Low-Power, Rail-to-Rail Out, Negative Rail In, Voltage-Feedback Operational Amplifiers*. 2021. URL: <https://www.ti.com/lit/gpn/opa836> (visited on 03/06/2024).
  - [105] Rezvan Abbasi et al. “Calibration and Characterization of the IceCube Photomultiplier Tube”. In: *Nuclear Instruments and Methods in Physics Research Section A Accelerators Spectrometers Detectors and Associated Equipment* 618 (July 2010), pp. 139–152. DOI: 10.1016/j.nima.2010.03.102.
  - [106] 3M. *Product Data Sheet—3M™ Conductive Film Products*. 2014. URL: [https://www.mouser.com/datasheet/2/107/desco\\_2004-543330.pdf](https://www.mouser.com/datasheet/2/107/desco_2004-543330.pdf) (visited on 06/19/2023).
  - [107] Comsol Multiphysics GmbH. *Comsol Multiphysics website*. 2024. URL: <https://www.comsol.de> (visited on 03/11/2024).
  - [108] Arbeitsgruppe Prof. Kappes. *Private communication*. Oct. 31, 2023.
  - [109] Christopher Wendt. *Private communication*. May 18, 2021.
  - [110] Sarah Mechbal. *IceCube Upgrade Hardware Meeting*. Unpublished internal document. Oct. 4, 2021. URL: <https://confluence.desy.de/pages/viewpage.action?spaceKey=ICECUBEMDOM&title=2021-10-04+IceCube+Upgrade+HW+Meeting>.
  - [111] Xilinx. *7 Series FPGAs Data Sheet: Overview*. 2020. URL: [https://docs.xilinx.com/v/u/en-US/ds180\\_7Series\\_Overview](https://docs.xilinx.com/v/u/en-US/ds180_7Series_Overview) (visited on 11/08/2023).
  - [112] Inc Analog Devices. *Low Noise, Low Drift, Low Power, 3-Axis MEMS Accelerometers - Datasheet ADXL354/ADXL355*. 2016-2018.
  - [113] Texas Instruments Incorporated. *TMP10x Temperature Sensor With I2C and SMBus Interface with Alert Function in SOT-23 Package*. 2002-2015. URL: <https://www.ti.com/lit/gpn/tmp101> (visited on 11/08/2023).
  - [114] STMicroelectronics. *LPS22HB - MEMS nano pressure sensor: 260-1260 hPa absolute digital output barometer - Datasheet*. 2017.
  - [115] Texas Instruments Incorporated. *TMP1075 Temperature Sensor With I2C and SMBus Interface in Industry Standard LM75 Form Factor and Pinout*. 2018-2021. URL: <https://www.ti.com/lit/gpn/tmp1075> (visited on 11/08/2023).
  - [116] Christopher Wendt. *Private communication*. Mar. 2, 2021.
  - [117] Bosch Sensortec GmbH. *BME280 - Combined humidity and pressure sensor - Datasheet*. 2022. URL: <https://www.bosch-sensortec.com/media/boschsensortec/downloads/datasheets/bst-bme280-ds002.pdf> (visited on 11/08/2023).



# Danksagung

Abschließend möchte ich mich bei folgenden Personen bedanken, die mich während meiner gesamten Arbeit unterstützt und begleitet haben. Mein besonderer Dank geht an:

**Prof. Dr. Gisela Anton** für die Möglichkeit, in diesem sehr spannenden Themenbereich zu promovieren und die mich immer voller Begeisterung unterstützt hat und bei schwierigen Entscheidungen zur Seite stand.

**Jonas Reubelt** für die hervorragende Betreuung, Unterstützung und Hilfe bei jeglichen Problemen selbst noch nach offiziellem Ausscheiden aus der Universität. Er hat sich immer viel Zeit für mich genommen. Die Zusammenarbeit war richtig toll, hat mir sehr viel Spaß gemacht und ich habe wahnsinnig viel gelernt.

**Dr. Timo Karg** für die Ermöglichung und Betreuung der mDOM-Arbeit am DESY, Standort Zeuthen. Auch nach Ende meines Aufenthalts am DESY konnte ich jederzeit Fragen aller Art stellen und er hat sich immer sehr viel Zeit genommen! Das war nicht selbstverständlich und ich bin sehr dankbar dafür!

**Prof. Dr. Uli Katz** für sein Verständnis, offenes Ohr, die Hilfe und Unterstützung sowie seine Einwilligung, mein Zweitgutachter zu sein.

**Karl-Heinz Sulanke** der mir jederzeit und geduldig meine Fragen zu Elektronik beantwortet hat und Änderungen an meinem Versuchsaufbau vorgenommen hat, als ich nicht mehr am DESY sein konnte.

**Die gesamte IceCube-Upgrade-Hardware-Gruppe am DESY** für die supernette Aufnahme in die Gruppe und die tolle Zusammenarbeit. Es war eine wundervolle Arbeitsatmosphäre, in der ich jederzeit Hilfe und Unterstützung erhalten habe.

**Meine Bürokollegen** für die angenehme Arbeitsatmosphäre, in der ich mich sehr wohl gefühlt habe. Ganz besonders möchte ich mich bei meinen langjährigen Bürokollegen Gerrit Wrede, Sebastian Schindler und Sebastian Fiedlschuster bedanken für die Unterstützung, die tollen Gespräche und das Verständnis! Zusammen haben wir einige Veränderungen erlebt und uns gegenseitig geholfen.

**Oleg Kalekin** für die Einblicke in die DOM-Integration, insbesondere dem Gelgießen, die Zeit und Geduld beim Erklären vieler PMT-Zusammenhänge, dadurch habe ich sehr viel gelernt!

**Rodrigo Gracia-Ruiz** für die Geduld beim Korrekturlesen und die Zeit, die er sich genommen hast, um mir einige physikalischen Zusammenhänge zu erklären.

**Tamas Gal, Johannes Schumann, Nicole Geißelbrecht** für den Spaß beim Gelgießen, Mittag essen, Gespräche im Gang, im Büro oder sonstwo.

**Meine Bürokollegen am DESY** für die nette Aufnahme, die Hilfe und Unterstützung.

**Prof. Dr. Claudio Kopper** und die gesamte IceCube-Arbeitsgruppe am ECAP für die Hilfe und Unterstützung, sowie die angenehme Arbeitsatmosphäre.

**Max Schuster** für seine Hilfsbereitschaft bei meinen Fragen zu Abläufen in verschiedenen Bereichen.

**Alle weiteren Mitarbeitenden** am ECAP, DESY und in der IceCube-Kollaboration, auch den nichtwissenschaftlichen Mitarbeitenden, sowie Frau Wöhler und ihrer Familie für die freundliche Aufnahme und Unterstützung.

**Meine Familie und Freunde** für die aufopfernde Unterstützung und Anteilnahme in jeglicher Form und den unterschiedlichsten Bereichen.

**Alle weiteren Personen** die ich nicht erwähnt habe für die Unterstützung während meiner Dissertation.